Development of Finite Element Models for Orbital Soft Tissues and Extra-Ocular Muscles

Thesis is submitted in accordance with the requirements of the University of Liverpool for the degree of Doctor in Philosophy

by

Ahmed Makarem (MEng (Hons) (University of Liverpool))

September 2022

Abstract

Studying the movement of the eye globe has significant implications for understanding the ocular support system and its response to exterior frontal loading. Existing numerical models of the ocular support system were either restricted to static simulation or simplified orbital mechanics and geometry. This project presents a novel three-dimensional (3D) biomechanical model of the ocular system to address the previously mentioned limitations. This project aims to lay the foundation for a biomechanical extra-ocular numerical representation that could be utilised in clinical applications and scientific research. First, a semi-automatic segmentation method was developed to acquire and reconstruct a 3D representation of the orbital wall through computerised tomography scans (CT scans). The reconstruction used literature-available ethnic-related data of the orbital rim. Numerical models of the eye globe were produced through the Ocular Mesh Generator developed by the Biomechanical Engineering group at the University of Liverpool. These models were used as a foundation to create the surrounding extra-ocular environment. We then describe the novel meshing technique that discretises the orbital medium using continuum elements. Furthermore, an overview of the custom-built software code, Orbital Mesh Generator (OMG), will be outlined. The OMG will facilitate the creation of numerical models that will then be used for various scientific research.

The orbital model was utilised in a few studies, producing new findings or confirming previously stated findings. First, a material optimisation process confirmed the significant role extra-ocular soft tissues (excluding adipose fatty tissue) have in supporting the globe. Second, the gradual addition of the extra-ocular muscles (EOMs) showed the significance of the oblique muscles in supporting the eye globe against frontal load-

ing. Consequently, the EOM primary gaze initial tension was used in a custom-built algorithm to optimise muscle actions during the loading phase of the Corvis procedure.

The OST model was utilised in a parametric study to estimate corneal material stiffness (SSI_o) and biomechanically corrected IOP (bIOP_o) through two separate algorithms. The outcome of these algorithms was validated using previously published experimental data and various clinical datasets of corneal response to Corvis. The results showed that the newly developed method of measuring IOP performed better than Corvis' and the current IOP. However, bIOP_o consistently underestimated IOP; hence it is not recommended for this method to be used clinically. The predicted IOP values either showed weak or no correlation with corneal biomechanics and age. The newly estimated biomechanical values have shown either no or weak correlation with IOP and corneal geometry and showed a strong correlation with age, indicating the change in corneal material stiffness. The experimental validation showed excellent agreement between in-vivo and ex-vivo measurements.

This research has produced a custom-built software code that produces a validated numerical representation. This representation of the visual support system can be developed further by adding intraocular components and assessing the progression of ophthalmological conditions such as retinal detachment.

Acknowledgements

I would like to acknowledge my supervisors, Professor A. Elsheikh, Dr A. Abass and Dr Xiaoyu Liu. I would also like to extend my thanks to Dr A. Aboulatta for his generous support and all the colleagues, both past and present, in the Biomechanics Group at the University of Liverpool for fruitful discussions and for creating a stimulating working environment over the past four years.

I particularly wish to thank Professor A. Elsheikh, without whom I would certainly have been lost. His encouragement and ideas were of utmost help to this work and are very much appreciated.

Last but not least, this endeavour would not have been possible without mi parents and brother's tremendous patience and support (in all its forms). I would also like to thank all mi friends for their generous support.

Declaration

I confirm that the thesis is my work, that I have not presented anyone's work as my own and that full and appropriate acknowledgement has been given where reference has been made to the work of others.

Ahmed Makarem

September 2022

List of Publications

- Aboulatta, A., Abass, A., Makarem, A., Eliasy, A., Zhou, D., Chen, D., Liu, X. and Elsheikh, A., 2021. Experimental evaluation of the viscoelasticity of porcine vitreous. Journal of the Royal Society Interface, 18(175), p.20200849.

- Makarem, A., Aboulatta, A., Abass, A., Elsheikh, A., Evaluation of Extra-Ocular Muscles' Role in the Ocular Support System (under review by *Frontiers in Bioengineering and Biotechnology*)

- Makarem, A., A., Abass, A., Elsheikh, A., Assessment of Age-related Change in the Ocular Support System (under review by *Frontiers in Bioengineering and Biotechnology*)

Table of Contents

List of Figures

List of Tables

Nomenclature

Acronyms

A

AFT *Adipose Fatty Tissue*
A1 *First Applanation*
A1L *A1 Length*
A1T *Applanation 1 Time*
A1V *Velocity*
ACG *Angle-closure Glaucoma*
AO *American Optical*
AP1 *Applanation Pressure 1*

B

BFS *Best Fit Sphere*
BioEG *Biomechanical Engineering Group*
bIOP *Biomechanically Corrected Intraocular Pressure*
bPar *Base Parameters*

C

CBI *Corneal Biomechanical Index*
CCT *Central Corneal Thickness*
CH *Corneal Hysteresis*
CL *Check Ligament*
CRF *Corneal Resistant Factor*
CVS *Corneal Biomechanical Index*
IOP$_{CVS}$ *Corneal Biomechanical Index*
CXL *corneal crosslinking*

D

DCR *Dynamic Corneal Response*
DCR *Dynamic Corneal Response*
DCT *Dynamic Contour Tonometry*
DeflAmpA1 *A1 Deflection Amplitude*
DeflAmpA1 *A1 Deflection Amplitude*
DeflAmpMax *Deflection Amplitude Maximum*

E

E *Young's Modulus*
EleFBFS8mm *Best Fit Sphere within 8mm Diameter*
E$_t$ *Tangent Modulus*

F

fIOP *Fluid Structure Interaction IOP*

G

GAT *Goldman Applanation Tonometry*

H

HC *Highest Concavity*
HCR *Radius at HC*
HCT *Highest Concavity Time*

I

IOP *Intraocular Pressure*
IOP$_{cc}$ *Corneal Compensated IOP*
IOP$_t$ *True Intraocular Pressure*
IOP$_g$ *Goldmann correlated IOP*

M

MD *Mean Deviation*
mmHg *Millimetre of Mercury*

N

NCT *Non-Contact Tonometry*
NTG *Normal-Tension Glaucoma*

O

OAG *Open-Angle Glaucoma*
OHT *Ocular Hypertension*
ONH *Optic Nerves Head*
ORA *Ocular Response Analyzer*

P

PCT *Peripheral Corneal Thickness*
PD *Peak Distance*

Q

QS *Quality Score*

R

Rmin *Minimum Radius of Curvature*

S

S *Sphericity*
SP *Stiffness Parameter*
SPA1 *Stiffness Parameter at A1*
SPHC *Stiffness Parameter at HC*
SSI *Stress-Strain Index*

W

WEM *Whole Eye Movement*

Ophthalmology Terms

Accommodation *ability of the eye to change its focus between distant objects and near objects.*

Angle (Drainage Angle) *drainage area of the eye formed between the cornea and the iris , named for its angular shape, which is why you see the word "angle" in the different glaucoma names.*

Anterior Chamber Space between the cornea and the crystalline lens , which contains aqueous humor.

Anterior ocular segment *part of the eye anterior to the crystalline lens , including the cornea , anterior chamber , iris and ciliary body.*

Aqueous humor *transparent fluid occupying the anterior chamber and maintains eye pressure.*

Choroid *the thin layer of major blood vessels that lies between the retina and sclera. The choroid supplies the retina with vital oxygen and nutrients. It thickens at the front of the eye to form the ciliary body.*

Ciliary body *the ring of muscle fibers that holds the lens of the eye. It also helps control intraocular pressure.*

Ciliary processes *the portion of the ciliary body that produces the eye's aqueous humor.*

Cornea *the dome-shaped window of the eye that provides most of the eye's optical power. Light enters through the cornea and is refracted by the cornea's angle toward the back of the eye.*

Emmetropia (the normal eye) *light focuses precisely on the retina, and near and far objects are seen clearly.*

Glaucoma *a group of diseases that result from increased intraocular pressure, which can result in damage to the optic nerve. A common cause of preventable vision loss.*

Myopia (nearsightedness) *a condition in which the visual images come to a focus in front of the retina of the eye because of defects in the refractive media of the eye or because of abnormal length of the eyeball, resulting especially in defective vision of* *distant objects.*

Optic nerve *the largest nerve of the eye. Comprised of retinal nerve fibers (but no rods and cones), the optic nerve connects the retina to the primary visual cortex of the brain. Visual input from the retina travels along the nerve fibers of the optic nerve to the brain. The brain interprets images sent by the optic nerve of each eye, reverses the images, and integrates them into the one three-dimensional image that you see.*

Sclera *the tough outermost layer of the eye joining the cornea; the visible part is the white of the eye. The sclera has a transparent covering, the conjunctiva. The sclera helps maintain the eyeball's shape, which is about one inch (25mm) in diameter.*

Strabismus *eye misalignment caused by an imbalance in the muscles holding the eyeball.*

Trabecular meshwork *the series of canals or tubes behind the iris that filters the aqueous humor and allows it to drain into the bloodstream.*

Uvea *the blood vessel-rich pigmented layers of the eye. It includes the iris, ciliary body and choroid. It contains the majority of the eye's blood vessels.*

Vitreous or vitreous humor *the clear jelly that fills the eyeball behind the lens. It helps support the shape of the eye and transmits light to the retina.*

With appreciation for guidance from the Dictionary of Eye Terminology, Second Edition, (1990), Barbara Cassin and Sheila A.B. Solomon, Melvin L. Rubin, M.D.[48]

Nomenclature

Abstract

Studying the movement of the eye globe has significant implications for understanding the ocular support system and its response to exterior frontal loading. Existing numerical models of the ocular support system were either restricted to static simulation or simplified orbital mechanics and geometry. This project presents a novel three-dimensional (3D) biomechanical model of the ocular system to address the previously mentioned limitations. This project aims to lay the foundation for a biomechanical extra-ocular numerical representation that could be utilised in clinical applications and scientific research. First, a semi-automatic segmentation method was developed to acquire and reconstruct a 3D representation of the orbital wall through computerised tomography scans (CT scans). The reconstruction used literature-available ethnic-related data of the orbital rim. Numerical models of the eye globe were produced through the Ocular Mesh Generator developed by the Biomechanical Engineering group at the University of Liverpool. These models were used as a foundation to create the surrounding extra-ocular environment. We then describe the novel meshing technique that discretises the orbital medium using continuum elements. Furthermore, an overview of the custom-built software code, Orbital Mesh Generator (OMG), will be outlined. The OMG will facilitate the creation of numerical models that will then be used for various scientific research.

The orbital model was utilised in a few studies, producing new findings or confirming previously stated findings. First, a material optimisation process confirmed the significant role extra-ocular soft tissues (excluding adipose fatty tissue) have in supporting the globe. Second, the gradual addition of the extra-ocular muscles (EOMs) showed the significance of the oblique muscles in supporting the eye globe against frontal load-

ing. Consequently, the EOM primary gaze initial tension was used in a custom-built algorithm to optimise muscle actions during the loading phase of the Corvis procedure.

The OST model was utilised in a parametric study to estimate corneal material stiffness (SSI_o) and biomechanically corrected IOP ($bIOP_o$) through two separate algorithms. The outcome of these algorithms was validated using previously published experimental data and various clinical datasets of corneal response to Corvis. The results showed that the newly developed method of measuring IOP performed better than Corvis' and the current IOP. However, $bIOP_o$ consistently underestimated IOP; hence it is not recommended for this method to be used clinically. The predicted IOP values either showed weak or no correlation with corneal biomechanics and age. The newly estimated biomechanical values have shown either no or weak correlation with IOP and corneal geometry and showed a strong correlation with age, indicating the change in corneal material stiffness. The experimental validation showed excellent agreement between in-vivo and ex-vivo measurements.

This research has produced a custom-built software code that produces a validated numerical representation. This representation of the visual support system can be developed further by adding intraocular components and assessing the progression of ophthalmological conditions such as retinal detachment.

Chapter 1

Introduction

1.1 Preface

Since ancient times, the eye has been known to be the organ responsible for vision; however, philosophers and scientists had many conflicting interpretations of how vision occurred. In the 4^{th} century B.C., Plato suggested that light rays were ejected from the eye, ensnaring an object, hence having the ability to see it. At this time, little was known about anatomy as dissection of human cadavers was not permitted and was frowned upon.[49] Despite lack of knowledge, Aristotle did not agree with Plato's theory and suggested that the eye received light rays rather than emit them, Figure 1.1.[50] In his book (*De Generatione Animalium*), Aristotle related that the change in eye colour may have been due to glaucoma.[51] A few centuries later, Demosthenes Philalethes continued Aristotle's work and described the colouration of the lens, which was assumed to be incurable.[52] During that time, cataract and glaucoma were confused, and it was thought both conditions caused stiffening of the ocular vessel.

In the 2^{nd} century, Galen, who helped create ophthalmology as a separate science went against Aristotle's theory and hypothesised that the light flowed from the brain through empty tubes to emit from the eye, calling it the emission theory. Galen also endorsed the view of Alexandria's anatomists, including Herophilus, who led the "*Golden Age of Greek Medicine*", which interestingly took place in Egypt.[49]

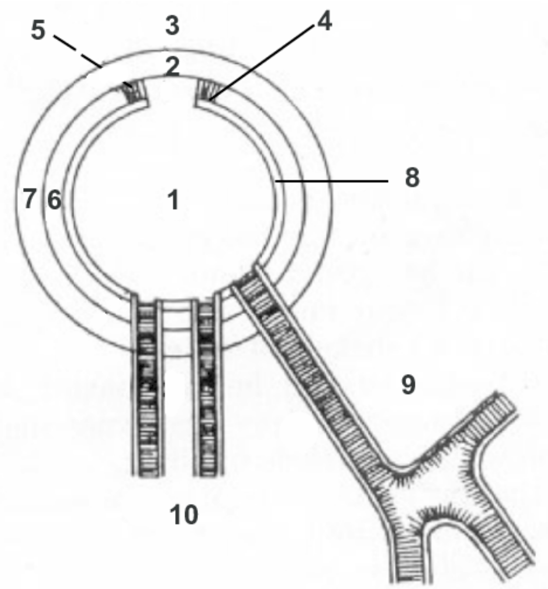

Figure 1.1: Depiction of the eye as Aristotle has conceived it. (1) Fluid. (2) Visual spirit. (3) Pupil. (4) Iris. (5) Cornea. (6) Choroid. (7) Sclera. (8) Arachnoid. (9) Vein to the eye. (10) Optic nerves.[1]

A leap in the medical field took place with the permission to dissect cadavers.[49] This action led to discovering the majority of the visual system, such as the retina, vitreous and aqueous humor, and the bony orbit where the eye rests. In the 10^{th} century, anatomical knowledge helped shed light on the contraction and dilation of the pupil, which agreed with the Aristotelian theory rather than Galen's long-lived emission theory.[50] Shortly after that, Ibn Sina outlined an examination process for glaucoma with ocular palpation and consequently suggested that those with stiffening in the cornea were less suitable for cataract surgery.[52] Ibn Sina also commenced work to improve the design of convex lenses, which Alhazen continued to explore in detail, based on the principles of image formation produced by light refraction.[53] With this knowledge, reading small texts on stones gradually became more common.[54] Also, in the 10^{th} century, Vesalius and Alessandro Achillini denied hollowness of the optic nerve, but shortly after that, Felix Platter asserted its importance in vision transmission.[50] With the lifting of the illegality of cadaver dissection for educational reasons, the early 10^{th} century witnessed significant advances in anatomical knowledge, which led to the theory of image formation on the retina suggested by Kepler.[50]

After much progress in subsequent centuries, Wilhelm Röntgen kick-started medical radiology in 1895 by discovering X-rays, which aroused scientists' interest,[55] leading, for example, to the X-ray radiograph of the human skull, shown in Figure 1.2. Despite the details of skull boundaries and main features, what was inside the bony structure remained invisible. It was only in 1925 when Harry A. Goalwin proposed an annotated head cap to align the subject's optic canal trajectory to horizontal and sagittal planes. This alignment methodology was improved over the following decades, allowing reproducible images of the canal.[56]

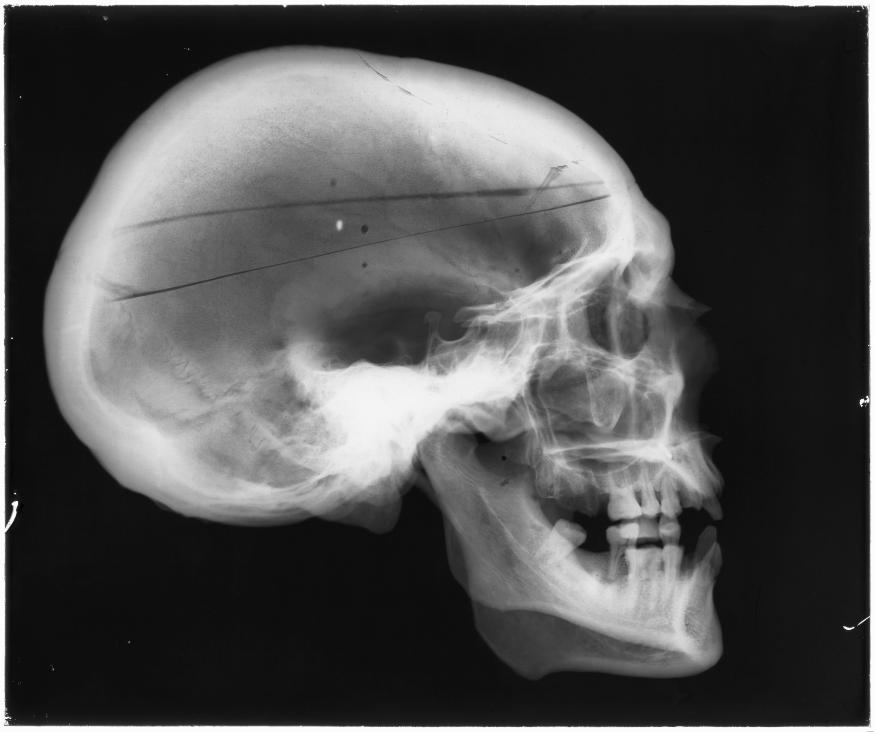

Figure 1.2: First radiograph of the human skull in 1901[2]

Röntgen's radiography technique remained dominant until the 1970s when Godfrey Hounsfield invented Computerised Axial Tomography (CAT or CT), Figure 1.3.[3] By the end of the 1970s, much work was being carried out on CT imaging leading to the rise of helical multi-slice scanners.[3] In the latter part of the 19^{th} and early 20^{th} century, and to assist glaucoma management, Von Graefe invented the first tonometer. Then Maklakoff developed the first relatively accurate applanation tonometer.[57] This progress allowed regular clinical monitoring of intraocular pressure (IOP), hence associating its elevation to glaucoma.[58] From the late 20^{th} century, the field of ophthalmology has seen fast developments with the characterisation of ocular biomechanics. This characterisation has allowed major work to transform the diagnosis and therapy of eye conditions.[59] This research builds on this progress and uses modern computing technologies to aid the progression of the field, ultimately reducing misdiagnosis and improving clinical practice.

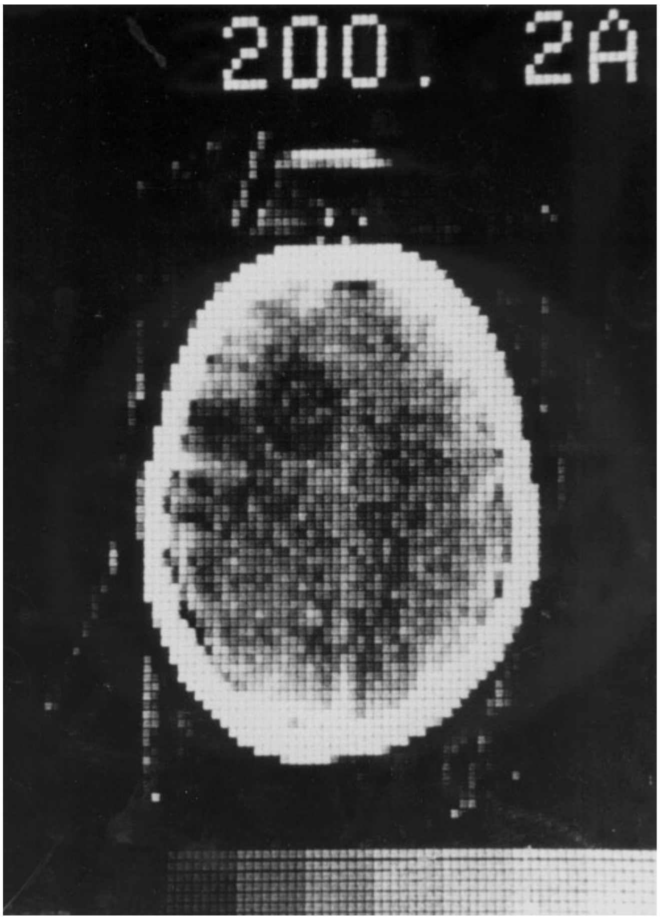

Figure 1.3: First patient image scanned on Computerised Axial Tomography prototype[3]

1.2 Background

1.2.1 Ocular system

The ocular system comprises the eye globe and orbital soft tissues (OST), including extraocular muscles and adipose fatty tissue, which are all bounded by the orbit. The orbit is a bony structure comprised of *four* walls, see Figure 1.4; superior(roof), inferior(floor), medial and lateral walls. The lateral rotation of the orbital structure causes the lateral wall to have a 45^o angle with its respective medial wall, giving the structure a conical-shaped structure within the skull.[60] Due to this rotation, the lateral portion of the orbital rim is the utmost posterior point. The orbital volume is roughly $30mL$, where the globe acquires less than a third of this volume while the other orbital soft tissues share the remaining two-thirds.[11,61] Orbital volume varies between individuals depending on gender and ethnicity. Hence this fact was considered within the numerical model developed for this project.[37]

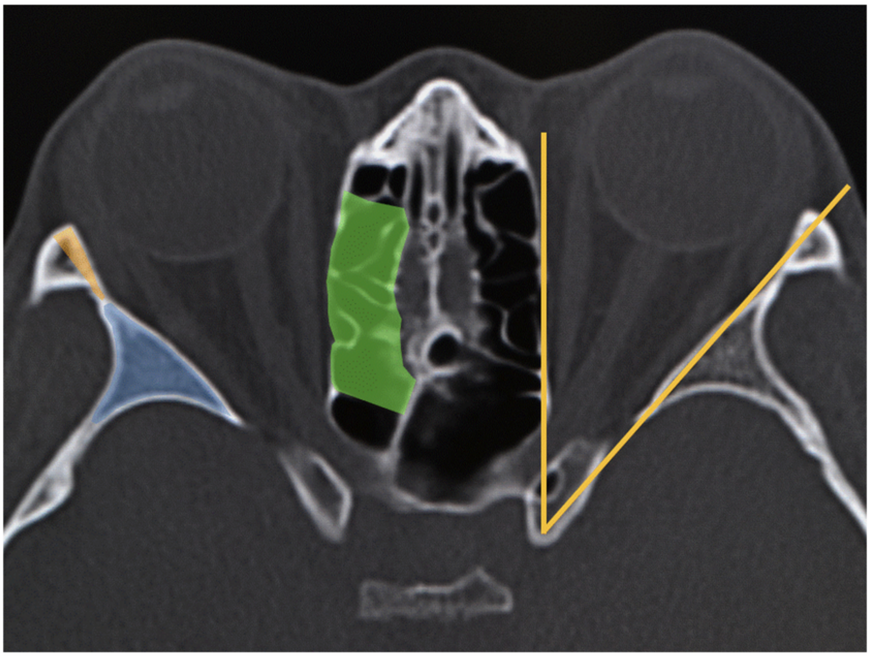

Figure 1.4: Axial computed tomographic image of the orbit. The lateral walls are oriented to an angle of 45^o lateral to the sagittal plane, whereas the medial walls of each orbit are oriented in the sagittal plane (the yellow solid lines)[4]

The globe is an organ that relays light to the brain via the optic nerve; hence, the vision was made possible. This optic organ comprises *three* three-layered chambers arranged posterior to one another. First, the inner layer mainly outlines a chamber filled with vitreous humor with the retina. The vitreous is a clear thick fluid, allowing light to travel through and providing rigidity to the globe. Secondly, the middle layer includes the iris, ciliary body, pigmented epithelium and choroid. Finally, the fibrous outermost exterior layer includes the cornea and sclera.[62]

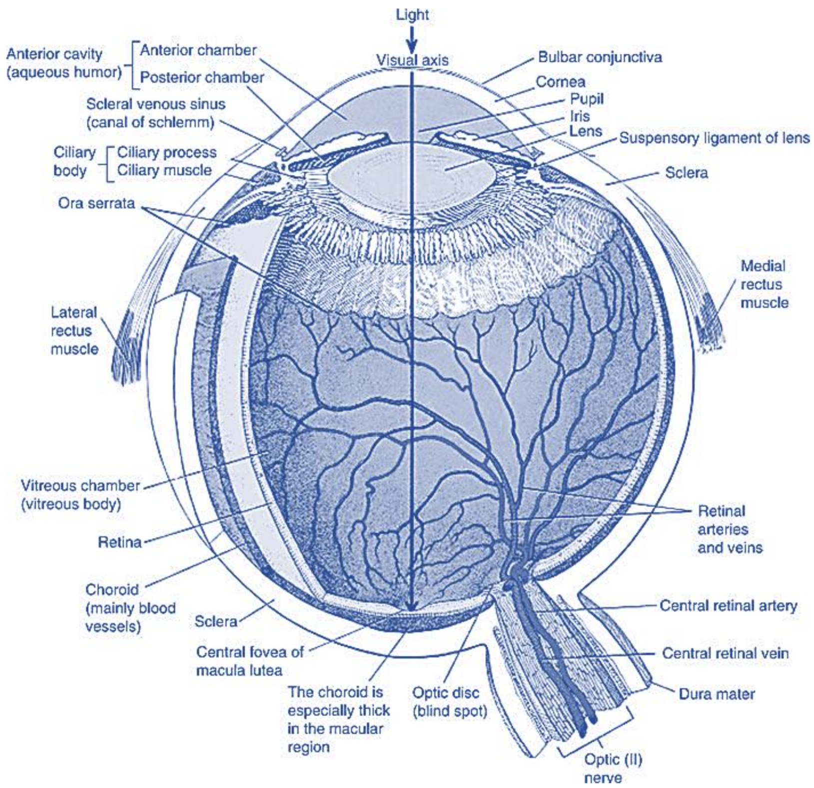

Figure 1.5: Currently known eye structure.[5]

Orbital soft tissues consume two-thirds of orbital volume.[61] As previously mentioned, OST constitute *three* types of tissues; adipose fatty tissue, extraocular muscles and other connective tissues. There are two types of muscles; recti muscles –accountable for vertical and horizontal rotations– and oblique muscles –accountable for torsional stability.[63] In addition to the muscular structure, there are *four* main distinguishable components of connective tissues dispersed throughout the orbit, one of which is a fascial sheath. This sheath envelopes the recti muscles and connects them. It also divides the Adipose Fat Tissue (AFT) into the intraconal retro-bulbar and extraconal peripheral fat. Other structural key components of connective tissues are the check ligaments, Tenon's capsule and orbital septa with collagen fibres. Those fibres connect Tenon's capsule to the periorbita providing a structural framework with high mechanical resistance.[11]

1.2.2 Intraocular Pressure

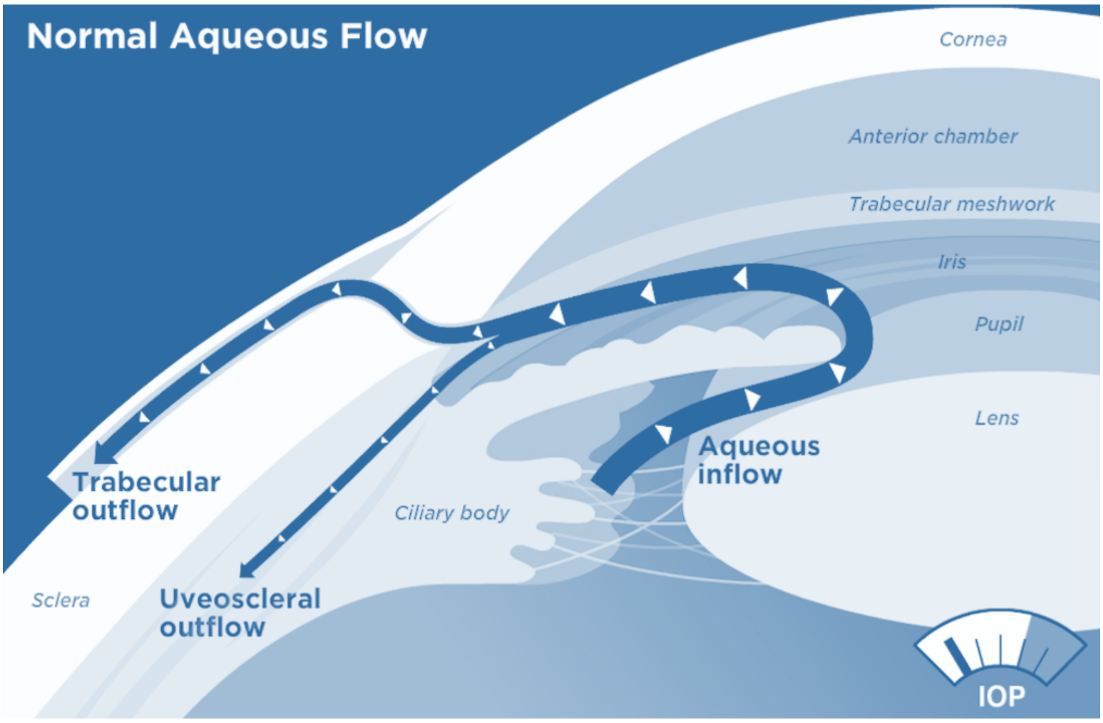

Figure 1.6: Aqueous outflow in normal subject[6]

The ciliary body produces aqueous humor in the cornea and drains it via uveoscleral outflow and the trabecular meshwork. The uveoscleral outflow is an anatomical route that drains aqueous humor.[64] Another drainage of aqueous humor is through a triangular porous tissue called the trabecular meshwork.[65] The eye globe has a constant flow of aqueous humor. Its production, circulation and drainage determine the IOP.[66] Changes in either production or drainage rate of aqueous cause changes in IOP, see Figure 1.6.[67] In young individuals, aqueous flow averages at $2.9\mu l/min$, then appears to reduce by 2.4% per decade, reaching $2.2\mu l/min$ in octogenarians.[68] The IOP distributes uniformly on the globe's internal surface.[69] A method of measuring this pressure is by applying a pre-determined pressure onto the cornea and quantifying the resulting corneal deformation. The higher the deformation, the lower the pressure and vice versa. The IOP normally fluctuates throughout the day; however, a healthy range is between 10 and 21 mmHg.[70] Examination of the IOP started with applying pressure on the closed eyelid, but decades after, contact and non-contact tonometry devices became widely used in the field of ophthalmology. Mechanical stiffness of the globe had a great influence on corneal deformation, which caused inaccuracies with most measurement methods.[70–72]

1.2.3 Glaucoma

Second to cataract, glaucoma is a leading cause of blindness. Glaucoma is an umbrella term for the occurrence of the optic nerve's irreversible degeneration. Patients with glaucoma endure irreversible degeneration of the optic nerve, which causes gradual loss of vision, ultimately leading to blindness. Over 64 million people suffer from glaucoma, where two-thirds of this population experience an elevation in IOP. On that note, patients with Ocular hypertension (OHT) are subjected to an elevated IOP yet are not considered glaucoma patients; however, regular check-ups are recommended to monitor any progression of side effects.[73] The three main types of glaucoma are primary open-angle (OAG), primary angle-closure (ACG) and congenital glaucoma.

Nonetheless, if any other identifiable factor damages the optic nerve head, the condition is called secondary glaucoma.[74] OAG is primarily common in the occidental population, where the anterior chamber seems normal, yet the IOP elevates. A subset of OAG is normal tension glaucoma (NTG), in which IOP is within the normal range, yet the vision is affected.[6] To the contrary, acute ACG causes an elevation in IOP due to blockage of aqueous drainage channels, as seen in Figure 1.7. This blockage is caused by a forward movement of the iris, leading to a mid-dilated pupil with a greenish-blue colour.[52] Chronic ACG is very similar to acute ACG; however, the progression in the latter is more severe. So far, it is evident that IOP is the only modifiable risk factor for the majority of glaucoma patients. This condition's slow progression and inaccuracies in IOP measurements cause damage to the optic nerve, leading to vision loss before being recognised by clinicians or even patients.[75]

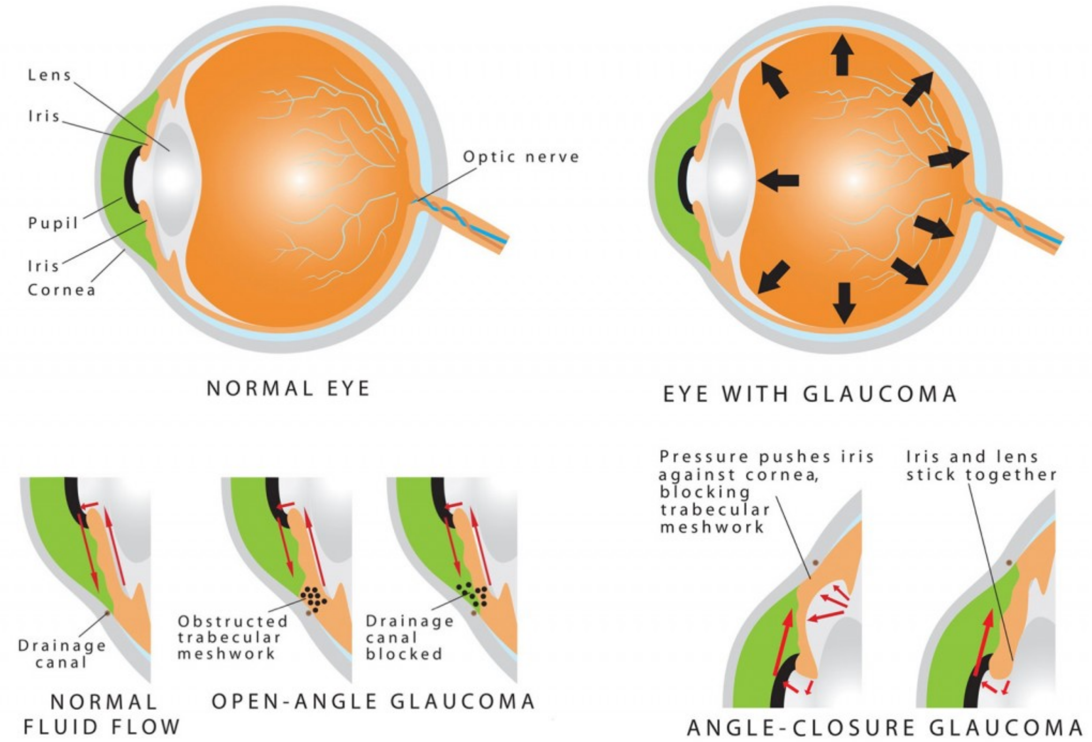

Figure 1.7: Schematic diagram showing the difference between OAG and ACG.[7]

1.2.4 Biomechanics

Biomechanics is the application of mechanics to the biological tissues, which offers a better grasp of living mechanic systems. Advancement in biomechanics was accompanied by the increasing interest of clinicians in this field.[76] To apply biomechanics to living tissues, their physical and chemical aspects are explored. Those two aspects play a significant role in understanding a fundamental characteristic in the field: a material's behaviour towards an applied load. The elastic behaviour of any given tissue refers to a material's ability to recuperate its original form after unloading a given applied force. Stress and strain are components which define this behaviour (see Figure 1.8).[77] The stress is defined as the applied load per unit area, while a strain is the ratio of stretch to the original dimension.

When a stress-strain relationship is defined by the energy density function, where this relationship is parabolic, it is a hyperelastic behaviour.[78] Another aspect of material behaviour is its homogeneity; if the material behaviour is homogeneous across its whole section, it is termed isotropic. However, if the behaviour varies depending on the orientation, this given material is anisotropic.[79–81] Generally speaking, an elastic material behaviour; is defined by a sole value called Young's modulus, which refers to the gradient of this linear behaviour. On the other hand, a hyperelastic material is defined by a tangent modulus, which refers to the tangential gradient at a given stress or strain.[82]

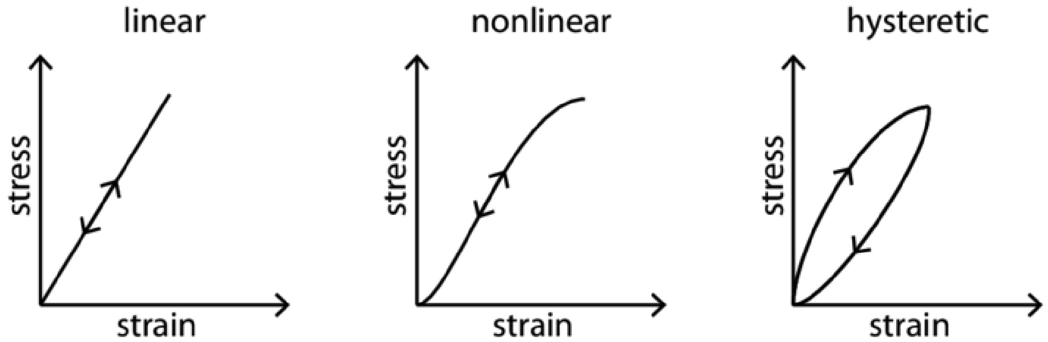

Figure 1.8: Stress-strain relationships; linear (left), non-linear (middle) and hysteretic.[8]

When a biological tissue such as the cornea encounters a fixed stress level over time, the strain tends to increase logarithmically; this aspect of material behaviour is called creep. Nonetheless, if the same tissue encounters a fixed strain level over time, the stress will decrease exponentially, where this behavioural aspect is called stress relaxation.[83,84] The level of hydration within corneal tissue and its collagen fibril microstructure controls viscoelastic features such as creep and stress relaxation.[85] Other features of a viscoelastic behaviour are time-dependent strain and hysteresis.[86,87] Time-dependant strain refers to how stiff the tissue acts according to its loading rate.[88] Moreover, hysteresis is the phenomenon given when the load stress-strain relationship does not match the corresponding relationship of unloading the same action due to energy stored within the tissue. This stored energy could be estimated by determining the area between the loading and unloading curves.[89]

1.3 Scope of the Study

About 50% of the world's population is affected by various eye conditions. Over *sixty-four* million people are affected by glaucoma.[90,91] Over the past few decades, much research, investment and development have taken place in this field, most of which are progressing by their harness of computational power and its utilisation in Finite Element Modelling (FEM). The use of FEM representation of the eye globe has vastly reduced inaccuracies present in diagnosing and treating these conditions, which occasionally caused misdiagnosis. Despite having this accurate FEM of the globe, boundary conditions are assumed in some numerical set-ups, which may provide inaccuracies in the globe's response to exterior loading.

This project has utilised knowledge of orbital biomechanics along with engineering, mathematical and statistical analysis through data management and programming by high-performance computing. On that note, this project introduces an extraocular biomechanical system, which will attempt to reduce inaccuracies in the representation of the orbital region and Extraocular Muscle (EOM) as a valid boundary condition to the eye globe. The project will primarily go through the methodology of developing the extraocular system. This system will aid in understanding the effect of applied tonometry air puff on ocular behaviour subjected to IOP and extraocular muscle primary gaze initial tension. Furthermore, clinical data of subjects who took Corvis-ST (OCULUS Optikgeräte, Inc. Wetzlar, Germany) and the tonometry examination measured corneal behaviour under external air pressure. This behaviour was monitored through a high-speed camera, offering 140 frames of corneal deformation over 32 *millisecond*. Whole eye movement was the leading clinical aspect employed in clinically validating the numerical model.

Consequently, a large parametric study was carried out, of-which its results were mathematically analysed to develop methods to estimate a corneal tissue stiffness metric, the Stress-Strain Index, as well as a biomechanically corrected IOP. Eventually, for validation purposes, the newly acquired numerical estimations will be compared to experimental values of previous studies. In addition, the developed algorithms will be applied to various datasets for performance evaluation.

1.4 Aim and Objectives

This project aims to develop a numerical model of orbital soft tissues and utilise it in developing a new method to accurately measure corneal material stiffness and IOP *in-vivo*. This aim was accomplished through the completion of the undermentioned objectives:

- To create a Matlab algorithm to help extract orbital boundary from CT-Scans;
- To create a bespoke software implementing a novel meshing technique, generating numerical models based on age, gender and ethnicity;
- To develop numerical extra-ocular muscles with pulleys acting as functional origins;
- To develop numerical models to be validated through clinical whole eye movement;
- To execute a parametric study with wide variations in significant geometrical and biomechanical parameters beyond the reported clinical ranges;
- To validate corneal stiffness and IOP methods experimentally and using a large clinical database

1.5 Thesis Structure

This thesis includes five chapters that deliver a thorough description of the approach taken within this project and its main findings. It starts with a summary of knowledge development throughout the years within ophthalmology and lists the study's aim and objectives. In Chapter 2, the literature review explores previous studies and the academic lessons gained from their findings regarding the aim of this project. Consequently, Chapter 3 provides a detailed description of the methodological approach and its relevance to the study's objectives. The study's main results are presented in Chapter 4, as well as the application of corneal material stiffness and IOP algorithms to clinical and experimental data. A thorough discussion of key findings and their comparison with earlier studies follows in the final chapter, as well as the concluding remarks, the study's limitations, and recommendations for future work.

1.6 Thesis Contribution

Thesis contributions to the field are as follows:

- Development of a Matlab algorithm to help manually extract orbital boundary from CT-Scans
- Development of a numerical model of extra-ocular muscles with pulleys acting as functional origins
- Development of a bespoke software code implementing a novel meshing technique, generating numerical models based on age, gender and ethnicity
- Validation of numerical models of extra-ocular soft tissues using clinical data of Corvis corneal deformation profiles
- Executing a parametric study with wide variations in significant geometrical and biomechanical parameters beyond the reported clinical ranges
- Validation of corneal stiffness and IOP methods experimentally and using a large clinical database

Chapter 2

Literature Review

2.1 Anatomy of the Ocular System

2.1.1 The Eye Globe

The eye globe occupies approximately a third of the orbital space, while the rest is shared amongst the other intra-orbital components.[61] The globe is comprised of three chambers; the anterior chamber (space between iris and cornea), the posterior chamber (space between lens and iris) and the largest one is the vitreous chamber (space between lens and retina). The globe comprises an outer fibrous tunic layer (the cornea and sclera), a middle vascular tunic layer (the uvea) and an inner neural layer comprised of the retina, Figure 2.1.[92] The internal posterior space is a chamber filled with vitreous humor, called the vitreous chamber. Vitreous humour is a clear, viscous fluid that provides the globe with rigidity, allowing it to maintain its shape while allowing light to travel through it to reach the retina. The vascular tunic layer includes the iris, ciliary body, pigmented epithelium and choroid. Finally, the fibrous exterior layer incorporates the cornea and sclera. Tenon's capsule, a fascial sheath encompassing the eye from the anterior portion of the sclera to the optic nerve, forms a socket separating the eye from the anterior orbital fat. The Extra-Ocular Muscle (EOM) tendons perforate Tenon's capsule to form a tubular sleeve, described in detail later in this section.[93]

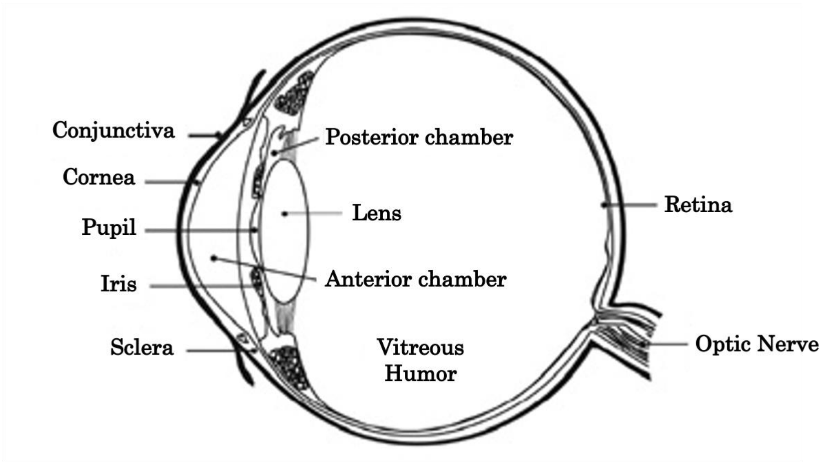

Figure 2.1: Schematic diagram of the globe and its contents[9]

Cornea

The cornea is a transparent rigid tissue located at the front of the globe. Corneal translucency permits light passage through the pupil and the vitreous humor to reach the retina. Corneal stiffness allows it to be a protective envelope for the pupil and iris. The anterior corneal surface is accountable for about 70% of the globe's refractive power. Therefore, deviation in shape may affect the ocular image transmitted to the brain. This deviation may be caused by an injury, a disease or a surgical procedure.[43] The superior-inferior corneal diameter is 11.75 mm, while the medial-lateral diameter is 10.6 mm giving the cornea an ellipsoidal shape.[94] The corneal surface transitions to the sclera at a junction called the limbus. This radial transitional zone is approximately 2 mm (superior-inferior) and 1.5mm (medial-lateral) wide. For an average adult, the total corneal surface is approximately a *sixth* of the sclera's, with its central radius being 7.8 mm and an asphericity of 0.82.[94] Corneal thickness tends to increase at the corneal periphery. On that note, central corneal thickness (CCT) in an average adult is about 550 μm; however, peripheral corneal thickness (PCT) reaches about 670 μm.[95] Previous studies have shown that CCT decreased with age progression.[96–98]

Sclera

The sclera binds to the cornea through the limbus to form the rest of the eye globe. Scleral extracellular matrix components allow it to resist the actions caused by eye movements and IOP fluctuations and ultimately maintain vision stability.[99] In addition, it protects intraocular structures upon impact and trauma, as well as the attachment of extraocular structures, such as the EOMs and Tenon's capsule.[11,100] Another important role of the sclera is changing the globe's axial for optimum refractive power.[101] The sclera is the largest region of the globe; it is spherical with a radius of about 11.5 mm.[102] Scleral thickness is not significantly correlated to age, gender, CCT or presence of conditions such as angler-closure glaucoma.[103] Anterior scleral thickness at the limbal junction ranges between $500 - 600$ μm, then thins out at the equator to $400 - 500$ μm, thenceforth thickens as it progresses posteriorly up to 1000 μm at the posterior pole.[104,105]

2.1.2 The Bony Orbit

The bony orbit is a conical-shaped structure within the skull. It has a maximum cross-sectional area at the orbital aperture (rim), which reduces posteriorly to a triangular entrance at the orbital apex.[60] The orbital rim is 40mm wide and 35mm high, while the orbital apex is 44-50mm deep into the skull, where all neurovascular structures and muscle origins are accommodated.[106] The orbit is comprised of *four* walls, see Figure 2.2; superior (roof), inferior (floor), medial and lateral walls. The orbital structure is laterally rotated, causing the lateral wall to have a 45^o angle with its respective medial wall. This rotation makes the lateral portion of the orbital rim the utmost posterior point. In addition, the medial walls of both the left and right orbits are parallel to the sagittal orbital plane, separated by a 25 mm wide ethmoid sinus.[60] The orbital volume is roughly 30 mL, and the eye globe occupies a third of this volume, while the other two-thirds are shared between other orbital soft tissues (OST). The OST includes the adipose fatty tissue (AFT), the extraocular muscles (EOMs) and other connective tissues.[11] The orbital volume varies between individuals depending on gender and ethnicity. Hence this fact was considered within the numerical model development carried out in this project, and a more detailed description will be outlined later in this chapter.[37]

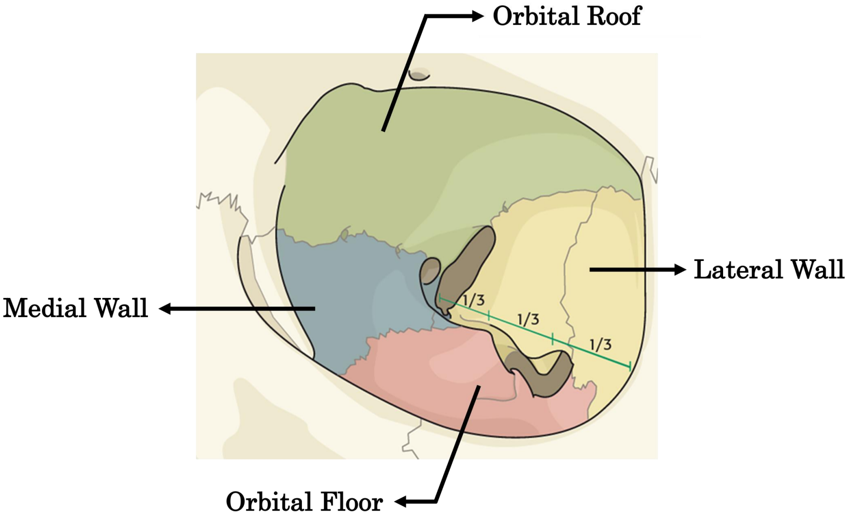

Figure 2.2: Schematic diagram of bony orbit.[10]

Medial Wall

This part of the orbital structure is roughly rectangular, extending from the anterior lacrimal crest to the optic canal at the orbital apex. The anterior portion of this wall is comprised of the lacrimal fossa. As the wall progresses to the mid-region, it thins out to a paper-thin bone called the *lamina papyracea*, which overlies the *ethmoid sinus*. This small bone thickness allows the spread of infections into the orbit in case of ethmoid sinusitis and makes this part of the orbit prone to fractures following blunt trauma. Consequently, the wall thickens out and adjoins the optic canal at the *sphenoid body*. The medial wall connects with the roof through *fronto-ethmoid suture*. At the same time, articulation with the floor is formed of a thick inferomedial bony strut called the *maxilla-ethmoid suture*. This bony strut plays a role in supporting the globe.[60,107,108]

Orbital Roof

The orbital roof is a convex rigid surface composed of a frontal bone with a contribution from the lesser wing of the *sphenoid*. This rigidity allows the roof to have reduced susceptibility to fractures under impact. The roof characterises the orbital rim with a supraorbital notch at the articulation between medial third and lateral two third of the rim.[60] At the anteromedial portion of the roof, few millimetres posterior to the rim, there is an indent where a cartilaginous pulley called trochlea, is housed.[108] It is highly recommended to be careful during extraperiosteally of the roof, as this may damage or scar the trochlea or its region, which may lead to Brown's syndrome.[109]

Lateral Wall

The lateral wall is undoubtedly the thickest and most rigid of all orbital walls, hence the most equipped one in withstanding crack propagation during blunt trauma.[110] The wall is formed anteriorly by the zygoma, while posteriorly, the greater wing of the sphenoid forms it to separate between the middle-cranial fossa and orbit. The superior orbital fissure and fronto-sphenoid suture separate the wall from the roof. In contrast, the wall separates from the orbital floor at the inferior orbital fissure.[60] One of the globe's support mechanism benchmarks is the lateral tubercle. This benchmark is located 3-4mm posterior to the lateral orbital rim, where several connective tissues are attached too, such as; the lateral rectus check ligament, Lockwood's ligament, lateral canthal tendon, the lateral horn of levator and finally, Whitnall's ligament. This wall's respective portion of the optical rim is the least projected, which enables a greater field of view.[108]

Orbital Floor

This orbit section is made of relatively thin bone separating the orbital space from the maxillary sinus. The floor tends to be triangular with a sudden dip anteriorly, followed by an upward slope that shifts medially as it progresses posteriorly. It is mainly formed of the orbital plate of the maxilla (roof of maxillary sinus), while the zygoma and palatine bones contribute anterolaterally and posteriorly, respectively. The lateral wall articulates from the floor at its posterolateral two-thirds by the inferior orbital fissure of the floor. The maxilla-ethmoid suture causes a subtle merge between the floor and the medial wall.[60,107,108]

2.1.3 Orbital Soft Tissues

Seventy-five per cent of orbital volume is consumed by OSTs. As previously mentioned, OST is comprised of *three* types of tissues; AFT, EOMs and connective tissues. EOMs have two types of muscles; recti muscles –accountable for vertical and horizontal rotations– and oblique muscles –accountable for torsional stability.[63] In addition to EOMs, there are *four* main distinguishable components of connective tissues dispersed throughout the orbit, one of which is a fascial sheath. This sheath envelopes the recti muscles and connects them. It also divides the AFT into intraconal retro-bulbar and extraconal peripheral spaces. Other structural key components of connective tissues are the check ligaments, Tenon's capsule and orbital septa. This septum is a $0.3mm$ thick, intricate collagenous fibres distributed in parallel with abundant smooth muscle. Those fibres connect Tenon's capsule to the periorbita providing a structural framework with high mechanical resistance, see Figure 2.3.[11]

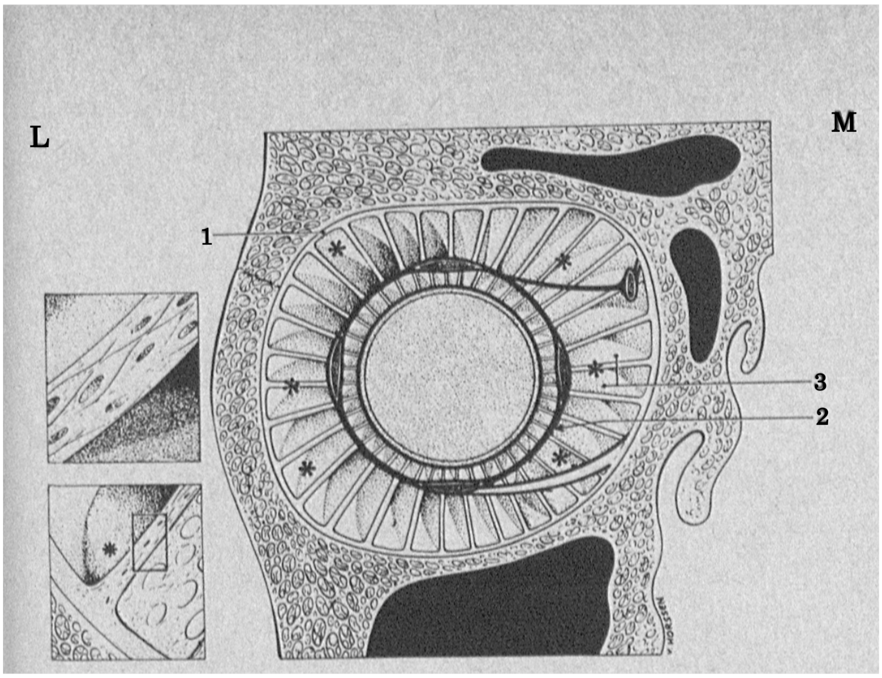

Figure 2.3: Schematic arrangement of the fibrous septa. Asterisks indicate the areas where smooth muscle tissue was found. 1: periorbit, 2: common muscle sheath at eyeball level, 3: fibrous septa. L indicates lateral; M, medial[11]

Adipose Fat Tissue

The AFT structure plays a significant role in enabling the tissue to act as a shock absorber while allowing the unhindered movement of the intraorbital structures in their respective degrees of freedom.[111] Bremond *et al.* identified two parts of the AFT; the peripheral, extraconal fat tissue and central, intraconal fat,[112] with this distinction being a consequence of cone formed by recti muscles along with the organisation of the conjunctival tissue enveloping it. Mesoscopic and histological differences were identified between the two parts, with the outer and inner parts constituting thick and thin conjunctival septa, respectively. These differences were related to the mechanical roles of the two parts, where the first part acted as a periorbita cushion that enabled high mechanical resistance. At the same time, the latter contributed significantly to maintaining the globe's position while allowing the optic nerve's movement in orbit.[108,113]

Connective Tissue

Orbital connective tissues are very abundant within the orbital space. They are comprised of *four* main components; Tenon's capsule, periorbita, fibrous orbital septa and Lockwood's ligament.[11] Tenon's capsule is a thin dense elastic, nearly avascular fascial sheath, which encapsulates the globe from $3mm$ posterior of the limbus to the optic nerve.[114] This sheath is attached to the scleral surface via extremely delicate connective tissue, which travels across episcleral space (sub-Tenon's).[115] Recti muscles enter sub-Tenon's by penetrating Tenon's capsule $10mm$ posterior to their insertions, while oblique muscles enter it just anterior to the equator.[116] From Tenon's capsule, fibrous orbital septa extend through extraconal fat to attach to periorbita (dense tissue lining orbital wall), forming a structural framework with high mechanical resistance, yet permitting rotation of the ocular vessel.[11,117] Another important tissue is the muscle sheath; it envelopes recti muscles; separating orbital space into the intra and extraconal space. The muscle sheath and orbital septa fuse to form medial and check ligaments. The medial ligament attaches to the medial wall at the posterior lacrimal crest, while the lateral check ligament attaches to Whitnall's tubercle located on the lateral wall $1mm$ posterior to the lateral orbital rim.[108]

Extra-Ocular muscles

Extraocular muscles consist of four recti muscles, two oblique muscles and levator superioris. Although levator superioris is considered one of the EOMs, it is the only one which is not responsible for any movement of the globe; instead, it is responsible for the movement of eyelids.[108] In contrast, rotation of globe around the *three* major axis is caused by recti and oblique muscles. The recti muscles are mainly accountable for vertical (superior & inferior) and horizontal (medial & lateral) rotation, while oblique muscles (superior & inferior) are accountable for torsion. Hence all of them are inserted into the globe.[118] Recti muscles form a conical shape, with its narrow apex at the orbital apex, while its anterior end is represented by the posterior portion of Tenon's fascial capsule, see Figure 2.4. This conical shape is covered by a sheath compiling all recti muscles together. In addition, this sheath is coupled to periorbita lining on the orbital wall via orbital septa, which provides a structural framework from the globe, EOMs and periorbita.[11]

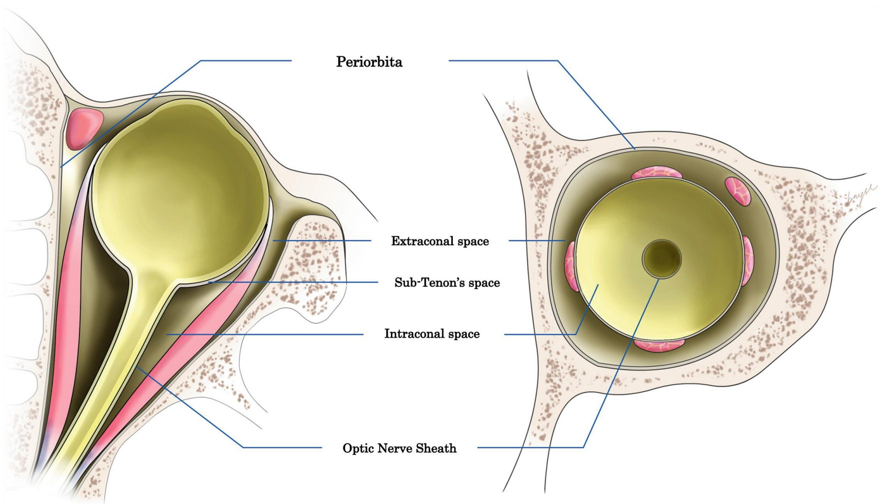

Figure 2.4: Different spaces of the orbit , axial and coronal views.[12]

To start with, superior oblique muscle (SO) is the thinnest, longest EOM, which originates at the lesser wing of the sphenoid body, near the frontoethmoidal suture, just medial to the optic canal.[119] Followingly, SO courses anterosuperiorly towards the trochlea −cartilage on medial orbital wall− where it passes through and out. Immediately after passing the trochlea, SO changes its course to run posterolaterally beneath the superior rectus (SR) to get inserted into the superior posterolateral aspect of the globe.[120] Due to the change of muscle direction, the trochlea acts as a pulley. Hence, when determining this muscle's actions, a line is drawn between its *effective* or *physiologic* origin and its *insertion*.[121] On the other hand, there is also the inferior oblique muscle (IO), which is almost the counterpart of SO. Unlike SO or other EOM, IO does not originate at the orbital apex; instead, its anatomic origin is at the anterior end of the orbit (see Figure 3.19). This muscle originates at the maxillary bone located just posterior to the inferior portion of the medial orbital rim.[122] The muscle courses through the inferior orbital space, where it is sandwiched between the inferior rectus muscle and the orbital floor until it reaches the inferior posterolateral aspect of the globe.[119,123] Both oblique muscles penetrate Tenon's capsule just anterior to the globe's equator, passing through sub-Tenon's space until they attach to their respected insertions on the sclera.[124]

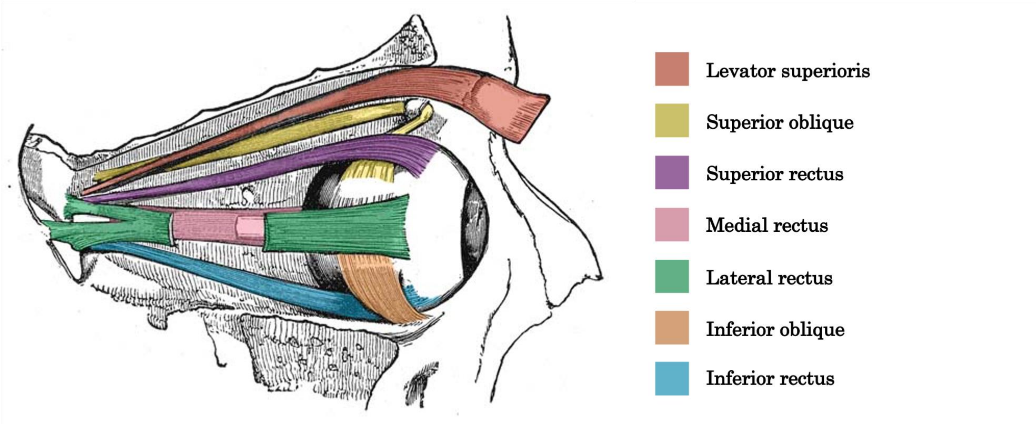

Figure 2.5: Lateral view of extraocular muscles and bony orbit.[13]

The next group of EOMs are the recti muscles. This group of muscles, as mentioned previously, form the conical shape. They all originate from the Annulus of Zinn −tendonous structure located at the orbital apex.[119] All muscles progress anteriorly towards their target, *insertions* on the sclera. However, before their arrival, all muscles, without exception, course from the orbital apex towards a connective tissue pulley just posterior to the globe's equator.[125] Before arrival to this pulley tissue, the recti muscle course is parallel to their respective orbital wall *i.e.* Superior rectus is parallel to the orbital roof. Nevertheless, after passing through the pulley, each muscle tends to change course following the globe's curvature to reach its insertion.[126] Due to the frequency of its use in convergence, the medial rectus muscle (MR) is the largest muscle.[119] MR is covered by a fascial sheath, which extends to fuse with orbital septa to form the medial check ligament (MCL). In addition, exact formation occurs within the lateral rectus muscle to form the lateral check ligament (LCL). MCL and LCL attach to medial and lateral orbital walls, respectively. Furthermore, both inferior muscles unite with their sheaths to form an inferior check ligament attached to the orbital floor. Eventually, all these ligaments are joined together to form Lockwood's suspensory ligament, contributing to the globe's support.[11]

2.2 Orbital Soft Tissue Biomechanics

As mentioned previously in subsection 2.1.3, the OSTs are comprised of the AFT, the EOMs, and other connective tissues. Each of these components contributes to the eye globe's support system.[88,127] This section goes through a review of literature about the biomechanics of these components; this will include previous studies and their in-vivo, ex-vivo and numerical efforts in evaluating the material behaviour of the AFT; as well as the evaluation of other structural aspects of the OST. In addition, a detailed description of the rectus muscle pulleys and their functional role within the support system. It also outlines previous studies' attempts to develop numerical models representing the ocular support system and their inaccuracies. A previous study used a mathematical model to estimate the EOMs' initial tension during the primary gaze of the eye globe.[36] A model summary will also be provided later in the section.

2.2.1 Elasticity of the AFT

The adipose fat is a connective tissue comprised of lipid-filled cells called adipocytes.[88] The majority of AFT weight is constituted of lipid ($60 - 80\%$), the least is protein ($2 - 3\%$), and the remaining is water ($5 - 30\%$). Lipid enforces incompressibility of the AFT, as it can be treated as an incompressible inviscid fluid.[128] A histology study suggested that the AFT behaves like an isotropic material based on its approximate isotropic structure.[129] Another previous study conducted an examination involving quasi-static tests, entailing fully reversed, large amplitude loading. This examination aimed to investigate the non-linear uniaxial response of the AFT over a range of strain and strain rates.[88] This study used a one dimensional Ogden constitutive material model (Equation 2.1) to fit experimentally acquired stress-strain data. Hwang et al.[39] suggested that the whole eye movement (WEM) during the Corvis procedure only represents 0.6% of the orbital depth. Thereby, the low strain rate Ogden material parameters of the AFT are interesting for this study.

$$U = \sum_{n=1}^{N} \frac{2\mu_i}{\alpha_i}(\bar{\lambda_1}^{\alpha_i} + \bar{\lambda_2}^{\alpha_i} + \bar{\lambda_3}^{\alpha_i} - 3) + \sum_{n=1}^{N} \frac{1}{D}(J_{el} - 1)^{2i} \tag{2.1}$$

Where U is strain energy per unit volume, $\mu = 0.4\ kPa$ the shear modulus, $\alpha = 23$ the strength hardening exponent, N the function order, $\bar{\lambda_i}$ principal stretch in each of the Cartesian planes, D is compressibility parameter and J_{el} is particle volume. All ocular tissue regions were assumed almost in-compressible with Poisson's ratio of 0.48.[130,131]

2.2.2 EOMs

2.2.2.1 Rectus Muscle Pulleys

The EOMs, apart from the lid-elevating levator palpebrae superioris muscle, are bi-laminar.[132] The global layer (GL) of the rectus EOMs is located adjacent to the eye globe's scleral surface.[133,134] On the other hand, the orbital layer (OL) is located on the orbital surface of rectus muscles. About 50% of all EOM fibres are contained in this layer. The OL terminates well posterior to the sclera, in which some of the fibres are inserted into a connective tissue pulley coupled to the orbital wall, Figure 2.6.[135,136] With this coupling in mind, any contractions in the OL fibres will stretch the connective tissue, resulting in a posterior displacement of the pulley.[137] Thereby, the pulleys are considered the functional mechanical origins of rectus EOMs.[14]

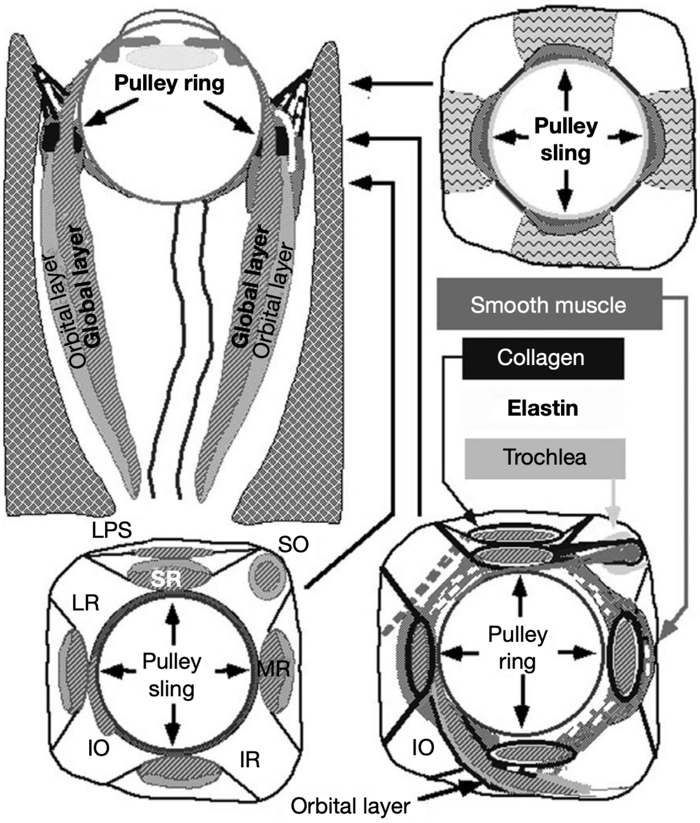

Figure 2.6: Schematic diagram describing global and orbital layer, as well as depiction of EOM pulleys[14]

2.2.2.2 Primary Gaze Initial Tension

In modelling and eye examinations, the eye globe is generally in its primary position (gaze) as the reference configuration. The globe is suspended in its primary gaze within the orbital space by conserving the EOM initial tension forces.[36] In theory, the 3-dimensional mechanical equilibrium of the globe depends on the force contributions of the six EOMs that attach to the globe, i.e. medial rectus (MR), lateral rectus (LR), inferior rectus (IR), superior rectus (SR), inferior oblique (IO) and superior oblique (SO). On that note, Gao et al.[36] estimated the EOMs' initial tension, contributing to the mechanical equilibrium of the globe's primary gaze position. This estimation was attempted by employing the theory of mechanics and optimising a proposed mathematical model. This study relied on previously published data on mean geometric parameters of human EOMs, Table 2.1.[33–35] It should also be noted that the EOM pulley mechanism was employed within the optimised mathematical model. The use of

EOM biomechanical behaviour to estimate the initial tension required (Table 2.2) for the mechanical equilibrium of the suspended eye globe coincides with modern orbital biomechanical theory.[138] On that note, it is a requirement to investigate the EOMs' initial tension in response to disruption to the globe's mechanical equilibrium.

Table 2.1: Mean geometric parameters of human EOMs[33–35]

Geometric parameter	EOM					
	MR	LR	SR	IR	SO	IO
Cross-sectional area A_0 (mm^2)	17.39	16.73	11.34	15.85	19.34	19.83
Resting length L_0 (mm)	35.40	44.60	39.30	39.80	20.86	30.60
Initial length L (mm)	39.42	50.51	44.70	45.00	22.17	31.21
Initial stretch λ (dimensionless)	1.11	1.13	1.14	1.13	1.06	1.02

Table 2.2: Initial tension required of EOMs keeping the globe in its primary gaze[36]

Extra-ocular muscle	Force (mN)
Medial rectus	89.2 ± 31.6
Lateral rectus	48.8 ± 14.2
Superior rectus	50.6 ± 17.6
Inferior rectus	46.2 ± 13.4
Superior oblique	15.6 ± 8.3
Inferior oblique	17.1 ± 12.1

2.2.3 Previous Efforts in OST Numerical Modelling

The orbital soft tissue has been the subject of several anatomical studies focusing on its structure.[137,139] This drove researchers to develop representations of the ocular support system. Jannesari et al.[15] attempted to estimate the biomechanical properties of the AFT by employing Corvis corneal deformations in an inverse analysis optimisation. However, their numerical set-up involved an idealised two-dimensional axisymmetric geometry of the cornea, while a viscoelastic boundary condition was applied at the limbal conjecture, Figure 2.7. Their numerical set-up had few inaccuracies. First, previous studies[39,88,140–142] provided experimental, as well as numerical findings, stating that the AFT is not the only form of support provided to the globe. Second, their assumption of the axisymmetric geometry may be suitable for the cornea. However, Corvis corneal deformations show a very prominent occurrence of nasal rotation during retraction of the eye globe.[143] This nasal rotation drove the need to employ a three-dimensional geometrical set-up, which implements irregularity and asymmetry of the orbital boundary.

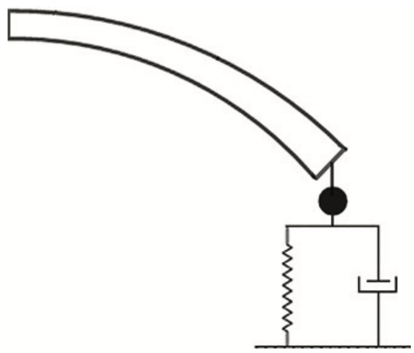

Figure 2.7: Two-dimensional axisymmetric geometry of the cornea, with a viscoelastic boundary condition applied at the limbal conjecture[15]

In contrast, other studies[144,145] developed numerical models of the OST, which included a 3-dimensional geometry of the orbital boundary. Both studies utilised their numerical models in applying blunt impact trauma onto the globe, hence, simulating retinal damage amongst effects on other intra-ocular components. The first of these previous works implemented the rectus muscles and an assumed rotational symmetry of the AFT surrounding the globe.[144] While the latter have implemented the irregularity of the orbital boundary without including any of the EOMs.[100] However, both studies did not include the oblique muscles. Furthermore, Karimi et al.[144] did not include the EOM pulleys within its suggested set-up.

2.3 Corneal Biomechanics

2.3.1 Elasticity

Literature has shown that most biological tissues have various degrees of anisotropy and behave non-linearly regarding strain caused by applied stress.[31] Collagen fibrils are mostly distributed in the cornea parallel to its surface; this microstructure arrangement of fibrils causes the cornea to have an anisotropic behaviour. Anisotropic microstructure models produce more accurate material behaviour but are computationally costly.[146] Several isotropic material constitutive models are utilised to precisely simulate this non-linear material behaviour, some of which are used in ocular modelling, such as Ogden, Neo-Hooke and Mooney-Rivlin models.[147] On that note, previous work has established that the Ogden material model can represent corneal biomechanics accurately.[42] Therefore, for large-sized long-simulation-based studies, it was essential to employ isotropic material models.[148–150]

2.3.2 Ex-vivo Measurement of Elasticity

The previous constitutive models require experimental load-deformation data to optimise the value of their constants. Experimental studies have focused on acquiring *ex-vivo* measurements of corneal behaviour.[151] These studies attempted to execute such a goal by resorting to one of two methods; either uni-axial or inflation tests.[152–155] First, uni-axial testing relied on a microstructure-invasive methodology, which excised corneal tissue into strips. Those strips were then clamped into a device, which applied force uni-axially while monitoring deformation, see Figure 2.8. Preconditioning took place to ensure the repeatability of tissue behaviour, which is the application of loading and unloading cycles onto the strips.[43] Consequently, this repeated deformation data and applied load were converted into a stress-strain relationship; its slope at any stress or strain is the tangent modulus of the tissue.[152,156] As corneal tissue is naturally curved and its fibres are distributed mainly parallel to its surface,[146] cutting tissue into strips causes a few implications. First, the testing load is applied on a flat cornea, which is unrealistic compared to IOP applied on a curved one. In addition, flattening the curved corneal strips causes initial strains. Second, fibres are cut by excision of tissue along the edges, affecting material behaviour. Due to these implications, inaccuracies arose and resulted in variations between experimental studies.[16,157]

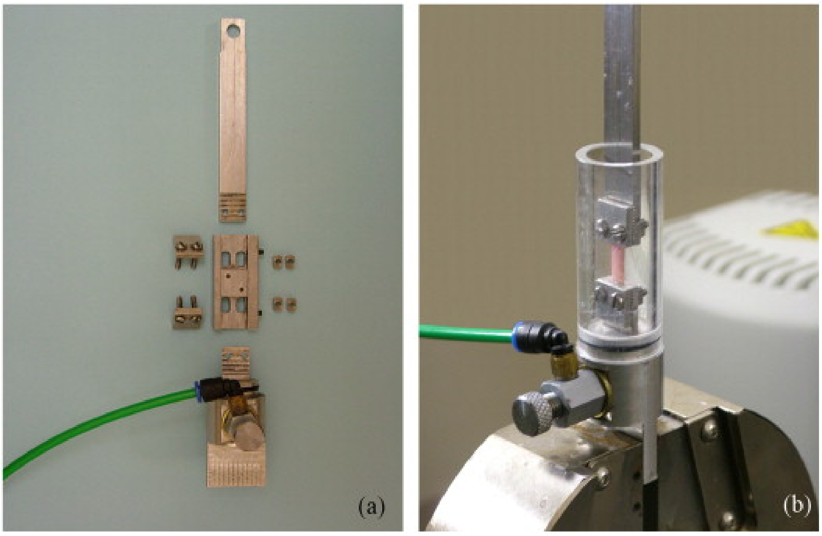

Figure 2.8: Test set up showing (a) components of mechanical clamps, and (b) a specimen fitted to mechanical clamps and connected to the material testing machine.[16]

Inaccuracies in uni-axial testing have gradually deviated from research to acquire corneal tissue behaviour through inflation testing. This form of testing allows corneal assessment in its natural form, where fluid pressure is applied internally. Hence, specialised test rigs were designed to hold components of the eye or the whole ocular structure during loading under an internal pressure simulating IOP.[158,159] Within these experiments, internal pressure is gradually increased to 60 $mmHg$ through fluid injection to the posterior of the globe.[160] This load application initiates deformation, which is monitored through digital cameras. A former study provided reliable ocular biomechanical behaviour by conducting inflation tests on 57 human corneas aged 30 to 99.[160] The study used Equation 2.2, 2.3 and 2.4−where, age is in "year" and stress in "MPa"−to produce an exponential stress-strain relationship, which indicated a hyperelastic tissue behaviour and gradual stiffening with progression of age, see Figure 2.9.

$$\sigma = A[e^{B\epsilon} - 1] \tag{2.2}$$

Where;

$$A = 35 \times 10^{-9} age^2 + 1.4 \times 10^{-6} age + 1.03 \times 10^{-3} \tag{2.3}$$

and

$$B = 0.0013 age^2 + 0.013 age + 99 \tag{2.4}$$

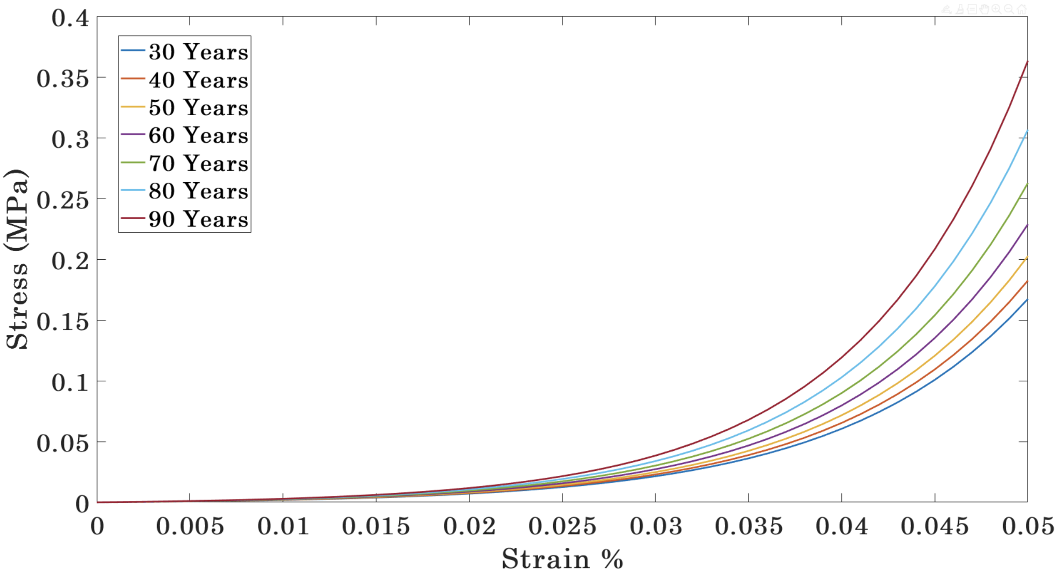

Figure 2.9: Corneal stress-strain behavior in relation to age[16–18]

2.4 Scleral Biomechanics

An ocular globe that can see far away objects with a sharp resolution is said to be in a state of emmetropia. During childhood, Emmetropization takes place. This phenomenon is where the axial length of an eye is adjusted to equal the focal length.[101] This adjustment is achieved by elongation of the posterior sclera. Too much elongation in the posterior sclera causes refractive errors preventing light from focusing on the eye's retina and blurriness in vision.[99] Eye globes with elongated sclera are myopic eyes. Myopia, like glaucoma and retinal detachment, is all directly related to scleral biomechanics.

The sclera connects to the cornea through the limbus to form an avascular tissue which forms the eye's primary load-bearing tunic. Structural stability is provided by scleral tissue against forces including IOP, the EOM action, blinking and impact trauma.[100] Almost two-thirds of the sclera is made up of water, while the other third comprises proteins, including collagen, proteoglycans and elastin.[161] Collagen is abundant within the sclera in the form of fibres. These fibres are distributed in a random manner giving the sclera its opaqueness. Furthermore, it was found that the tissue behaves non-linearly regarding strain, similar to the corneal material behaviour. However, due to the randomness of fibril distribution, there have been complications in simulating microstructure behaviour in numerical models of the sclera, see Figure 2.10.[45,162] At birth, scleral thickness tends to be homogeneous throughout. However, with the progression of age, elongation of the posterior sclera occurs, resulting in a variety of tissue thicknesses. This thickness inhomogeneity ranges approximately from 500-600μm at the limbus, thinning to 400-500μm at the equator, then thickens to 1000μm at the posterior pole.[104,105] This high thickness in the posterior region maintains structure stability, which allows light rays to be received at the correct retinal location resulting in a clear, in-focus vision.[99]

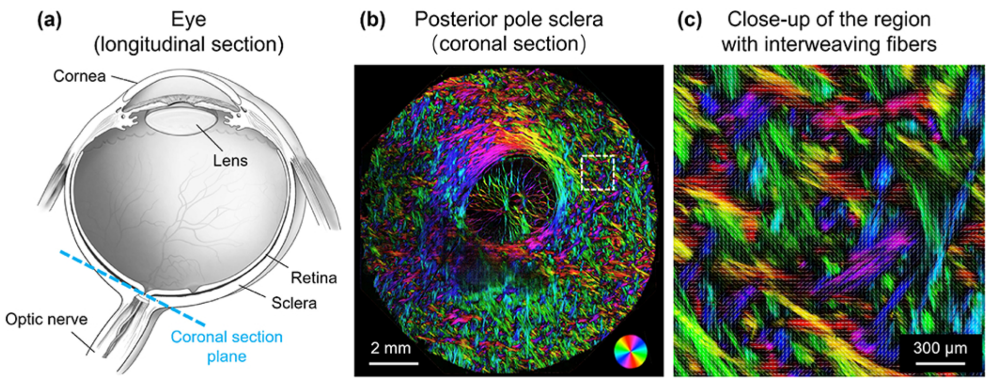

Figure 2.10: (a) Schematic of an eye sectioned longitudinally. (b) A polarised light microscopy image of a coronal section of the posterior pole of the sclera in a sheep eye. Colours indicate local fibre orientation, whereas intensity is proportional to collagen fibre density. (c) Close-up of a region in the sclera exhibiting interweaving fibers[19]

Scleral biomechanics plays a significant role in evaluating the eye globe's response to surgeries, intra and extraocular actions, and better insight into conditions and diseases such as glaucoma and retinal detachment. A previous study demonstrated *ex-vivo* experiments on 36 human sclerae to obtain thickness variation as well as material behaviour and their correlation with age.[16,43] That study concluded that the sclera was split into three regions, each with its unique material behaviour and considered age dependent. It is, therefore, essential to have a better understanding of this ocular region.

2.5 Geometry of the Bony Orbit and EOMs

In this section, geometrical properties used in developing orbital and EOM numerical models are discussed. First, variations of orbital structure, behaviour and dimensions are scrutinised; this includes the change of orbital volume and aperture properties with ethnicities and gender. In addition, age-related changes to the orbital aperture are also outlined in this section, followed by considering the difference in the eye globe's position between ethnicities. Studies have shown a significant age-related change in ocular protrusion.[20] Second, functional geometrical properties of EOMs are discussed, where insertion locations for Caucasian and Asian eyes are stated, as well as the insertion width of each EOM. Moreover, positions of muscle pulleys and origins are also indicated. To conclude, this section provides a review of literature on orbital and ocular geometry, which was utilised to develop in the numerical models and found to vary based on ethnicity, gender and age.

2.5.1 Variations of Orbit

The geometry of orbital space plays a major role in the orbit's biomechanical behaviour. This section dissects variations in orbital geometry with ethnicity, gender and age.

Orbital Volume

In this study, two ethnicities were considered in developing the numerical model, Caucasian and Asian. Previous studies carried out quantitative measurements of the orbital soft tissue volume. These measurements included orbital volume (OV), adipose fatty tissue volume (AFTV) and cumulative muscle volume (MV).[37,38] The outcome of this exercise was no significant change in orbital volume with age. However, due to the significant age-related increase in AFT volume, the AFTV/OV ratio also increased. In addition, both studies[37,38] showed significant differences in OV and AFTV, yet the difference in AFTV/OV ratio between genders was not significant. The previously mentioned studies stated no significant age-related change regarding orbital volume. Upon these findings, four bound volumes of the bony orbit were used in the numerical models in this study. As shown in Table 2.3, in Caucasian males, OV is about 14% greater than in Caucasian females and 10% greater than in Asian males. Nonetheless, gender-related orbital volumetric differences were higher in Caucasians than in the Asian population.

Table 2.3: Male and female mean orbital volume (cm^3) within Caucasian and Asian population[37,38]

Ethnicity	**Gender**	
	Male	**Female**
Caucasian,	29 ± 2.4	25 ± 2.2
Asian,	22 ± 2.2	20 ± 1.5

Darcy *et al.*[163] carried out a Magnetic Resonance Imaging (MRI) characterisation of orbital changes with age. The outcome of that study suggested a significant increase in the anterior inferior periocular soft-tissue volumes, mainly due to the expansion of fatty tissue in this region. It was also suggested that this trend might be the reason for the lower eyelid prominence, affecting the eye globe's anterior-posterior position within the orbital space. Other studies,[20,164–168] showed changes in exophalmetery value with progression of age, and the most recent study[20] showed an average reduction of 0.066 $mm/year$ in ocular protrusion within both genders, as represented by the linear regression in Figure 2.11. In that study, ocular protrusion was measured from the farthest lateral part of the orbital rim to the corneal apex.

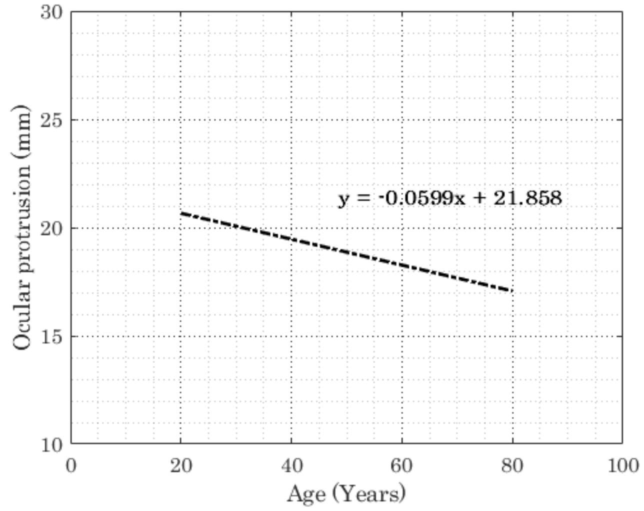

Figure 2.11: Change in ocular protrusion in Caucasian male and female population[20]

Orbital Rim

Kahn *et al.*[21] conducted a three-dimensional computed tomographic study to outline the effect of age on the orbital aperture. The study used a 3D reconstruction of CT scans, followed by measuring orbital aperture width as the distance between the *frontozygomatic suture* and the posterior *lacrimal crest*. This study demonstrated significant changes between age and gender groups in orbital aperture width and area, Figure 2.12. They also reported that the area increase in the aperture was not uniform across the boundary. In Caucasian males, most of the increase in area was due to a receding boundary at the superior-nasal portion of the rim and a recession of the entire inferior orbital rim, Figure 2.13.

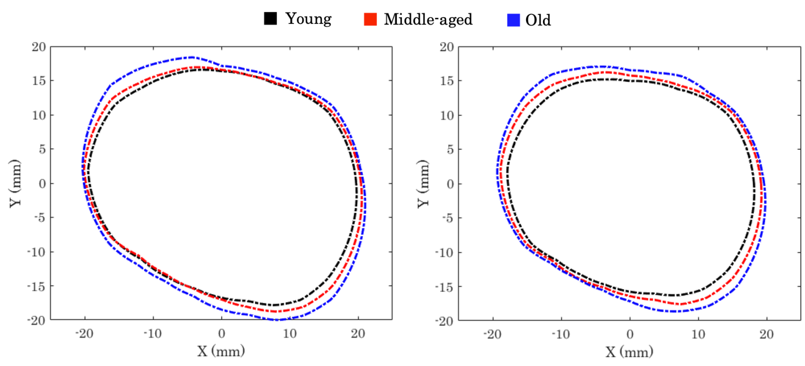

Figure 2.12: Orbital aperture age-related variation in Caucasian males (left) and females (right)[21]

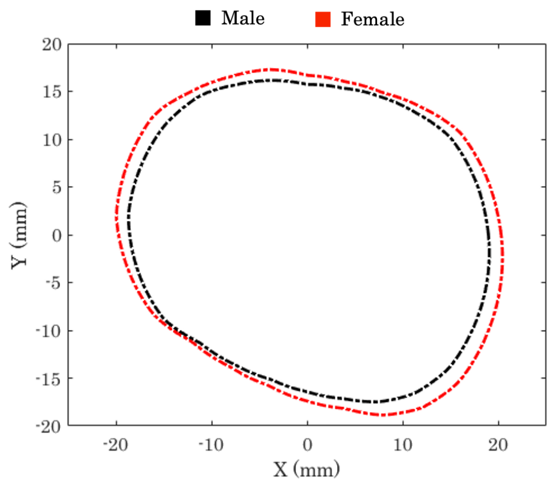

Figure 2.13: Mean orbital aperture of both genders in a Caucasian population[21]

On other aspects of the orbital rim, Eckstein *et al.*[22] utilised a 3-dimensional reconstruction of orbits without the orbital pathological disease to characterise the position of the eye globe relative to the orbital rim in the Asian population and a Caucasian population. As seen in Figure 2.14, there was almost no difference in elevation at the superior and medial regions of the rim. However, there was a clear difference in the inferior and lateral regions. This significant difference makes an Asian orbit look shallower than a Caucasian orbit. Another aspect is the radial distance between the globe's equator and the orbital rim. As seen in Figure 2.15, the radial distance in both genders was similar except in the superior region, where the Caucasian population tended to have a small extra space between the rim and the globe's equator.

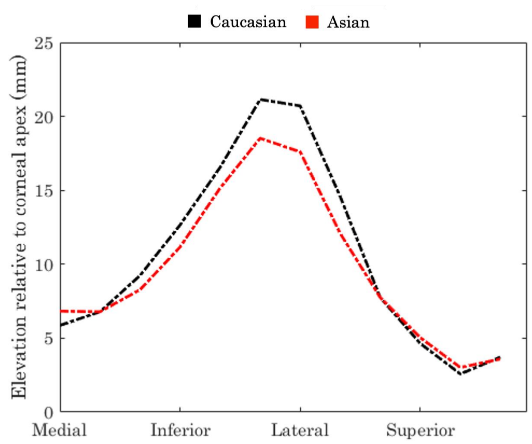

Figure 2.14: Comparison of the mean elevation relative to the corneal apex of Caucasian and Asian orbital rims in the sagittal plane[22]

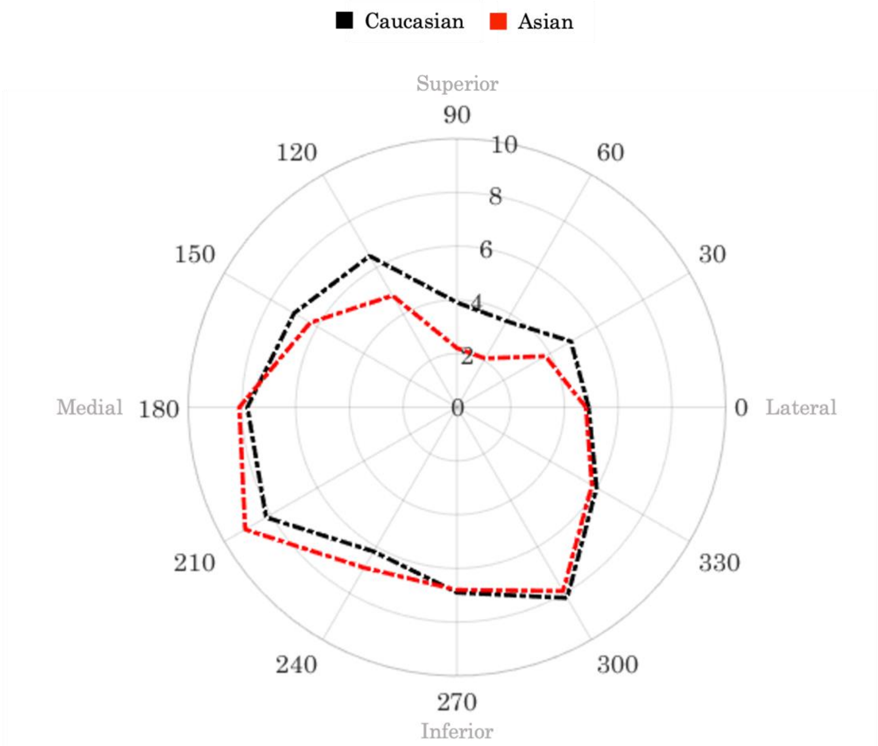

Figure 2.15: The mean radial distance between the coronal projection of the orbital rim and the maximum circumference (Equator) of the globe[22]

2.5.2 Extra-ocular Muscles

The EOMs have different regions with various roles. Those regions are as follows; insertion points, pulleys and muscle origin. Most EOMs extend from the *Annulus of Zinn* at the orbital apex to perforate Tenon's capsule, forming a tubular sleeve with the muscle sheath.[61] The muscle tendons follow the globe's curvature until their insertion locations on the sclera a few millimetres from the limbus in a spiral-looking shape called *Spiral of Tillaux*.[169] On the other hand, oblique muscles attach to the posterio-lateral side of the globe, where their insertions are attached perpendicular to the rectus muscles, see Figure 2.16.

At the globe's equator, there are muscle pulleys. Clark *et al.*[170] demonstrated through CT scans that muscle pulleys stabilised the path of rectus muscles. A previous study implemented the muscle pulley theory to estimate the initial tension in EOMs during the primary gaze of the eye globe.[39] Each of the rectus muscle pulleys was constrained to move only in the direction parallel to the one to its origin. Locations of the insertion points are listed in Table 2.4, as well as their pulley and origins where applicable.

Table 2.4: Showing functional geometrical details used for extraocular muscles in this project. Insertion distance resembles distance from the tendon midpoint to the limbus. All data are given in mm.[36,39–41]

EOM	Insertion		Pulley location			Origin location		
	Distance	Width	X	Y	Z	X	Y	Z
Medial rectus	5.3	9.9	-14.2	-0.3	-3.0	-17.0	0.6	-30.0
Lateral rectus	6.9	9.2	10.1	-0.3	-9.0	-13.0	0.6	-34.0
Inferior rectus	6.8	8.7	-4.3	-12.9	-6.0	-16.0	-2.4	-31.8
Superior rectus	7.9	9.8	-1.7	11.8	-7.0	-16.0	3.6	-31.8
Superior oblique	15.9	7.1	-	-	-	-15.3	12.3	8.2
Inferior oblique	17.8	9.2	-	-	-	-11.1	-15.5	11.3

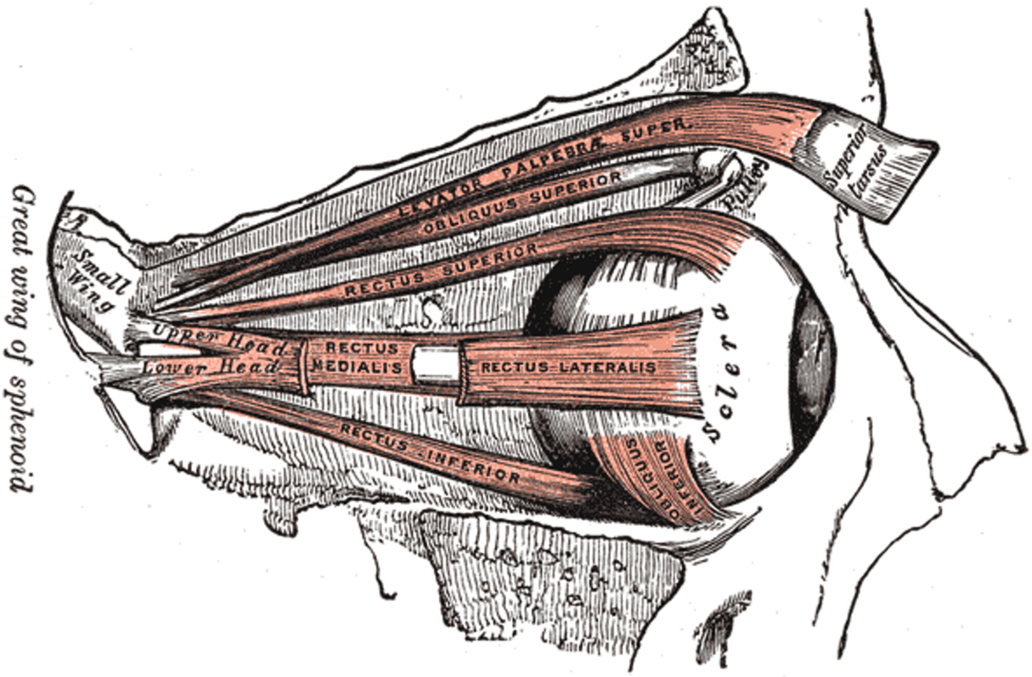

Figure 2.16: Schematic cross-section of the orbit[23]

2.6 IOP and Tonometry Devices

The ocular globe has a constant flow of aqueous humour production, circulation and drainage that determine the IOP. Changes in aqueous production or drainage rate lead to variation in IOP.[67] An increased IOP is an identifiable risk factor for glaucoma, which is caused due to loss of retinal ganglion cells, leading to a damaged optic nerve.[171] To conclude, IOP is a modifying factor which may manage this disease. Second to cataract, glaucoma is one of the leading causes of blindness; however, it is the most common ocular disease.[90,172] As mentioned previously, aqueous flow is a significant parameter in the maintenance of IOP. In 2013 it was reported that 64.7 million individuals in their 40s or older were affected by glaucoma. This immense number of patients increased by 18% in 2020, and speculated that this number to reach 111.8 million by 2040.[90,91] The WHO estimated in 2002 that an eighth of the world's blind population is due to glaucoma.[173] Owing to this substantial ratio, much importance was given to clinical examination to monitor IOP accurately. Hereafter, this section will delve into types of tonometry devices used throughout the years, thenceforward compare commonly used ones and their monitoring technique.

2.6.1 Types of Tonometry Devices

Various tonometry devices were in use by the early 20^{th} century. With two centuries' worth of technological advancement, the number of models was climbing. However, the tonometry devices available commercially in the current market are all functionally based on an old concept suggested in the mid 19^{th} century. This concept assumed the eye globe to be a hydraulic vessel in which pressure is uniformly distributed on its internal surface. A historical exploration of this concept and tonometry devices is described below.

2.6.1.1 Impression and Indentation Tonometry

In 1862, a Prussian-German ophthalmologist named Albrecht von Graefe was credited with the first attempt to estimate IOP mechanically.[174] However, in the mid-1860s, a friend of his, Professor Frans Cornelius Donders, was the first to design and estimate IOP using a mechanical instrument, albeit not accurately. Impression tonometry is principled around displacing intraocular fluid by applying a known weight to the eye, which was covered by the eyelid. Later in the 1880s, the discovery of cocaine and its use in corneal anaesthesia paved the way for impression tonometry, where it became the conclusive IOP measuring tool. By the end of the 19^{th} century, Professor Hjalmar Schiøtz improved the accuracy of IOP measurement by adding a fine plunger to the set-up (Figure 2.17) where it indents the cornea allowing for a minimal amount of intraocular fluid to displace and producing less variability in measurements. Due to contact with cornea, alcohol or heat disinfection was essential before testing a patient. By the 1910s, Schiøtz tonometer was the new gold standard for clinical examination.[175–178]

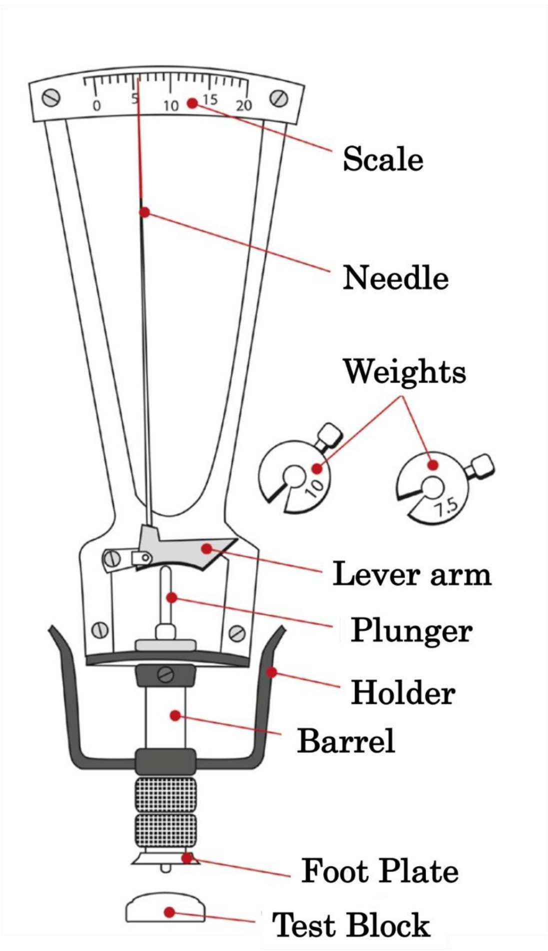

Figure 2.17: Schiøtz tonometer where test block used for calibration check procedure.[24]

2.6.1.2 Applanation Tonometry

In 1867, Adolf Weber had a breakthrough by designing the first applanation tonometer, which estimated IOP through a defined applanation of the cornea rather than indentation of the tissue.[176] By the late 1880s, Alexei Maklakoff, among others, rediscovered applanation tonometry and introduced more innovative versions of applanation tonometry devices. Nonetheless, among ophthalmologists, the "gold standard" was digital palpation tonometry, known for the fingertip test.[57]

Goldmann Applanation Tonometry

In the 1950s, Hans Goldmann broke through the design of the first applanation tonometer, which was considered corneal biomechanics. The Goldmann applanation tonometer (GAT) soon enjoyed widespread approval in the clinical community and became the "gold standard" in tonometry (ISO, 2001) −a status that has been maintained until now.[25] This tonometer was the first of its kind to follow the Imbert-Fick law. This law suggests that a load (W) would flatten an area (A) of a thin membraned dry sphere; if and only if this distributed load is equivalent to pressure (P) within this sphere, see Equation 2.5.[179]

$$P = \frac{W}{A} \tag{2.5}$$

Misusing this concept of the cornea suggests that the globe has a dry surface and an elastic infinitely-thin cornea.[180] in efforts to consider the cornea's true conditions, it was necessary to modify Equation 2.5 to involve the curved moist surface of the cornea. Two more variables were added to the relationship; corneal bending resistance and surface tension, see Figure 2.18. It was then decided to fix the applanation area at $7.35mm^2$, which assumed a central corneal thickness of $520\mu m$. This assumption would negate corneal bending resistance with its surface tension.[72,181,182] GAT was a breakthrough in tonometry, though it did assume major corneal characteristics and fixed them in the device. Patients' corneas vary in curvature, rigidity, or thickness; all these factors contribute to inaccuracies of IOP estimation. These variations play a major role in the diagnosis and management of glaucoma.[183,184] Other than GAT's technical issues with IOP estimation, there have been implications with the use of local anaesthetics and the presence of human error, which is due to the manual process by GAT.

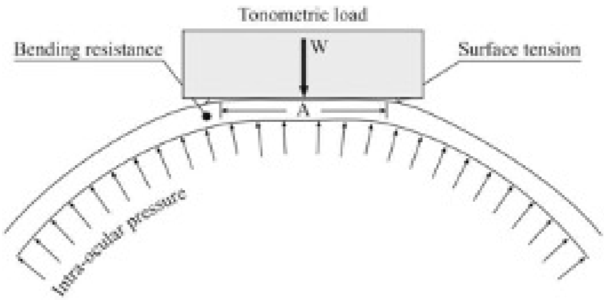

Figure 2.18: Factors influencing the IOP measurement by GAT, including the surface tension created by the corneal tear film and its bending resistance[25]

2.6.1.3 Dynamic Contour Tonometry

Dynamic contour tonometry (DCT) was developed to improve the accuracy of IOP, and this endeavoured in response to GAT's dependence on corneal stiffness. The most important property is that the tonometer tip is curved and pushed against the corneal surface until it matches the tip's curvature. This property reduces the corneal deformation and hence dependence on corneal stiffness.[185] DCT is principled on Blaise Pascal's law of hydrostatic pressure, which states that gases and liquids within a confined space have constant pressure applied perpendicularly to all its boundaries.[186] On that note, after the application of local anaesthetics, slight pressure is applied by the device onto the corneal surface; this forces the surface to take the shape of the tip's curvature, see

In contact with the corneal surface, the tonometer tip is a $7mm$ ring with a curvature of $10.5mm$ and a hollow tube in the centre. The dimension of this tip was elected to match an average corneal topography, while the hollow tube was designed to house a tiny piezoelectric sensor. This sensor measures pressure on the outside corneal surface, assuming it equals the pressure inside (IOP).[187] Each pressure measurement of the sensor lasts 6 seconds with a total duration of 2.5 minutes. The requirement for more than one reading for most patients makes the test duration a major drawback. Nevertheless, due to the semi-automation of the process, human error is reduced, which makes this technique one of the more accurate ways to estimate the IOP of the globe.[188] Figure 2.19.

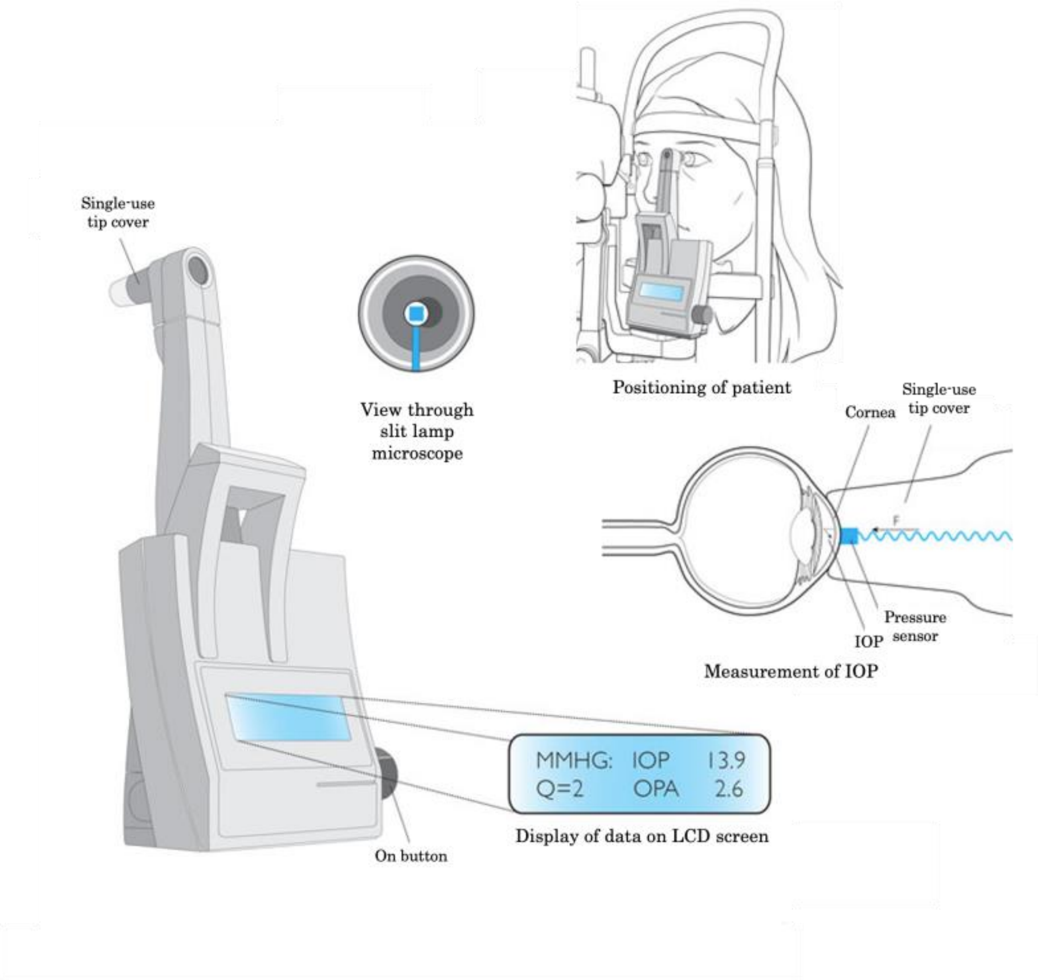

Figure 2.19: The DCT and its methodology in measuring IOP[26]

2.6.1.4 Non-Contact Tonometry

In 1972, American Optical (AO) introduced the first non-contact tonometer (NCT). This device has paved the way for a more feasible glaucoma screening. NCT differs from other tonometer types by replacing an object with an air pulse to deform the cornea. With sensors and high-speed cameras, more information was acquired about the corneal response, i.e. 1^{st} and 2^{nd} applanation. Like GAT, corneal applanation is a crucial stage for IOP measurement; therefore, the pressure for 1^{st} applanation was recorded. While applying this burst of air, secondary to corneal deformation, there is a slight yet notable whole-eye movement (WEM).[189] Previous studies suggested that these WEM amplitudes may be related to elastic properties of deeper structures behind the globe. This tonometry device required the clinician to align the globe for pressure application. The patient was asked to fixate on a light. However, due to the noisy nature of air bursts, blinking occurs, which causes errors and may need the procedure to be repeated.[190] In 1986, Keeler Pulsair introduced the first tonometer, which eliminated the need for a specialist to carry out the procedure, making it easier to use.[191] Modern tonometry devices −Ocular Response Analyser (ORA) and Corvis ST− developed over the past decade are discussed below.

Ocular Response Analyzer

In 2005, the Ocular response analyser (ORA) was introduced, not as a tonometer for IOP measurement only but also for corneal biomechanics measurements, including Corneal Hysteresis (CH) and the Corneal Resistance Factor (CRF). An electro-optical sensor identifies the time and pressure at which a flattened surface is obtained −applanation pressure− in both the loading (P_1) and unloading (P_2) conditions of the corneal surface, see Figure 2.20. The difference between first and second applanation pressures is CH ($CH = P_1 - P_2$), while $CRF = k_1P_1 + k_2P_2$, where k_1 and k_2 are constants obtained through optimisation relative to clinical data.[192] The mean value of P_1 and P_2 provides a repeatable simulation of Goldmann-corrected IOP (IOP_g), while CH enables evaluation of corneal-compensated IOP (IOP_{cc}). IOP_{cc} is less influenced by corneal biomechanics.[193] Due to measurement taking a few milliseconds, it has been shown that it is influenced by cardiac cycle, as well as ocular pulse.[194] Despite of correlation of IOP measurement in ORA with corneal biomechanics, it is not the same as measurements of GAT.[195–197] Another problem with ORA is that its measurements (CH and CRF) are not related to mechanical properties (i.e. tangent modulus), and therefore it is not known for sure what they represent.[198]

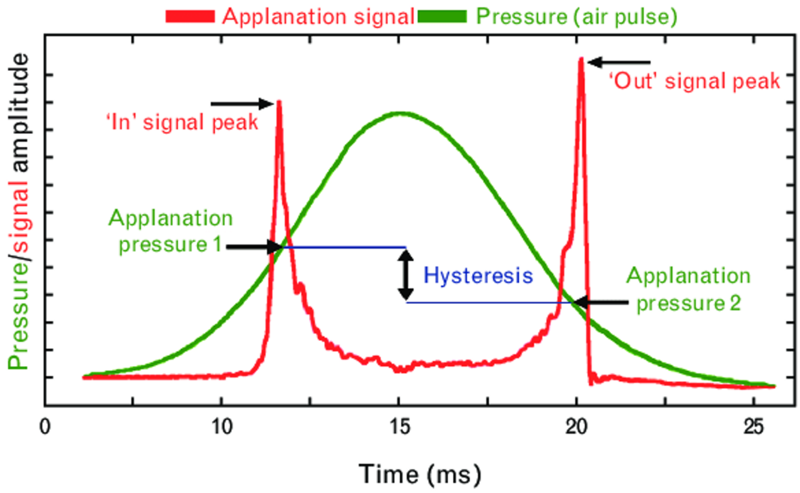

Figure 2.20: Ocular response analyser reading.[27]

Corvis ST

In 2010, OCULUS Optikgeräte GmbH (Wetzlar, Germany) developed CorVis ST. This device shed light on a detailed investigation of dynamic corneal response (DCR) to air-puff pressure. DCRs were accurately obtained through analysis of 132 frames of corneal deformation, Figure 2.21. Those frames are taken by a high-speed camera, based on the Scheimpflug principle, able to take 4330 frames per second, covering 8.5mm of the horizontal corneal meridian.[199] The Scheimpflug principle is also used in corneal topography mapping. In addition, Corvis enabled corneal thickness measurement by providing corneal posterior surface information. This measurement allowed extensive research to be conducted, producing parameters that facilitate analysis of corneal biomechanics, which led to obtaining more accurate IOP measurements. Imperative information is provided by parameters, such as Stress-strain index (SSI) and biomechanically corrected IOP (bIOP).[31,200,201] Additional parameters, such as; Stiffness Parameter (SP) and Corneal Biomechanical Index (CBI), able to measure overall corneal stiffness and to determine corneal keratoconus, respectively.[202,203] Furthermore, Koprowski et al.[204] highlighted that the corneal response to Corvis air pressure is subjected to the indentation at the corneal apex as well as a prominent WEM noticed at the periphery of the captured frame. Another study observed temporal retardation in the WEM causing nasal rotation of the globe and suggested relations to properties of deeper orbital structures behind the eye globe.[143] Corvis' DCR parameters allowed considerable progression in the field of ophthalmology, as such development of bIOP and SSI using some of these parameters,[31,205] and they are as follows:[28]

- **Pachy:** This is the central corneal thickness (CCT);
- **1^{st} and 2^{nd} Applanation Time (A1T and A2T):** This is the time at which the cornea becomes flat, the first applanation is during pressure loading, while the second is during unloading;
- **1^{st} and 2^{nd} Applanation Lengths (A1L and A2L):** This is the length at which the cornea becomes flat, the first applanation is during pressure loading, while the second is during unloading;
- **1^{st} and 2^{nd} Applanation Velocities (A1V and A2V):** This is the velocity at which the cornea becomes flat, the first applanation is during pressure loading, while the second is during unloading;
- **1^{st} and 2^{nd} Applanation Pressures (AP1 and AP2):** This is the length at which the cornea becomes flat, the first applanation is during pressure loading, while the second is during unloading;
- **A1 Deflection Amplitude (DeflAmpA1):** This is the displacement covered by the cornea from the natural position until A1 Time;
- **Deflection Amplitude Maximum (DeflAmpMax):** This is the maximum displacement covered by the corneal apex to the highest concavity. This value was obtained by identifying the most prominent apical deformation profile during the air-puff procedure;
- **Highest Concavity Time (HCT):** This is the time index at which DeflAmpMax was identified;
- **Radius at Highest Concavity (HCR):** This is the radius of the circle of best fit;

- **Peak Distance (PD):** This is the distance between two peaks on the cornea where the highest concavity occurred;

- **Stiffness Parameter at A1 (SPA1):** This parameter was initially introduced by Cynthia Roberts et al.,[206] in which it is acknowledged to be interrelated with overall corneal stiffness, **Equation 3.8**

$$SPA1 = \frac{AP1 - IOP}{DeflAmpA1} \tag{2.6}$$

- **Stiffness Parameter at HC (SPHC):** This parameter has a very similar approach of calculation to SPA1; however, this stiffness parameter only considers deformation occurred between A1 time and HC time, **Equation 3.9**

$$SPHC = \frac{AP1 - IOP}{DeflAmpMax - DeflAmpA1} \tag{2.7}$$

- **Corneal Asphericity (P and R Values):** X-Y coordinates of each relaxed and after corneal inflation profile were utilised with corneal asphericity Equation 3.10 and an optimisation process to determine apical radius (R) and shape factor (P) value, Figure 3.46;[29]

$$Y^2 = 2 \times R \times X - P \times X^2 \tag{2.8}$$

Where:

P = Shape factor R = Apical radius

When:

P > 1	P = 1	P < 1
Oblate ellipse	Circular	Prolate ellipse

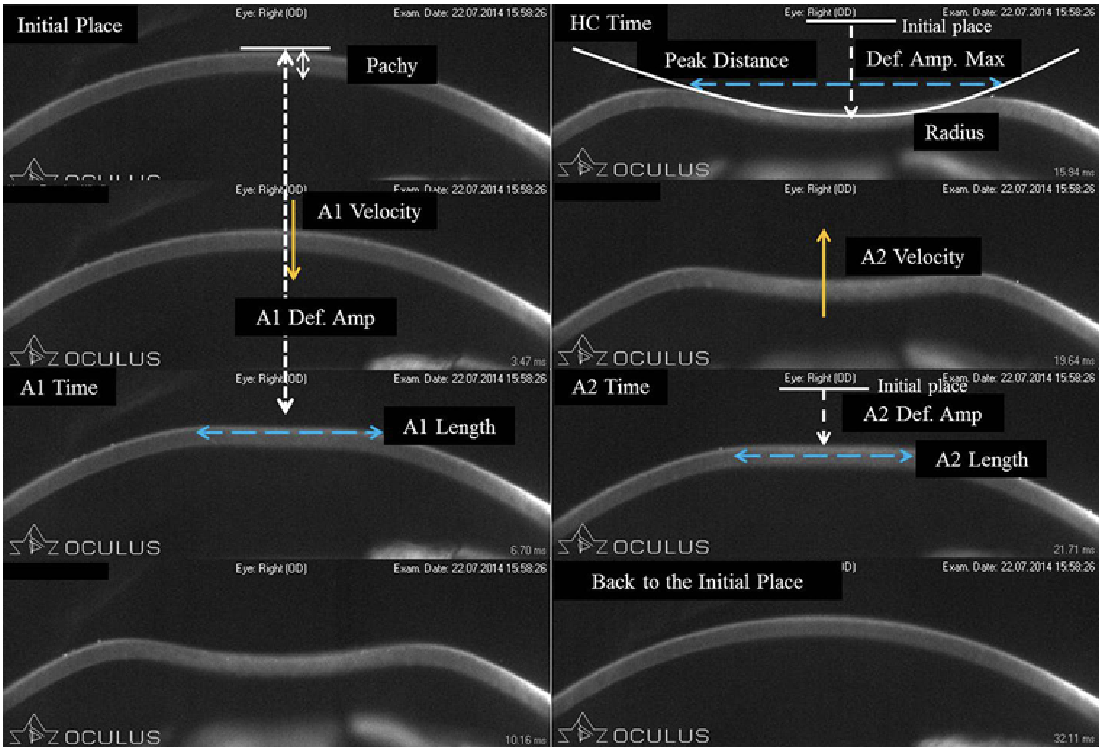

Figure 2.21: Dynamic Corneal Response (DCR) parameters extracted from corneal response to Corvis air-puff; the initial position of the cornea (top left), to the highest concavity (top right) to finally back to the initial position (bottom right)[28]

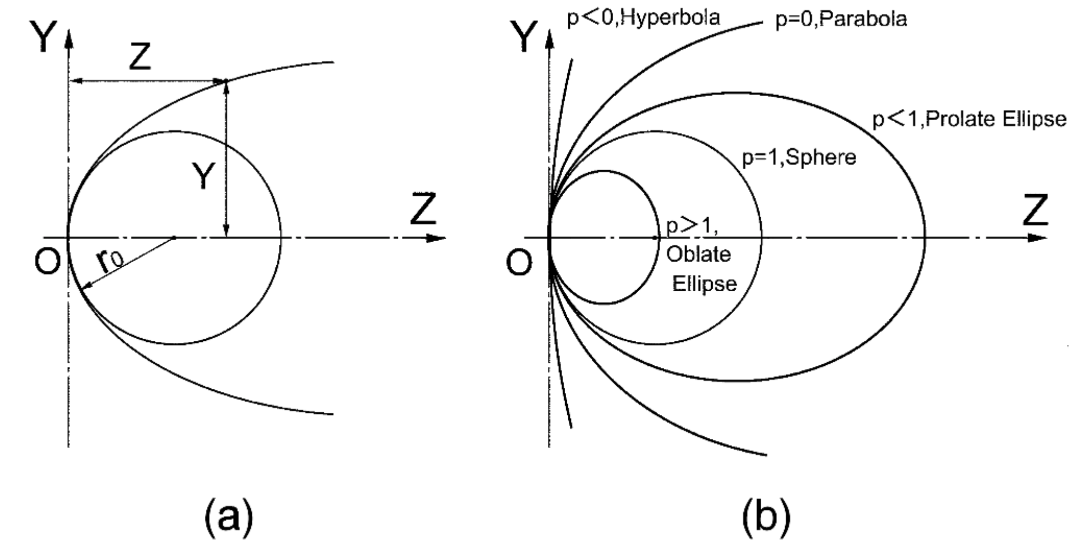

Figure 2.22: (a) Apical radius shown on Cartesian coordinates (b) The family of shape factors[29]

2.6.1.5 Continuous Tonometry

Prior studies showed that IOP fluctuates throughout the hours of the day.[70] Therefore, to accurately diagnose severe glaucoma patients, continuous tonometry was essential to monitor those fluctuations in pressure. Sensimed Triggerfish claims that its device can monitor fluctuations in IOP over 24 hours. This monitored data is wirelessly transferred through a communication unit, which is then sent to the recorder for analysis purposes, Figure 2.23.

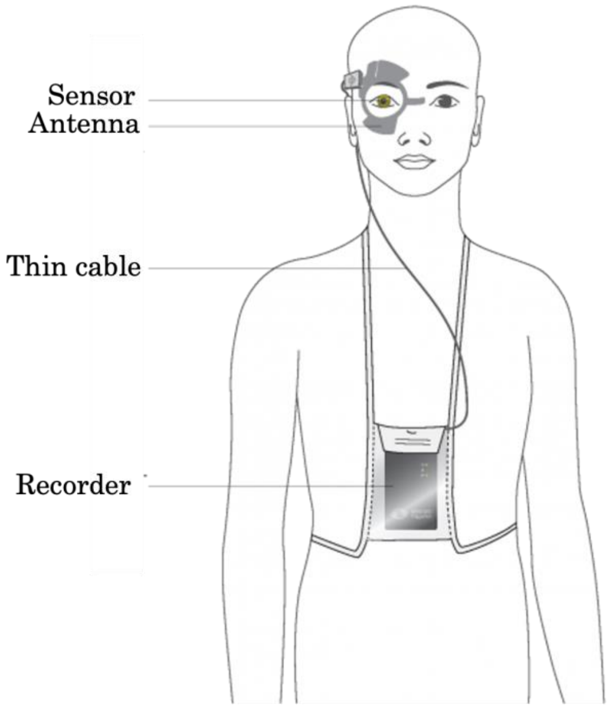

Figure 2.23: Sensimed Triggerfish set-up.[30]

The device is a contact lens-like which is placed on a corneal surface. Over 24 hours, 144 measurements are recorded. The device estimates the IOP by measuring changes in limbal cornea curvature through a telemetric sensor. This measurement leads to an inaccurate estimation of IOP, hence an error in glaucoma diagnosis. Additionally, this monitoring technique requires a surgical procedure to implant the device. Therefore, it is only prescribed to patients with severe glaucoma conditions, where damage to the optic nerve head may be caused due by IOP fluctuation.[207–209]

Chapter 3

Methodology

3.1 Introduction

This chapter discusses the methodology of the numerical model development, starting with how the orbital boundary was acquired from clinical CT scans. The orbital space between the outer boundary and the global cavity was discretised using a novel meshing technique implemented in an in-house software code explicitly developed to generate orbital numerical models with various geometrical specifications, some of which depended on age, gender and ethnicity. Thenceforth, a mesh density study was carried out to obtain the optimum mesh density, where stable results were acquired with the minimum possible computation time. Validation of the numerical model then took place using clinical data. This validation was done using a numerical model without EOMs and their pulley representation. EOMs were then added to the model, and the validation was repeated against clinical data, including Whole Eye Movement (WEM), as well as the globe's rotation during the Corvis pressure application. Clinical WEMs were then utilised in an optimisation process to estimate the changes in EOMs' initial tension during the Corvis ST procedure. The outcome of this optimisation was used in building a database for a parametric study to develop algorithms to estimate the cornea's material stiffness and a biomechanically corrected IOP. Finally, these algorithms were validated with *ex-vivo* and further clinical data.

3.2 Numerical Model Development

Age-gender-specific numerical models were developed to understand the corneal response to Corvis air-puff. Contrary to previous studies, rigid body motion of the eye globe was not prevented. Hence the resulting whole eye movement was utilised in validating numerical models encompassing contents of the orbit, including the eye globe, using clinical profiles. This project mainly focused on corneal biomechanics and the mechanics of exterior boundary conditions on the globe. In addition, due to the size of the numerical model and the studies it serves, adding detailed structures would be computationally expensive. Therefore, it was not essential to add detailed intraorbital structures. Instead, aqueous and vitreous were simulated by introducing fluid cavity as an incompressible fluid with a density of $1,000\ kg/m^2$.[62, 210, 211]

This section will start by describing how CT-Scans were utilised to describe the geometry of the bony orbital walls. This is followed by exploring a novel meshing technique, which uses a single element type to mesh irregular, unsymmetrical shapes. After that, a Matlab algorithm is presented, showing the methodology followed in selecting elements in EOM insertion regions. Consequently, the boundary conditions of the whole model are discussed, including those on the EOMs pulleys. In addition, a custom-built Matlab algorithm will present how corneal anterior surface geometry was utilised to accurately apply Corvis air pressure on the cornea of the numerical models. A bespoke software code was developed and used to produce three batches of models; the first of just the globe with varying corneal mesh density, while the second varied of scleral mesh density only. The final batch included variation in the orbital mesh density. As a result, the most reliable nodal output data with the least computational time was acquired, and the numerical model was ready for validation.

3.2.1 The Eye Globe

The first step in the numerical modelling of the ocular system is to create the globe's geometric model. The University of Liverpool Biomechanics group developed a custom-built Matlab code (Ocular Mesh Generator) to recreate ocular geometry in the form of a Finite Element Model (FEM) numerical structure. To recreate a realistic set-up, the model was constituted of three main regions; the cornea, limbus and sclera. As seen in Figure 3.1, the Ocular Mesh Generator produces models by controlling several geometrical features and mesh density options. The globe's numerical model is formed by discretised 15-noded continuum elements (C3D15H) arranged in a number of layered rings. The mesh density of the model is controlled by defining the number of corneal and total rings and the number of ocular layers.

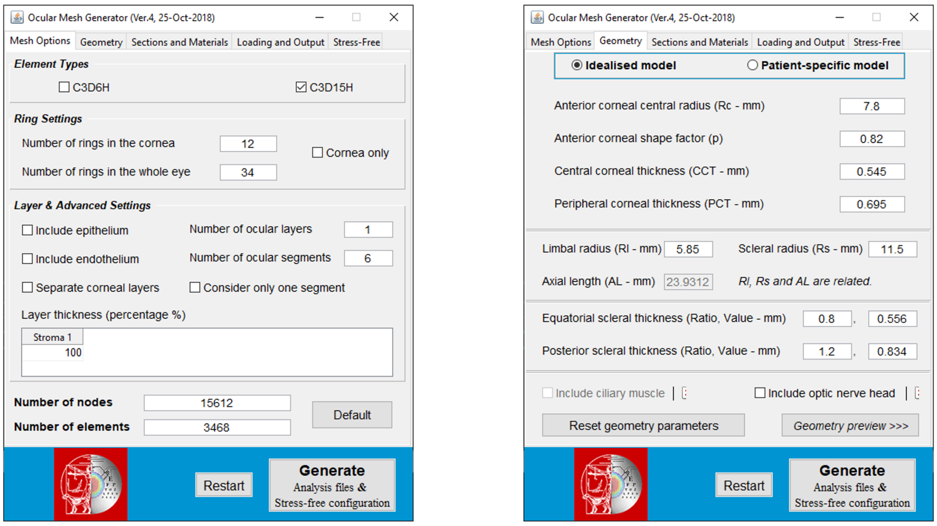

Figure 3.1: Screenshots of Ocular Mesh Generator graphical user interface.

The globe is divided into five element sets, one for the cornea, one for the limbus and three for the sclera, Figure 3.2. This was done because only one set of material parameters is commonly used for the cornea. In contrast, the scleral part of the globe is divided into three regions (anterior, equatorial and posterior), each of which is assigned a unique set of material parameters that were obtained from previous studies.[16,17,160] The idealised model assumed rotational symmetry around the anterior-posterior axis. A further assumption was that different geometrical factors defined the corneal ellipsoidal shape. Those factors included the anterior central radius, Rc; central corneal thickness, CCT; peripheral corneal thickness, PCT and anterior shape factor, p. On the other hand, a spherical exterior surface with radius, Rs, was employed for the scleral part of the idealised model. In addition, scleral thickness was assumed to reduce linearly from PCT at the limbus to $0.8PCT$ at the equatorial scleral thickness, (EST), followed by a linear increase to $1.2PCT$ at the posterior pole, (PST). Mean geometrical measurements of healthy subjects were used in an initial build-up of the orbital medium, Table 3.1, bearing in mind that these geometric values could be redefined to suit patient-specific data.

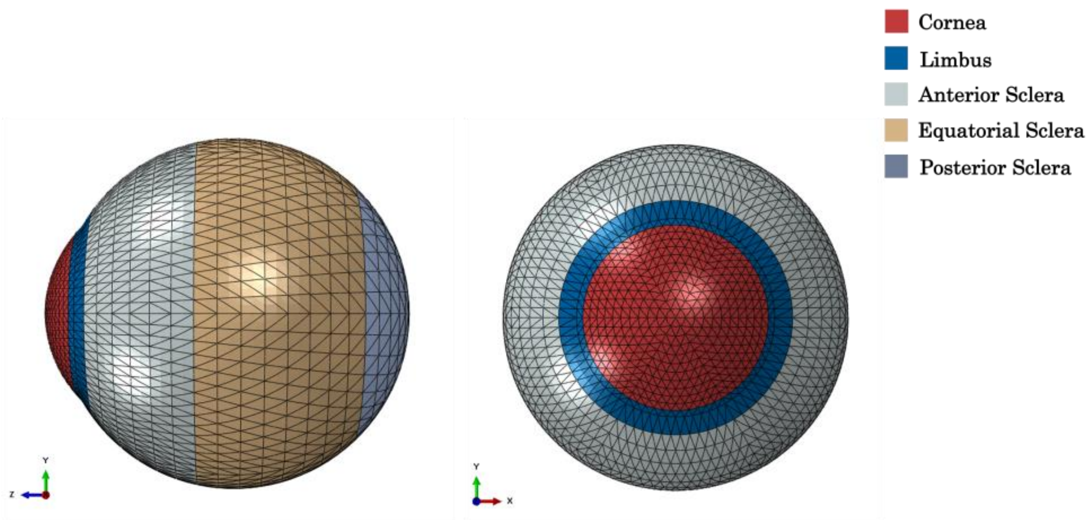

Figure 3.2: Ocular globe generated by the custom-built Matlab Ocular Mesh Generator.

Table 3.1: Mean geometrical measurements of healthy subjects.[42–47]

Geometrical characteristic	Mean value
Anterior central radius, Rc	7.8 mm
Central corneal thickness, CCT	0.545 mm
Peripheral corneal thickness, PCT	0.695 mm
Equatorial scleral thickness, EST	$0.8PCT$
Posterior scleral thickness, PST	$1.2PCT$
Scleral radius, Rs	11.5 mm
Limbal radius, Rl	5.85 mm
Axial length, Al	23.9 mm
Shape factor, p	0.82

3.2.1.1 Element Types

The Biomechanical Engineering Group at the University of Liverpool has relied on using 6-noded elements (C3D6H) for globe simulation during previous research.[42] Wang[212] later compared models of 6 and 15-noded elements (Figure 3.3) in terms of model stability, rate of convergence and computational time. It was established from that study that the soft material of the cornea was more likely to cause model instability with 6-noded elements.[213] Therefore, it was recommended to use the 15-noded elements for the globe in future work and include this project. Furthermore, a similar study was carried out to compare the optimality of element types in the orbital medium. Contrary to the globe, it was established that models based on 6-noded and 15-noded elements resulted in identical output. However, the simulation time of 15-noded element models was greater than with the 6-noded elements. Hence, it was recommended to use 6-noded in the OST and the insertion elements of EOMs.

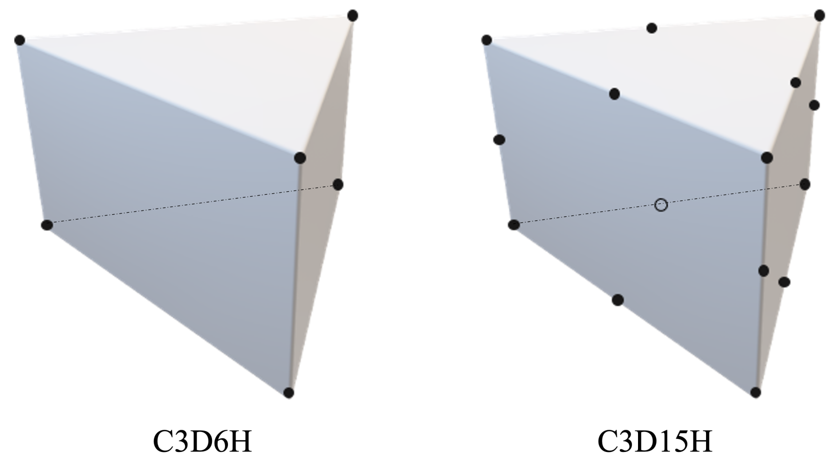

Figure 3.3: Difference between Finite element types 6 and 15-noded elements.

3.2.2 Geometry of Bony Orbit

During this project, the new numerical models employed a 3-dimensional representation of the orbit. This 3D representation was acquired using CT scans, which Beijing Advanced Innovation Centre provided for Biomedical Engineering at Beihang University. The CT scans belonged to three young Chinese female subjects aged 27, 34 and 40 years. They were loaded on RadiAnt DICOM Viewer; an application utilised to display and process medical images in DICOM format (Digital Imaging and Communications in Medicine). Once all data was loaded, a few tasks were required to be carried out:

- Check-up for any geometrical abnormalities of the bony orbit
- Adjust capture angle of CT-scans

- Distance measurement and annotation
- Saving all subjects' scans as images compatible with the image processing algorithm

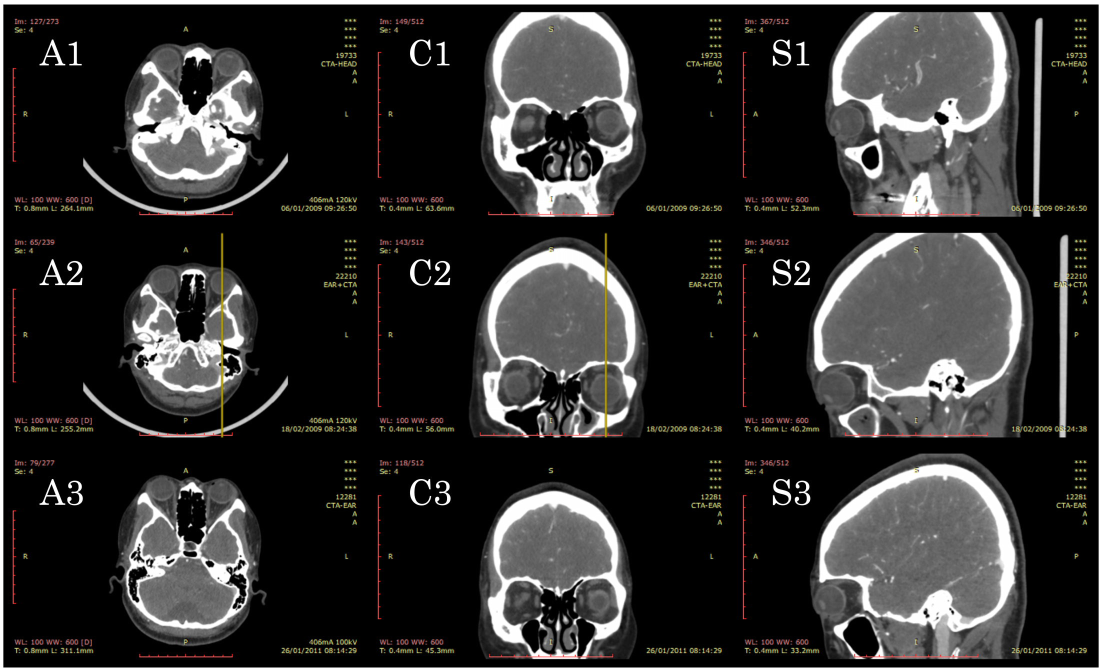

Figure 3.4: CT-scans of subjects used in the numerical reconstruction of the orbital boundary. (A1-3), (C1-3), and (S1-3) are axial, coronal and sagittal planes, respectively.

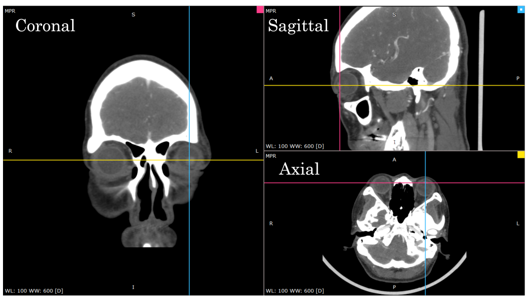

(a) Misaligned

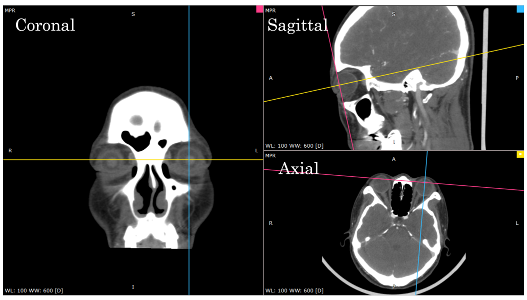

(b) Aligned

Figure 3.5: 3-Dimensional Multi-planar Reconstruction tool used to tilt base planes to counteract the tilt of the skull.

First, an experienced clinician at Beihang University examined all subjects for any geometrical abnormalities, which may cause inaccuracies in the orbital representation, and the examiner concluded that all subjects had healthy orbital geometry with no abnormalities. However, it was pointed out that the subjects' skulls were tilted inferiorly and nasally, see S1-3 in Figure 3.4. Therefore, it was essential to adjust the capture angle to align slices with the globe's axial length. A feature in the DICOM reader is 3D Multi-planar reconstruction (MPR). This 3D-MPR tool provides insight into anatomical visualisation by allowing the DICOM reader to reconstruct images in arbitrary planes. This tool was brought into play to adjust CT slices to overcome the tilt of the skull. As seen in Figure 3.5(b) compared to Figure 3.5(a), the coronal plane has significantly changed, where the superior and inferior portions of the orbital rim started to be visible in the same slice.

Furthermore, The DICOM viewer had a feature of distance measurement and annotation on CT slices, where it measured the distance between two user-defined points to the nearest 0.01 *cm*. This feature was made use of by marking 4 points on a slice on which one pair were aligned horizontally while the other pair were aligned vertically. This alignment was followed by measurement of the inner distances between each aligned pair, then annotated accordingly as vertical and horizontal distances, see Figure 3.6(a). This calibration slice was then exported as a Portable Graphics Format image (.png) to be adopted during a pixel-mm calibration process. It is essential to avoid adjusting anything to the view of the CT slice, as this would cause inaccuracies in the calibration process due to an unaccounted change in pixel-mm ratio. Hence, measurement of horizontal and vertical distances was carried out on the first slice, as shown in Figure 3.6, while the view was kept consistent, as can be seen with the remainder of the slices in Figure 3.7.

Once the view and size of the slice were set and locked, slices were started to be saved as images for image processing. The image processing of these slices had a few procedures concerning preparation. First, previously saved slice images were loaded into an image editor where curved polygons were drawn accurately onto orbital boundary as well as marking globe's and optic nerve boundary when visible, see 3.6(b) and Figures 3.7(d)-(l). Consequently, the orbital polygon colour was then defined using an RGB scale combination, while boundaries of the globe and optic canal were defined using a different colour combination. In the coronal view of the skull, there were an average of 573 CT slices per subject. Hence, it would have been very time-consuming to prepare 1719 slices. Therefore, only a reduced set of thirteen slices were acquired for each subject at equal intervals. Due to the tilt of the bony orbit with regard to the primary gaze of the globe, geometry acquirement of the orbital rim from CT scans was neglected. This was decided to save time on unnecessary complexity in the data processing. In addition, ethnic (Asian and Caucasian) orbital rim elevation regarding the corneal apex is available in the literature and shall be used during this numerical model's development.[20,37,38] Thus, the first attained slice was when the lateral portion of Zygomatic bone starts to be visible, see 3.6(b). For each subject, thirteen CT-slices were analysed, the first being at level with the lateral orbital rim, while the final at the orbital apex, see Figure 3.7.

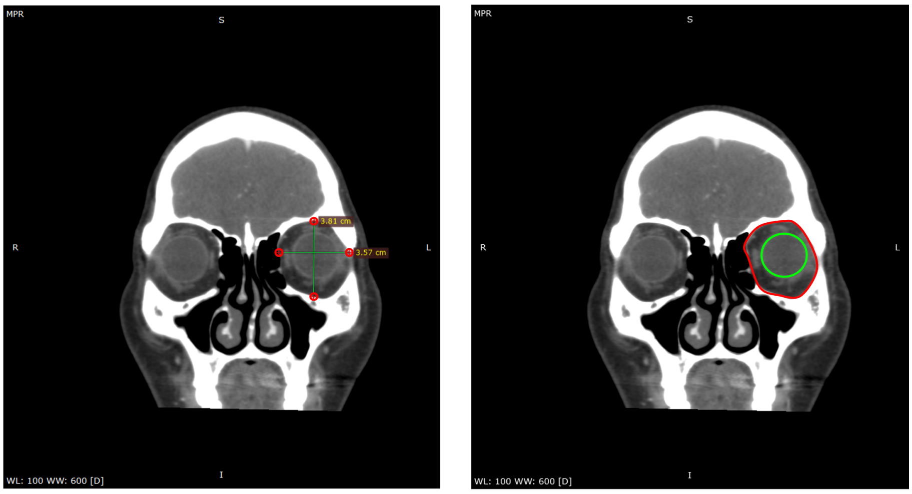

(a) Annotated vertical and horizontal distances used in pixel calibration

(b) Marked polygon indicating an estimation of globe's position

Figure 3.6: Indicates how the first slice of CT scans was used to calibrate and estimate the globe's position in orbit.

CT scans used during this process had a consistent slice spacing; however, when the scans' planes were tilted using 3D-MPR, it was impossible to use the previously specified spacing, as the plane has now changed. Therefore, the distance between the first and last slices used in the boundary definition was measured. This measurement was done by marking the locations of each slice on the sagittal plane and then measuring the distance between anterior and posterior locations, which are represented by arrows in Figure 3.8. Therefore, to acquire slice spacing (SS), Equation 3.1 was used, where $Depth_{O_A}$ is orbital apex depth and NoS is the number of slices.

$$SS = \frac{Depth_{O_A}}{NoS - 1} \tag{3.1}$$

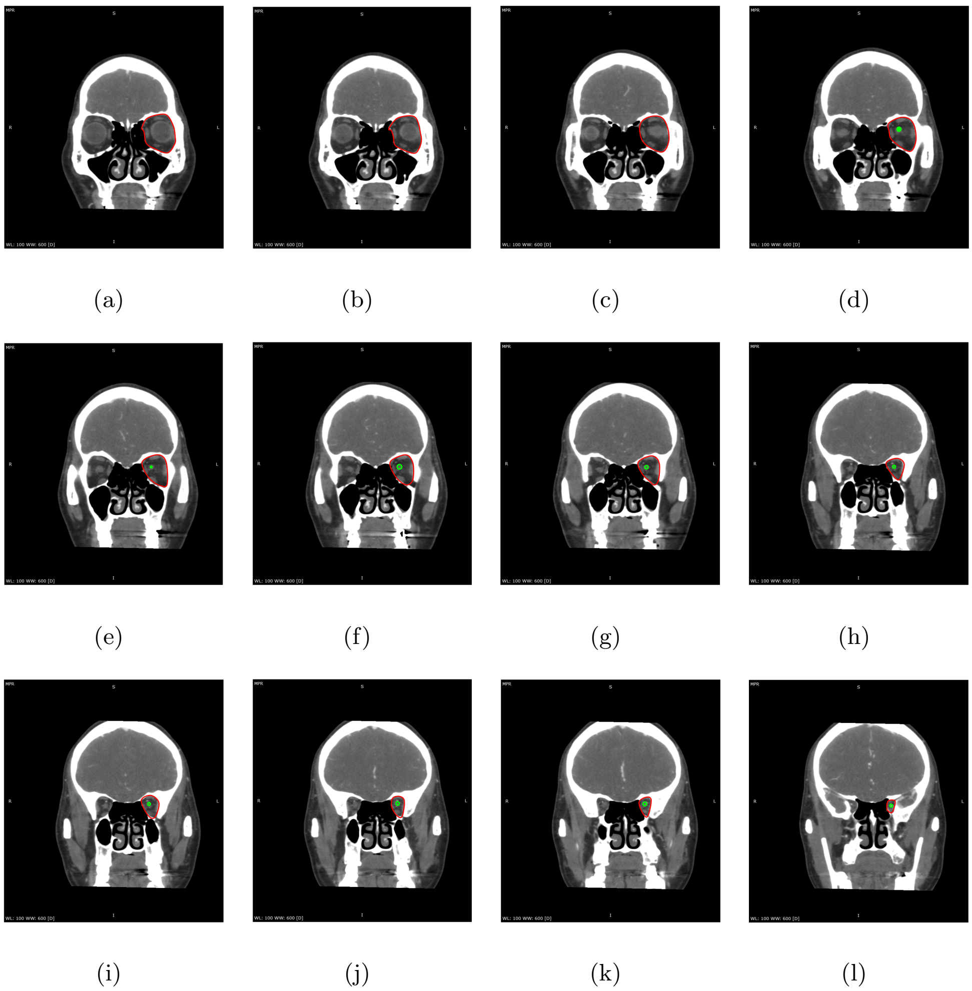

Figure 3.7: (a-l) Showing slices posterior to lateral orbital rim till orbital apex.

At this point, *forty-two* CT-scan images –*fourteen* images per subject– were acquired from the DICOM viewer. At this point, images were ready to be loaded onto the in-house developed image processing tool. This image processing algorithm was developed to extract coordinates of previously marked orbital boundaries, the globe's X-Y position, and the optic canal's path. However, prior to this, the calibration slice was loaded onto the algorithm, where all marked points were detected and compared to clinical lengths for pixel calibration, see Figure 3.6(a). As seen in Figures 3.7 and 3.6(b), orbital border was assigned a red boundary with an RGB combination of [255 0 0], while the globe's position and optic canal were assigned a green boundary with a combination of [0 255 0]. The algorithm employed previously defined RGB scale combinations in the extraction of boundary coordinates, achieved by filtering out image pixels with RGB combinations that did not match any of the previously stated combinations, see Figure 3.9.

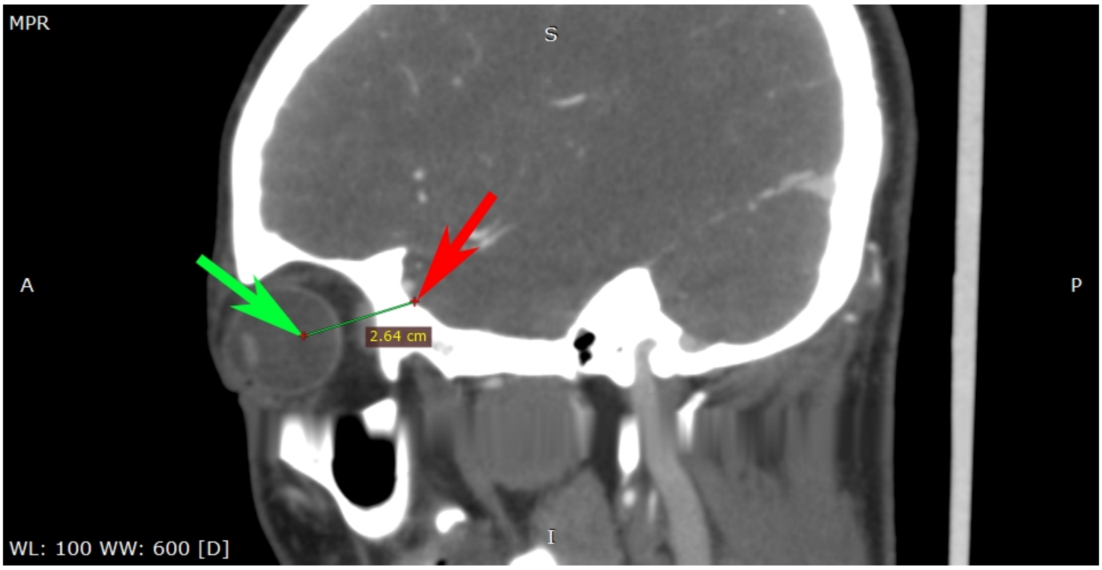

Figure 3.8: Technique used to estimate the partial depth of orbital apex from first slice position (Green arrow) till the apical position of the orbit (Red arrow).

Consequently, horizontal and vertical positions of filtered-in pixels were calibrated accordingly to attain their positions in mm. Furthermore, slice spacing calculated by Equation 3.1 was then used as a benchmark for determining the orbital depth of each slice. This boundary detection process was repeated for all *thirteen* slices, where all data points were eventually compiled. As a result, orbital X-Y-Z coordinates of a clinical subject were acquired in a vector form, facilitating data processing, hence progression onto the following stage of model development. This boundary detection process was repeated with the other two subjects, thenceforward a mean orbital geometry was produced, see Figure 3.11.

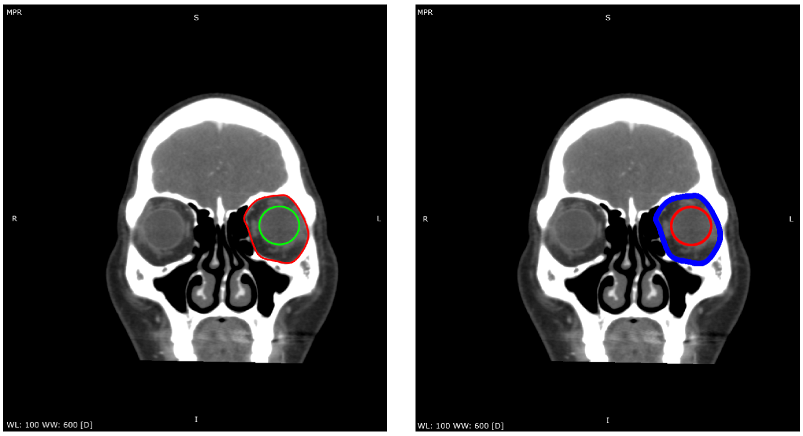

(a) (b)

Figure 3.9: (a) Showing original CT-slice loaded in the imaging processing tool. (b) Original CT slice after both boundaries were detected and plotted onto the original slice.

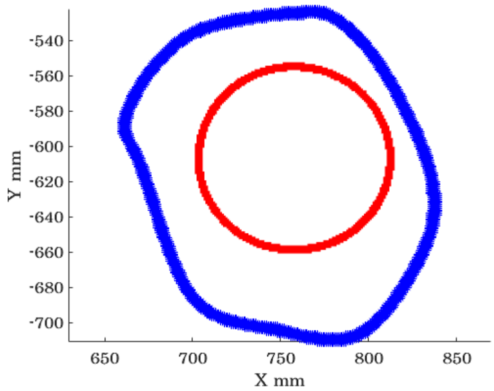

Figure 3.10: Both boundaries are stored to be compiled with the boundaries of the rest of the slices.

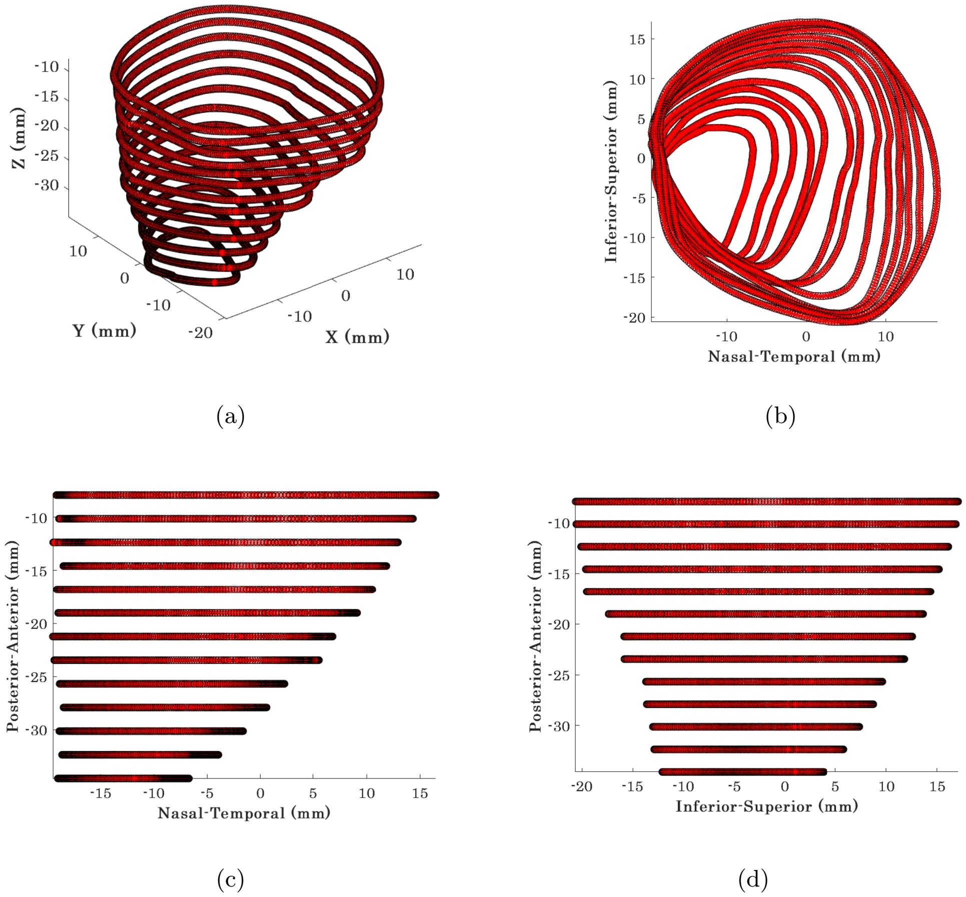

Figure 3.11: Showing mean geometry produced from three young female subjects, where: (a) Perspective 3-dimensional view. (b) X-Y plane view. (c) X-Z plane view. (d) Y-Z plane view.

Attaining accurate geometry of the orbital rim from CT scans could have been a complex process. Nevertheless, it was assumed that non-symmetric elevation of the orbital rim might be essential in the numerical recreation of the globe's support system. Therefore, accurate data of the orbital rim elevation to the corneal apex was acquired from a previous study as mentioned in Figure 3.12. This study had orbital rim geometry for two ethnic groups: Asian and Caucasian. Asian orbital rim data were used with the initial preparation of the numerical model, as the CT scans belonged to Asian subjects. However, later in this project, with reference to the literature, orbital geometry was altered to suit the Caucasian population, which was then used in a parametric study later in this project.

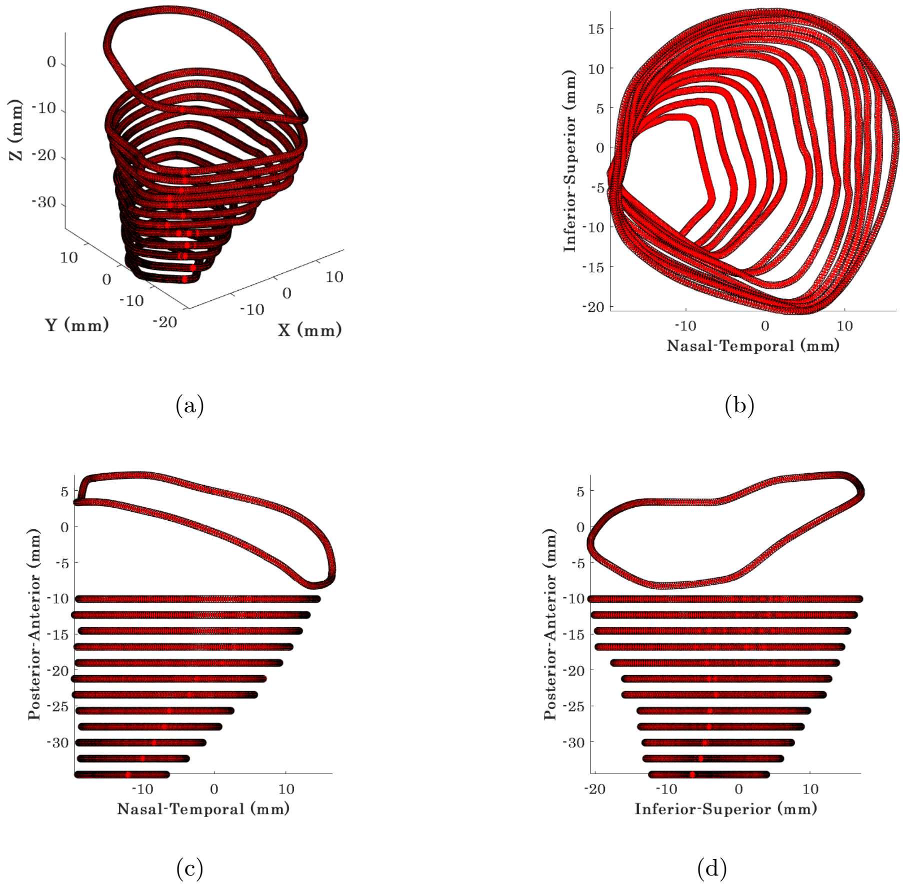

Figure 3.12: Showing mean geometry produced from three young female subjects after orbital rim elevation was applied, where: (a) Perspective 3-dimensional view. (b) X-Y plane view. (c) X-Z plane view. (d) Y-Z plane view.

3.2.3 Orbital Geometry Discretization

The geometrical discretisation of the orbital medium is essential for FEM, as it will split the orbital volume into discrete elements (Mesh) connected by nodal points. Up to this point, 3-dimensional reconstruction of the bony orbital boundary was achieved from clinical CT scans. Nevertheless, the global cavity and optic canal were added to the geometry to complete the geometrical preparation for discretisation. These two components form an inner boundary for the orbital medium. The centroid of the globe's position was located from earlier stages of this development process. In addition, the optic canal's path was estimated by marking the optic nerve boundary in the CT slices where it was visible. To start the discretisation process, the orbital boundary was divided into a number of rings (NoR) around the Z-Z axis, the number of which is defined by the user, see Figure 3.13(a). The precise fitting of the globe to its cavity is ensured by employing the globe's numerical nodal coordinates and using them as nodal coordinates of the cavity.

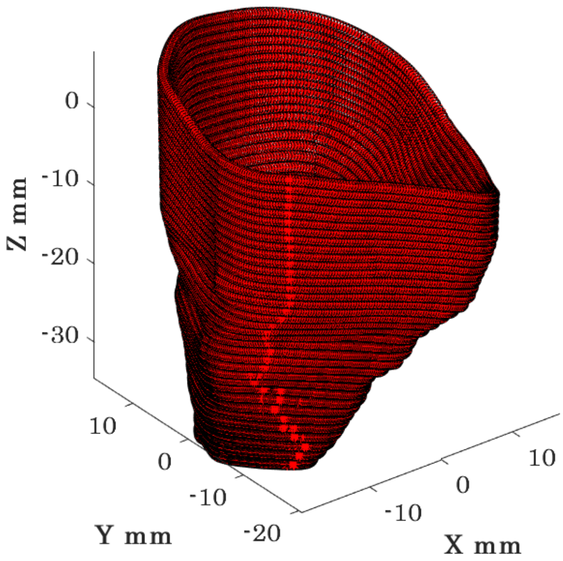

(a)

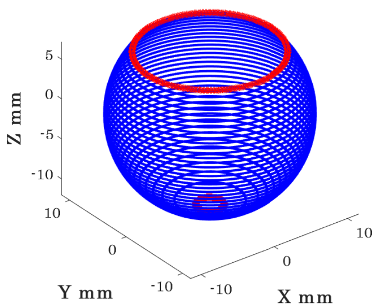

(b)

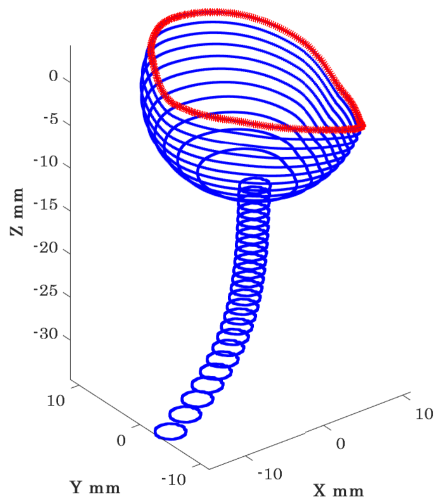

(c)

Figure 3.13: (a) Outer boundary of the orbital space. (b) Cavity nodes retraced from global nodal data. (c) The inner boundary of the orbital space.

However, as can be seen in Figure 3.13(b), two portions were removed from those nodes, the larger portion from the top, to allow for an engulfing recreation of the globe and its surrounding orbital soft tissues. In a similar manner, removal of the smaller posterior portion allowed for where the optic canal path starts. The optic canal was simulated as a tunnel connecting the cavity to the orbital apex. Computational complications of FEM often occur due to excessive distortion of high aspect ratio elements. Hence, sharp edges within the model were avoided to eliminate this source of error. Therefore, the anterior edge of the cavity was modified to have a similar shape to the orbital rim, see Figure 3.13(c). Similar to the outer orbital boundary, the inner boundary was divided into the same number of priorly defined rings, see Figure 3.14(a).

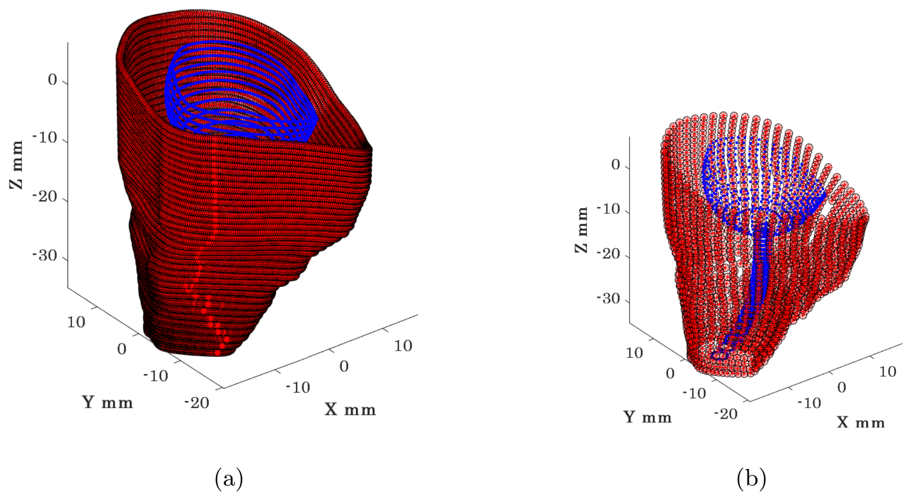

Figure 3.14: Inner and outer boundaries of the orbital space combined in one geometry (a) Each ring is divided into *360* sectors. (b) Rings split into *50* sectors

Both orbital boundaries initially had rings split into sectors with equal angular spacing. For example, in Figure 3.14(a), the rings are split into *359* points with a 1^o angle interval between every two adjacent points. The finer the discretisation gets, the more computationally accurate it can become and the more computationally expensive it gets. Therefore, this bespoke discretisation algorithm allows for changes in spacing between points, whether it is an angular spacing between two points on a ring; or the vertical spacing between two points on the Z-axis. As shown in Figure 3.14(b), number of sectors (NoS) on rings was reduced from *360* sectors to *50*. Next, the intermediate space between outer and inner orbital boundaries was divided into discrete points, which formed a number of layers (NoL) between the two boundaries, see Figure 3.15. The numbers of rings, sectors and layers were variables affecting the meshing density of the whole numerical model. As mentioned previously, it was essential to produce discrete elements with acceptable aspect ratios. Therefore, not all combinations of meshing variables would be suitable for a stable numerical solution.

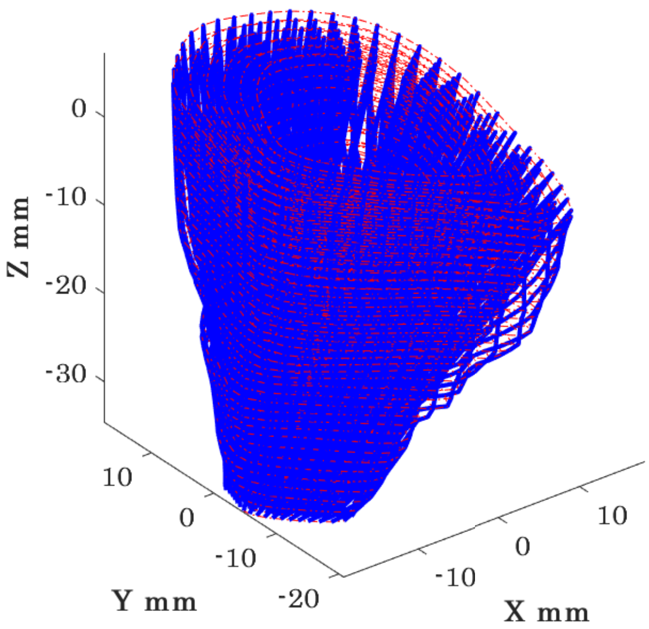

Figure 3.15: Intermediate space between boundaries divided into layers.

To this point of the discretisation process, nodal points were generated to split the model into the desired mesh. However, Abaqus CAE (FEM solver) requires the user to define element information in the input file. An essential information in element file reading is the sequence and arrangement of nodes. Arrangement of the nodes is important, as every *three* nodes form an element face, while the node sequence of all faces should be consistent (Clockwise/Counter-Clockwise). The discretisation algorithm had the option to either use 15 or 6-noded elements. It was decided to use tetrahedron elements, as two opposing elements (i.e., A & B) would combine to form a six-faced structure. Elements A and B will belong to a group of elements, which are phased out by 180^o, see Figure 3.16. In order to form the different elements, each group will have a different arrangement of nodes. Node number arrangement in each of the six-noded element groups is as follows:

Element A

$[NN,\ (NN+NoS+2),\ (NN+NoS+1),\ (NN+(NoS\times NoR)),\ (NN+(NoS\times NoR)+2+NoS),\ (NN+(NoS\times NoR)+1+NoS)]$

Element B

$[NN,\ (NN+1),\ (NN+1+NoS),\ (NN+(NoS\times NoR)),\ (NN+(NoS\times NoR)+2),\ (NN+(NoS\times NoR)+1+NoS)]$

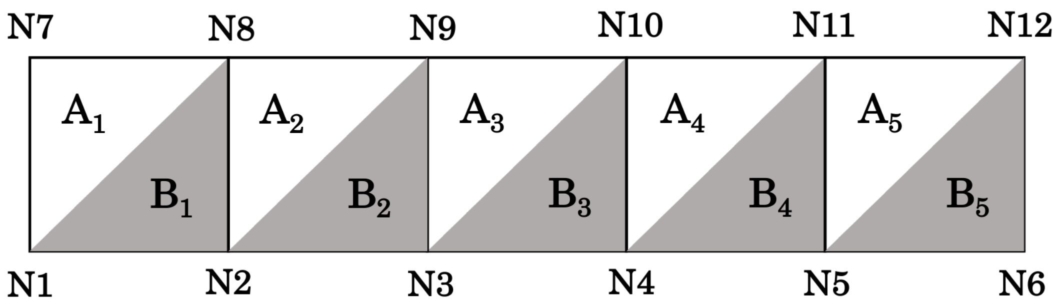

Figure 3.16: Schematic diagram explaining the two groups of elements used in meshing the orbital medium

Eventually, the meshing algorithm writes nodal and element information onto a pre-written ABAQUS input file. This input file includes various options, such as contact properties, boundary conditions applied on the orbital boundary, and loading conditions. ABAQUS compiled this input file to produce a 3D numerical model of the globe encompassed by the OST as depicted in Figure 3.17. It should be noted that this figure does not include the EOMs yet.

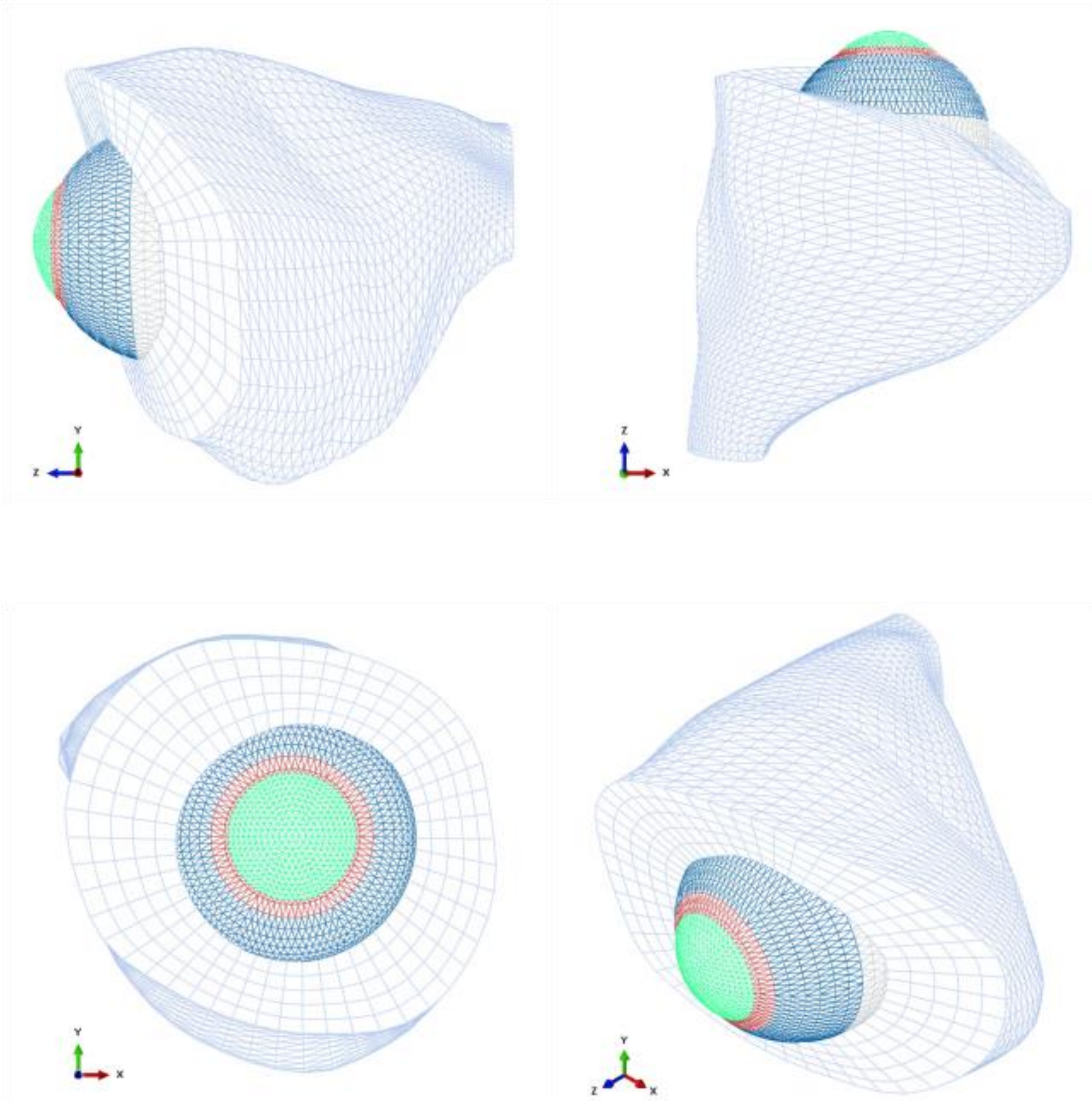

Figure 3.17: Orbital finite element model used in the project

3.2.4 Extra-Ocular Muscles

So far, the numerical model of the ocular system only includes the globe and the orbital soft tissues. The steps followed to add the extra-ocular muscles (EOMs) to the numerical model are explained. First, an algorithm was created to utilise insertion geometry from the literature and develop its numerical counterpart. The muscle insertion widths and positions (distances from sclerocorneal limbus) were loaded onto the algorithm. The code then scanned the globe's element information, including the element number and the node numbers associated with this element. Consequently, nodal data of elements was used to locate the centroid of each element. Thereupon, clinical measurements of each rectus muscle were employed as limits in the selection procedure of element centroids. As a result, as can be seen in Figure 3.18, four groups of points were selected, representing all recti muscles.

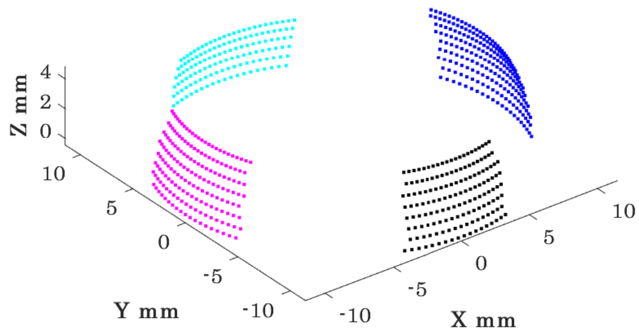

Figure 3.18: Edge elements of each recti muscle not aligned. Inferior rectus (Black), Superior rectus (Cyan), Lateral rectus (Blue), Medial rectus (Magenta).

As also seen in Figure 3.18, the selection process produced groups of elements where edge elements were not aligned. This nonalignment of elements causes unrealistic stress concentration, which may lead to incomplete simulations. Therefore, aligning the line of the edge elements was essential. To do so, elements were either manually added or removed; to achieve edge alignment of the set, see Figure 3.19. Another factor that may cause computational complications was the definition of contact between muscle elements and the globe. For this reason, it was decided to allow muscle elements to share nodes with previously selected globe elements. On that account, exterior nodes of previously selected elements were duplicated and radially shifted. Due to a lack of information, tendon thickness was assumed to be 0.5mm; hence, duplicated nodes were radially shifted by this value. The muscle FE model consists of various components that collectively allow ocular motility. Firstly, it attaches to the globe through the insertion elements as seen in Figure 3.19. The recti muscles have a physiological path provided by orbital soft tissues. In that sense, the recti muscles were assumed to have nodal points acting as pulleys, which are delegated as functional origins during ocular motility.[127]

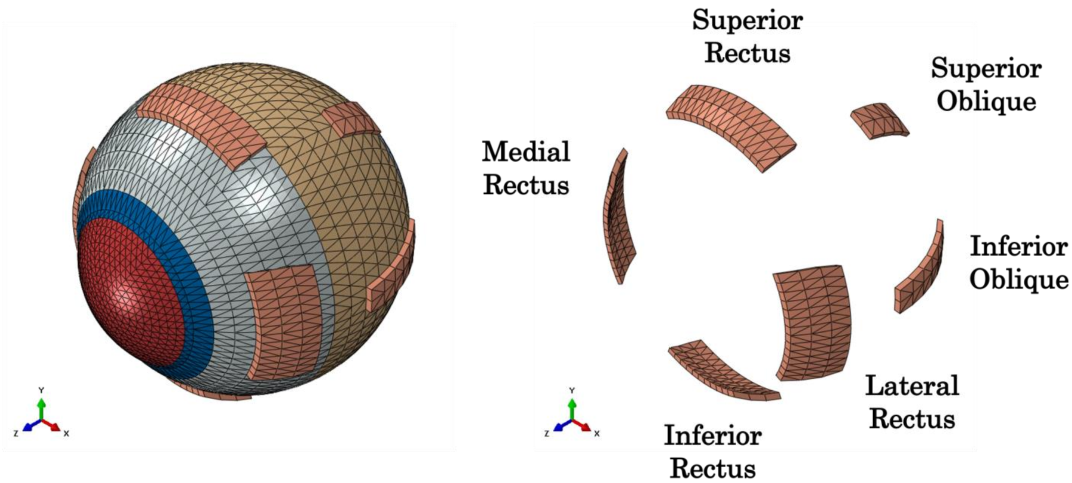

Figure 3.19: Extra-Ocular finite element model used in the project

3.2.5 Boundary Conditions

Previous studies[31,42,214] have implemented a few constraints on the globe to act as boundary conditions. These boundary conditions were comprised of equatorial nodes being constrained to displace in the anterior-posterior direction and another equatorial node being constrained in the superior-inferior direction to prevent rotation around the globe's central axis during simulation. In addition, the posterior pole node was constrained in the temporal-nasal and superior-inferior directions. However, it was allowed to displace in the anterior-posterior direction to allow for expansion during the application of IOP.

Contrary to previous studies,[31, 44, 215] the numerical models of the current study had no constraints applied directly to the globe. However, outer nodes of the orbital structure were constrained against displacement in any direction but allowed rotation and hence deformation of OST elements. In addition, recti muscles follow a physiological path provided by the OST; thus, the recti muscles are assumed to have pulleys acting as the functional origins during ocular motility.[127] Consequently, Gou *et al.*[41] have previously stated that using a roller component at the pulley is an effective way to simulate muscle actions while maintaining the path of the recti muscles. Accordingly, pulleys were implemented within the model, Figure 3.20. In addition, each recti muscle has a separate datum in the direction parallel to the muscle pulley unit vector, $\hat{\boldsymbol{U}}$, with respect to its origin at the orbital apex. The pulley node was constrained to only move in the direction parallel to $\hat{\boldsymbol{U}}$. This constraint ensured that the roller pulley maintained its physiological path.

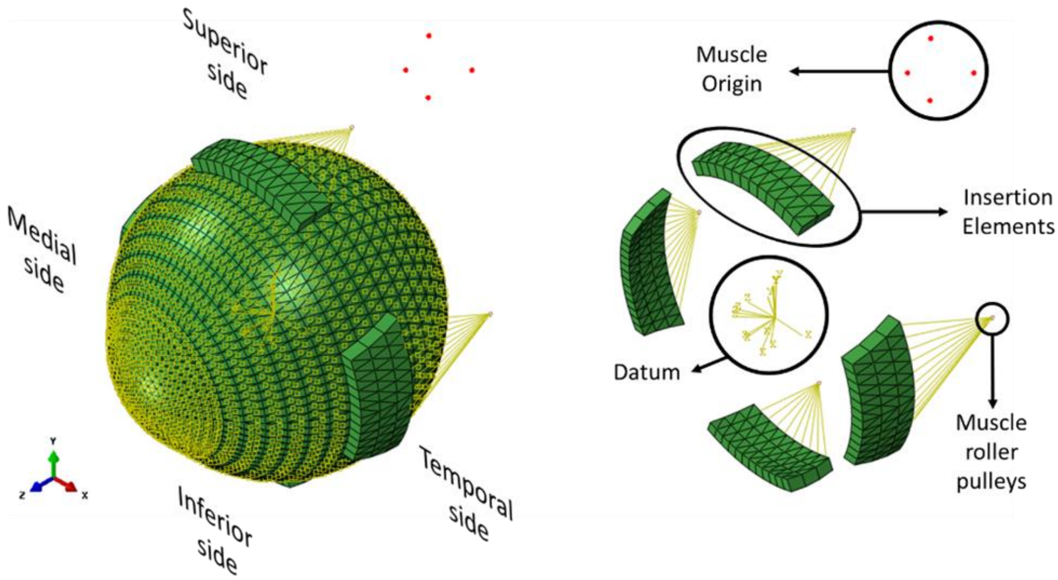

Figure 3.20: Numerical model of the globe with rectus muscles inserted, where pulley interactions and boundary conditions are depicted. Oblique muscles were not included in the figure

3.2.6 Corvis Pressure Distribution

Corvis applies a jet of pressurised air to the central region of the cornea for a duration of 32 ms. A prior experimental study[31] has concluded that air-puff fired from the nozzle has twice the pressure magnitude than the one in contact with the corneal surface, see Figure 3.21. It was necessary to use an accurate time-pressure distribution. Therefore, 130 pressure profiles of healthy clinical subjects were assessed intervalley throughout the air-puff procedure. It was established that all pressure profiles follow the same trend, where the standard deviation was below 4.3% of maximum applied pressure at the nozzle; hence, only one pressure-time distribution was used in the remainder of the project. In addition, an earlier study obtained the pressure distribution applied on the corneal apex and the spatial reduction in pressure away from the apex and towards the limbus.[216] Henceforth, all numerical simulations adopted the mean clinical time-pressure distribution and the spatial-pressure distribution.

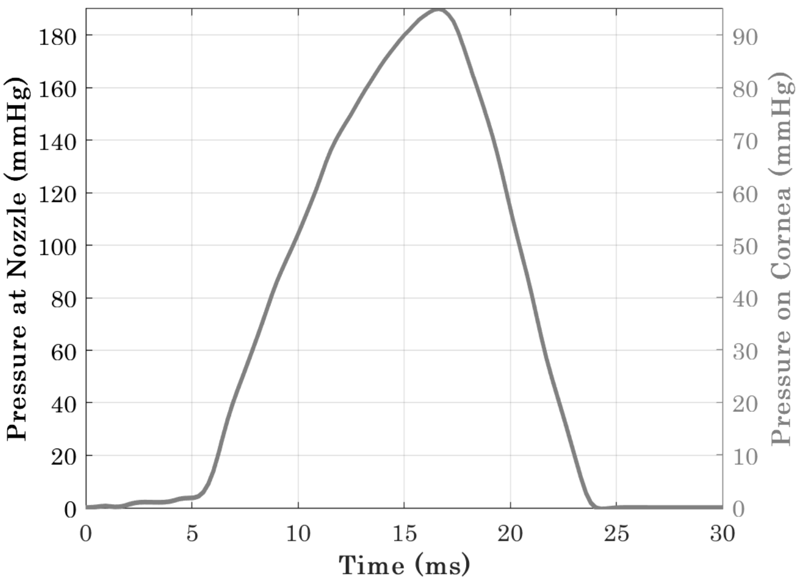

Figure 3.21: Pressure distribution at the nozzle and the cornea for the duration of Corvis[31]

An earlier study used Arbitrary Lagrangian-Eulerian (ALE) deforming mesh to conclude the non-significance of variations in corneal shape on the pressure distribution of the air-puff on the corneal surface.[217] A Matlab algorithm was developed to calculate the pressure applied normal to elements' anterior surface. It reads input files (node and element) produced by orbital mesh generator software and then locates the midpoint of each element's surface. Subsequently, the distance from the corneal apex to each of those midpoints was obtained to compute the pressure at these midpoints using linear interpolation and mean clinical profile. In addition, the algorithm includes the option for a user to modify the radial region of the simulated air pressure. Eventually, the algorithm outputs two files, which specify the pressure-time distribution, and the other specifies the pressure distribution across the corneal elements, see Figure 3.21.

3.2.7 Mesh Generator

One of the main objectives of this project was to develop a Graphical User Interface (GUI) for a software code which produces OST mesh around an existing numerical model of the globe. This GUI will give users the choice of EOMs addition, loading conditions, meshing options and patient-specific data (age, gender and ethnicity). This GUI facilitated the production of the orbital numerical model, while its source code was used to mass produce models with variation in geometry, loading conditions and mesh densities.

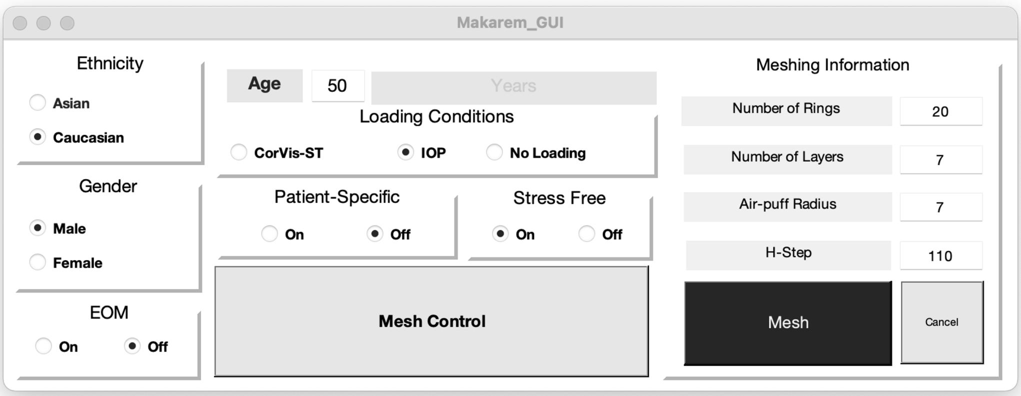

Figure 3.22: Graphical User Interface of the orbital meshing software

3.2.8 Mesh Convergence Study

A mesh convergence study was conducted to determine the optimum mesh density of the numerical models used in this study was carried out in three steps. The first step concentrated on optimising corneal mesh and involved 6 model representations with the number of elements ranging between 3072 and 22188 arranged in rings as shown in Figure 3.23. In all 6 models, the sclera was represented by twenty-six rings, which consists of 2777 elements, see Table 3.2. However, the corneal rings ranged between 6 and 60. Once the corneal convergence analysis was complete, the optimum corneal mesh density was used for all models of the following step. Consequently, extra 6 models were generated which shared the same number of corneal rings but with scleral rings that varied from 12 to 62. Those models had a number of elements that ranged from 1728 to 16428, requiring 7782 to 73932 nodes, respectively, see Table 3.3. Similar to the first step, the optimised number of scleral rings was used for the remainder of this project.

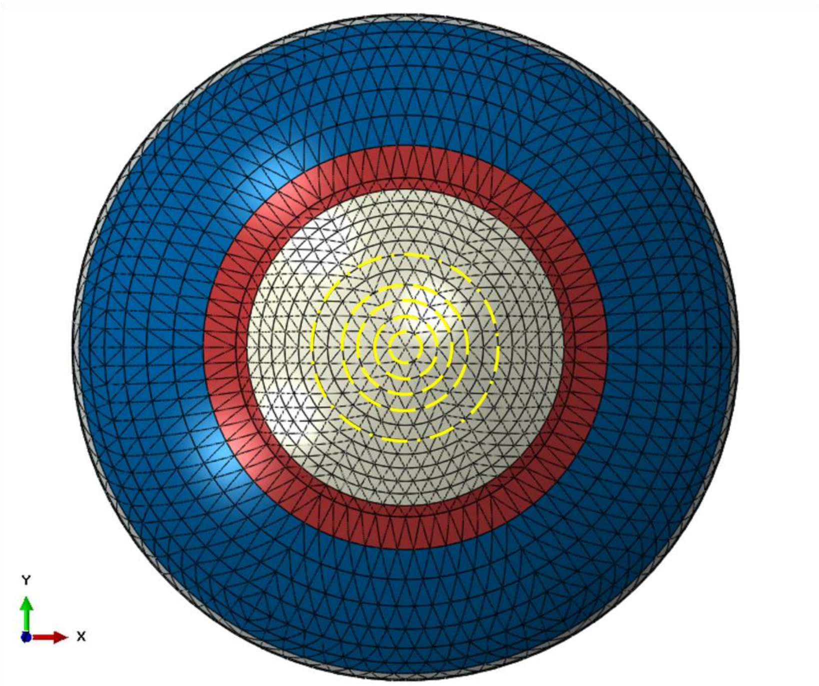

Figure 3.23: Pressure distribution at the nozzle and the cornea for the duration of Corvis

Once the optimum mesh of the globe was determined, it was time to repeat the mesh optimisation process, where the orbital mesh density was increased gradually. As done previously, a total of six models were submitted for Corvis simulation, where all models shared the same mesh of the globe. As stated in Table 3.4, the models started with a coarse discretisation of geometry with only 840 nodes and 1040 elements. The mesh

Table 3.2: Models with changing meshing properties due to change in corneal rings only

Characteristic	Models					
	1	2	3	4	5	6
Corneal Rings	6	12	24	36	48	60
Node Count, 10^3	13.83	19.5	33.8	51.9	73.9	99.9
Element Count, 10^3	3	4.3	7.5	11.5	16.4	22.2

Table 3.3: Models with changing meshing properties due to change in scleral rings only

Characteristic	Models					
	1	2	3	4	5	6
Scleral Rings	12	22	32	42	52	62
Node Count, 10^3	7.8	15.6	26.1	39.3	55.3	73.9
Element Count, 10^3	1.7	3.5	5.8	8.7	12.2	16

density was then increased gradually until it reached 100×10^3 nodes and 145.5×10^3 elements. During this optimisation, two factors were monitored; the first was the deformation of the posterior pole of the globe, while the second was computation time. It should be noted that, while changing the mesh density, it was vital to create elements with satisfactory aspect ratios, allowing for computational stability.

Table 3.4: Models with changing mesh density of the orbital medium

Characteristic	Models					
	1	2	3	4	5	6
Node Count, 10^3	0.8	5.6	10.8	26.9	41.8	100
Element Count, 10^3	1	8.6	17.5	46	73	145.5

3.2.9 Material Model

Previous studies[16,32] quantified stress-strain behaviour of various regions of the globe (the cornea and sclera) based on experimental work done on human donor eyes. A previous study[160] has performed an optimisation analysis to obtain constitutive Ogden material parameters, which provided similar material behaviour as previously acquired experimental data for the cornea and sclera of different age groups. This optimisation was achieved by splitting scleral tissue into three regions. Therefore, the globe's fifteen-noded numerical models have relied on Ogden's constitutive material model in this study. Abaqus Theory Guide Documentation has provided hyperelastic Ogden strain energy equation, see Equation 3.2.

$$U = \sum_{n=1}^{N} \frac{2\mu_i}{\alpha_i}(\bar{\lambda_1}^{\alpha_i} + \bar{\lambda_2}^{\alpha_i} + \bar{\lambda_3}^{\alpha_i} - 3) + \sum_{n=1}^{N} \frac{1}{D}(J_{el} - 1)^{2i} \tag{3.2}$$

Where U is strain energy per unit volume, μ the shear modulus, α the strength hardening exponent, N the function order, $\bar{\lambda_i}$ principal stretch in each of the Cartesian planes, D is compressibility parameter, and J_{el} is particle volume. All ocular tissue regions were assumed almost in-compressible with Poisson's ratio of 0.48.[130,131] Several previous studies have used the Ogden material model and proved its ability to represent ocular tissue material behaviour.[31,192,218,219] Therefore, this material model required no further investigation during this study and age-related Ogden material parameters were used, Table 3.5.

Table 3.5: Controlling parameters of Ogden constitutive material model in relation to age as obtained from experimental data.

Age (Years)	$\mu (MPa)$				α			
	Cornea	Anterior Sclera	Equatorial Sclera	Posterior Sclera	Cornea	Anterior Sclera	Equatorial Sclera	Posterior Sclera
0	0.104	1.678	0.922	0.433	119.8	31.543	41.521	53.016
25	0.115	1.913	1.081	0.554	119.8	35.303	43.876	53.016
50	0.132	2.224	1.291	0.743	119.8	40.265	46.983	53.016
75	0.157	2.633	1.568	1.096	119.8	46.815	51.084	53.016
100	0.197	3.174	1.934	1.830	119.8	55.458	56.494	53.016

3.3 Validation of Numerical Model

This section will mainly describe the methodology used in the clinical validation of the numerical models developed in this study. The section starts with explaining the main aspect used in the validation, which is the whole eye movement under Corvis pressure. This was followed by a brief description of how the clinical corneal profiles were used to determine whole eye movement. The following part will then define the process used to optimise the material properties of orbital soft tissues. It should be noted that within this material optimisation process, the EOMs were not included in the numerical model. Next will be the portrayal of EOMs addition and how this modification helped with the validation process. The validation process has led to the need to carry out another optimisation process. However, this time round, it would be for EOMs' actions during the Corvis procedure. See Figure 3.24 for the outline of this section.

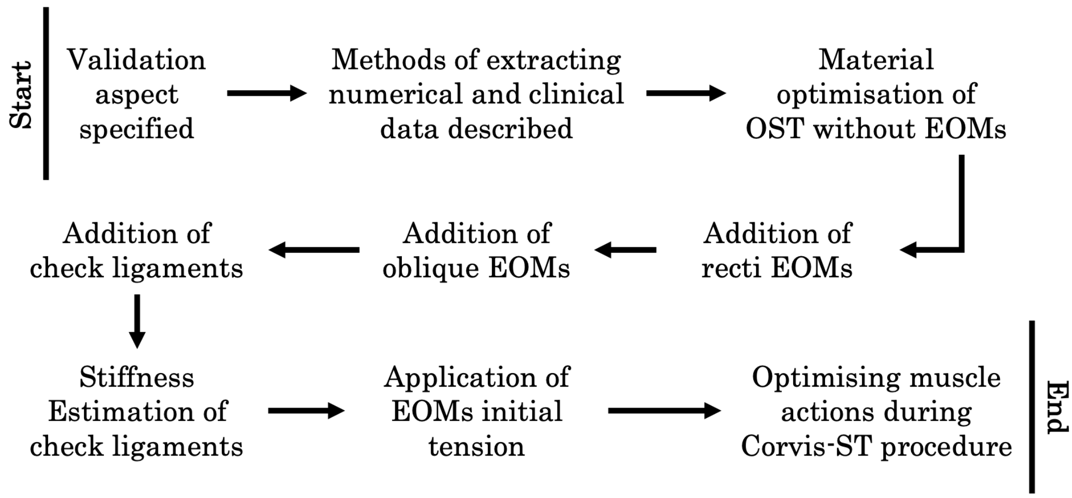

Figure 3.24: Outline showing the development of the validation process used in this section

3.3.1 Whole Eye Movement

Loading by Corvis pressure pushes against the cornea and causes corneal deformation with a slight WEM. In this study, clinical WEM will be used to validate numerical models of the ocular support system. Prior studies[31,44,215] used numerical models which did not consider the orbital space and EOMs; however, boundary conditions were set on the globe to hold it in place. Therefore, there was no whole eye movement, leading to the exclusion of WEM from validation using clinical corneal deformation produced by Corvis.

The WEM was identified at the edges of the corneal horizontal meridian deformation profile, which happens to be $4mm$ from the corneal apex.[31] Due to the curve fitting of the profile, the points near the edge may be influenced by fitting errors. All the clinical profiles had the missing data in the outer $400\mu m$ sides of the $8mm$ meridian. Therefore, the $400\mu m$ sides of the $8mm$ wide measurement region were excluded from the profile. In addition, a further $60\mu m$ were averaged to two singular deformation values representing the nasal and temporal WEM, see **Figure 3.25**.

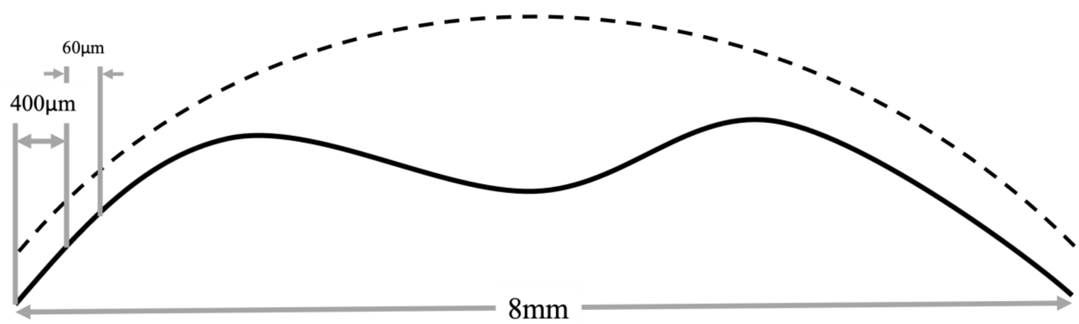

Figure 3.25: Schematic diagram of whole eye movement during Corvis, stating the regions that were averaged and excluded

3.3.2 Reading Data

3.3.2.1 Clinical Data

Part of the Corvis package is a software which processes images produced by the analyser and produces numerical deformations using curve fitting. The numerical deformation profile is exported as a "CSV" file, which could be read later for use in this study. However, Some of the clinical data had missing data points; see **Figure 3.26**. A MatLab algorithm was used to scan all clinical data and check for any missing data; if any were found, the whole clinical profile was excluded and not used in the study.

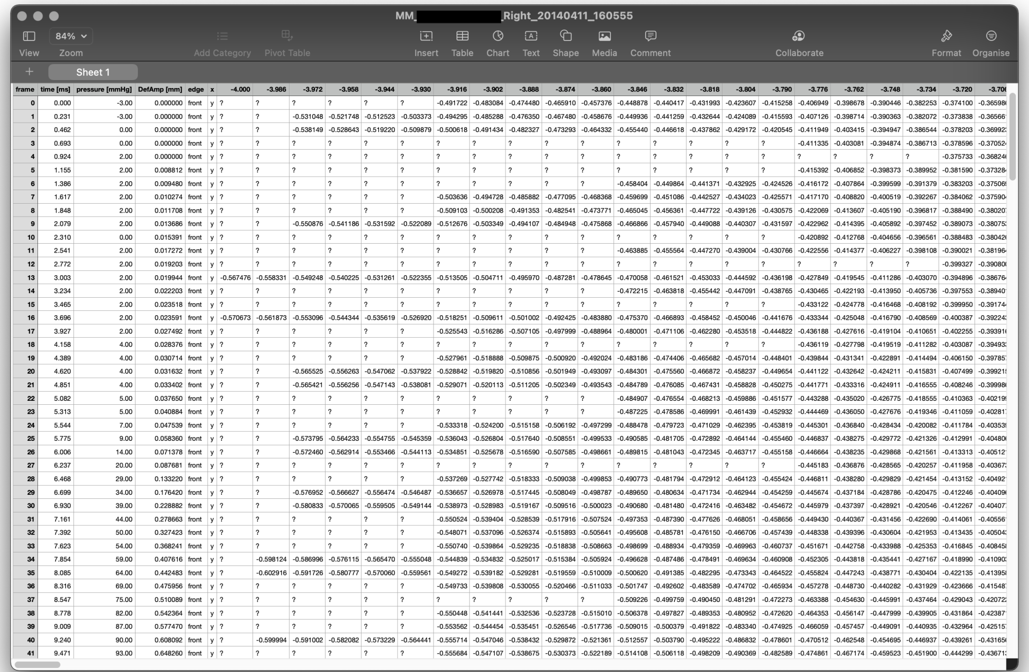

Figure 3.26: Missing information in a clinical corneal profile

3.3.2.2 Numerical Data

To validate the numerical models, their response was compared to their respective clinical data with matching age, gender and ethnicities. Once models were complete, an output database (.odb) file was produced. This file included the numerical response to the 32.34-millisecond Corvis air-puff simulation in the form of 140 increments of 0.231 milliseconds. A Python algorithm was utilised to extract nodal data of the horizontal corneal meridian and feed it into a Matlab code, where it scanned the nasal and temporal peripheral points to estimate whole eye movement. To ensure accuracy in comparison, these chosen points on the numerical meridian were at the exact position of their clinical counterpart. Consequently, using root mean square error (RMSE), Equation 3.3, data from 140 increments of simulated air-puff were compared to the ones from their time-corresponding 140 frames of clinical procedure. The numerical model was optimised to aim for the minimum RMSE mismatch value, hence the agreement of numerical data with its clinical counterpart. This process was used throughout the optimisation process to estimate how muscle actions change during the Corvis procedure.

$$RMSE = \sqrt{\frac{\sum_{n=1}^{N}(Numerical - Clinical)^2}{N}} \tag{3.3}$$

3.3.3 Material Optimisation of Orbital Soft Tissues

This section will describe how a clinical dataset of the Chinese population was utilised in a material optimisation process, see Figure 3.27. In this process, an inverse analysis was employed to determine the optimum parameters for Ogden constitutive material model, which aims for a close match between clinical and numerical WEM. The clinical dataset will be showcased in the first part of this sub-section, and details will be given on the subjects' age groups used in this particular study. Second, numerical model generation with patient-specific corneal profiles and various orbital geometrical aspects regarding the subject's age. Last but not least, the inverse analysis will take place, where it will attempt to optimise material properties to match the subject-specific numerical deformation profile to its clinical counterpart. The final stage of this process would be the analysis of the most optimum material parameter of each subject and how this varies with age.

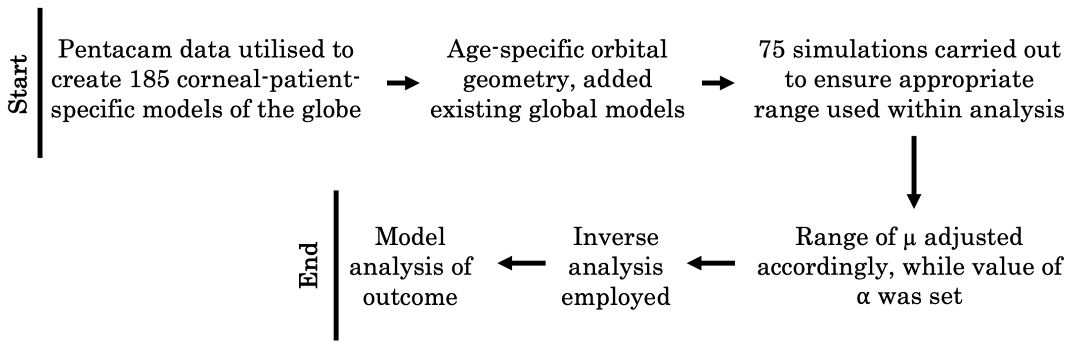

Figure 3.27: Process outlining methodology used in material optimisation OST.

3.3.3.1 Clinical Dataset

A fully anonymised database of 185 Chinese ophthalmologically healthy subjects was retrospectively reviewed. According to the University of Liverpool research ethics policy, approval for this record review using fully anonymised secondary data was ruled unnecessary. Nonetheless, written informed consent was obtained from each participant to use their data in the research. The study was conducted according to the tenets of the Declaration of Helsinki as set out in 1964 and revised in 2013.

Table 3.6: Age groups used in the current study

Age Group	Age range (Years)	Number of samples	Mean age±SD (Years)
Young	20-40	100	29.8±5.4
Middle-aged	41-60	50	51.2±6.7
Old	61-91	35	72.9±6.0

Earlier studies suggest that orbital health conditions, such as thyroid orbitopathy, affect WEM in response to the air pulse produced by Corvis.[39, 220] Therefore, all participants were subject to a complete ophthalmic examination, including tests using the Corvis and Pentacam (OCULUS Optikgeräte GmbH; Wetzlar, Germany). Subjects with a history of use of hypotonic therapies, glaucoma, previous eye disease or ocular surgery were excluded. For consistency, one clinician carried out Corvis examinations for all participants. An experienced corneal specialist reviewed all exams to ensure that only good-quality scans were included in the study.

3.3.3.2 Model Generation

During this parametric study, the in-house mesh generator −described in subsection 3.2.1− was used to generate corneal-patient-specific models of the globe (see Figure 3.35). In addition, each subject's Central Corneal Thickness (CCT) was implemented in its respective numerical model. On that note, Peripheral Corneal Thickness (PCT) was set to be $150 \mu m$ additional to CCT. Consequently, thickness varied across the sclera, where anteriorly it was the same as PCT, then decreased to 80% of PCT at the equatorial region, thenceforth at the posterior region it increased to 120% of PCT. Further parameters such as shape factor, limbal radius and scleral radius were set to 0.82, 5.85mm and 11.5mm, respectively. The material stiffness ratio of the five global regions was changed according to age using Equation 3.5, in chapter 2. Also, as described in that chapter, age variation played a major role in the variation of orbital geometry. The automated algorithm used age as an input to change two aspects. The first was the size of the orbital aperture, while the second was the globe's position relative to the lateral portion of the orbital rim. Another variation was a gender-related variation of orbital volume. Due to the inability to differentiate between male and female clinical data, a mean orbital volume of $21 \pm 1cm^3$ was used for all subjects. Therefore, all geometrical, loading and material stiffness aspects mentioned above were used to generate numerical models.

Based on the mesh density study executed earlier in subsection 3.2.8, it employed a numerical model of the globe with 15600 nodes and 3500 elements arranged in a single layer of 12 corneal and 22 scleral rings. Six-segment models using 15-noded C3D15H elements were adopted in the model generation stage of this study. In addition, the mesh density study employed a numerical model of the orbit with 10800 nodes and 17500 6-noded C3D6H elements. It should be noted that the numerical models generated in this section did not include any of the EOMs. The epithelium layer in this model was not considered as a separate discrete layer, as it was found that its effect tended to be negligible for the findings of this study, yet it was considered in the total corneal thickness.[221] In addition, a previous study found that the optic nerve head had an insignificant effect on corneal deformation; therefore, it was not considered within the study.

3.3.3.3 Material Optimisation Algorithm

The optimisation process has employed an inverse analysis approach to determine the optimum material parameter. Before the commencement of the primary analysis, a batch of simulations was carried out as part of an initial analysis to ensure an appropriate range was used during optimisation. This analysis was done by constructing a custom-built MATLAB code, which generated a 15×5 grid of μ (5×10^5 to 5×10^3MPa) and α (0.1 to 50), respectively. This grid produced seventy-five combinations of the OST material parameters, as shown in Figure 3.28. Those combinations allowed for acquiring various numerical corneal profiles, which were then compared to their clinical counterpart as described in subsection 3.3.2. This initial analysis resulted in two outcomes. The first was that the range for μ was appropriate; due to the root mean square error (RMSE) error following a positive parabolic shape. Second, the RMSE changed very slightly (below 1%) with changes in α, therefore the parameter α was set at a value of 23 in all the numerical simulations.

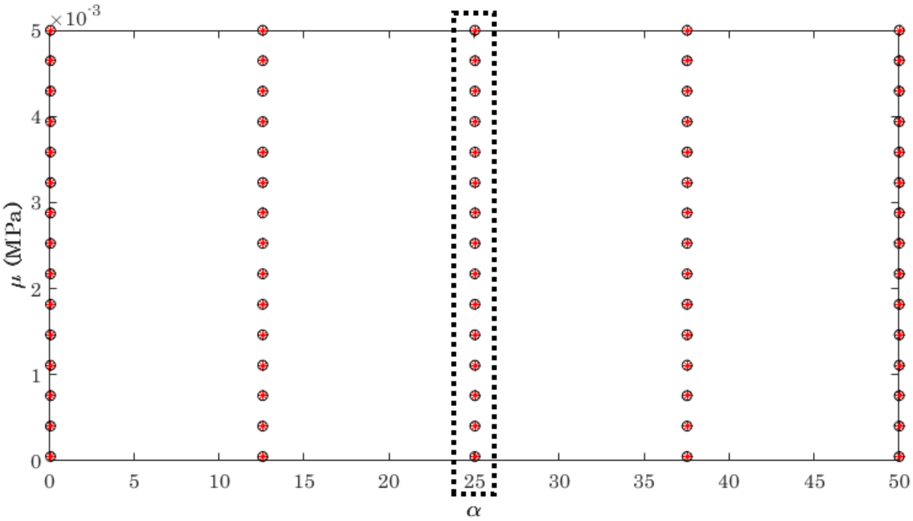

Figure 3.28: Grid of μ and α was used before the inverse analysis. The dashed box is the combination used in optimisation.

Now it was assured that the range of μ is suitable and no computational time will be wasted with multiple values of α. The inverse analysis will determine the optimum OST material parameter for each subject. Now that α is a set value that does not change, only fifteen models will need to run for each case rather than seventy-five. Once these models are complete, the numerical deformation is compared to clinical data. If the RMSE is below the tolerance pre-agreed on, this value of μ was saved aside, and the rest of the simulations for this case are ignored. However, if all simulations were complete without reaching the specified tolerance, material parameters resulting in the minimum RMSE are chosen as the most optimum parameters. The globe-orbit numerical model takes around 25 minutes to complete the simulation of a Corvis procedure. Therefore, the 185 clinical cases within this study will result in 2,775 simulations to be carried out, with a total duration of over eight weeks. Hence, a custom-built Matlab code was developed to automatically carry out the whole process. Clinical subjects were split into three groups, where the optimisation algorithm could perform the analysis in parallel, reducing the total duration to just three weeks. It should be noted that the analysis was done on the University of Liverpool's Linux cluster system.

3.3.4 Addition of Extra-ocular Muscles

The outcome of the material optimisation process previously done in this section has pointed out some issues within the numerical model. First, the optimum material parameters determined by the analysis produced an average RMSE value of 0.0288mm. On that note, it should be kept in mind that WEM comparison during the course of the study outlined in subsection 3.3.3 used the average WEM for RMSE calculation rather than nasal and temporal. This was due to an occurrence of nasal rotation, which was evident in clinical corneal profiles, see Figure 3.29. In contra, the numerical corneal profile did not show this rotation, but results showed rotation in the opposite (temporal) direction.

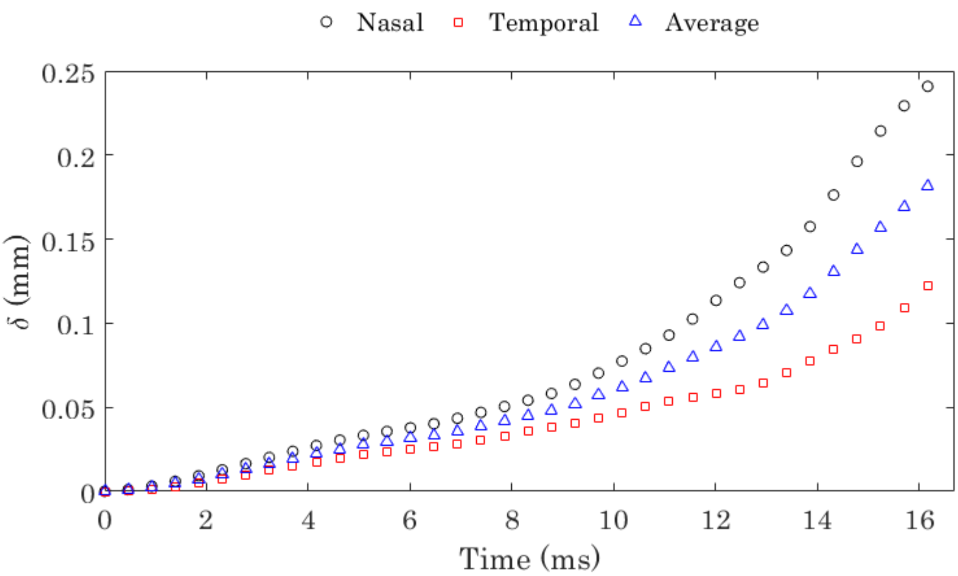

Figure 3.29: Example of a clinical WEM variation across the corneal profile, showing an evident nasal rotation during loading condition of Corvis.

Moreover, the optimum material parameters determined by the analysis were about four times stiffer than those of AFT, which were experimentally acquired.[88] Therefore, it was assumed that this difference in stiffness was due to the absence of EOMs. Therefore, in this section, EOMs will be gradually added to the model, and their effect on simulated deformation profiles will be recorded. However, before the addition of the EOMs, the material parameters of orbital elements will be set $0.4kPa$ for shear modulus, μ, and 23 as the strain hardening exponent, α.[88] When those parameters were used in the material model, the numerical deformation profile showed a huge RMSE mismatch between clinical data, see Figure 3.30. In addition to the excessive discrepancy in deformation, the numerical model did not show the anticipated rotation of the globe. In fact, near the end of the loading period, there was a slight temporal rotation.

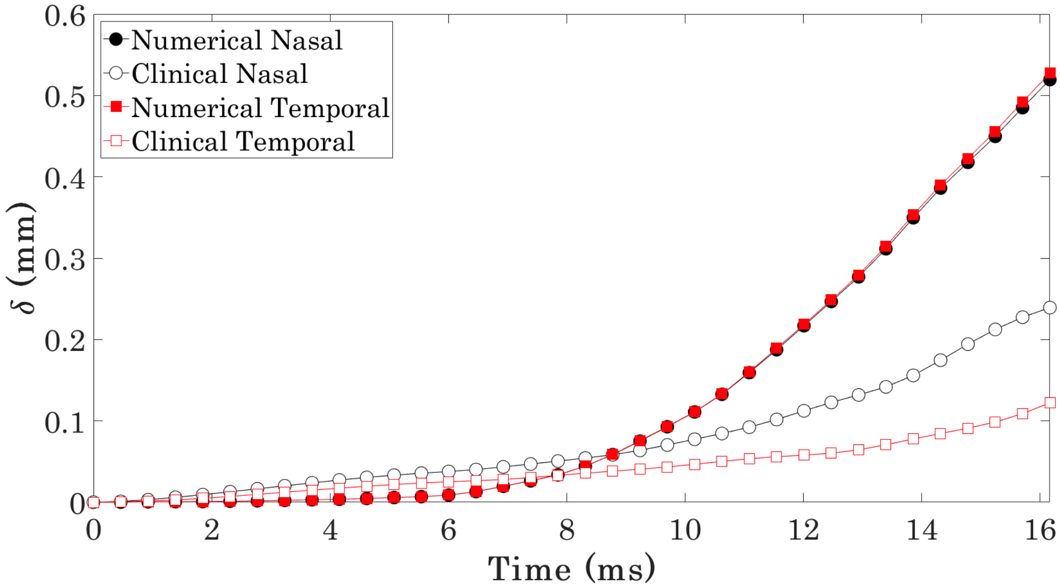

Figure 3.30: Deformation outcome of experimentally acquired parameters and its comparison to clinical data.

As shown in Figure 3.30, the globe needed some support to reduce the excessive WEM resulting from Corvis pressure. Therefore, as described in subsection 3.2.4 rectus muscles were added onto the globe through their respective insertion position as mentioned in chapter 2. As seen below in Figure 3.31, four rectus muscles are marked in different colours. In addition, each muscle has its three primary functional components, insertion elements, pulley node and origin node. The pulley nodes are coupled to their respective surfaces, see Figure 3.31, where translation in any of the Cartesian coordinates is transferred to the nodes and vice-versa. However, constraint in the rotation was not included in this coupling setting. Furthermore, each pulley node (filled out circle) was constrained to move in only one plane, that being the one common to its respective origin (hollow circle). Refer to subsection 3.2.5 for more details.

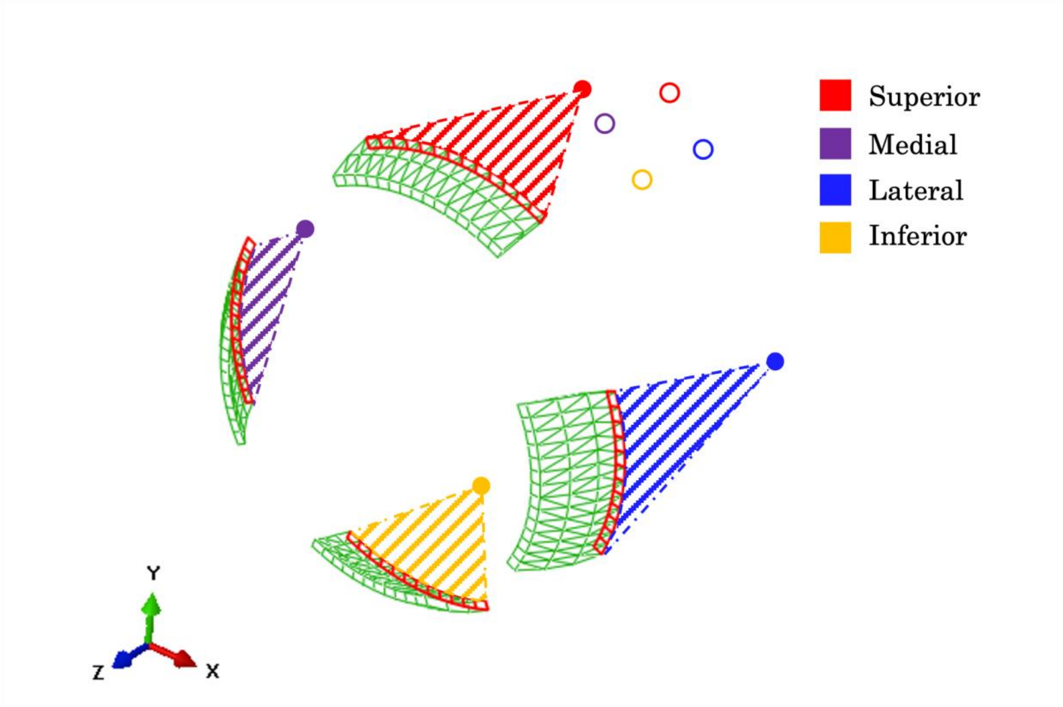

Figure 3.31: Numerical model including rectus muscles and orbit (not included n figure). A shaded coloured pattern represents surface-node coupling, while solid and hollow circles are pulley and origin nodes, respectively.

Once rectus muscles are added to the model, another clinical comparison occurs; refer to subsection 3.3.2 for a detailed description. As a result of this addition, rectus muscles have significantly reduced numerical WEM, hence, reducing the RMSE mismatch value. However, despite this mismatch improvement, there was still a disagreement on the direction of the globe's rotation. Henceforth, the next was to add another modification to the model and study its effect on the displacement of the globe. This modification was the inclusion of superior and inferior oblique muscles. Similar to rectus muscles, they included a node coupled to insertion elements, which is then constrained to movement in one plane. Worth bearing in mind that the origin of the superior oblique is at the orbital apex. However, its functional origin is located at the anterior portion of the medial wall, see Figure 3.32.

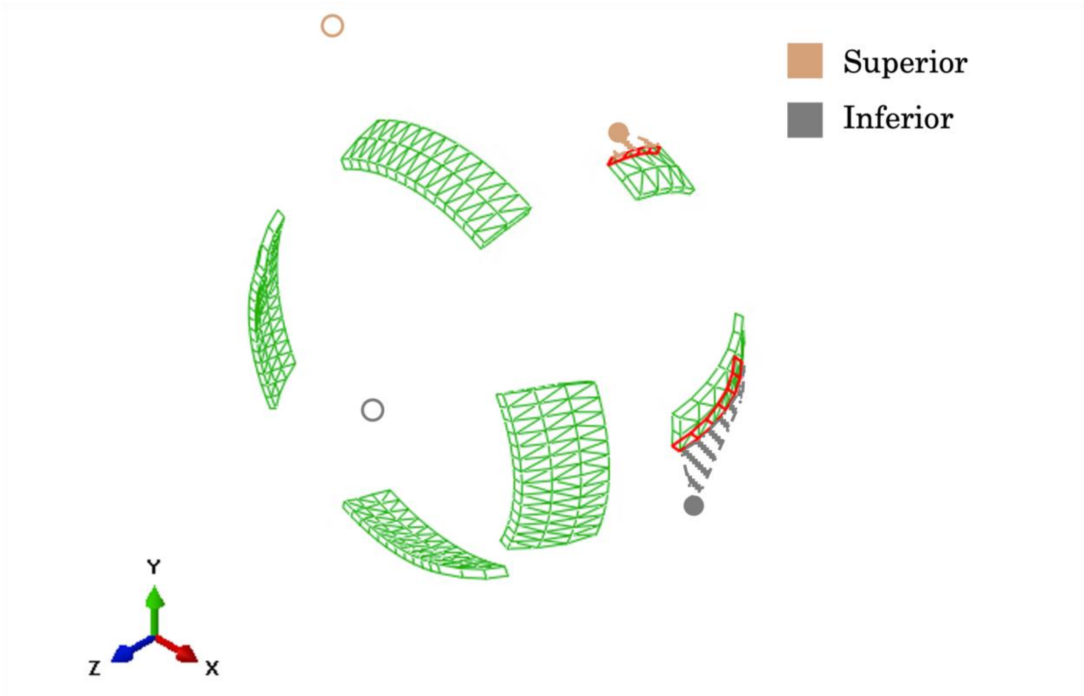

Figure 3.32: Numerical model including all EOMs and orbit (not included n figure). A shaded coloured pattern represents surface-node coupling, while solid and hollow circles are pulley and origin nodes, respectively.

3.3.5 Force Distribution Optimisation

This subsection will scrutinise the methodology for estimating EOM actions during Corvis loading conditions. This would start with classifying the corneal deformation profile of healthy clinical data into three gendered age groups. Consequently, six models were generated accordingly to both genders of all age groups, where orbital geometry varied and the corneal material stiffness. An inverse analysis algorithm was developed to optimise numerical corneal deformation by applying actions onto all EOMs and comparing it to clinical data using the least mean square technique.

3.3.5.1 Clinical Dataset

A fully anonymised database of 52 Caucasian (28 male and 24 female) ophthalmologically normal subjects with healthy corneas was retrospectively reviewed. According to the University of Liverpool research ethics policy, approval for this record review using fully anonymised secondary data was ruled unnecessary. Nonetheless, written informed consent was obtained from each participant to use their data in the research. The study was conducted according to the tenets of the Declaration of Helsinki as set out in 1964 and revised in 2013.

Table 3.7: Age groups used in the current study.

Gender	**Age Group**	**Age range (Years)**	**Number of samples**	**Mean age±SD (Years)**
Male	Young	20-40	9	33.2±5.25
	Middle-aged	41-60	11	49.2±4.2
	Old	61-80	8	69.1±4.9
Female	Young	20-40	8	28.8±5.12
	Middle-aged	41-55	10	47.3±4.2
	Old	61-75	6	69.6±5.6

Earlier studies suggest that orbital health conditions, such as thyroid orbitopathy, affect WEM in response to the air pulse produced by Corvis.[39,220] Therefore, all participants were subject to a complete ophthalmic examination, including tests using the Corvis and Pentacam (OCULUS Optikgeräte GmbH; Wetzlar, Germany). Subjects with a history of use of hypotonic therapies, glaucoma, previous eye disease or ocular surgery were excluded. For consistency, one clinician carried out Corvis examinations for all participants. An experienced corneal specialist reviewed all exams to ensure that only good-quality scans were included in the study.

3.3.5.2 Model Generation

Using the in-house mesh generator mentioned in subsection 3.2.7, models in this section were generated to the exact geometrical specifications described in subsubsection 3.3.3.2. However, in this section, all six EOMs were added to the numerical model at their respective insertion points, as described in chapter 2, subsection 2.5.2. In addition, these models did include pulley mechanisms of EOMs, where initial muscle tension was applied and optimised during the coarse air-puff simulation, Table 3.8 stating initial tension applied on each EOM. As seen in Table 3.7, six models were generated in this study, three for each gender, representing three age groups; young, middle-aged and old. The geometrical aspects of those models were set according to age and gender inputs. Those models were then kept aside for validation of the optimised muscle actions. For the optimisation process, a model was created with specifications of an average age of all clinical data available, while a mean volume was set −due to gender-related volumetric variation. Now, this model is ready to be used by the optimisation algorithm described next.

Table 3.8: Initial tension required of EOMs keeping the globe in its primary gaze.[36]

Extra-ocular muscle	**Force** (mN)
Medial rectus	89.2 ± 31.6
Lateral rectus	48.8 ± 14.2
Superior rectus	50.6 ± 17.6
Inferior rectus	46.2 ± 13.4
Superior oblique	15.6 ± 8.3
Inferior oblique	17.1 ± 12.1

3.3.5.3 Optimisation Algorithm

The optimisation of EOM actions was carried out through an in-house developed algorithm. The framework of this custom-built Matlab algorithm was to utilise intervals of clinical corneal deformation profiles as targets for numerical output. The applied force within EOMs was controlled using time and fraction of applied force (0.5 is 50% of applied force used at the specified time), which was included in a separate amplitude file, see example in Table 3.9 for better understanding of the input.

Table 3.9: An example of how the amplitude input is used to control force distribution with time. A force of 1mN represents 100%.

Time (ms)	Amplitude	Amplitude (%)	Force (mN)
0	0	0	0
0.231	0.01	1.00	0.0100
0.693	0.04	3.91	0.0391
1.155	0.07	6.82	0.0682
1.617	0.10	9.74	0.0974
2.079	0.13	12.65	0.1265
2.541	0.16	15.56	0.1556
3.003	0.18	18.47	0.1847

The optimisation would start by conducting a numerical simulation of the Corvis procedure, applying an initial estimate of muscle actions. Upon completion, output nodal data were extracted and compared to the corresponding clinical data using a standard error calculation method, described in Equation 3.4, unlike the one used in subsection 3.3.2. It was essential to allow the error value to be either negative or positive, as the sign of the error value would determine the change of amplitude, *i.e.*:

$$Error = Numerical - Clinical \tag{3.4}$$

if, Error is ***negative****, amplitude value* ***increased***

if, Error is ***positive****, amplitude value* ***decreased***

It should be noted that the amount of increase in amplitude would not be equivalent to its decrease, as this may have caused the algorithm to be stuck in a loop. The model will continue running and checking error mismatch until it reaches the tolerance specified. Once tolerance is reached, the amplitude value for this time step is saved and used as an initial estimate of the following time step. All the previous optimisation steps are repeated for all the following time step intervals. Eventually, when the final time step amplitude is optimised, a final run is carried out with the produced optimised amplitude then RMSE is calculated as described in subsection 3.3.2.

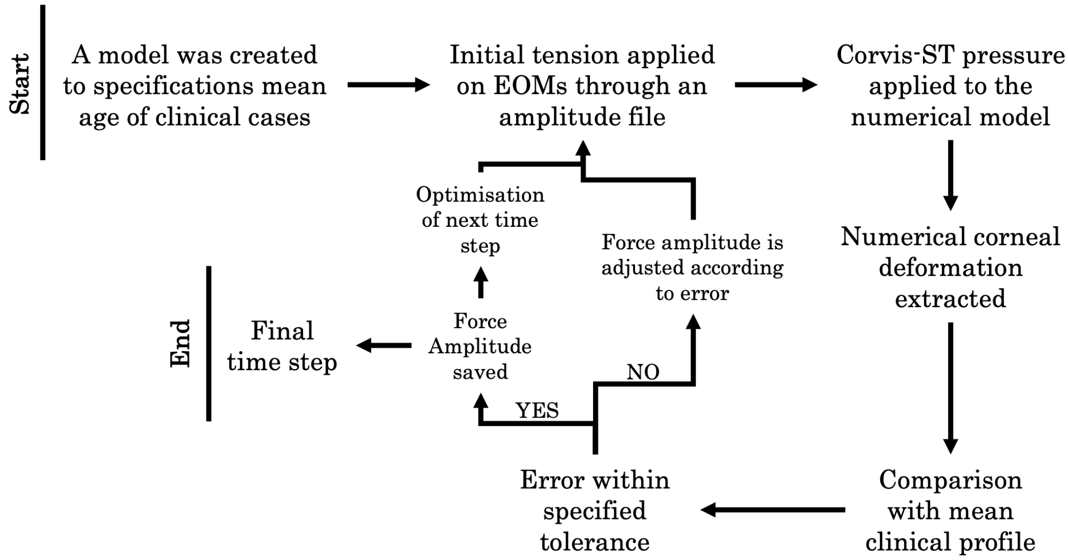

Figure 3.33: Process followed within muscle action optimisation during the Corvis procedure.

3.3.5.4 Model Analysis

In this final part of the section, the six gender-age specified models that were generated and set aside in subsubsection 3.3.5.2, will be used. The optimised force distribution will be applied to EOMs' pulleys of those generated models. Subsequently, deformation profiles output is compared to their respective clinical data −described in subsubsection 3.3.5.1. This comparison was achieved by comparing clinical WEM to its numerical counterpart. It should be noted that this comparison included the determination of RMSE mismatch of nasal, temporal and average WEM. This was done to validate the globe's slight rotation during the procedure, as mentioned in previous studies.[143]

3.4 Parametric Study

This section will define the methodology of conducting a parametric study. This study involved building a database to develop updated equations to estimate corneal material stiffness and IOP *in-vivo*. The database included variations in the globe's geometrical features, material stiffness, and IOP applied. In addition, orbital geometry and the globe's position were adjusted to age and gender. Each simulation within this study required 45 minutes for completion, where a total of 1728 simulations were carried out. Therefore, to optimise the time scale, the process had to be automated; hence an algorithm was developed to automatically carry out the process shown in Figure 3.34.

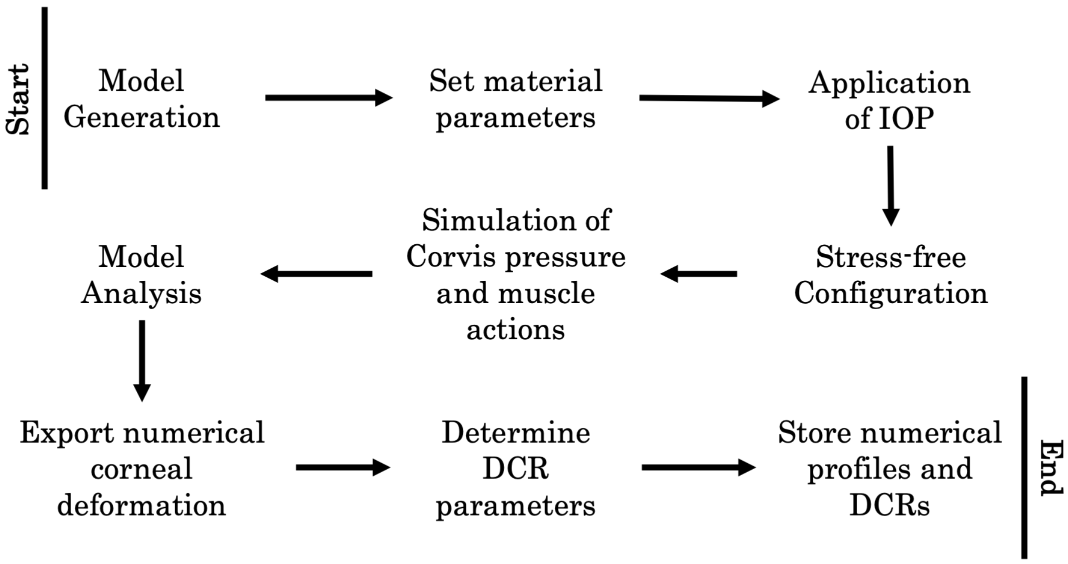

Figure 3.34: Process adopted for building the required database for developing material stiffness and IOP estimation equations.

3.4.1 Model generation

During this parametric study, the in-house mesh generator −described in subsection 3.2.1− was used to generate idealised models of the globe (see Figure 3.35). Based on the mesh density study executed earlier in subsection 3.2.8, a numerical model of the globe with 15600 nodes and 3500 elements arranged in a single layer of 12 corneal rings and 22 scleral rings. Six-segment models using 15-noded C3D15H elements were adopted in the model generation stage of this study. The epithelium layer in this model was not considered as a separate discrete layer, as it was found that its effect tended to be negligible for the findings of this study, yet it was considered in the total corneal thickness.[221] In addition, a previous study found that the optic nerve head had an insignificant effect on corneal deformation. Therefore, it was not considered within the study.[31] Listed below are variables used in generating numerical models with various geometrical and loading specifications, as well as stiffness aspects of the globe. Parameter 1 changed the volume of orbital space based on gender, while parameters 2 to 5 changed the globe's geometrical aspects and material stiffness, and IOP was applied before the Corvis pressure application. The suitable ranges for those aspects were obtained from the literature.[31,43,94,222]

1. **Gender:** Male and Female ($\times 2$)
2. **CCT** (μm)**:** 395 to 645 at steps of 50 ($\times 6$)
3. **Age (Years):** 20 to 90 at steps of 10 ($\times 8$)
4. **Radius** (mm)**:** 7.2, 7.8 and 8.4 ($\times 6$)
5. **IOP** ($mmHg$)**:** 10 to 35 in steps of 5 ($\times 6$)

Other geometrical aspects of the globe were set based on previously mentioned parameters, while other aspects were fixed for all models. On that note, Peripheral Corneal Thickness (PCT) was set to be $150\mu m$ additional to CCT. Consequently, thickness varied across the sclera, where anteriorly it was the same as PCT, then decreased to 80% of PCT at the equatorial region, thenceforth at the posterior region it increased to 120% of PCT. Further parameters such as shape factor, limbal radius and scleral radius were set to 0.82, $5{,}85mm$ and $11.5mm$, respectively. All these parameters were attained from the literature.[31] As mentioned in chapter 2, experimental studies demonstrated that tissue behaviour is best represented by dividing the sclera into three regions.[43] On the other hand, the cornea was only represented through one region with one set of material stiffness parameters.

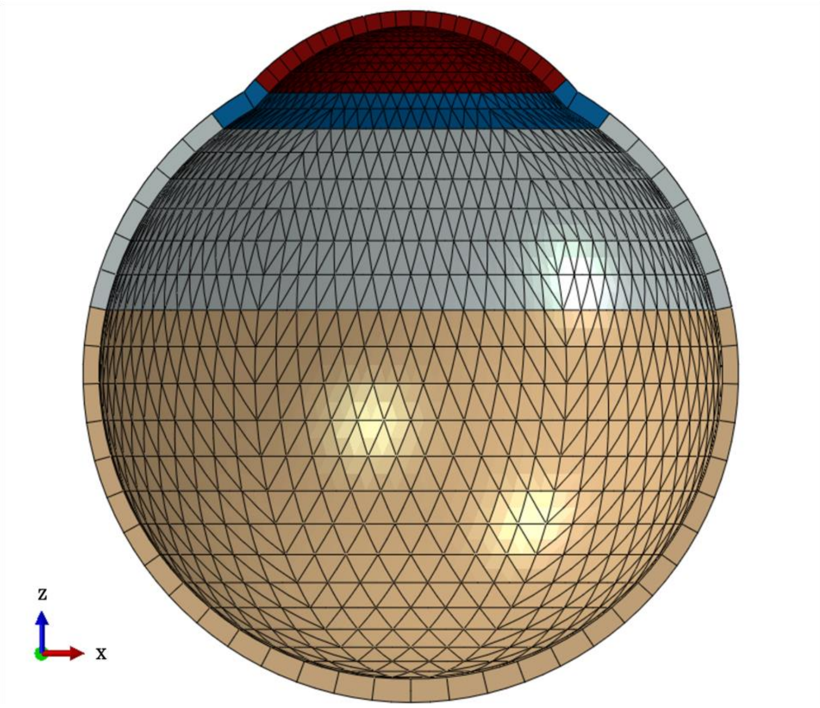

Figure 3.35: Cross-section of globe's numerical model used within this study along with orbital space (not included), different colours show different materials used.

The material stiffness ratio of the five global regions was changed according to age using Equation 3.5. As mentioned in chapter 2, age variation played a significant role in the variation of orbital geometry. The automated algorithm used age as an input to change two aspects. The first was the size of the orbital aperture, while the second was the globe's position relative to the lateral portion of the orbital rim. Another variation was a gender-related variation of orbital volume. Therefore, all geometrical, loading and material stiffness aspects mentioned above were used to generate numerical models of both aspects. All models had the same scleral insertion positions of the six EOMs, while pulley and origin locations were adjusted to change the volume between genders. Based on the mesh density study executed earlier in subsection 3.2.8, it employed a numerical model of the orbit with 10800 nodes and 17500 6-noded C3D6H elements.

3.4.2 Material Parameters

This section will discuss a variation of corneal and scleral material parameters. Corneal material properties were found to be correlated with age. Previously in subsection 3.2.9, Ogden constitutive material model and its controlling parameters were described, hence used within simulations of this parametric study. The relationship between corneal material stiffness and age is described as Equation 3.5.[160]

$$Beta = 0.5852 \times e^{0.0111 \times Age} \tag{3.5}$$

Corneal stress-strain behaviour is provided *Beta* in the equation above. Equation 3.5 allowed for acquiring material stiffness variation with age. Previous studies utilised this age-stiffness relationship as target curves, which will be employed in an optimisation technique.[16] This optimisation provided constitutive parameters of the Ogden material model, where experimental corneal and scleral material behaviour matched. As a result, age became a universal parameter controlling the whole globe's material behaviour, see Table 3.10.

Table 3.10: Controlling parameters of Ogden constitutive material model in relation to age as obtained from experimental data.

Age (Years)	$\mu(MPa)$				α			
	Cornea	Anterior Sclera	Equatorial Sclera	Posterior Sclera	Cornea	Anterior Sclera	Equatorial Sclera	Posterior Sclera
0	0.104	1.678	0.922	0.433	119.8	31.543	41.521	53.016
25	0.115	1.913	1.081	0.554	119.8	35.303	43.876	53.016
50	0.132	2.224	1.291	0.743	119.8	40.265	46.983	53.016
75	0.157	2.633	1.568	1.096	119.8	46.815	51.084	53.016
100	0.197	3.174	1.934	1.830	119.8	55.458	56.494	53.016

So far, variations of hyperelastic material stiffness in different regions of the globe have been described above. On the other hand, hyperelastic material stiffness of the adipose fatty tissue (AFT) was set the same for all models of this study. Earlier studies mentioned priorly in chapter 2 have best fitted Ogden constitutive model to experimental uniaxial compression data using values for shear modulus (μ) and strain hardening exponent (α) of 0.4MPa and 23, respectively. Moreover, a previous study has done some experimental testing on acquiring the stress-strain relationship of bovine extraocular tendons (EOTs). As a result, EOTs found to have a uniform stress-strain relationship, where Young's moduli for fibre bundles from all six EOTs were determined. Mean Young's moduli for fibre bundles were similar for the six anatomical EOTs: superior rectus 59.66±2.64 (±SD) MPa, lateral rectus 60.12±2.69 MPa, medial rectus

56.92±1.91 MPa, inferior rectus 59.69±5.34 MPa, superior oblique 59.15±2.03 MPa and inferior oblique 57.7±1.36 MPa.[223] Finally, effective Young's moduli used for medial and lateral check ligaments were acquired from an analysis performed earlier in this project, resulting in a 1 kPa.

3.4.3 Application of IOP

The IOP was an initial loading condition applied to the internal surface of the globe in the form of a fluid cavity, Figure 3.36. The IOP values ranged in this parametric study from 10 $mmHg$ to 35 $mmHg$. Hence, a code was constructed to convert the IOP value from millimetre mercury (mmHg) to Mega Pascal (MPa), Equation 3.6 then define it in the input file to apply the specified internal pressure.

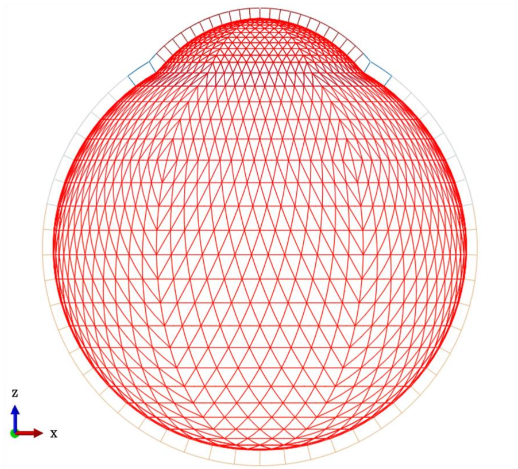

Figure 3.36: Cross-section of the globe, where IOP is applied on its interior surface. Elements with different colours representing different regions of the globe

$$IOP_{MPa} = IOP_{mmHg} \times 0.000133322 \tag{3.6}$$

Generally, there is an effect of internal pressure waves acting on the eye, as well as a direct effect of external pressure. Throughout the application of IOP, the internal pressure of the eye changes, this difference in pressure results in the expansion of the ocular shell. The role of the fluid cavity is to allow for the pressure to be altered, though it was not essential in this study to quantify this change. The two effects mentioned above were considered in estimating the behaviour during this study.

3.4.4 Stress-Free Configuration

In preparation for this parametric study, a batch of numerical models with various geometrical specifications was generated using the bespoke orbital mesh generator mentioned in subsection 3.2.7. However, with the application of IOP, the globe's geometry tends to deform according to the boundary condition, which is the orbital medium. Therefore, it was required to carry out an iterative method used in a previous study[224] to produce a Stress-free Form (SFF) estimating the globe's geometry before inflation. In these prior studies,[31,42,44,215] the numerical model has assumed boundary conditions on the pole and equatorial nodes, mentioned priorly in this chapter. On the other hand, this study has focused on estimating the SFF while not applying any boundary condition on the globe and allowing the OST and EOMs to support the globe fully, see Figure 3.37.

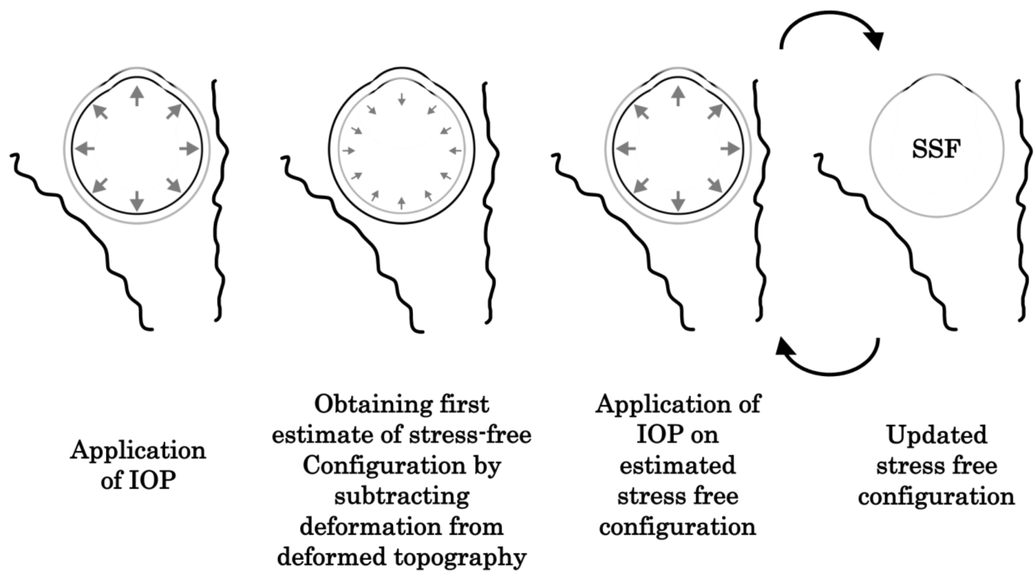

Figure 3.37: A schematic diagram showing the iterative process of stress-free form estimation.

3.4.5 Corvis Air-puff

Stress-free configuration is the final step, which changes the geometry of the globe. Therefore, once the globe's stress-free form (SFF) was obtained, another form of loading was incorporated to follow the globe's inflation step. This second step of loading simulated 32 ms of applied Corvis pressure. An algorithm was developed to read corneal geometrical data from the SFF model and calculate the maximum pressure applied to each element. As discussed in subsection 3.2.6, time and horizontal distance from the cornea determine how maximum pressure would change across corneal elements. In addition, another text file stated how this maximum pressure changed across the 32 milliseconds of the procedure. As shown in Figure 3.38, loading is applied to the normal of each element.

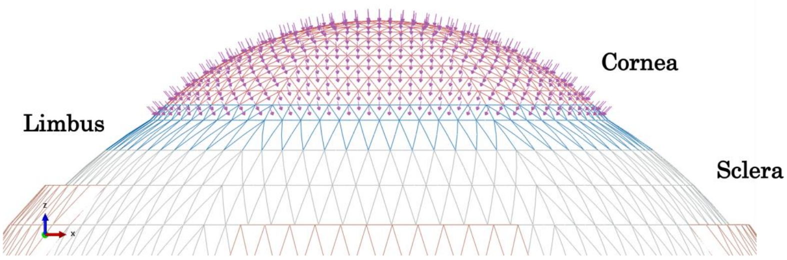

Figure 3.38: A numerical model shows the simulation of Corvis pressure applied on corneal elements. Load is represented by purple arrows directed normal to the element's anterior surface

3.4.6 Model Analysis

At this stage, 864 models were created per gender. In addition, the SFF of all models was obtained; then, pressure distribution on corneal elements was determined; hence, models are ready for simulation. One thousand seven hundred twenty-eight models were split into two batches according to gender. Each batch was split into three groups, each assigned to a computing unit (4-Core Intel-i7). The IOP and 32-millisecond Corvis simulation of each model took 45 minutes to complete. Henceforth, with all available computing units, completion of all simulations took 18 days. Consequently, upon simulation completion, a python algorithm was running to export anterior and posterior corneal deformation profiles onto a text file. Eventually, all files not required for re-runs or analysis; were deleted to save storage space.

3.4.7 Calculation of Dynamic Corneal Response (DCRs) parameters

Nodal Cartesian coordinates of anterior and posterior corneal surfaces over time were extracted in a text file generated by a python code, see subsubsection 3.3.2.2. Due to the application of IOP, CCT was influenced. Therefore, CCT had to be re-calculated at this stage by determining apical corneal thickness. Some extra information was provided from previous steps, such as; IOP, corneal radius and corneal material stiffness. The Numerical Corvis profile was exported from Abaqus' output database file in a similar manner to clinical data to execute DCR calculations, defined and illustrated in this section.

- **Applanation 1 Time (A1T):** This is usually in the first third of the air-puff procedure at which the cornea becomes flat. This measurement was calculated using the first derivative of the deformed corneal profile. A1T was detected by distinguishing the profile before which the cornea has three nodal points with a derivative equal to zero, **Figure 3.39**.

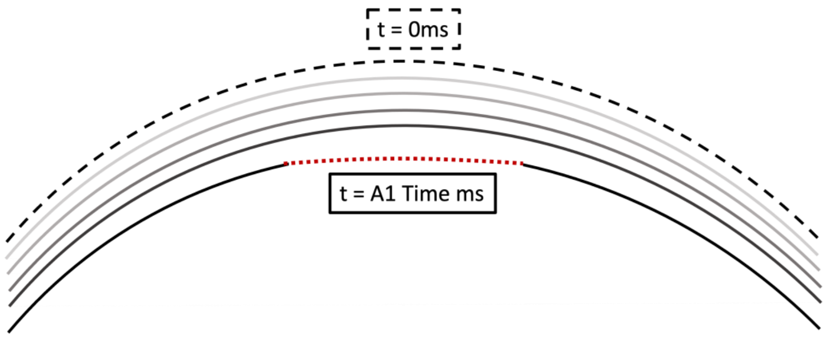

Figure 3.39: A schematic diagram shows corneal deflection until the first applanation

- **A1 Length (A1L):** This is the length at which all nodal points have a range of first derivative. According to Corvis ST, this range was ±10 microns, **Figure 3.39**.

- **A1 Deflection Amplitude (DeflAmpA1):** This is the displacement covered by the cornea from natural position until A1 Time, **Figure 3.40**.

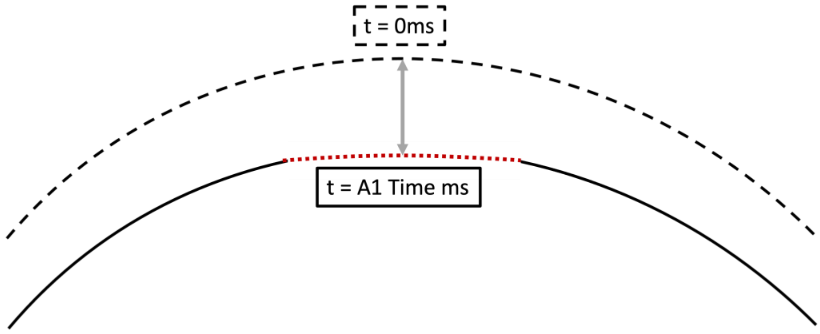

Figure 3.40: A schematic diagram shows A1 Deflection Amplitude of corneal profile.

- **Applanation Pressure 1 (AP1):** This is the nozzle pressure at which the first applanation occurred. This pressure value was determined precisely using provided simulation pressure amplitude time and A1 Time through interpolation, **Figure 3.41**.

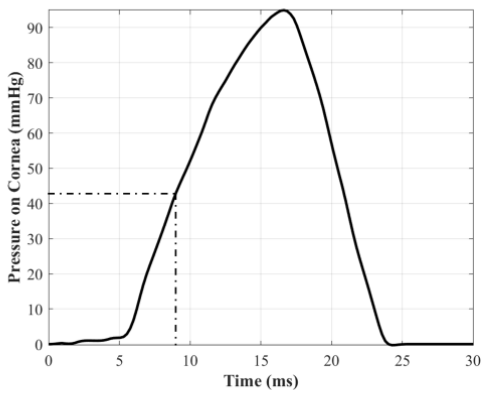

Figure 3.41: A schematic diagram showing the determination of AP1 using A1Time of corneal profile.

- **A1 Velocity (A1V):** This is the velocity of cornea's displacement from natural position until A1 Time position, **Equation 3.7**, see **Figure 3.39**.

$$A1V = \frac{DeflAmpA1}{A1T} \tag{3.7}$$

- **Stiffness Parameter at A1 (SPA1):** This parameter was initially introduced by Cynthia Roberts et al.,[206] in which it is acknowledged to be interrelated with overall corneal stiffness, **Equation 3.8**

$$SPA1 = \frac{AP1 - IOP}{DeflAmpA1} \tag{3.8}$$

- **Deflection Amplitude Maximum (DeflAmpMax):** This is the maximum displacement covered by the corneal apex to the highest concavity. This value was obtained by identifying the most prominent apical deformation profile during an air-puff procedure, **Figure 3.42**.

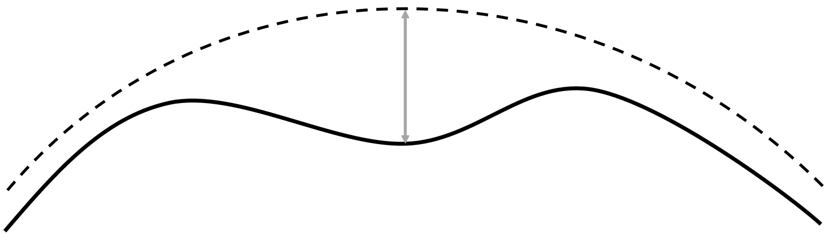

Figure 3.42: A schematic diagram showing maximum deflection of corneal profile.

- **Stiffness Parameter at HC (SPHC):** This parameter has a very similar approach of calculation to SPA1; however, this stiffness parameter only considers deformation occurred between A1 time and HC time, **Equation 3.9**

$$SPHC = \frac{AP1 - IOP}{DeflAmpMax - DeflAmpA1} \tag{3.9}$$

- **Highest Concavity Time (HCT):** This is the time index at which DeflAmpMax was identified, **Figure 3.43**.

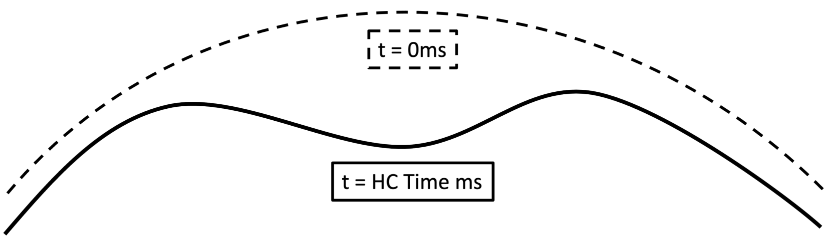

Figure 3.43: A schematic diagram showing measured peak distance of corneal profile.

- **Peak Distance (PD):** This is the distance between two peaks on the cornea where the highest concavity occurred. This parameter was calculated by obtaining the difference between the highest two points at the most deformed profile, **Figure 3.44**.

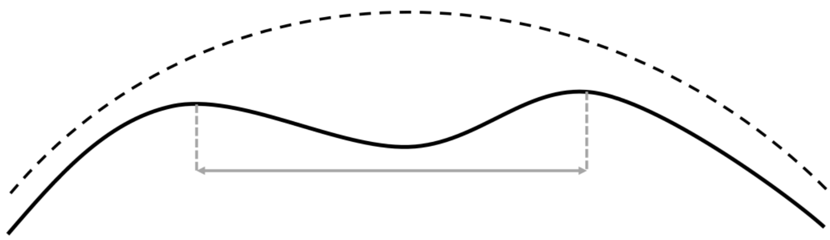

Figure 3.44: A schematic diagram showing measured peak distance of corneal profile.

- **Radius at Highest Concavity (HCR):** This is the radius of the circle of best fit, which was estimated by MATLAB in-built optimisation function, Figure 3.45.

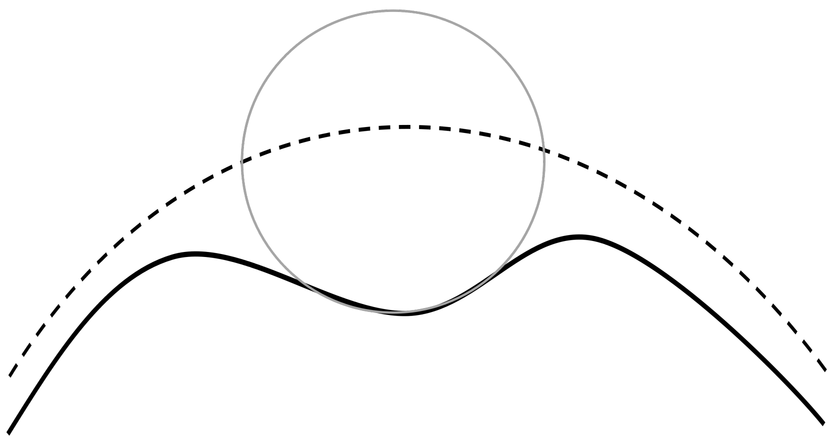

Figure 3.45: Schematic graphical description of HC Radius.

- **Corneal Asphericity (P and R Values):** X-Y coordinates of each relaxed and after corneal inflation profile were utilised with corneal asphericity Equation 3.10 and an optimisation process to determine apical radius (R) and shape factor (P) value, Figure 3.46. The optimisation process employed the "fminsearch" Matlab function to optimise R and P values, which allows Equation 3.10 to predict Y values with minimum error to actual corneal elevation data.

$$Y^2 = 2 \times R \times X - P \times X^2 \tag{3.10}$$

Where:

P = Shape factor

R = Apical radius

When:

P > 1 Oblate ellipse (steepens from centre to periphery)

P = 1 Circular

P < 1 Prolate ellipse (flattens from centre to periphery)

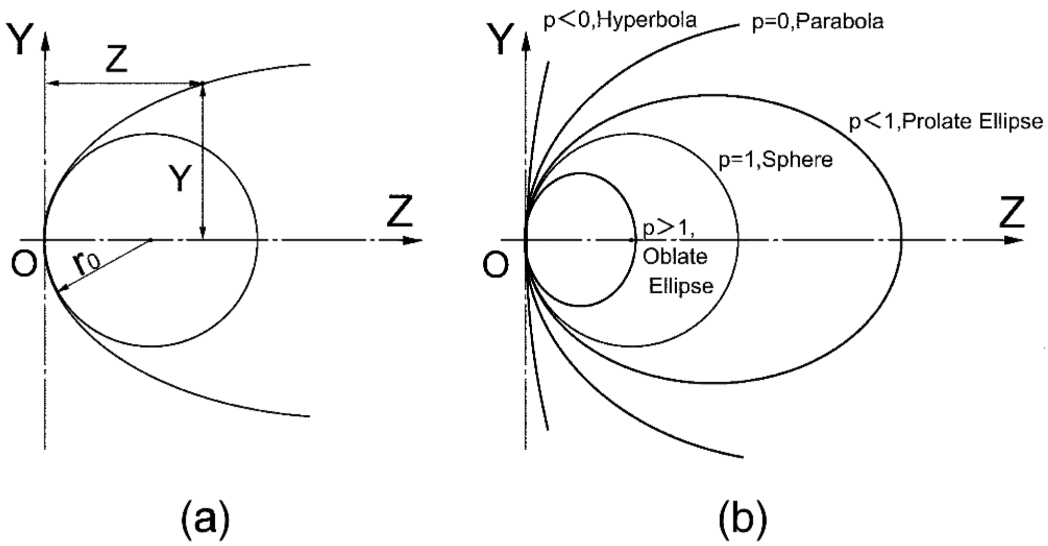

Figure 3.46: (a) Apical radius shown on Cartesian coordinates (b) The family of shape factors[29]

The analysis and calculations above were applied to all 1728 models. After completing this part of the process, all DCRs were saved and ready for the following stage of equation development.

3.5 Development of IOP and Material Stiffness Equations

The methodology used in developing the equations will be scrutinised during this section. The equations were developed to accurately estimate bio-mechanically corrected Intraocular pressure ($bIOP_o$) and Stress-Strain Index (SSI_o), which relates to the material stiffness of the eye.

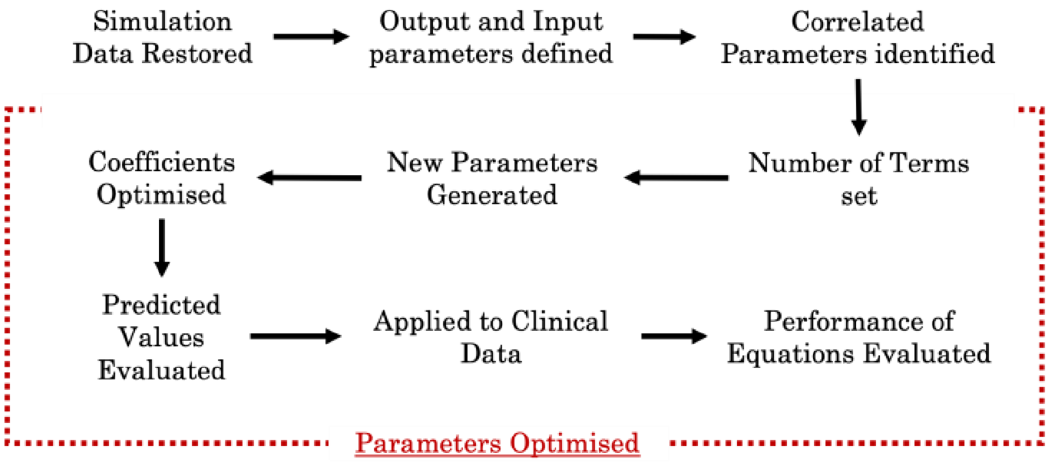

Figure 3.47: Optimisation methodology followed to generate equations.

As seen in Figure 3.47, a step within the optimisation process was to evaluate the predicted values of parameters of interest (SSI_o and $bIOP_o$). This evaluation process was done by comparing predicted values produced by the developed equations with their actual counterpart, which was used in the numerical model simulation. There were three possible regression methods to evaluate those predicted values.

First is Least Absolute Deviation (LAD), a statistical optimality criterion used in robust statistical optimisation techniques. However, this method lacks the stability of the solution.[225] See Equation 3.11 below.

Least Absolute Deviation:

$$J(y_i, h(x_i)) = \frac{1}{n} \sum_{i=1 \to 1728}^{n} |y_i - h(x_i)| \tag{3.11}$$

On the hand, there is the second method, Least Squares Deviation (LSD), considers an implicit assumption. It assumes that errors are either "Zero" or delimited to be negligible. However, as seen in Figure 3.48, when the residual (r_i) is non-negligible, it affects the weight of J majorly.[226]

Least Squares Deviation:

$$J(y_i, h(x_i)) = \frac{1}{n} \sum_{i=1 \to 1728}^{n} (y_i - h(x_i))^2 \tag{3.12}$$

Due to applying a general theorem onto a set, instability occurs in LAD, while in LSD, outliers majorly influence the weight of J. Therefore, a robust M-estimate function was utilised in optimising the predicted value. This cost function could transition between two conditional parts, linear or quadratic. With the use of one free parameter, δ, a transition point is defined; thus, outliers with high absolute residuals will be assigned a lower weight by the cost function, see Equation 3.13.[227]

Huber M-estimate cost function:

$$J(y_i, h(x_i)) = \frac{1}{n} \sum_{i=1 \to 1728}^{n} \begin{cases} 0.5(y_i - h(x_i))^2, if|y_i - h(x_i)| < \delta \\ \delta(|y_i - h(x_i)| - 0.5\delta), otherwise \end{cases} \tag{3.13}$$

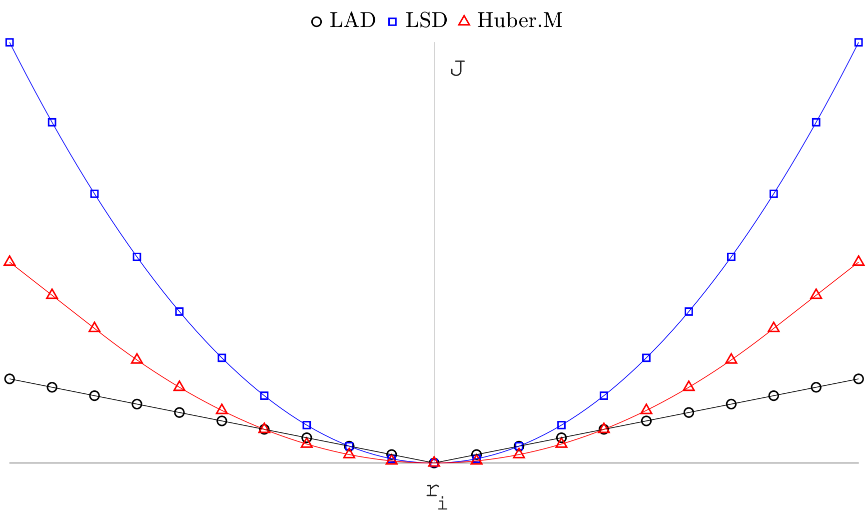

Figure 3.48: Optimisation methodology followed to generate equations.

3.5.1 Biomechanically Corrected IOP

This subsection portrays the technique applied to acquire the $bIOP_o$ equation for healthy subjects. In subsection 3.4.7, various corneal data were extracted from the numerical simulation and split into two batches accordingly to gender. Consequently, those two batches of data were deployed into a Matlab script written explicitly to find the optimum equations. A statistical analysis took place to evaluate all parameters' correlation with IOP. Any parameter that showed correlation was selected and considered in developing the $bIOP_o$ prediction equation. Those selected base parameters ($bPar_s$) were used as domains for $h(x_i)$, while function's range was defined as IOP, see Equation 3.14.

$$bPar_s = [CCT, Age, HCT, PD, DefAmpMax, DeflAmpA1, A1V, R, P, AP1, HCR] \tag{3.14}$$

In the developed optimisation algorithm, attaining the optimum equation required using ($bPar_s$) in several different combinations to obtain three unique terms, $Te_{x,y,z}$, with high accuracy could predict the IOP. These terms were combined with their respective coefficients (C_i) to produce a formula as shown in Equation 3.15.

$$bIOP_o = C_1 \cdot Te_x + C_2 \cdot Te_y + C_3 \cdot Te_z + C_4 \tag{3.15}$$

The main goal of this optimisation is to minimise the calculated error between actual IOP applied in the numerical simulations against its predicted counterpart using Equation 3.13. Each term of this equation could have one of the undermentioned combinations.

- $bPar_x$
- $bPar_x^2$
- $bPar_x^3$
- $bPar_x \times bPar_y$
- $bPar_x \times bPar_y \times bPar_z$

For each case, the code modified the terms using different sets of the parameters mentioned above; see Equation 3.15. In each case, the code optimises the coefficients to minimise the error between the actual IOP and its predicted counterpart, $bIOP_o$. Once the optimum terms and their corresponding coefficients were acquired, the optimisation was complete. To follow was to test this optimised equation DCRs of clinical datasets described in subsection 3.6.1. Once the predicted values of IOP were computed using the optimised equation and DCRs, a correlation assessment of IOP with Age and CCT was carried out. Then if needed, some modifications were made to improve the accuracy of the prediction. Several datasets were then utilised to validate the equation with final modifications. It must be noted that clinical data corneal profiles were used to calculate parameters of corneal asphericity, just as described in subsection 3.4.7.

3.5.2 Stress-Strain Index

As portrayed in subsection 2.3.1, corneal tissue behaves non-linearly, indicating corneal stiffness variation at different stress and strain levels. Biomechanical Engineering Group at the University of Liverpool directed a study which demonstrated a strong correlation between corneas of different age groups and their stress-strain behaviour.[32,160] As observed in Figure 3.49, with the progression of age, the stress-strain curves tend to get a steeper gradient without intersection. This linear change in gradient indicates age-related stiffening of corneal tissue, which is described by Equation 2.4 in subsection 2.3.1. Using this concept allows corneal stiffness calculation of various age groups relative to the stiffness of a 50-year-old healthy subject. Therefore, an age-related stress-strain curve could be acquired with a single parameter (SSI), allowing clinics to use this value and theoretically measure corneal mechanical behaviour *in-vivo*.

This section will outline the methodology for obtaining SSI_o equations. This equation was developed to accurately predict corneal material stiffness of healthy subjects with no previously stated abnormality or surgical procedures, which may influence the mechanical response of the globe or OST. In the case of not knowing if the eye had keratoconus or endured a refractive correction, the developed SSI_o equation would still be applicable. However, the prediction may be prone to inaccuracy. Listed below is the methodology employed to develop the SSI_o equation.

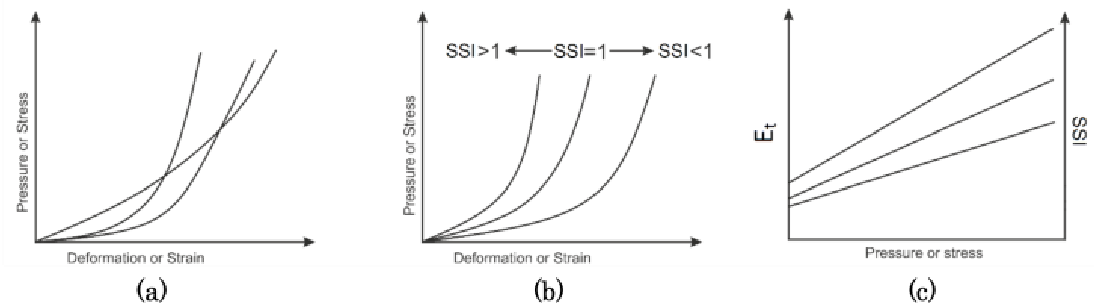

Figure 3.49: Corneal stress-strain behaviour changes with age without any intersection as indicated in sub-figure (a) but instead consistently changes as shown in sub-figure (b), which translates to change of tangent modulus with stress as seen in sub-figure (c). SSI=1 represents material stiffness of a healthy cornea aged 50 years; as age increases, stiffness increases and vice versa.[32]

Similar to subsection 3.5.1, the SSI_o equation was obtained through the same optimisation procedure, see Figure 3.47. The correlated parameters with corneal material stiffness were selected as base parameters, which are used as domains in a function that will output the predicted corneal material stiffness. The base parameters are as follows:

$$\begin{aligned} bPar_s = [&bIOP_o, CCT, Age, HCT, PD, DefAmpMax, \\ &DeflAmpA1, A1V, R, P, AP1, HCR, SPA1, SPHC] \end{aligned} \tag{3.16}$$

A similar equation was developed and optimised to Equation 3.15. The main goal of this optimisation is to minimise the calculated error between actual corneal material stiffness set in the numerical simulations against its predicted counterpart using Equation 3.13. Each term of this equation could have one of the undermentioned combinations.

- $bPar_x$
- $bPar_x^2$
- $bPar_x^3$
- $bPar_x \times bPar_y$
- $bPar_x \times bPar_y \times bPar_z$
- $\frac{bPar_x}{bPar_y}$

- $\frac{bPar_x+bPar_y+bPar_z}{bPar_a+bPar_b}$

To follow was to test this optimised equation DCRs of clinical datasets described in subsection 3.6.1. As done previously in subsection 3.5.1, the optimum terms and their corresponding coefficients were acquired, and the optimisation was complete. Once the predicted values of SSI_o were computed using the optimised equation and DCRs, a correlation assessment of SSI_o with Age, CCT and IOP was carried out, then if needed, some modifications were made to improve the accuracy of the prediction. Several datasets were then utilised to validate the equation with final modifications.

3.6 Validation of Equations

3.6.1 Healthy Clinical data

This section provides clinical information from data obtained from healthy participants. Institutional review boards at all institutions ruled that approval was not needed for record review studies. However, ethical approval for using the data in research had been secured at both institutions when the data was collected, anonymised, and used in earlier studies,[203, 228] before which participants' informed and written consent was secured before collecting the data. Nonetheless, written informed consent was obtained from each participant to use their data in the research. The study was conducted according to the tenets of the Declaration of Helsinki as set out in 1964 and revised in 2013. Earlier studies suggest that orbital health conditions, such as thyroid orbitopathy, affect whole eye movement (WEM) in response to the air pulse produced by Corvis.[39, 220] Therefore, all participants were subject to a complete ophthalmic examination, including tests using the Corvis and Pentacam (OCULUS Optikgeräte GmbH; Wetzlar, Germany). Subjects with a history of use of hypotonic therapies, glaucoma, previous eye disease or ocular surgery were excluded. For consistency, one clinician carried out Corvis examinations for all participants. An experienced corneal specialist individually reviewed all exams to ensure that only good-quality scans were included in the study, enabling the calculation of all Corvis dynamic corneal response parameters (DCRs).

Chapter 4

Results

4.1 Introduction

This chapter will present the numerical model results, starting with the orbital boundary extracted from each of the available head CT scans; subsequently, a mean boundary of all three orbital boundaries will be acquired and used as the base geometry for geometrical discretisation. The optimised mesh densities of the cornea, sclera and orbit will also be presented; this native mesh will then be used in a material optimisation process, where the outcome of an inverse analysis will be described, with results including the mean stress-strain relationship, as well as simulated WEM. In the consequent section, the experimental shear modulus of a previous study is utilised to validate the numerical model. Furthermore, the effect of rectus and oblique muscles will be described by comparing clinical WEM with their numerical counterpart. Muscle forces produced from force distribution optimisation will be outlined. Optimised force distribution will then be applied to clinical data from patients of different ages and genders, and root mean squared error (RMSE) mismatch values are compared. Finally, the end of this section will focus on the outcome of the parametric study, including validation of the produced algorithms with previously acquired experimental data. Lastly, the newly developed algorithms will be applied to various clinical datasets for performance evaluation.

4.2 Orbital Boundary

This section presents the orbital boundaries of three young female subjects. As mentioned in **??**, the boundary extracted from CT scans starts at the lateral wall towards the orbital apex. This location was decided to allow for the addition of ethnic-specific orbital rims. As depicted in Figure 4.14.1(d), the anterior portion of the orbital boundaries did not differ between the three subjects; however, there was a slight difference in the size and position of the orbital apex, which may have been due to image processing human error.

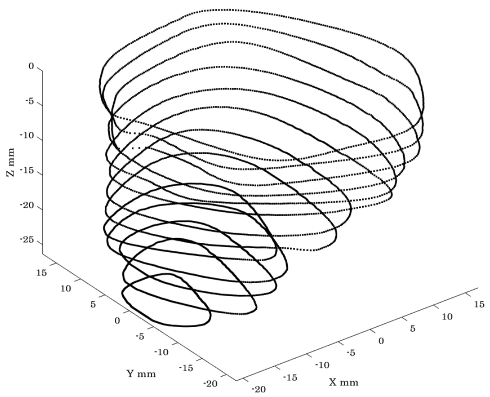

(a)

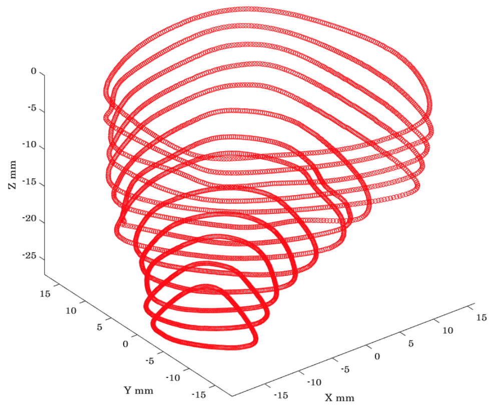

(b)

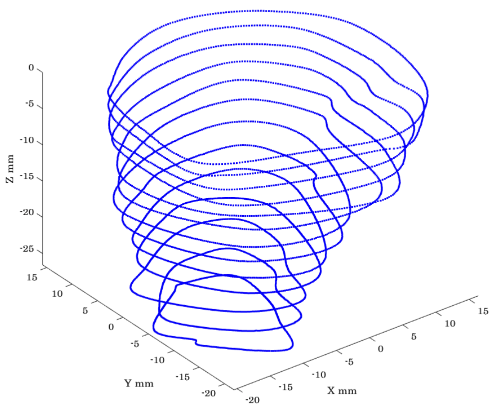

(c)

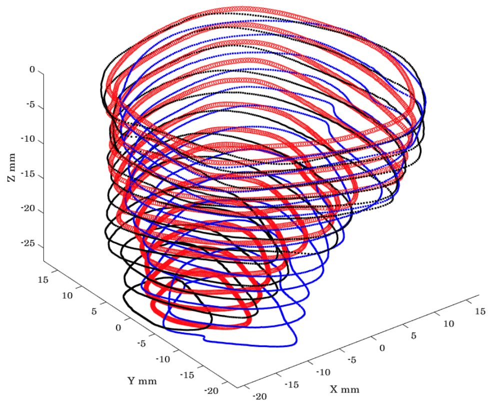

(d)

Figure 4.1: (a-c) represent the orbital boundary for each of the three subjects, while (d) shows overlapping boundaries

The mean geometry of the three subjects was then acquired, ready for application of the ethnic-specific orbital rim (see Figure 4.2).

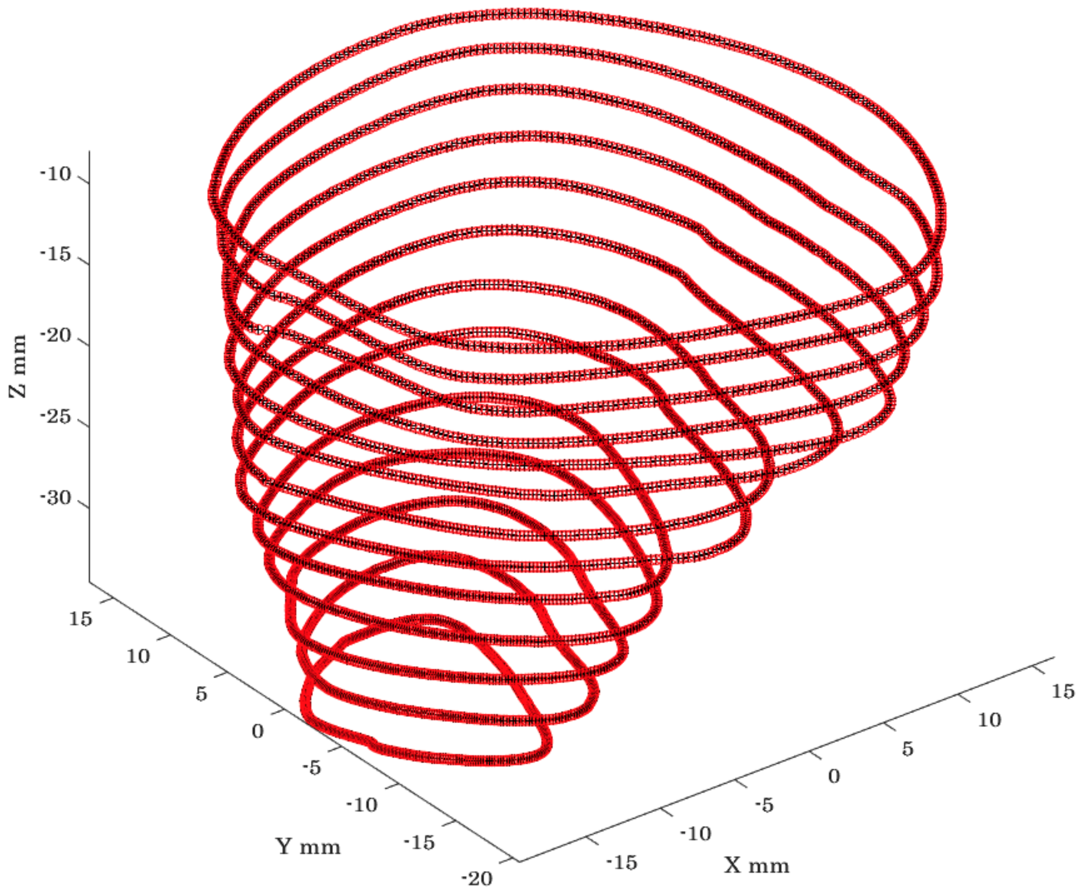

Figure 4.2: Mean orbital geometry of extracted geometry

4.3 Numerical Simulation

4.3.1 Mesh Density Study

The mesh density study employed six models with varying corneal rings while keeping scleral rings fixed to 26. Corneal rings varied from 6 to 60 rings, while element numbers varied from 3000 to 22000 elements. The study involved applying Corvis pressure while monitoring the deformation of the corneal apex. The change of corneal rings from 6 to 12 increased apical deformation by about 9% (see Figure 4.3). Any further increase in corneal mesh density resulted in no significant change in the cornea's numerical deformation (±0.6%); computational time, however, increased dramatically (see Figure 4.3). Therefore, a model with 12 corneal rings was used for the remainder of the work done during this research.

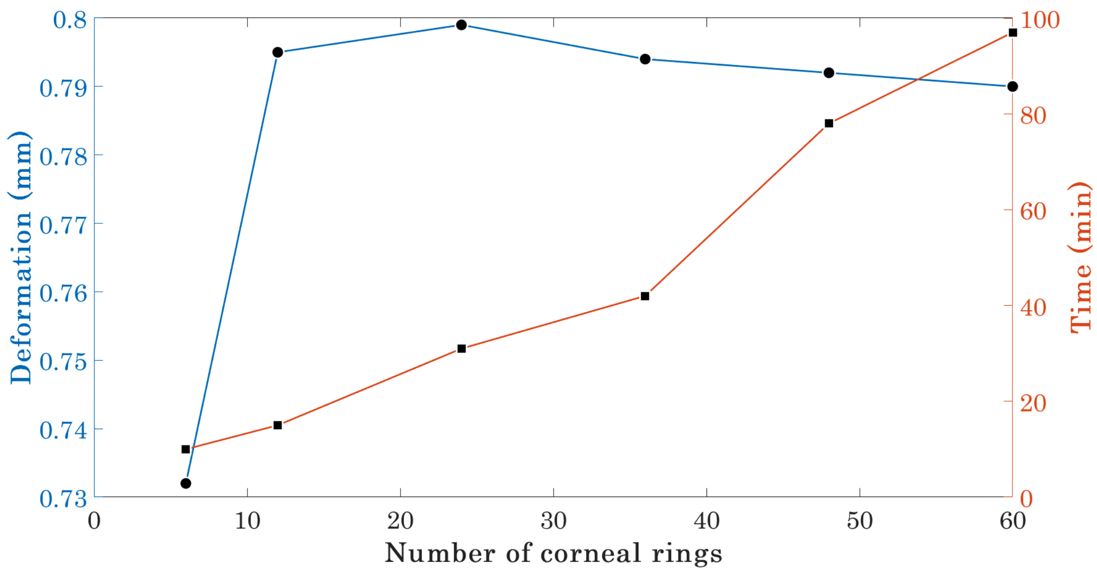

Figure 4.3: Outcome of mesh density study carried out by changing the number of corneal rings while keeping the number of scleral rings constant

A similar method was used for the sclera's second mesh density study. The number of corneal rings was fixed to the optimum corneal density (12 rings), while scleral rings varied from 12 to 62. As shown in Figure 4.4, there was no significant change in apical deformation (±0.1%) with the change of scleral mesh density. However, 22 scleral rings were selected as the scleral native mesh density as a sanity check. Therefore, an eye model was produced with 3500 elements and 15600 nodes arranged in 34 rings (12 corneal and 22 scleral rings).

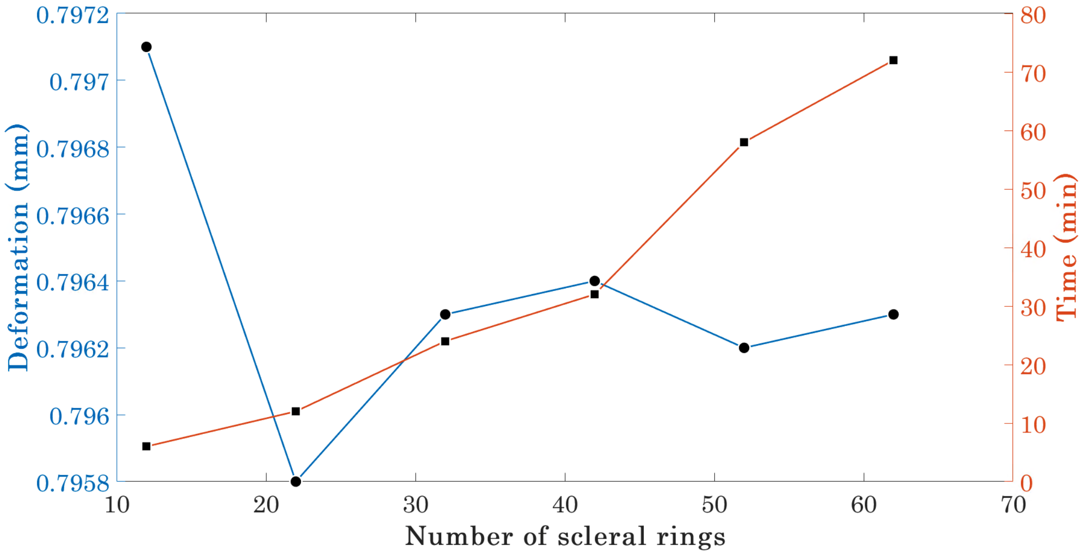

Figure 4.4: Outcome of mesh density study carried out by changing the number of scleral rings while keeping the number of corneal rings constant

The outcome of the previous mesh density studies was then used along with a variation of mesh densities of the orbital medium. The orbital elements of the models ranged from 1000 to 145000 elements. The model with the coarsest mesh crashed due to initial penetration between orbital and global elements. The deformation monitoring node was changed to the posterior node of the globe, compared to the corneal apex used in previous density studies; this location was chosen to monitor the orbital elements' deformation rather than the globe. As seen in Figure 4.5, when density was changed from 8600 to 17500, deformation increased by 10%, and computational time almost doubled. Density higher than 17500 elements caused minimal increases in deformation but continued to be associated with a significant increase in computational time. Deformation seemed to consolidate at an orbital mesh density of 17500 elements and 10800 nodes. Therefore, that density was chosen to be the orbit's native mesh density used in the remainder of this research.

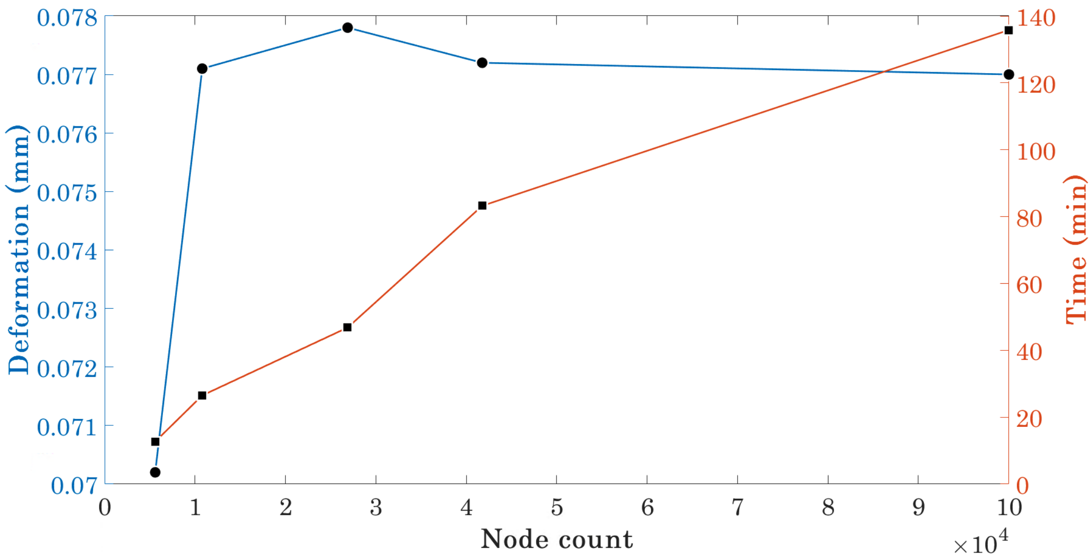

Figure 4.5: Outcome of mesh density study carried out by changing orbital mesh density, while the globe's mesh density was kept constant

4.4 Validation of Numerical Model

This section will describe the validation results of the numerical model. At the start of the section, the results of the material optimisation analysis will be reported. Those results include various plots such as a comparison between numerical and clinical WEM, stress-strain behaviour of different age groups and the corresponding tangent modulus, E_t. Also reported are results regarding the use of experimental stiffness of AFT and how this affects the WEM clinical mismatch; the effect of rectus and oblique muscles will be described and aid in the validation process. The final part of this section will go through the optimised EOMs force distribution and their effect on clinical data of different age groups.

4.4.1 Material Optimisation

After optimising the mesh density of the developed model, an inverse analysis was executed to find the optimum shear modulus, μ, and strength hardening exponent α. This study began by submitting 75 jobs simulating Corvis pressure. Those jobs varied in their material parameters, in which all possible combinations of μ (5×10^5 to 5×10^3MPa $n = 15$) and α (0.1 to 50 $n = 5$). This outcome was that μ had a much greater influence on RMSE clinical mismatch, while α had a negligible effect, as shown in Figure 4.6. In order to find the minimum value of RMSE, the Matlab built-in '*pchip*' interpolation method was used to acquire a more detailed range, identifying the minima of $0.02935mm$. The corresponding value of α to the localised minima was set as the strength hardening exponent for the remainder of this study.

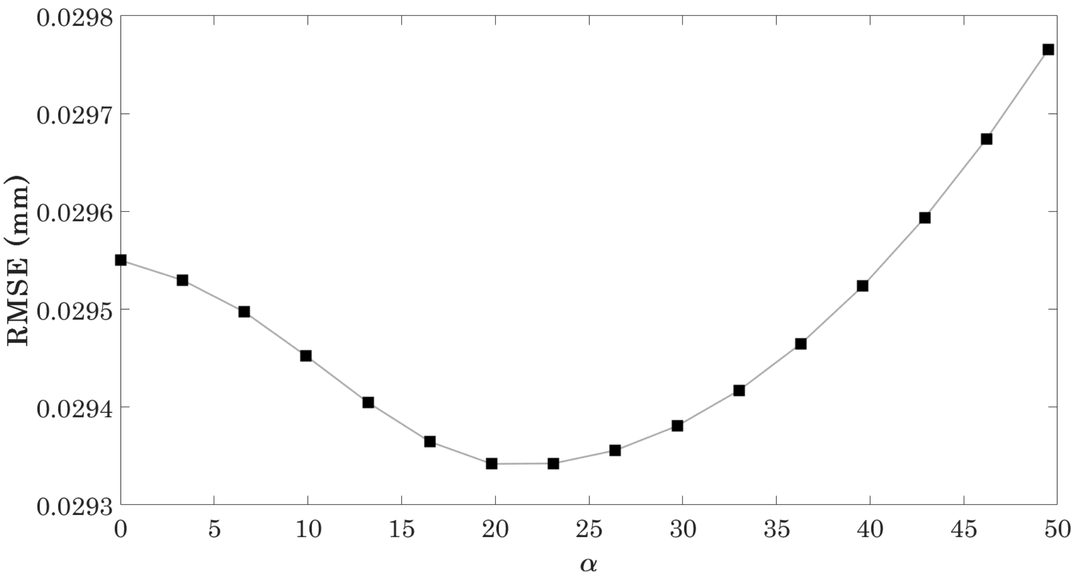

Figure 4.6: A detailed range of α with interpolated RMSE values using *'pchip'* interpolation

The inverse analysis process becomes less complex, and computational time is reduced drastically once one parameter is fixed. There were 185 clinical profiles of subjects' corneas deforming to Corvis pressure. The range and spacing of μ were the same as that used in the optimisation of α. Due to material parameter variations, μ, numerical deformation of the cornea varied. Ultimately, each clinical profile was used as a validation benchmark and compared to 15 numerical profiles. The parameter resulting in the most negligible RMSE value is stored along with the age and IOP of the subject, and then the process is repeated for a different clinical profile. Figure 4.7 indicates each optimum μ and the related subject's age.

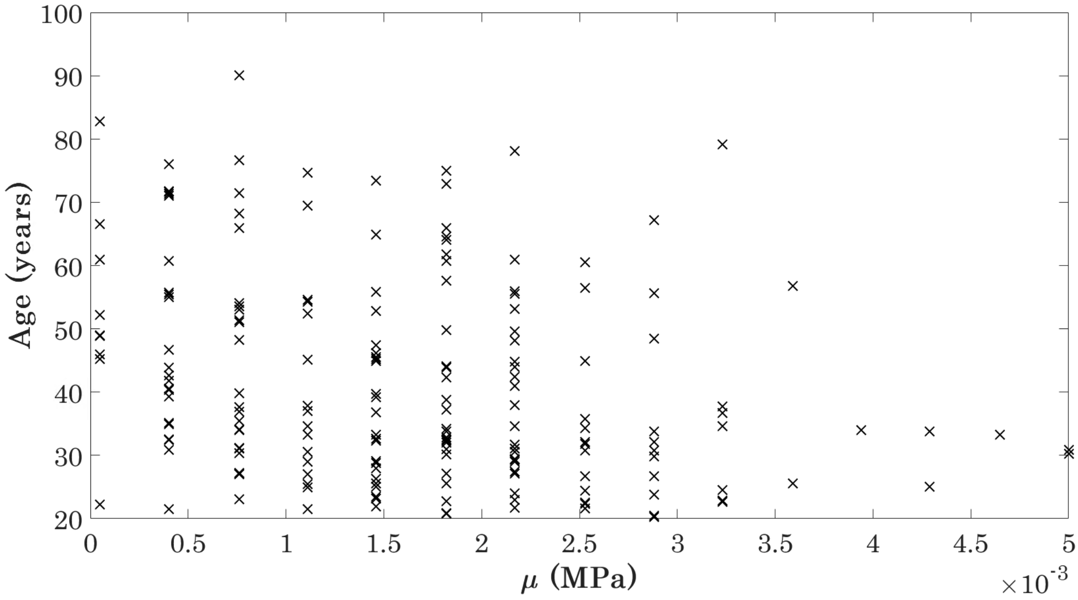

Figure 4.7: Scatter plot of μ values determined by minimum RMSE found for each clinical case

After eight weeks, 2,775 simulations for 185 subjects were complete. Each of the stored values of μ was filtered out. This filtration process ensured that all μ values had corresponding RMSE values less than 0.025mm. This process reduced the volume of data to be analysed and removed anomalies that may cause false outcomes. Ogden's constitutive strain energy relationship with μ and α; Equation 4.1 was used to describe the stress-strain relationship using Ogden's material parameters. Since, no lateral forces were applied, principal stretches in Equation 3.2 could be simplified as; $\bar{\lambda_2} = \bar{\lambda_3} = \bar{\lambda_1}^{\frac{1}{2}}$, hence

$$U = \sum_{n=1}^{N} \frac{2\mu_i}{{\alpha_i}^2}(\bar{\lambda_1}^{\alpha_i} + \bar{\lambda_1}^{\frac{\alpha_i}{2}} + \bar{\lambda_1}^{\frac{\alpha_i}{2}} - 3) \tag{4.1}$$

Simplifying similar terms,

$$U = \sum_{n=1}^{N} \frac{2\mu_i}{{\alpha_i}^2}(\bar{\lambda_1}^{\alpha_i} + 2\bar{\lambda_1}^{\frac{\alpha_i}{2}} - 3) \tag{4.2}$$

Differentiating U with respect to λ

$$\sigma = \frac{\partial U}{\partial \lambda} = \sum_{n=1}^{N} \frac{2\mu_i}{\alpha_i}(\bar{\lambda_1}^{\alpha_i - 1} - \bar{\lambda_1}^{\frac{\alpha_i}{2} - 1}) \tag{4.3}$$

where

$$\lambda = 1 + \epsilon \tag{4.4}$$

Therefore, stress could be represented by strain, shear modulus and strength hardening exponent. Their relationship is described in the following uniaxial mode;

$$\sigma = \sum_{n=1}^{N} \frac{2\mu_i}{\alpha_i}((1+\epsilon)^{\alpha_i - 1} - (1+\epsilon)^{\frac{\alpha_i}{2} - 1}) \tag{4.5}$$

Equation 4.5 was used along with a given strain range to plot the stress-strain relationships of mean μ values of each age group, as shown in Figure 4.8.

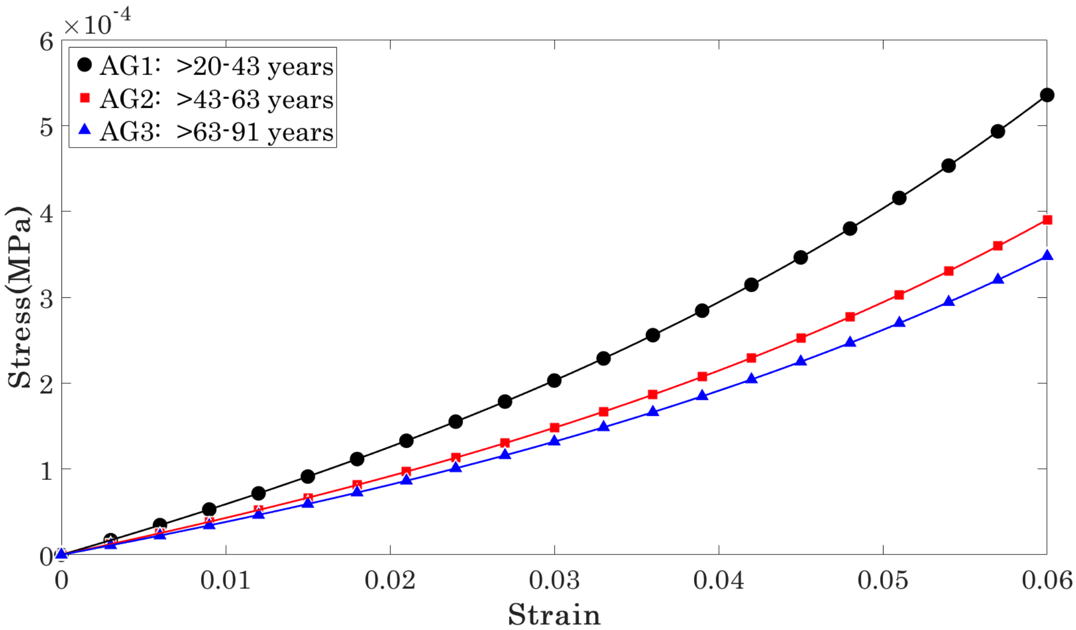

Figure 4.8: Stress-strain curves computed using Ogden's material model along with the average values of μ for each age group, where α was set to 23

Subsequently, the stress-strain relationship described in Figure 4.8 was utilised to determine the tangent modulus, E_t, at any given point on the curve. This was achieved by acquiring the change in stress and the change in strain and then dividing the former by the latter, as described in Equation 4.6. In Figure 4.9, E_t-strain relations are plotted for all age groups.

$$E_t = \frac{\delta\sigma}{\delta\epsilon} \tag{4.6}$$

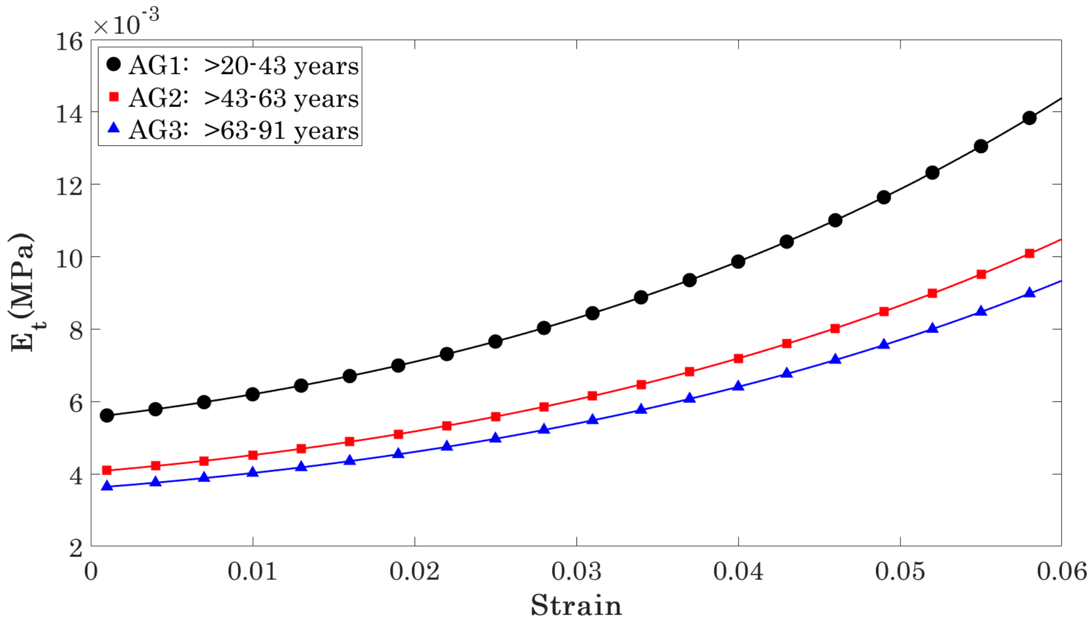

Figure 4.9: E_t-strain curves for all age groups; changes in stiffness are referred to as stress/strain increases

The acquirement of the tangent modulus represents the stiffness of the tissue at a given stress. Three stresses were used to interpolate the E_t value for all subjects. This interpolation aids in testing the statistical significance of stiffness changes between age groups. This statistical analysis is performed later in that section. The mean μ value was determined to be 1.6 ± 1 kPa. This shear modulus value was then used in another simulation to evaluate WEM and compare it to the mean clinical WEM. In Figure 4.10, the latter part of the simulated WEM (9ms onward) agrees with clinical data.

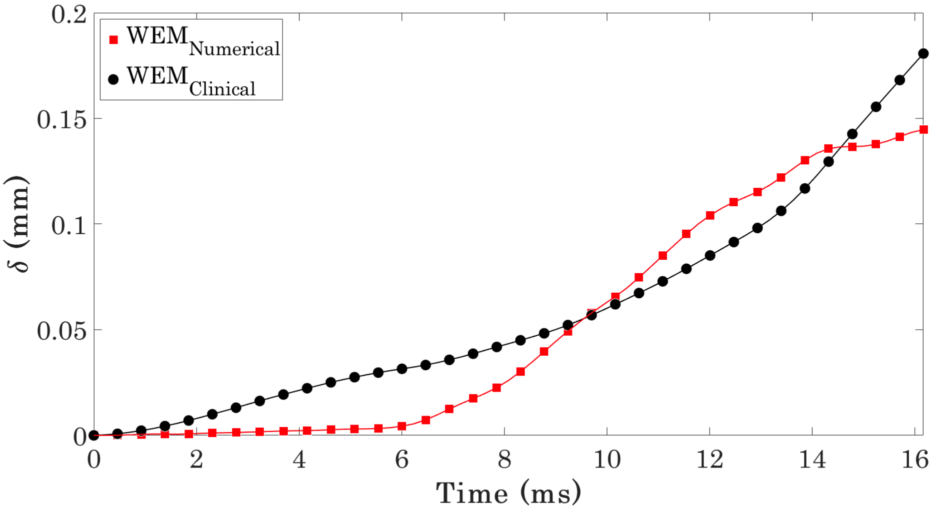

Figure 4.10: Mean clinical WEM of the whole dataset, compared to WEM resulting from the application of Corvis pressure where μ was set to 1.6kPa. This plot shows the average WEM of nasal and temporal movements

On the other hand, there was a significant difference between numerical and clinical WEM. This difference was present even at a much lower stiffness. Furthermore, rotation of the globe during application of Corvis air-puff was of interest; with mean clinical WEM, there is a significant nasal rotation that occurred from the start of the procedure (see Figure 4.11). This rotation tended to increase gradually throughout loading conditions. Nevertheless, this rotation could not be observed in the numerical WEM per the current numerical set-up.

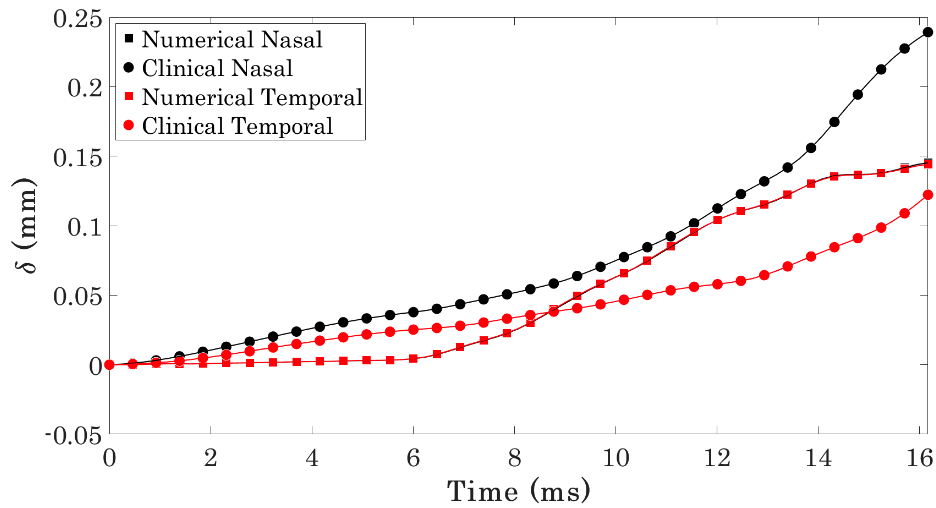

Figure 4.11: Mean clinical WEM of the whole dataset, compared to WEM resulting from the application of Corvis pressure, where μ was set to 1.6kPa. This plot shows nasal and temporal WEMs

4.4.2 Effect of Extra-ocular Muscles on WEM

In the last part of this validation process, the material optimisation analysis of the orbital soft tissue showed that the optimised material stiffness was four times stiffer than that supplied by data in the literature for the adipose fatty tissue (AFT). Therefore, experimental stiffness of AFT (0.4kPa) will be employed in this part of the validation process, where the current study will thoroughly present the effectiveness of EOMs within two aspects of the ocular support system; anterior-posterior displacement and nasal-temporal rotation. In addition, this study will also present the six EOMs' major roles they play in supporting the eye globe.

4.4.2.1 Anterior−Posterior Displacement

First, the experimental stiffness parameter of AFT was utilised in the numerical set-up; 32ms Corvis air-puff was then applied. It should be noted that validation only considered loading conditions (0-16.17ms) due to the exclusion of corneal hysteresis. Whole eye movement shown in Figure 4.12 refers to the average of nasal and temporal WEM ($\pm 3.6\ mm$). The maximum WEM resultant from a set-up without EOM was 0.52mm at the 16^{th} millisecond; its clinical counterpart was 0.19mm. Numerical WEM at the 7.2mm corneal diameter was also compared to its corresponding clinical dataset throughout the loading stage of the procedure, resulting in an RMSE value of 0.133mm. Subsequently, this numerical procedure was repeated with three different set-ups. In the first set-up, rectus muscles were attached to the eye globe, reducing the average WEM slightly, with a maximum WEM of 0.45mm. The resultant numerical displacement provided an RMSE mismatch value of 0.106mm. After that, oblique muscles were added to the set-up and, as seen in Figure 4.12, this addition had an immense effect on WEM, reducing it to 0.20mm. This numerical set-up produced data resulting in an RMSE value of 0.019mm. Eventually, an extra numerical model was developed, which did not include orbital geometry or elements. This model resulted in the largest maximum WEM, 0.73mm, and an RMSE value of 0.30mm.

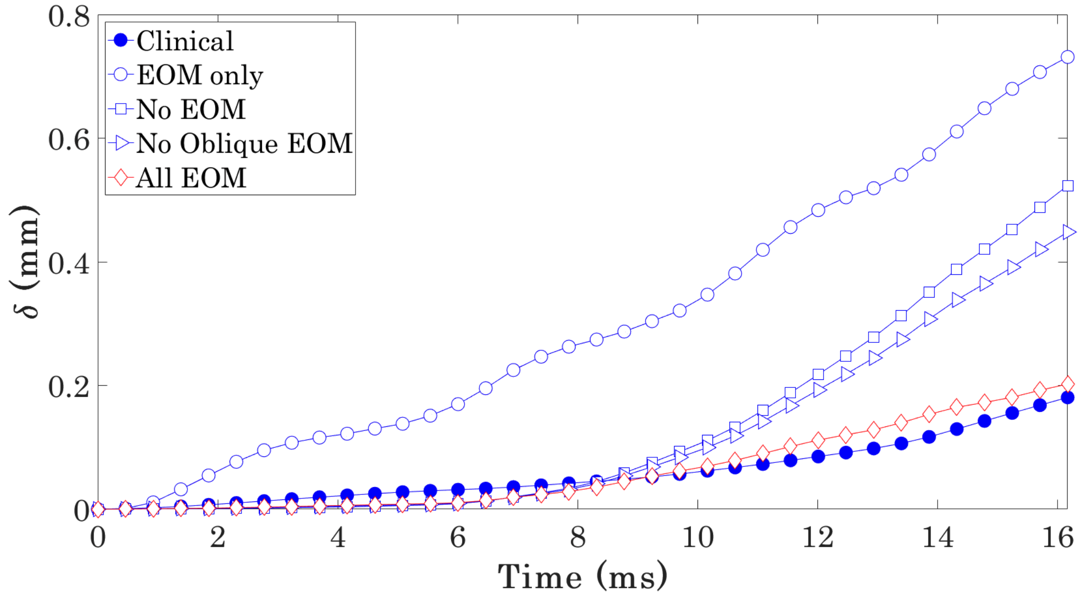

Figure 4.12: Average WEM showing anterior−posterior displacement of four different set-ups compared to their clinical counterpart.

4.4.2.2 Nasal−Temporal Rotation

The previously carried out material optimisation process produced an average WEM that matched the average clinical WEM; however, as presented in Figure 4.11, there was a significant nasal rotation in the clinical datasets of the Corvis procedure. Thus, here we discuss the effect of EOMs on the rotation of the eye globe during Corvis. The same numerical set-ups are used in this process to assess anterior−posterior displacement. In the initial set-up, with the exclusion of EOMs, numerical rotation did not align with the clinical counterpart, with the latter model displaying a very slight temporal rotation and not a nasal one. The numerical rotation of this set-up was compared to clinical rotation and produced an RMSE value of 0.42^o; see Figure 4.13.

Consequently, rectus muscles were added to the set-up, and as shown previously, this addition reduced anterior-posterior displacement. Nasal-temporal rotation, however, did not agree with clinical data, where the slight temporal rotation mentioned previously increased considerably. This increase resulted in an RMSE mismatch value of 0.70^o. Subsequently, oblique muscles were added to the set-up, and the analysis was repeated. As illustrated in Figure 4.13, the addition of oblique muscles significantly reduced nasal and temporal WEM. Temporal (versus nasal) WEM showed a more significant reduction, resulting in the nasal rotation reported in literature[143] and evidenced in the clinical displacement data of Corvis. Comparison to clinical data with this numerical set-up produced an RMSE value of 0.11^o. Finally, orbital elements were removed from the set-up, and the process was repeated. The outcome was that the direction of rotation agreed with clinical data. However, nasal rotation was overestimated, resulting in an RMSE mismatch value of 0.18^o.

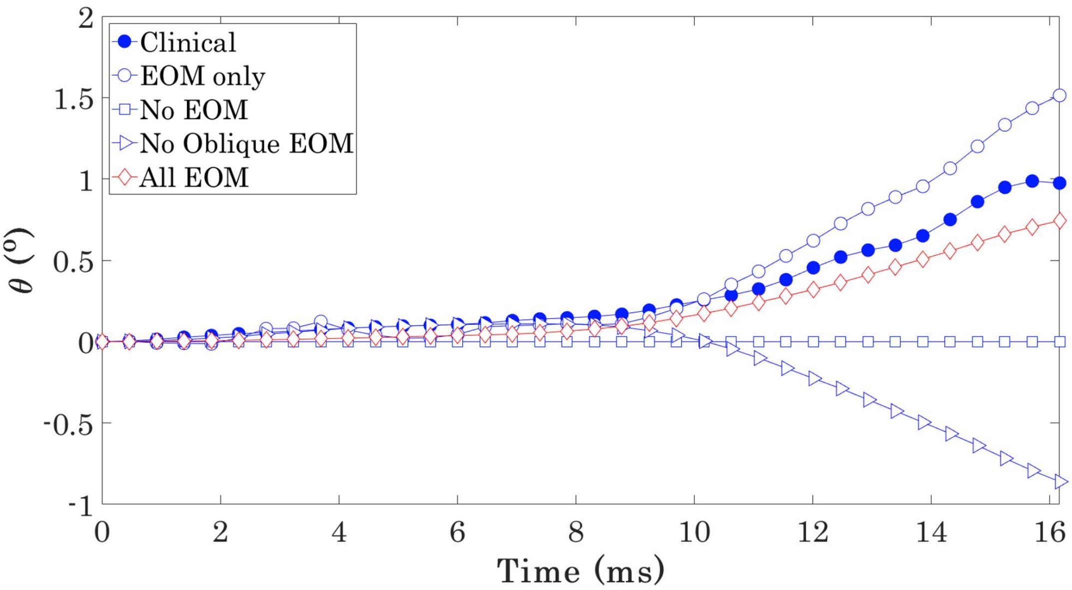

Figure 4.13: Average WEM showing nasal−temporal displacement of four different set-ups compared to their clinical counterpart.

Summary of Results

Without the inclusion of EOMs, there was a mismatch of over 173% between clinical and numerical maximum WEM. This mismatch was reduced to just over 136% by adding the four rectus muscles; however, this addition caused a rotation of almost 100% in the opposite direction of clinical data. Eventually, adding the oblique muscles reduced mismatch to just over 10% while fixing the rotation of the eye globe. The exclusion of orbital elements showed a mismatch of over 280%. It should be stated that all set-ups that included orbital elements had very slight to no displacement in the first 8ms; this should be investigated further.

4.4.3 Force Distribution Optimisation

Thus far, the WEM produced following the application of Corvis pressure reduced substantially with the addition of all EOMs, particularly the oblique muscles. In addition, the degree of nasal rotation produced by the simulated procedure aligned with clinical data. Despite these improvements, most numerical set-ups showed minimal displacement in the first 9ms of the procedure. It was hypothesised that this displacement might be due to initial tension within the EOMs that stabilise the globe in its primary gaze. Therefore, an optimisation algorithm was developed to optimise those initial muscle actions and monitor changes to force magnitudes to produce WEM with a better agreement with corresponding clinical data; a more detailed description is outlined in subsection 3.3.5. The application of optimised muscle forces during the Corvis procedure resulted in the numerical average WEM presented in Figure 4.14. Compared to the clinical dataset, numerical displacement produced RMSE values of 0.013, 0.009 and 0.019mm for average, nasal and temporal WEM, respectively. In addition, there was a better agreement with clinical WEM in the first 8ms of the procedure. Abaqus CAE allows users to control the force during specified times through an amplitude file. For this instance, the amplitude of forces starts the procedure with 100% of all EOMs' initial forces. However, the optimisation process produced an amplitude that indicates the type of exponential decay of the initial tension within the EOMs. Table 4.1, shows the change of force amplitude and the corresponding forces applied on each EOM.

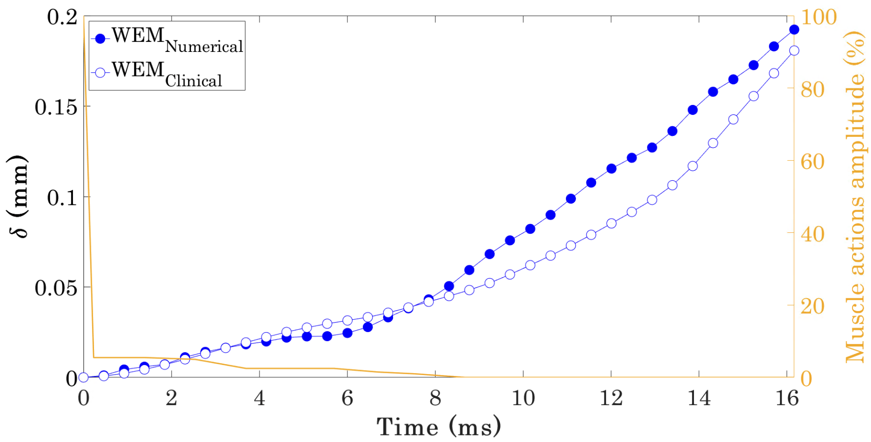

Figure 4.14: Average WEM resulting from the application of optimised muscle forces during Corvis procedure

Table 4.1: Optimised amplitude produced by force distribution optimisation algorithm

Time (ms)	Amplitude (%)	Force (mN)					
		MR	LR	SR	IR	SO	IO
0	100	89.2	48.8	50.6	46.5	15.6	17.1
0.231	5.5	4.91	2.68	2.78	2.56	0.86	0.94
1.386	5.5	4.91	2.68	2.78	2.56	0.86	0.94
2.541	5	4.46	2.44	2.53	2.33	0.78	0.86
3.696	2.5	2.23	1.22	1.27	1.16	0.39	0.43
4.541	2.5	2.23	1.22	1.27	1.16	0.39	0.43
5.696	2.5	2.23	1.22	1.27	1.16	0.39	0.43
6.696	1.5	1.34	0.73	0.76	0.70	0.23	0.26
7.541	1	0.89	0.49	0.51	0.47	0.16	0.17
8.696	0	0	0	0	0	0	0

4.4.3.1 Application of Optimised Force onto Clinical Data

Optimised muscle actions were then applied to age and gender-specific numerical models. Numerical displacements were compared to clinical data of corresponding age groups and gender using the RMSE method.

Male Subjects

In this part of the analysis, the optimised amplitude of muscle forces was applied to three age groups of male subjects. Age- and gender-specified numerical models were developed, where orbital geometry (volume, orbital rim aperture and exophthalmometry) was adjusted. In Figure 4.15, clinical evaluation of simulated nasal and temporal WEM of young, middle-aged and elderly subjects. Numerical simulation of Corvis resulted in an overestimated average WEM in young subjects, while there was better agreement in average WEM produced by the elderly and middle-aged subjects' numerical model. In Figure4.15(a), numerical comparisons to clinical data have produced RMSE values of 0.007mm and 0.026mm for nasal and temporal WEM, respectively; clinical data showed greater rotation than the numerical estimate. In Figure4.15(b), numerical models of middle-aged subjects produced WEM with slightly better agreement on the nasal side (RMSE = 0.006mm), while temporal WEM had better agreement with clinical data than in young subjects. Lastly, Figure4.15(c) presents a WEM numerical-clinical comparison in elderly subjects, where numerical agreement slightly decreased in this age group; RMSE values were 0.011mm and 0.018mm for nasal and temporal WEM, respectively.

Female Subjects

The optimised amplitude of muscle forces was also applied to three age groups of female subjects. Age- and gender-specified numerical models were developed in a similar manner to the male subject models. Generally, female subjects' clinical data had a greater degree of rotation than the males' clinical data. While average WEM and the direction of rotation were aligned in the numerical models and the clinical data, the magnitude of rotation was more significant in the clinical data. In young subjects (Figure4.16(a)), a comparison of the numerical model to clinical data produced RMSE values of 0.011mm and 0.016mm for nasal and temporal WEM, respectively. The agreement of numerical-clinical WEM was similar in the middle-aged versus young subject groups, with the former producing RMSE values of 0.011mm and 0.018mm for nasal and temporal WEM, respectively. Finally, in the elderly subjects, average WEM was aligned with its clinical counterpart; however, the clinical data suggested excessive rotation in elderly subjects. This excessive rotation was not estimated numerically. Numerical-clinical comparison in this subgroup produced RMSE values of 0.017mm and 0.019mm for nasal and temporal WEM, respectively.

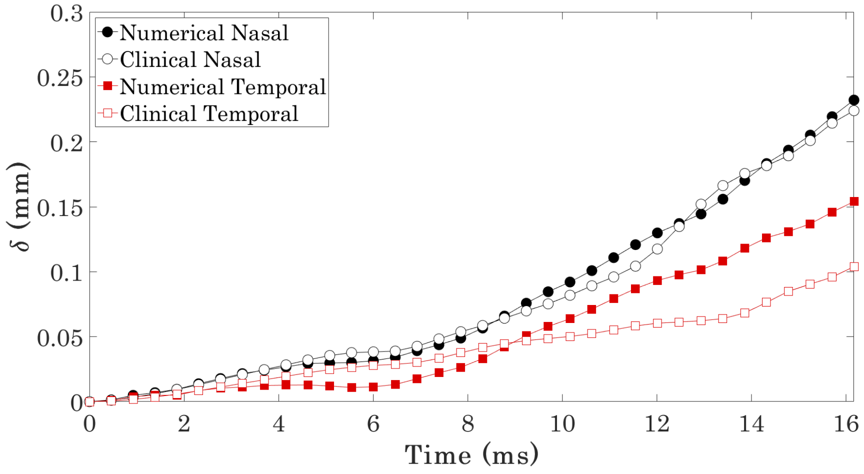

(a)

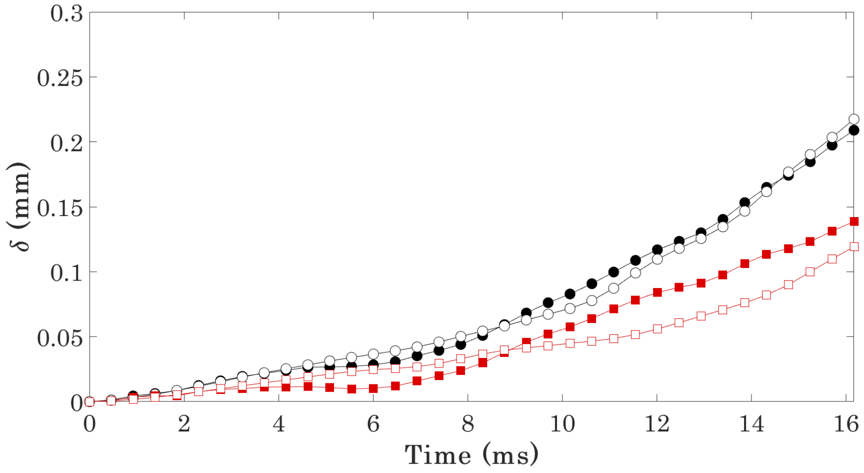

(b)

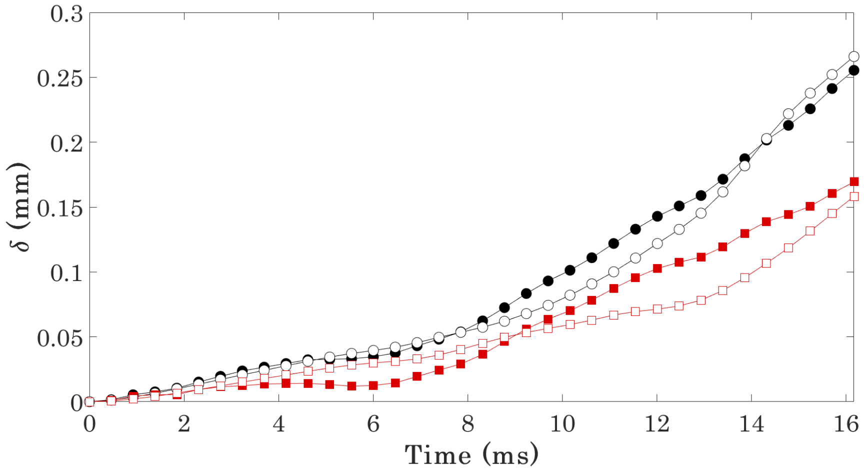

(c)

Figure 4.15: Male clinical comparison of numerical WEM resulting from Corvis air-puff and muscle forces. a)Young. b)Middle-aged. c)Elderly

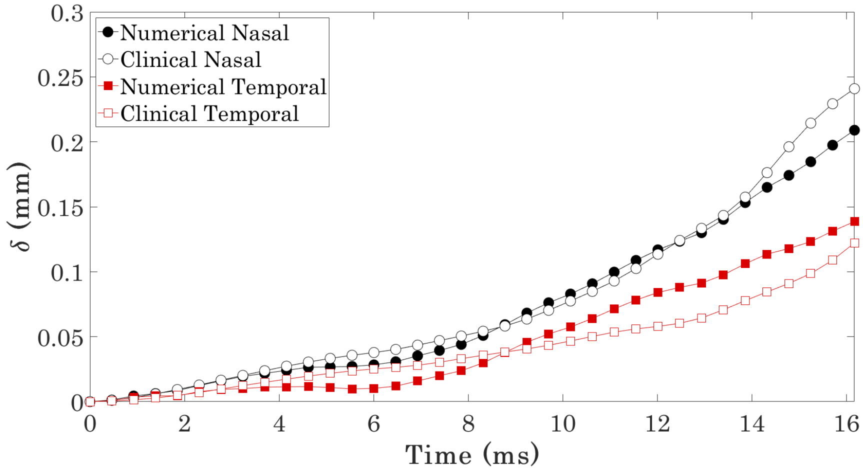

(a)

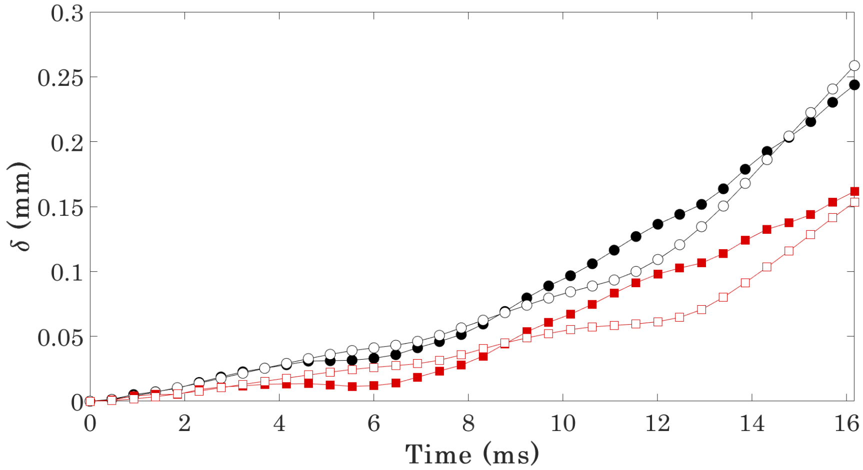

(b)

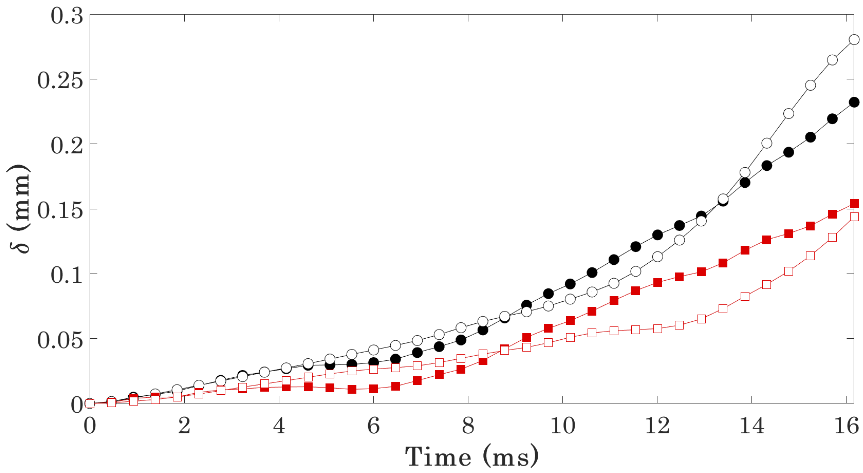

(c)

Figure 4.16: Female clinical comparison of numerical WEM resulting from Corvis air-puff and muscle forces. a)Young. b)Middle-aged. c)Elderly

4.5 Equations

This section will outline the results of the parametric study described in section 3.4. It will start by presenting the equation used to determine biomechanically corrected IOP (bIOP_o); this will then be evaluated against an experimental reading of true IOP and applied to healthy clinical datasets. In addition, the bIOP_o equation will be applied to glaucoma patients to evaluate its performance. Subsequently, another equation will be presented that evaluates the Stress-Strain Index (SSI_o) considering the newly developed bIOP_o. The correlation of SSI_o with IOP, CCT and age; will be compared to correlations of previously developed SSI. Finally, the SSI_o equation will be applied to various datasets of different ethnicities to evaluate its performance.

4.5.1 Biomechanically Corrected IOP (bIOP_o)

This subsection will present detailed results regarding bIOP_o. It will start with showcasing the equation and Corvis parameters used. After that, the experimental validation results will be presented, in which bIOP_o will be compared to bIOP and true IOP. Next, the bIOP_o equation will be applied to 7 healthy clinical datasets, where correlation with age and CCT will be evaluated. Last, bIOP_o will be compared to other IOP readings from various tonometer devices such as IOP_{GAT} produced by the Goldmann Applanation Tonometer (GAT), and IOP_g and IOP_{cc} produced by Ocular Response Analyser (ORA).

4.5.1.1 bIOP_o Equation

Relying purely on DCR parameters obtained through Corvis, the bIOP_o equation was produced for healthy eyes. In this context, "healthy eyes" refers to standard corneal and orbital geometries with no deformities due to disease. For evaluation purposes, the equation will be applied to various datasets, including Hypertension Glaucoma (HTG) and Ocular Hypertension (OHT) patients. Presented in Equation 4.7 are parameters which have estimated IOP while compensating for geometrical and biomechanical variation, hence their selection for the bIOP_o equation.

$$bIOP_o = f(CCT, Age, HCT, PD, DefAmpMaxA1V, AP1, HCR) \tag{4.7}$$

Where CCT is the central corneal thickness (μm), HCT is the time at which highest concavity occurs (ms), PD is the peak distance at highest concavity, DeflAmp1 is deflection amplitude at applanation one (mm), DefAmpMax is maximum deflection amplitude (mm).

4.5.1.2 Experimental Validation

The next part of this study was to evaluate the performance of the newly developed IOP algorithm. This evaluation was attempted by comparing the produced bIOP_o measurements with true experimental IOP measurements (IOP_t) obtained in a controlled environment. This experimental work was conducted as a part of a previous study to compare how IOP_{CVS} differed from IOP_t.[200] In Table 4.2, different samples with a wide range of CCTs were utilised to estimate IOP values obtained through different measurements, which were then compared to IOP_t. The results presented in Table 4.2 show that in samples where CCT exceeds 1000 microns, IOP_{CVS} and bIOP have considerably overestimated IOP, producing mean errors of 117.1±70.6% and 509.1±187.2%, respectively. On the other hand, for the same sample, bIOP_o underestimated all IOP readings except for the ten mmHg reading. These readings resulted in a mean error of -14.4±13.8% for samples of this particular CCT. The overall mean prediction error with IOP_t was 58.0±53.7%, 58.0±227.3.0% and -18.4±26.5% for IOP_{CVS}, bIOP and bIOP_o, respectively. All IOP readings were statistically different to IOP_t.

Table 4.2: Correlation of IOP measurements (mmHg) with CCT (μm) and age (years); to compare various tonometer devices to bIOP and bIOP_o

Sample	Age	CCT	True IOP	IOP_{CVS}	Error	bIOP	Error	bIOP_o	Error
		461±12.2	10	14.5±0.4	45.0	16.1±0.1	61.0	5.5±4.2	-44.5
		481.5±2.5	15	18.5±0.50	23.3	19.6±0.30	30.7	10.1±3.49	-32.5
1	67	490±1.4	20	23.5±0.00	17.5	24.4±0.09	21.8	16.9±0.92	-15.7
		495.3±1.1	25	28.0±0.35	12.0	29.0±0.52	15.8	22.3±3.12	-10.8
		485.4±5.6	30	31.9±0.92	6.3	33.5±0.88	11.8	29.8±3.03	-0.6
		518.2±6.1	10	15.5	54.7	15.5	54.5	4.2	-57.7
		531.4±27.0	15	21.0±0.4	40.0	21.0±0.5	40.2	7.3±0.3	-51.2
2	63	544.8±4.9	20	23.1±5.5	15.4	23.0±5.4	15.1	13.0±5.9	-34.9
		571.7±1.9	25	27.8±4.7	11.0	28.0±4.8	11.9	19.5±10.4	-21.9
		583.3±7.5	30	30.5±6.2	1.7	30.6±6.3	1.9	27.5±10.1	-8.4
		620.3±1.7	15	30.5±0.4	103.3	25.9±0.2	72.4	5.7±5.8	-62.2
3	67	623.4±13.2	20	32.8±4.2	64.0	27.9±3.9	39.4	18.3±3.8	-8.4
		622.3±2.1	25	41.3±0.5	65.3	35.8±0.5	43.3	29.9±3.1	19.5
		624.7±2.4	30	47.3±0.2	57.8	41.3±0.3	37.6	45.3±0.9	51.0
		1028±5	10	32.5	225.0	89.1	791.0	10.1	0.6
		1125.6±9.4	15	37.0±2.00	146.7	104.4±6.55	595.7	9.6±3.15	-36.3
4	67	1177.2±4.7	20	39.5±2.00	97.5	111.3±6.40	456.5	16.6±4.54	-16.9
		1184.4±2.2	25	41.0±0.00	64.0	116.4±0.10	365.6	22.7±6.92	-9.2
		1195.1±7.9	30	45.6±1.08	52.1	131.0±3.49	336.5	27.0±3.37	-10.0

4.5.1.3 Healthy Participants

Healthy dataset 1 contains 329 subjects with a mean CCT of 545 ± 34 $(459 - 681)$ μm and age of 36.9 ± 16.4 $(7.0 - 85.0)$ years. The acquired mean IOP values for bIOP_o, bIOP and IOP_{CVS} were 15.1 ± 1.7 $(10.4 - 25.7)$ mmHg, 14.3 ± 2.0 (7.8 -21.7) mmHg and 15.5 ± 2.2 $(10.5 - 24.5)$ mmHg, respectively. IOP_{CVS} showed the least correlation with age (R:-0.007, p:0.896), and the greatest correlation with CCT (R:0.391, p:0.000). CCT had a stronger correlation with bIOP_o (R:0.057, p:0.403) than with bIOP (R:-

0.035, p:0.531. Age, however, had a stronger correlation with bIOP (R:-0.265, p:0.000) than with bIOP$_o$ (R:-0.131, p:0.248), see Figure 4.17.

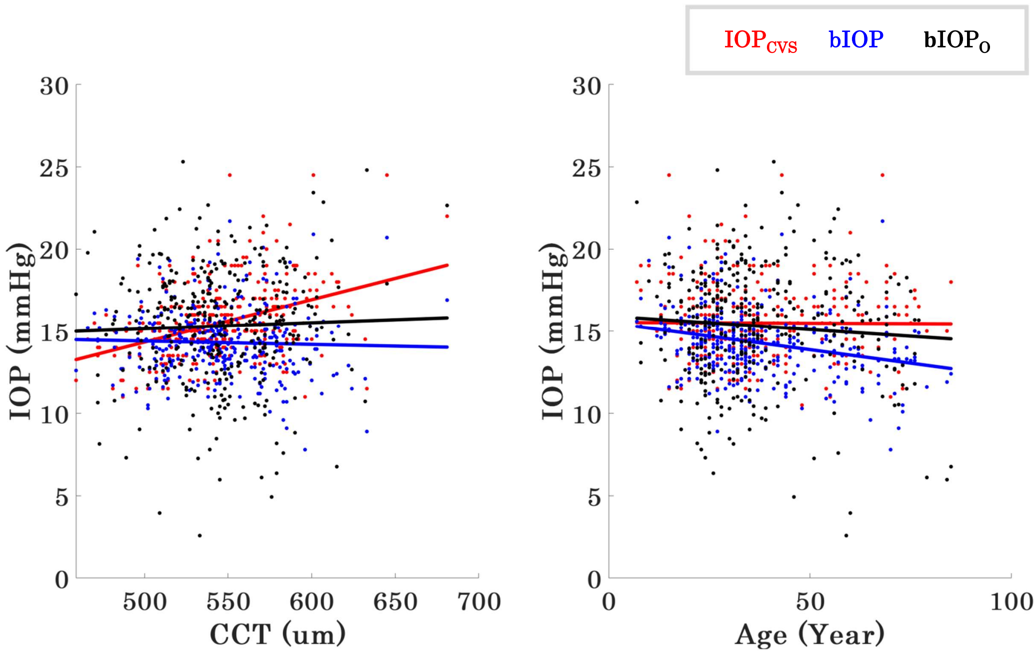

Figure 4.17: Relationship of IOP estimations with age (*right*) and CCT (*left*)

4.5.1.4 Comparison between GAT, DCT, ORA and Corvis ST

This healthy dataset contains 422 subjects with a mean CCT of 543 ± 28 $(474 - 630)$ μm and age of 27.1 ± 5.5 $(17.0 - 42.0)$ years, respectively. The obtained IOP values were 14 ± 1.9 $(8.8 - 20.8)$ mmHg for IOP$_{CVS}$, 13 ± 2.2 $(6.5 - 18.5)$ mmHg for IOP$_{GAT}$, 17.2 ± 2.7 $(10.3 - 28.1)$ mmHg for IOP$_{DCT}$, 14.72.7 $(7.3 - 23.3)$ mmHg for IOP$_{ORA_g}$, 15.4 ± 3.5 $(8.5 - 66.5)$ mmHg for IOP$_{ORA_{cc}}$, 13.7 ± 1.7 $(9.4 - 19.1)$ mmHg for bIOP and 15.1 ± 1.8 $(12.2 - 19.3)$ mmHg for bIOP$_o$. Correlations of each of the IOP measurements with CCT and age are listed in Table 4.3 and depicted in Figure 4.18. The results show that bIOP was least influenced by CCT, while bIOP$_o$ was least influenced by age.

Table 4.3: Correlation of IOP measurements (mmHg) with CCT (μm) and age (years); to compare various tonometer devices to bIOP and bIOP$_o$

IOP measurement	CCT		Age	
	p	R	p	R
IOP_{CVS}	< 0.01	0.401	< 0.01	-0.143
IOP_{GAT}	< 0.01	0.264	< 0.01	-0.120
IOP_{DCT}	< 0.01	0.274	0.012	-0.124
IOP_{ORA_g}	< 0.01	0.452	< 0.01	-0.151
$IOP_{ORA_{cc}}$	< 0.01	0.189	< 0.01	-0.152
bIOP	0.726	0.017	< 0.01	-0.138
bIOP$_o$	0.09	-0.083	0.472	-0.041

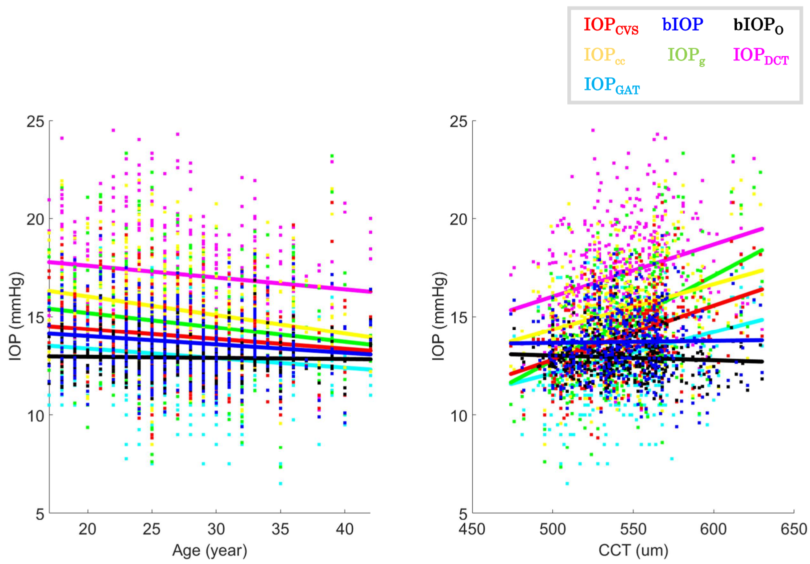

Figure 4.18: Correlations with CCT (*left*) and age (*right*) of various IOP measurements

Summary

A correlation analysis was conducted to evaluate and compare seven IOP measurements acquired from 422 healthy subjects using various tonometer devices. The devices used were Corvis ST, GAT, DCT and ORA. Three IOP measurements were acquired from

Corvis (IOP_{CVS}, bIOP, $bIOP_o$); two from ORA (IOP_{ORA_g} and $IOP_{ORA_{cc}}$), and the remaining two from DCT and GAT. Generally, Corvis IOP measurements were the least correlated with CCT and age. Nonetheless, a significant correlation showed that both parameters influenced IOP_{CVS}. Furthermore, there was an insignificant correlation between $bIOP_o$ and age or CCT, while bIOP was influenced by age. This correlation indicates the efficiency of $bIOP_o$ in estimating an IOP that is minimally influenced by geometrical variations or corneal biomechanics.

4.5.1.5 Glaucoma Patients

This dataset included two groups of patients, Ocular Hypertension (OHT) and Hypertension Glaucoma (HTG) patients. The first group included 122 OHT patients with a mean CCT and age of 552 ± 37 $(476 - 640)$ μm and 65.1 ± 11.2 $(34.0 - 86.0)$ years, respectively. The acquired mean IOP values for $bIOP_o$, bIOP and IOP_{CVS} were 17.2±1.7 (4.8−26.2) mmHg, 16.9±2.0 (8.9-29.1) mmHg and 19.0±4.0 (11.5−30.5) mmHg, respectively. CCT was not correlated with IOP_{CVS} (R:0.069, p:0.447) and $bIOP_o$ (R:0.072, p:0.422), while significant correlation was evident with bIOP (R:-0.243, p:0.007). On the other hand, only $bIOP_o$ was significantly correlated to age (R:-0.253, p:0.003), while IOP_{CVS} (R:-0.010, p:0.912) and bIOP (R:-0.010, p:0.912) were not, see Figure 4.19.

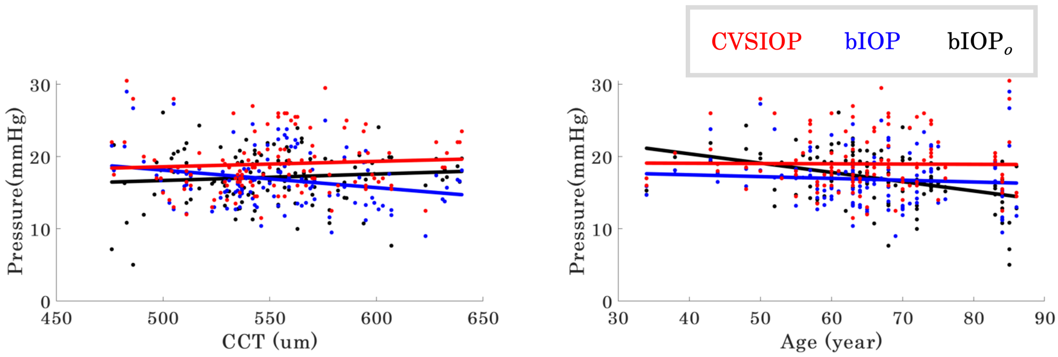

Figure 4.19: Correlation of CCT (*left*) and age (*right*) with $bIOP_o$ in Ocular Hypertension subject group

The second group included 111 HTG patients with a mean CCT and age of 523 ± 37 $(451 - 597)$ μm and 72.3 ± 9.7 $(38.0 - 91.0)$ years, respectively. The acquired mean IOP values for $bIOP_o$, bIOP and IOP_{CVS} were 16.8 ± 4.7 $(4.8 - 27.3)$ mmHg, $14.6 \pm$

3.3 (9.8-26.4) mmHg and 15.7 ± 4.0 $(10.0 - 31.5)$ mmHg, respectively. CCT was not correlated to $bIOP_o$ (R:0.093, p:0.276) and bIOP (R:0.243, p:0.112), while there was a clear significant correlation with IOP_{CVS} (R:0.331, p:0.000). On the other hand, there was insignificant correlation of age with IOP_{CVS} (R:-0.037, p:0.702) and bIOP (R:-0.058, p:0.543), while $bIOP_o$ was influenced by age (R:-0.431, p:0.000), see Figure 4.20.

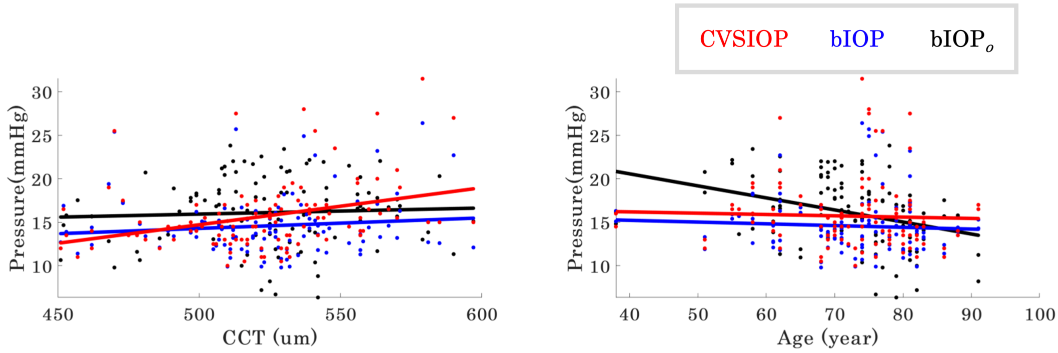

Figure 4.20: Correlation of CCT (*left*) and age (*right*) with $bIOP_o$ in Hypertension Glaucoma subject group

Summary

In the OHT subgroup, the acquired mean IOP values for $bIOP_o$, bIOP and IOP_{CVS} were 17.2 ± 1.7 $(4.8 - 26.2)$ mmHg, 16.9 ± 2.0 (8.9-29.1) mmHg and 19.0 ± 4.0 $(11.5 - 30.5)$ mmHg, respectively. This indicates that the lowest produced IOP measurement was bIOP, while the largest was IOP_{CVS}. On the other hand, in the second group, HTG patients produced mean IOP values for $bIOP_o$, bIOP and IOP_{CVS} were 16.8 ± 4.7 $(4.8 - 27.3)$ mmHg, 14.6 ± 3.3 (9.8-26.4) mmHg and 15.7 ± 4.0 $(10.0 - 31.5)$ mmHg, respectively. In the HTG group, the trend was different, with bIOP producing the lowest measurement and $bIOP_o$ the largest.

4.5.2 Stress-Strain Index (SSI_o)

In this section, results regarding SSI_o will be presented. First, optimised equations and parameters included will be outlined. The equation will be evaluated using experimental data on corneal material stiffness and the previously developed SSI. Finally, the performance of SSI_o will be evaluated by applying it to the various clinical datasets.

4.5.2.1 SSI$_o$ Equation

An SSI$_o$ equation was developed using a similar approach to that used for selecting DCR parameters in the bIOP$_o$ equation. SSI$_o$ intends to improve the correlation with age while reducing its correlation with CCT and IOP. The equation will be applied to clinical datasets of healthy corneas, where correlations of SSI$_o$ will be compared to the previously developed SSI. The IOP used in this section was computed through the previously developed bIOP$_o$ equation, as it offered a more accurate IOP, which compensated for corneal biomechanics. Presented in Equation 4.8 below are the parameters implemented within the function.

$$\begin{aligned} SSI_o = f(bIOP_o, CCT, Age, HCT, PD, DefAmpMax, A1V \\ AP1, HCR) \end{aligned} \tag{4.8}$$

Where bIOP$_o$ is the newly developed biomechanically corrected IOP, CCT is the central corneal thickness (μm), HCT is the time at which the highest concavity occurs (ms), PD is the peak distance at the highest concavity, DeflAmp1 is deflection amplitude at applanation one (mm), DefAmpMax is maximum deflection amplitude (mm).

4.5.2.2 Experimental Validation

An earlier study[160] conducted *ex-vivo* work on human donor corneas by applying inflation through the eye globe's posterior region. The study results were available in this thesis as a form of validation for the newly developed SSI$_o$, allowing a comparison of SSI$_o$ versus SSI performance. This comparison demonstrated that SSI$_o$ had a stronger correlation with age than SSI, yet a weaker correlation than ex-vivo SSI. The relationship trend between "*ex-vivo* SSI and age" and "SSI and age" were very similar in most of the datasets, while "SSI$_o$ and age" had a steeper trend in general, as seen in Figure 4.21. Further details on correlation and significance of data are presented in Table 4.4, as well as mean and standard deviations of differences between "ex-vivo SSI and SSI" and "ex-vivo SSI and SSI_o". In subsequent sections, more information about the correlations of SSI_o with age, $bIOP_o$ and CCT for the seven datasets.

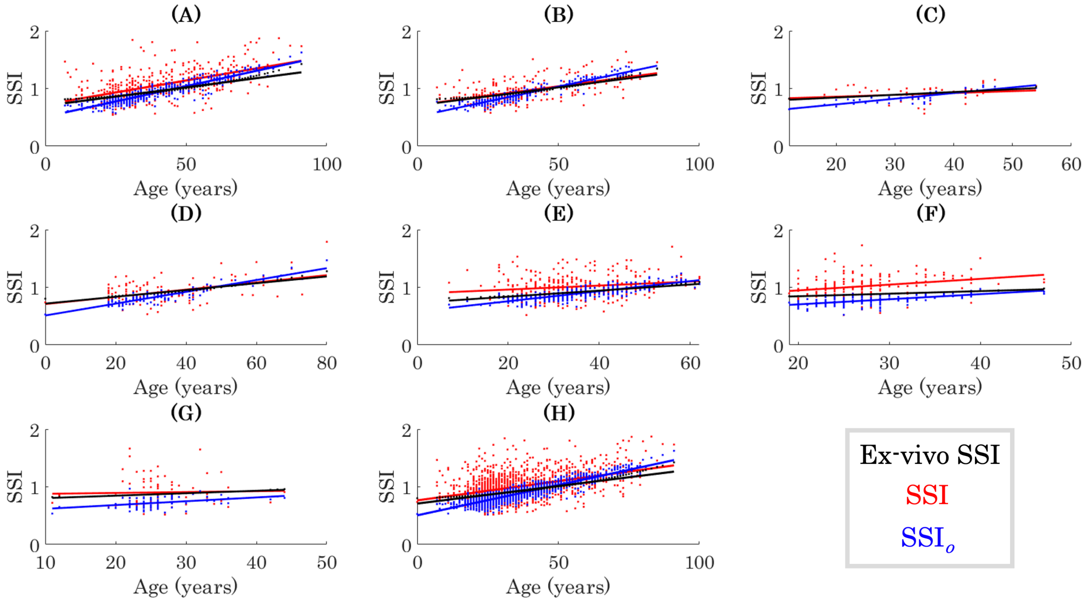

Figure 4.21: Results of comparison between SSI, SSI_o and *ex-vivo* SSI values −obtained from human corneas− against age in 7 different datasets (A-G) and all of them combined (H)

Table 4.4: Correlation of SSI, SSI_o and *ex-vivo* SSI values with age, and mean and standard deviation of differences between SSI and SSI_o, and *ex-vivo* SSI values

Dataset	SSI		SSI_o		Ex-vivo SSI		Ex-vivo vs SSI	Ex-vivo vs SSI_o
	R	p	R	p	R	p	Mean±SD	Mean±SD
A	0.540	<0.01	0.924	<0.01	0.970	<0.01	0.24±0.22 (p<0.01)	0.10±0.10 (p<0.01)
B	0.549	<0.01	0.944	<0.01	0.981	<0.01	0.16±0.16 (p:0.105)	0.10±0.09 (p<0.01)
C	0.209	<0.01	0.847	<0.01	0.990	<0.01	0.13±0.13 (p:0.702)	0.08±0.07 (p<0.01)
D	0.466	<0.01	0.926	<0.01	0.978	<0.01	0.16±0.16 (p:0.740)	0.10±0.08 (p<0.01)
E	0.174	<0.01	0.795	<0.01	0.989	<0.01	0.21±0.19 (p<0.01)	0.08±0.07 (p<0.01)
F	0.266	<0.01	0.637	<0.01	0.995	<0.01	0.24±0.19 (p<0.01)	0.13±0.06 (p<0.01)
G	0.035	<0.01	0.401	<0.01	0.991	<0.01	0.25±0.25 (p:0.278)	0.17±0.09 (p<0.01)
H	0.419	0	0.905	0	0.980	0	0.21±0.20 (p<0.01)	0.10±0.09 (p<0.01)

4.5.2.3 Healthy Participants

Healthy dataset "A" contains 329 subjects with a mean CCT of 545 ± 34 $(459 - 681)$ μm, age of 36.9 ± 16.4 $(7.0 - 85.0)$ years, bIOP of 14.3 ± 2.0 (7.8 -21.7) mmHg, bIOP$_o$ of 15.1 ± 1.7 $(10.4 - 25.7)$, SSI of 1.01 ± 0.20 (0.52-1.71) and SSI$_o$ of 0.96 ± 0.32 (0.43-1.61). Regarding CCT, SSI showed a significant correlation (p:0.009, R:0.145), while SSI$_o$ correlation (p:0.766, R:-0.018) was not shown. In correlation with bIOP$_o$, both SSI and SSI$_o$ had significant but opposite correlations, where SSI was positively correlated with bIOP$_o$ (p:0.000, R:0.387), while SSI$_o$ was negatively correlated with bIOP$_o$ (p:0.000, R:-0.336). Furthermore, SSI and SSI$_o$ have shown significant correlations with age, with SSI$_o$ showing a stronger correlation (p:0.000, R:0.721) than SSI (p:0.002, R:0.174).

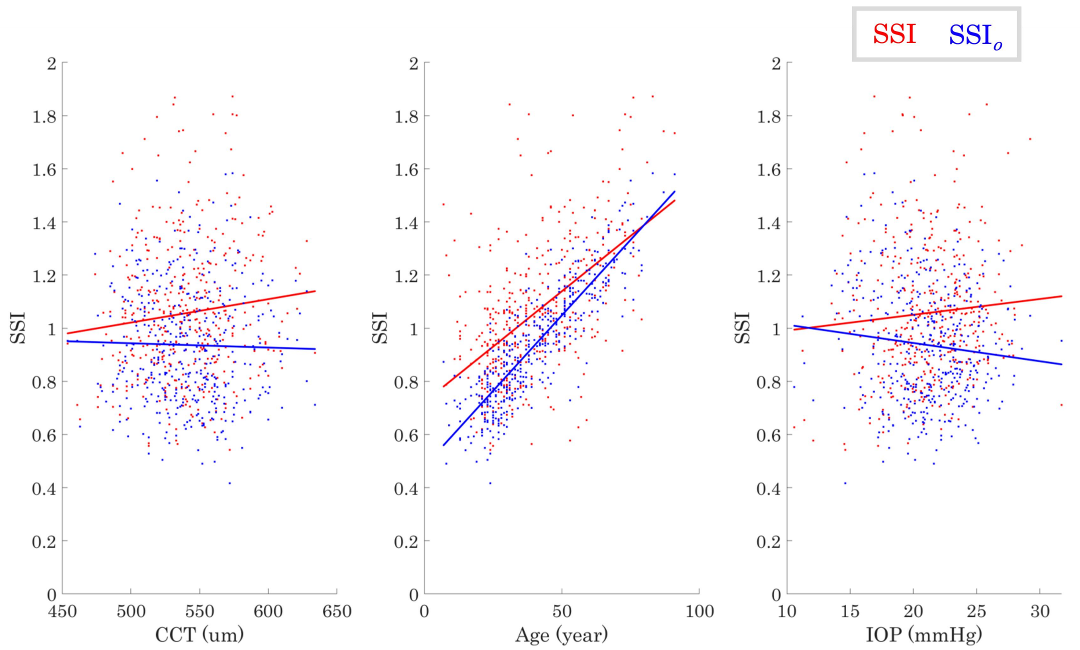

Figure 4.22: Correlations of SSI and SSI$_o$ with CCT (*left*), age (*middle*) and bIOP$_o$ (*right*) in Dataset "A"

4.6 Concluding Remarks

This chapter outlines the results of various processes showing development, optimisation, validation and an example application of the numerical model. The chapter has shown the orbital geometry extracted for all three female Chinese subjects. The numerical model was then utilised in conducting a mesh density study to prove that the numerical model would converge most of the time. Consequently, a material optimisation was carried out to assess the mechanical stiffness of the OST as a whole. The results from this optimisation were compared to previous experimental work on the AFT, proving the effectiveness of the EOMs and other connective tissues in supporting the eye globe. A study was carried out to gradually add EOMs to the numerical set-up, hence showing their effect on WEM and WER. Lastly, in further validation efforts, an in-house algorithm was developed to carry out EOM force distribution optimisation to estimate the change in EOM initial tension. Subsequently, the validated model was used in a parametric study, with the end goal of producing two equations predicting bIOP_o and SSI_o. The predicted bIOP_o was compared to true IOP, which was acquired experimentally in a previous study. This prediction was one of the factors used to evaluate the performance of the equation. The optimum bIOP_o equation was applied to various clinical datasets from various clinics around the world, where correlations with age and CCT were assessed. Predicted values of bIOP_o were used within the development of the SSI_o equation. Finally, the optimum equation was chosen based on assessing correlations with IOP, age and CCT.

Chapter 5

Discussion

5.1 Material Optimisation

In this study, 185 numerical models were built while considering corneal tomography in each eye as measured by the Pentacam. The models also included an idealised geometry of the sclera and OST. They were analysed to simulate the performance under intraocular pressure (IOP) and air pressure experienced in Corvis tests. The models then used the corneal deformation profiles recorded by the Corvis under air pressure in an inverse analysis exercise to estimate the material behaviour of the OST. Each subject's model was run 15 times within the inverse analysis with varying material stiffness. Material stiffness producing the most optimum deformation to its corresponding clinical data was saved for this subject along with its age and IOP, ready for further age-related analysis.

Results of the inverse analysis enabled estimation of OST's tangent modulus (E_t) for each of the 185 eyes included in this study. The results indicated a weak correlation of E_t with the progression of age, regardless of the stress at which E_t was calculated. However, there was evidence of significant differences in E_t between some of the age groups. There was statistical evidence of significant differences between E_t in the age range $20 < years < 43$ relative to E_t in OST with age ranges $43 < years < 63$ (p=0.022) and $63 < years < 91$ (p=0.011). In contrast, E_t in OST with age ranges $43 < years < 63$ and $63 < years < 91$ were not significantly different (p= 0.863).

Despite efforts to create age-specific numerical models of the eye globe and OST, where some geometrical (and other age-related) variables changed, material optimisation produced 1.6±1kPa as the mean optimum material stiffness for OST. Prior studies[88,229] have developed a micro-mechanical model for the soft biological tissue. This proposed model suggested material stiffness of AFT being 0.4kPa, which is significantly low (4 times softer) compared to the optimised material stiffness estimated in the current study. Hwang et.al[39] stated that EOMs play a significant role in supporting the eye globe. Nevertheless, the discrepancy between the experimental stiffness of AFT[88] and the optimised stiffness of the current has indirectly quantified the support provided to the eye globe through EOMs and other connective tissues such as Lockwood's ligament. This quantification of mechanical stiffness confirms Hwang's findings[39] and provides a comparative scenario of how various OSTs collectively support the globe against an exterior form of frontal loading.

In another study, Jannesari et al.[15] attempted to estimate biomechanical properties of AFT using a very similar methodology to the current study; by employing an inverse analysis optimisation along with Corvis corneal deformation. However, their numerical set-up involved an idealised two-dimensional axisymmetric geometry of the cornea, while a viscoelastic boundary condition was applied at the limbal conjecture. This study and previous work[39,88,140–142] experimental and numerical findings were produced suggesting that the AFT is not the only form of support provided to the globe. The assumption of an axisymmetric geometry may be suitable for the cornea; however, Corvis corneal deformations show a very prominent occurrence of nasal rotation during retraction of the eye globe.[143] This nasal rotation drove the need to employ a three-dimensional geometrical set-up in this study, which implements irregularity and asymmetry of the orbital boundary. The orbital soft tissue has been the subject of several anatomical studies focusing on its structure.[137,139] These studies report that most common eye movements involve sliding within the Tenon's capsule of the OST. Indeed, Shoemaker et.al[111] have attempted to estimate viscoelastic material properties by assessing the degree of deformation of AFT in eye globe rotation. In this study, a hyper-elastic material model was used to save computational time due to the Corvis pressure loading scenario's simulation. This study differed from Shoemaker's work in the loading conditions, where frontal loading was applied instead of the application of rotations onto the globe. The current study attempted to validate the hyper-elastic material model of OST using Corvis clinical corneal deformations, as suggested by Hwang.[39]

In conclusion, this study utilised inverse finite element analysis with clinical measurements of the WEM under Corvis air pressure to estimate the OST's stiffness and how this changes with age. The OST E_t has shown a weak correlation with age progression at the three different stress levels while showing significant differences between some age groups. With this information, numerical modelling of the eye globe, especially those simulating WEM, can now include models of the OST rather than introducing non-physiologic boundary conditions simulating its effect.[15,215] Nevertheless, despite consideration of the orbital geometry's irregularity, numerical simulations did not accurately represent the nasal rotation aspect of clinical retraction of the eye globe. The authors of this study suggest that this rotation may be due to deeper orbital structures, such as EOMs, Lockwood's ligament or other connective tissues.[137,141] Thus, it is highly recommended to investigate the rotational response of the globe further, as this will have a considerable effect on future work regarding the simulation of impacts or exterior loading applied to the globe or even the orbital structure as a whole.

The study quantified the amount of support provided to the eye globe by the OST other than the AFT and stated that the nasal rotation occurring during Corvis was not due to irregularity of the orbital geometry. Therefore, the next stage of this project was to further develop the numerical set-up of the OST by including the six EOMs and then assessing their effect on the ocular support system.

5.2 EOM's Role in the Ocular Support System

The initial set-up of the ocular support system involved all extra-ocular orbital tissues being modelled as one entity without involving any of the EOMs structurally. Previous studies[144,145] have similarly used numerical models. These studies, as mentioned above, utilised their numerical models in applying blunt impact trauma onto the globe, hence, simulating retinal damage amongst effects on other intra-ocular components.[145] The presented results in subsection 4.4.1 have proven with clinical comparisons that the current OST numerical set-up did not respond to Corvis pressure realistically, as clinical nasal rotation was not visible numerically. A previous study has confirmed with statistical analysis the occurrence of this rotation as a response to Corvis pressure.[143] This discrepancy demonstrates that the current OST model requires further development to allow for a more natural response to frontal loading applied onto the globe. Achieving this realistic response of the ocular system will be of great use in future work regarding impact loading onto the eye globe.

First, the material stiffness of the orbital elements was set to the experimentally determined stiffness (0.4kPa) suggested by a previous study.[88] As was previously stated in Figure 4.12, the numerical set-up that did not include EOMs had the second highest WEM, which was expected based on data in the literature.[39] This overestimation in numerical WEM was more than double of its clinical counterpart. Furthermore, the model's outcome did not align with clinical data, producing negligible temporal rotation. Adding the rectus muscles to the set-up reduced WEM to some degree and was still over double the clinical WEM. This reduction conveyed that little effect was seen on WEM even with the application of Demer's EOM pulley theory[230] onto rectus muscles.

The considerable reduction in WEM and correction of nasal rotation has communicated the immense structural effect of the oblique muscles on the ocular support system regarding posterior−anterior displacement, as well as nasal−temporal rotation of the globe. On the other hand, adding the oblique muscles resulted in a significant drop in the average WEM. In addition, this final modification corrected the eye globe's resultant rotation during the Corvis pressure simulation. Eventually, the final set-up excluded the orbital boundary to evaluate how EOMs would support the globe by themselves. This set-up resulted in the highest WEM; however, due to the presence of the oblique muscles, the numerical model still produced the nasal rotation.

This study has outlined several aspects of the ocular support system. First, the use of pulleys as functional origins of the corresponding rectus muscles did not show significant decreases in WEM. The model showed a slight increase in lateral rotation as a response to Corvis pressure. Contrarily, the addition of the boundary conditions indicated that the oblique muscles play the most significant role in supporting the eye globe in response to posterior−anterior displacement and nasal−temporal rotation. Henceforth, applying this modification to numerical models involving displacement of the globe as a whole is highly recommended. Another highlighted aspect was the excessive WEM that occurred with the exclusion of the orbital boundary. This set-up revealed the importance of having a numerical set-up combining orbital boundary with EOMs' functional geometry when simulating the ocular support system.

Vroon et.al[44] have developed an FEM of the globe, which suggests that head movements and saccades play a role in the progression of retinal detachment, with head movements having a larger effect on the condition. Further efforts[100,144] were carried out on retinal detachment, where an FEM of the globe and orbit was utilised to evaluate the effect of impact trauma on the globe and its intra-ocular components. The first of these previous works Incorporated the rectus muscles and an assumed rotational symmetry of the AFT surrounding the globe into the numerical model used;[144] the latter implemented the irregularity of the orbital boundary without including any of the EOMs.[100] Both of those studies did not include the oblique muscles, which, based on the findings of this study, play a major role within the globe's support system. Liu et.al[100] applied the impact of a BB gun pellet to their model, inducing pressure over 12×10^3kPa onto the globe, and the application of maximum Corvis pressure (13.33kPa) caused the globe to rotate about 1^o nasally. Therefore, realistically the BB impact should produce a much larger nasal rotation, which according to Vroon's[44] findings, this rotation would progress retinal detachment even further. The current study suggests using its numerical set-up to investigate further the effect of impact trauma on intra-ocular components and the progression of retinal detachment.

This study used gradual development of the ocular support system to indicate the cause of rotation noticed clinically.[143] Henceforth, it is recommended to apply EOMs boundary conditions onto the globe, especially those of the oblique muscles, given that they have the most significant effect on reducing WEM and producing nasal rotation. Thus, further development is needed for the final numerical set-up. Clinical data show obvious WEM in the first eight milliseconds of the Corvis procedure. This displacement was underestimated by the numerical model, even with the set-up that did not include EOMs, which produced more than double the maximum WEM. In a similar matter, Jannesari et.al[15] ran an optimisation analysis to evaluate optimum viscoelastic parameters. The optimum parameters produced numerical WEM in agreement with corresponding clinical data. However, as in the current study, displacement in the first eight milliseconds was underestimated too. Gao et.al[36] indicated through the development of a mathematical model that, for the eye globe to be in primary gaze equilibrium, all six EOMs must have initial tension. This tension led the authors to suggest that displacement may be due to the EOMs' initial tensions. Further work is recommended to investigate this matter. It is also worth mentioning that the check ligaments were not included in this set-up. This was decided due to a lack of information such as quantification of traction to the medial, inferior and lateral rectus muscles. It is suggested that the produced numerical WEM was slightly more than its clinical counterpart due to this exclusion which indirectly attaches the globe to the orbital wall.[141]

5.3 Biomechanically corrected IOP (bIOP$_o$)

Elevation of IOP significantly correlates with pathological eye conditions, such as glaucoma and ocular hypertension.[231] This correlation measures this variable as essential in the diagnosis and treatment of those conditions. As mentioned previously in chapter 2, glaucoma is one of the most common conditions in ophthalmology and one of the leading causes of blindness, only second to cataract. IOP is associated with glaucoma and is recognised to be the only modifiable risk factor.[58] Indeed, it was documented that risk of glaucoma increases by 11% for every one mmHg increase of IOP within the ocular vessel.[231] For that reason, the acquirement of accurate measurements for this pressure is essential to clinicians, especially those who diagnose glaucoma. Goldmann Applanation Tonometer is currently recognised as the gold standard for IOP measurement; a detailed description of the technique is captured in section 2.6.1.2.[180] To sum up, this technique assumes an infinitely thin-walled sphere for the eye globe at which GAT makes contact. Once in contact, the pressure is increased gradually until the surface applanates. This applanation pressure is assumed to be equal to the inner vessel pressure. This theory is only valid if the cornea is an infinitely thin-walled sphere. However, this is inaccurate due to corneal susceptibility to biomechanical variables such as thickness or curvature. Hence, significant correlations were present between corneal biomechanical variables and GAT IOP measurement.[232,233]

Due to the risk of inaccurate IOP measurements (i.e. potential misdiagnosis of glaucoma), many efforts have been made to estimate this modifiable factor accurately. Over the past decades, various tonometry devices have been developed to reduce measurement errors. Some of these devices rely on Goldmann's previously mentioned principle, such as Corvis ST and Ocular Response Analyser (ORA).[199,234] Others used a different concept, such as Dynamic Contour Tonometer (DCT); this is described in further detail in subsection 2.6.1.[187] This measurement principle of DCT was adopted to reduce the corneal biomechanical influence on the estimated IOP.

Nonetheless, the device was influenced by corneal geometrical aspects such as its curvature.[235,236] Non-contact tonometry has permitted the capture of detailed corneal deformation and has facilitated adjustments which enable further analysis of corneal response.[237, 238] ORA utilises a laser-based system to capture corneal deformation; however, this only captures corneal applanation. On the other hand, Corvis ST utilises a high-speed Scheimpflug camera to record corneal deformation at the horizontal meridian and includes deformation of anterior and posterior corneal surfaces. It has been previously documented that the most accurate IOP estimation was bIOP from Corvis, followed by DCT and, subsequently, corneal corrected IOP (IOP_{cc}) from ORA.[189, 216, 239]

Previous studies[199, 240] have used clinical datasets to evaluate the effectiveness of various IOP measurements. These studies have examined correlations of the estimated IOP against various corneal parameters, such as the subject's age or central corneal thickness (CCT). In addition, researchers[200] have conducted an ex-vivo study, which attempts to estimate the IOP of an eye globe attached to a transducer in a controlled environment. This study allowed for obtaining the most precise estimation of true IOP. However, the scale of these studies was very limited due to complications of the procedure, whether the high cost of donor eye globes or difficulty in obtaining them. Consequently, numerical models were utilised to conduct a parametric study for healthy corneas. Four parameters were used to develop bIOP: age, CCT, first applanation pressure (AP1) and Highest Concavity Radius (HCR). Previous work has reported improved performance in estimating IOP within healthy subjects using bIOP.[241] However, a further study reported a correlation with age, indicating the effect of changes in material stiffness.[242]

A recent study used the same four parameters in bIOP to develop a new IOP function (fIOP) for healthy subjects.[243] This study conducted numerical simulations with more complexity than this work, utilising a novel, numerical, multi-physics, fluid-structure interaction of the Corvis air-puff procedure. The numerical model was used in a parametric study, where geometrical (CCT and curvature), biomechanical (material stiffness) and loading (IOP) aspects varied. This model simulated Corvis pressure using turbulent computational fluid dynamics. The study's authors concluded that fIOP and bIOP have similar performance; implementation within Corvis was not assessed.

As with bIOP, the main goal of this study was to estimate IOP measurements which are not influenced by geometrical components or biomechanically; hence, a new biomechanically-corrected IOP ($bIOP_o$) was developed for healthy eye globes. IOP was introduced by utilising the fluid cavity to apply internal loading onto the FEM of the eye globe. The fluid cavity was in-compressible to maintain ocular globe volume throughout the analysis. As such, the indentation of the cornea through external loading would decrease volume and increase ocular pressure. The cornea and sclera expand to accommodate this pressure increase, ultimately increasing their surface tension.[244]

The OST numerical set-up was used in this parametric study to evaluate the performance when more realistic boundary conditions were used instead of an assumed one. Predictions of $bIOP_o$ were compared to IOP estimations of previous measurements (IOP_{CVS} and bIOP) and evaluated against IOP_t. It should be noted that IOP_t values were acquired from previous experimental work done by the Biomechanical Engineering Group at the University of Liverpool; multiple readings were acquired for each donor's eye, and so the data presented in this study may differ slightly from that presented in the published work.[200] A wide range of corneal thicknesses were employed to evaluate the performance of $bIOP_o$. In general, all IOP measurements showed better estimations with higher IOP. In addition, experimental validation indicated the poor performance of IOP_{CVS} and bIOP regarding IOP estimation of high thickness corneas, while $bIOP_o$ has shown much better performance. Furthermore, $bIOP_o$ has constantly underestimated true IOP measurement. Based on this, the overall mean prediction error with IOP_t was 58.0±53.7%, 58.0±227.3.0% and -18.4±26.5% for IOP_{CVS}, bIOP and $bIOP_o$, respectively. It should be noted that all IOP readings were statistically different to IOP_t.

5.4 Stress-Strain Index (SSI_o)

In the past decades, there has been progress in the field of ophthalmology with a vast interest in corneal biomechanics and its effect on IOP measurement, the outcome of surgeries, and the progression and management of diseases.[245,246] Several attempts have been made to quantify in-vivo corneal biomechanics, such as the Corneal Resistance Factor (CRF), Brillouin modulus, Integrated Inverted Radius (IntInvR) and Stiffness Parameter (SP) provided by Corvis ST, and Corneal Hysteresis provided by Ocular Response Analyser (ORA).[189,206,239,247] A more recent study utilised Dynamic Corneal Response (DCR) parameters acquired from Corvis to estimate corneal material stiffness in-vivo through the development of a Stress-Strain Index algorithm. This study sought to determine corneal stress-strain behaviour as a whole rather than a particular value of tangential modulus (E_t).[31] Due to the nonlinearity of corneal tissue behaviour, the latter point is of significance, with stress-strain behaviour, deformation behaviour and ultimately, E_t experiencing a gradual increase with the application of load.[248]

The cornea's resistance to deformation under internal (IOP) and external (eyelid and tonometric pressure) loading is represented by its overall stiffness. Two major components in this stiffness; are corneal geometrical stiffness and material stiffness. Geometrical stiffness of the cornea is mainly controlled by its central thickness (CCT); hence, correcting the IOP measurement was emphasised to compensate for CCT. In addition, corneal curvature and diameter contribute to the geometrical stiffness.[249] There were considerable challenges with quantifying material stiffness until recently due to difficulties estimating corneal stress-strain behaviour in-vivo. Due to the nonlinearity of corneal material behaviour, SSI was introduced to estimate corneal material stiffness under different IOP loading. Experimental and clinical evidence was presented, reporting that the SSI demonstrated its independence from both IOP and CCT.[31,200]

The development of an SSI algorithm was based on a large parametric study involving numerical models with geometrical (CCT), stiffness (SP) and loading (bIOP) variations. With those three main parameters in mind and a material stiffness set, it was demonstrated that a 3D surface (using CCT, SP and bIOP) could be formed with changes in material properties. Moreover, with changes in stiffness, 3D surfaces are formed with no intersections; as such, unique combinations of material properties are achieved. Therefore, with the help of numerical modelling, the three main parameters were used to develop a database of 3D surfaces, which eventually will allow for the estimation of corneal material stiffness.[31] This principle allowed SSI to be the first parameter to provide insight to the field regarding corneal material stiffness in-vivo. Despite this insight, bIOP (one of the main three parameters used in SSI) is influenced by corneal biomechanics (CCT and age), and it was expected to affect the efficacy of the algorithm's estimation of material stiffness.[242] Furthermore, SSI utilised numerical models that ignored extra-ocular realistic boundary conditions and instead used assumed ones, which keeps the eye globe in place.[31]

Maklad et al.[217] used a similar approach as the previously developed SSI to develop another algorithm with the utilisation of more complex numerical models. The study simulated air-puff interaction with the cornea using a multi-physics fluid-structure interaction model and conducted a parametric study using numerical representations of human eyes. The new algorithm (fSSI) utilised three parameters used previously with SSI; SP, CCT and their newly developed fIOP; a detailed description of the latter is in the previous section. It was concluded that fSSI performed very similar to SSI and, as a result, was not implemented within Corvis ST. The study's findings demonstrated that a multi-physics fluid-structure interaction model would be unnecessarily complex for a parametric study of this size.

Unlike previously mentioned studies, this study utilised the same optimisation algorithms used with bIOP_o to obtain the most optimal algorithm for SSI_o. All plots regarding SSI_o correlations were compared to ones of SSI to evaluate the performance of the newly developed algorithm. This methodology brought several advantages, such as noise compensation in clinical data, the use of bIOP_o (which was developed in subsection 4.5.1) and, finally, the use of a more geometrically representative numerical model without any assumed boundary conditions acting on the eye globe.

Regarding experimental validation, correlations of SSI/SSI_o with age were compared against age-correlated corneal stiffness acquired from inflation tests on ex-vivo human donor cornea conducted in a previous study.[160, 250] This study produced an age-related stress-strain relationship in the following form:

$$\sigma = A[e^{B\epsilon} - 1] \tag{5.1}$$

where σ = stress, ϵ = strain, while A and B are dimensionless parameters represented by:

$$A = 35 \times 10^{-9} Age^2 + 1.4 \times 10^{-6} Age + 1.03 \times 10^{-3} \tag{5.2}$$

$$B = 0.0013 Age^2 + 0.013 Age + 99; \tag{5.3}$$

differentiating Equation 5.1 with respect to strain will outcome Equation 5.4:

$$E_t = \frac{d\sigma}{d\epsilon} = ABe^{B\epsilon} = B(\sigma + A) \tag{5.4}$$

where E_t is the tangent modulus. When *age*=50 and SSI_50=1.0, the ratio between SSI at any age and SSI_50 will be equal to the ratio between E_t at any age and $E_{t_{50}}$; therefore, SSI can be obtained at any given age. See Equation 5.5.

$$\frac{E_t(age)}{E_t(50)} = \frac{SSI_{age}}{SSI_{50} = 1.0} \tag{5.5}$$

Using the equations above, it was possible to evaluate *ex-vivo* SSI of the seven available healthy clinical datasets. As such, the outcome of the newly developed SSI_o algorithm can be compared to material stiffness obtained experimentally through artificial inflation of human corneas.[160] Both of the presented material stiffness parameters demonstrated correlations with age. In addition, a very similar general trend to *ex-vivo* was visible from both algorithms. However, SSI_o showed a stronger correlation with age than SSI, while SSI and *ex-vivo* SSI had parallel linear regression lines in some of the datasets. Moreover, SSI_o data showed much less spread than that of SSI. In addition, the mean value of SSI_o was lower than the mean *ex-vivo* SSI, while the mean value of SSI was greater than that of the *ex-vivo* SS. In all seven datasets, SSI_o showed significant correlation with *ex-vivo* SSI, while four datasets did not show correlation of SSI with *ex-vivo* SSI. The correlation of ex-vivo SSI with age was used to validate the newly developed material stiffness and indicated improvements.

To conclude the discussion section, a numerical model of the ocular support system was built, developed, validated and put in a clinical application. A novel meshing technique was developed to create the discretise the orbital volume into continuum elements. To follow, various stages of validation has took place to reach the agreement with the available Corvis corneal deformation profiles (one-meridian corneal deformation profile). That being said, the validation methods that were used within this projects shall not be limited to the one-meridian corneal deformation profile. However, the method could make use of multi-meridian corneal imaging of air-puff induced deformation.[251] This method of imaging allowed for more detailed corneal deformations in multiple meridians and have been proved to improve detection of ocular biomechanical abnormalities.[251–253] Therefore, these data would shed some light (if exists) on another rotation phenomena happening in the superior-inferior axis, or even an ocular movement that may resemble torsional rotation within the orbital medium. In addition, the developed force optimisation algorithm (see subsection 3.3.5) could also be utilise the presence of rotations in multiple axis to optimise each EOM tension during the air-puff procedure. In conclusion, the validation methods developed in this study, are not in anyway, shape or form limited to Corvis-ST deformations profiles. Therefore, could be slightly adjusted to validate the numerical model of ocular support system with other available clinical corneal deformation profile, such as ones from swept-source optical coherence tomography (SSOCT).[251]

Chapter 6

Conclusion

In conclusion, this project aimed to build, develop and validate a numerical model of the ocular support system. In both of the results and discussion chapters, the numerical model was validated using Corvis clinical corneal deformations profiles of healthy subjects. One of the main findings of this project was the validation method. This method is not limited to only Corvis deformation profiles, but also other deformation profiles could be utilised to improve numerical model accuracy.

In this final chapter, it will have three main sections; study limitations, recommendations for future work and the final concluding remarks to conclude the findings of the project. While best efforts were made to minimise the limitations of this study, the project did run into some challenges, and they will be listed later in this chapter. To follow would be the future recommendations which would adjust some of the study's limitations and allow for continuation of progress in the this niche field of ocular biomechanics. Lastly, the final concluding remarks of the projects will be outlined, summarising the execution of objectives and achievement of the aim through creating , developing and validating the numerical model of the ocular support system.

6.1 Concluding Remarks

This project aimed to develop and validate a numerical model of the OST to provide additional insight into the response of the globe to external loading. As such, this numerical model could be utilised in various applications, including to produce two equations for $bIOP_o$ and SSI_o in which orbital components were the acting boundary conditions onto the globe. The predicted outcome of those two equations was then validated with clinical data and experimental results of previous studies. The main concluding remarks of the work are as follows:

- An algorithm was developed in this study to mark up an orbital boundary on CT scans, which was then fed into a meshing algorithm through a user-friendly graphical interface that discretises the orbital medium into continuum elements. This allowed for instant model creation, hence facilitating further studies to be carried out;
- OST material optimisation carried out in this project's first study concluded that the optimum material stiffness was four times stiffer than that acquired from previous experimental work. This confirms previous findings that EOMs play a significant role in supporting the globe against posterior displacement;
- The role of the EOMs in providing support for the globe against posterior displacement −especially the oblique muscles− was assessed while correctly simulating nasal rotation of the globe during the Corvis procedure;
- EOM force distribution optimisation estimated a reduction of muscle forces during Corvis procedure loading conditions. This optimisation allowed for simulation of WEM in agreement with the clinical corneal deformation profile, especially in the first ten milliseconds of the procedure;
- A parametric study was carried out, which adapted for corneal geometric variations and orbital geometry variations regarding age and gender. This study produced two equations attempting to better understand corneal behaviour with response to Corvis air puff during loading conditions;
- Both ($bIOP_o$ and SSI_o) were compared to previous experimental work and applied on various clinical datasets, and evaluated against other previously developed methods/equations;

- $bIOP_o$ showed a significant reduction in correlation with CCT when compared to IOP_{CVS}, but has performed similar to the previously developed bIOP;

- SSI_o showed a stronger correlation with age and a lower correlation with IOP and CCT versus the previously developed SSI.

- The validation methods developed with this study, could be slightly adjusted to validate the numerical model of ocular support system according to the available clinical corneal deformation profile and not limited to only Corvis-ST corneal deformations profiles.

6.2 Limitations of the Study

While best efforts were made to minimise the limitations of this study, the project did run into some challenges; these are as follows:

- Due to the unavailability of CT scans, mean orbital boundary was extracted from three young-aged female subjects, where the geometry was then modified to suit various ethnicities, gender and age groups. The assumptions considered in the study may not have been sufficient as clinical data showed more significant nasal rotation in females than in males;

- Due to the unavailability of Body Mass Index (BMI) data, numerical models did not consider variations regarding subjects with various BMI, as this would influence variation in AFT volume and, hence, affect the globe's position within the orbital space;

- Optic nerve head (ONH) was not included in the numerical set-up; instead, elements of this region had different material properties. This was done to reduce model instability caused by ONH−globe and ONH−AFT contact properties. The addition of ONH with suitable contact properties may affect WEM produced during the procedure;

- Optimisation of the eye globes regional material parameters were taken from previous studies, which produced parameters from Corvis numerical simulations using assumed boundary conditions;

- EOMs' insertion points were not accurately positioned onto the globe due to the nodal arrangement being limited to the validated mesh of the globe. This inaccuracy may have caused inaccuracies in the estimation of EOM forces during the Corvis procedure;

- EOMs' initial tensions used in force distribution optimisation were acquired from a previous study, which used one set of EOM geometry. Variations in EOM geometry would cause variation in initial tensions;

- Corneal deformation of the Corvis unloading stage (highest concavity back to neutral position) was not considered due to a lack of proper knowledge regarding corneal hysteresis. The reason behind this was that numerical simulations were not able to adapt to corneal hysteresis;

- Precision of equations developed in this thesis may have been influenced by minor inherent variations in measurements taken by Corvis;

- Ex-vivo testing on fresh donor human eyes may have been ideal for validating SSI_o through comparison of experimental data acquired from inflation (similar to true IOP) with corneal material stiffness estimate of Corvis. However, access to fresh samples was limited, not least due to prohibitive cost;

- Some clinical datasets had distorted eye readings, in which manual triggering of air-puff may have been required. This element may cause human error where the nozzle may be either closer or further than 11 mm, hence resulting in higher or lower pressure applied onto the cornea;

- Validation of the numerical model relied heavily on WEM taken from a single horizontal meridian of the corneal deformation profile produced by Corvis. For that reason, it is nearly impossible to clinical validate any vertical rotation that occurs around the globe. SSI_o and $bIOP_o$ equations relying on other imaging techniques (Rotating Sheimpflug topographers) may produce results with lower variability;

6.3 Recommendations for Future Work

The creation of an orbital soft tissue numerical set-up has shown promising performance. However, it could be improved in future studies through the following recommendations:

- Availability of more CT scans from various regions of the world would allow for more ethnic-specific numerical models to be developed and, hence, will strengthen the database of the Orbital Mesh Generator for future work;

- Availability of CT scans belonging to patients with orbital diseases such as Thyroid Eye Disease would allow for the creation of numerical models with accuracy regarding the globe's position and increased OST volume due to inflammation. These numerical models will facilitate validating Thyroid Eye Disease numerical models using the corresponding WEM produced by Corvis. In addition, geometrical details of the inflamed EOMs would help estimate their initial tension;

- The addition of ONH with appropriate contact properties with the globe would shed light on its role in resistance to posterior displacement;

- A parametric mathematical analysis with geometrical variations of EOMs would be beneficial to allow for estimation of EOMs' initial tension; it may also allow for a more accurate estimate of WEM simulation using the force distribution algorithm;

- The numerical model is currently suitable and ready for any addition of intraocular structures such as vitreous and retina. This addition would allow for simulations showing the progression of retinal detachment due to saccades, head movements and blunt trauma;

- To ensure perpendicular shooting of air-puff onto the corneal apex, it is essential to improve the Corvis fixation target to align the nozzle with the geometrical axis rather than the visual axis;

- It is vital to capture at least two meridians (horizontal and vertical) of the corneal profile during the Corvis procedure. This data would allow for further numerical validation;

- It is recommended to measure the distance from the nozzle to the cornea for each examination, which will lead to adjusting pressure, hence increasing the accuracy of simulations as well as equations;

- Numerical simulations could be improved through a better understanding of corneal hysteresis. This characteristic will allow for more corneal deflection data between the cornea's highest concavity and its neutral position. In addition, understanding corneal hysteresis will pave the way to better understanding WEM during the unloading phase of Corvis;

- It is highly recommended to carry out a more extensive parametric study with variations in WEM. It would be helpful to implement WEM within the equations to compensate for orbital diseases while predicting IOP and corneal material stiffness;

Bibliography

[1] Francois Retief, Andries Stulting, and Louise Cilliers. The eye in antiquity: history of medicine: Samj forum. *South African Medical Journal*, 98(9):697–700, 2008.

[2] Collection Wellcome. X-ray of a human skull, england, 1901-1930. `https://wellcomecollection.org/works/dkvu8re9`, December 2017.

[3] Elizabeth C Beckmann. Ct scanning the early days. *The British journal of radiology*, 79(937):5–8, 2006.

[4] Yasuhiro Takahashi and Hirohiko Kakizaki. Horizontal eye position in thyroid eye disease: a retrospective comparison with normal individuals and changes after orbital decompression surgery. *PLoS One*, 9(12):e114220, 2014.

[5] Stan Z Li and Anil Jain. *Encyclopedia of biometrics*. Springer Publishing Company, Incorporated, 2015.

[6] C. Toris and J. Kiel. Aqueous outflow and glaucoma drug mechanisms of action. `https://www.aao.org/basic-skills/animation-of-aqueous-flow`, 2017.

[7] Matthiew Emanuel. Types of glaucoma. `https://www.glaucomaassociates.com/glaucoma/types-of-glaucoma/`, December 2017.

[8] Ferdinand Stöckhert. *Fracture mechanics applied to hydraulic fracturing in laboratory experiments*. PhD thesis, Ruhr-Universität Bochum, 2015.

[9] Robert K Maloney and Neda Shamie. Cataract surgery. 2020.

[10] Scott Bartlett, Michael Ehrenfeld, Gerson Mast, and Adrian Sugar. Bony anatomy of the orbit. `https://surgeryreference.aofoundation.org/cmf/further-reading/bony-anatomy-of-the-orbit`, May 2012.

[11] Leo Koornneef. New insights in the human orbital connective tissue: result of a new anatomical approach. *Archives of Ophthalmology*, 95(7):1269–1273, 1977.

[12] Shantha Amrith and Stephanie Ming Young. *Anatomy*, pages 3–11. Springer Singapore, Singapore, 2019.

[13] Oliver Jones. The extraocular muscles. `https://teachmeanatomy.info/head/organs/eye/extraocular-muscles/`, november 2020.

[14] Joseph L Demer. Mechanics of the orbita. *Neuro-Ophthalmology*, 40:132–157, 2007.

[15] Mohammad Jannesari, Mahmoud Kadkhodaei, Peiman Mosaddegh, Henryk Kasprzak, and Mahmoud Jabbarvand Behrouz. Assessment of corneal and fatty tissues biomechanical response in dynamic tonometry tests by using inverse models. *Acta of bioengineering and biomechanics*, 20(1), 2018.

[16] Brendan Geraghty, Stephen W Jones, Paolo Rama, Riaz Akhtar, and Ahmed Elsheikh. Age-related variations in the biomechanical properties of human sclera. *Journal of the mechanical behavior of biomedical materials*, 16:181–191, 2012.

[17] Ahmed Elsheikh, Defu Wang, Michael Brown, Paolo Rama, Marino Campanelli, and David Pye. Assessment of corneal biomechanical properties and their variation with age. *Current eye research*, 32(1):11–19, 2007.

[18] Ahmed Elsheikh, Daad Alhasso, and Paolo Rama. Biomechanical properties of human and porcine corneas. *Experimental eye research*, 86(5):783–790, 2008.

[19] Bingrui Wang, Yi Hua, Bryn L Brazile, Bin Yang, and Ian A Sigal. Collagen fiber interweaving is central to sclera stiffness. *Acta biomaterialia*, 113:429–437, 2020.

[20] H Ahmadi, PN Shams, NP Davies, N Joshi, and MH Kelly. Age-related changes in the normal sagittal relationship between globe and orbit. *Journal of plastic, reconstructive & aesthetic surgery*, 60(3):246–250, 2007.

[21] David M Kahn and Robert B Shaw Jr. Aging of the bony orbit: a three-dimensional computed tomographic study. *Aesthetic Surgery Journal*, 28(3):258–264, 2008.

[22] Lauren A Eckstein, Joseph M. Shadpour, Ravi Menghani, and Robert A Goldberg. The relationship of the globe to the orbital rim. *Archives of Facial Plastic Surgery*, 13(1):51–56, 2011.

[23] Henry Gray. Antomy of the human body. *Annals of surgery*, 68(5):564–566, 1918.

[24] Ismael Cordero. Understanding and caring for a schiotz tonometer. *Community eye health*, 27(87):57, 2014.

[25] Elliot M Kirstein, Ahmed Elsheikh, and Pinakin Gunvant. Tonometry–past, present and future. *Glaucoma-Current Clinical and Research Aspects*, pages 88–89, 2011.

[26] Semay Johnson. Semay johnston medical art. `http://www.semayjohnston.com/#prettyPhoto[portfolio2]/14/`, january 2011.

[27] Madhvi Deol, David A Taylor, and Nathan M Radcliffe. Corneal hysteresis and its relevance to glaucoma. *Current opinion in ophthalmology*, 26(2):96, 2015.

[28] Yoshitake Kato, Shunsuke Nakakura, Ryo Asaoka, Kanae Matsuya, Yuki Fujio, Yoshiaki Kiuchi, and Ocular Biomechanics Study Group. Cataract surgery causes biomechanical alterations to the eye detectable by corvis st tonometry. *PLoS One*, 12(2):e0171941, 2017.

[29] Jinglu Ying, Mingguang Shi, and Bo Wang. Anterior corneal asphericity calculated by the tangential radius of curvature. *Journal of biomedical optics*, 17(7):075005, 2012.

[30] SENSIMED Triggerfish. About sensimed triggerfish. `https://www.sensimed.ch/sensimed-triggerfish/`, january 2021.

[31] Ashkan Eliasy, Kai-Jung Chen, Riccardo Vinciguerra, Bernardo T Lopes, Ahmed Abass, Paolo Vinciguerra, Renato Ambrósio Jr, Cynthia J Roberts, and Ahmed Elsheikh. Determination of corneal biomechanical behavior in-vivo for healthy eyes

using corvis st tonometry: stress-strain index. *Frontiers in bioengineering and biotechnology*, 7:105, 2019.

[32] A Elsheikh, B Geraghty, D Alhasso, and P Rama. Regional biomechanical behavior of the human sclera and its variation with age. *Investigative Ophthalmology & Visual Science*, 50(13):3948–3948, 2009.

[33] Joel M Miller and David A Robinson. A model of the mechanics of binocular alignment. *Computers and Biomedical Research*, 17(5):436–470, 1984.

[34] P Pascolo and R Carniel. From time series analysis to a biomechanical multibody model of the human eye. *Chaos, Solitons & Fractals*, 40(2):966–974, 2009.

[35] Robert A Clark, Joel M Miller, and Joseph L Demer. Three-dimensional location of human rectus pulleys by path inflections in secondary gaze positions. *Investigative ophthalmology & visual science*, 41(12):3787–3797, 2000.

[36] Zhipeng Gao, Hongmei Guo, and Weiyi Chen. Initial tension of the human extraocular muscles in the primary eye position. *Journal of theoretical biology*, 353:78–83, 2014.

[37] Yi Du, Bing-Yao Lu, Jun Chen, and Jian-Feng He. Measurement of the orbital soft tissue volume in chinese adults based on three-dimensional ct reconstruction. *Journal of Ophthalmology*, 2019, 2019.

[38] Noortje I Regensburg, Wilmar M Wiersinga, Mirjam EJ van Velthoven, Tos TJM Berendschot, Frans W Zonneveld, Lelio Baldeschi, Peerooz Saeed, and Maarten P Mourits. Age and gender-specific reference values of orbital fat and muscle volumes in caucasians. *British journal of ophthalmology*, 95(12):1660–1663, 2011.

[39] Ho Sik Hwang, Eun Chul Kim, Man Soo Kim, and Suk-Woo Yang. A novel method for quantifying the biomechanical parameters of orbital soft tissue using a corneal dynamic scheimpflug analyser: a retrospective study. *BMC ophthalmology*, 19(1):1–9, 2019.

[40] Yu-Hung Lai, Wen-Chuan Wu, Hwei-Zu Wang, and Hsin-Tien Hsu. Extraocular muscle insertion positions and outcomes of strabismus surgery: correlation analysis and anatomical comparison of western and chinese populations. *British journal of ophthalmology*, 96(5):679–682, 2012.

[41] Hongmei Guo, Zhipeng Gao, and Weiyi Chen. The biomechanical significance of pulley on binocular vision. *Biomedical engineering online*, 15(2):507–516, 2016.

[42] Ahmed Elsheikh and Defu Wang. Numerical modelling of corneal biomechanical behaviour. *Computer methods in biomechanics and biomedical engineering*, 10(2):85–95, 2007.

[43] Ahmed Elsheikh, Brendan Geraghty, Daad Alhasso, Jonathan Knappett, Marino Campanelli, and Paolo Rama. Regional variation in the biomechanical properties of the human sclera. *Experimental eye research*, 90(5):624–633, 2010.

[44] J Vroon, JH De Jong, A Aboulatta, A Eliasy, FCT Van Der Helm, JC Van Meurs, D Wong, and A Elsheikh. Numerical study of the effect of head and eye movement on progression of retinal detachment. *Biomechanics and Modeling in Mechanobiology*, 17(4):975–983, 2018.

[45] Dong Zhou, Ahmed Abass, Ashkan Eliasy, Harald P Studer, Alexander Movchan, Natalia Movchan, and Ahmed Elsheikh. Microstructure-based numerical simulation of the mechanical behaviour of ocular tissue. *Journal of the Royal Society Interface*, 16(154):20180685, 2019.

[46] David P Piñero, Ana Belén Plaza Puche, and Jorge L Alió. Corneal diameter measurements by corneal topography and angle-to-angle measurements by optical coherence tomography: evaluation of equivalence. *Journal of Cataract & Refractive Surgery*, 34(1):126–131, 2008.

[47] Hassan Hashemi, Mehdi Khabazkhoob, Mohammad Hassan Emamian, Mohammad Shariati, Abbasali Yekta, and Akbar Fotouhi. White-to-white corneal diameter distribution in an adult population. *Journal of current ophthalmology*, 27(1-2):21–24, 2015.

[48] Barbara Cassin, Sheila Solomon, and Melvin L Rubin. *Dictionary of eye terminology.* Triad Publishing Company Gainesville, 1990.

[49] Leon L Wiltse and T Glenn Pait. Herophilus of alexandria (325-255 bc): The father of anatomy. *Spine*, 23(17):1904–1914, 1998.

[50] Nancy G Siraisi. *Medieval and early Renaissance medicine: an introduction to knowledge and practice.* University of Chicago Press, 2009.

[51] MARIA VARLAMOVA. De generatione animalium. *13* , page 94, 2019.

[52] Christopher T Leffler, Stephen G Schwartz, Tamer M Hadi, Ali Salman, and Vivek Vasuki. The early history of glaucoma: the glaucous eye (800 bc to 1050 ad). *Clinical ophthalmology (Auckland, NZ)*, 9:207, 2015.

[53] David C Lindberg and David Charles Lindberg. *Theories of Vision from al-Kindi to Kepler.* University of Chicago Press, 1981.

[54] Edward Grant et al. *A source book in medieval science*, volume 13. Harvard University Press, 1974.

[55] Wilhelm Conrad Röntgen. On a new kind of rays. *Science*, 3(59):227–231, 1896.

[56] Jeffrey L Taveras and Barrett G Haik. Radiography of the eye and orbit: A historical overview. *Survey of ophthalmology*, 32(5):361–368, 1988.

[57] Christoph Kniestedt, Michelle Nee, and Robert L Stamper. Dynamic contour tonometry: a comparative study on human cadaver eyes. *Archives of ophthalmology*, 122(9):1287–1293, 2004.

[58] Robert L Stamper. A history of intraocular pressure and its measurement. *Optometry and Vision Science*, 88(1):E16–E28, 2011.

[59] Cynthia J Roberts, William J Dupps, and J Crawford Downs. *Biomechanics of the Eye.* Kugler publications, 2018.

[60] C René. Update on orbital anatomy. *Eye*, 20(10):1119–1129, 2006.

[61] Ajay Malhotra, Frank J Minja, Alison Crum, and Delilah Burrowes. Ocular anatomy and cross-sectional imaging of the eye. In *Seminars in Ultrasound, CT and MRI*, volume 32, pages 2–13. Elsevier, 2011.

[62] Unal Nedim and Elcioglu Omur. Anatomy of the eye from the view of ibn ai haitham [965-1039]. the founder of modern optics. 2009.

[63] Burton J Kushner. The role of ocular torsion on the etiology of a and v patterns, 1985.

[64] Albert Alm and Siv FE Nilsson. Uveoscleral outflow–a review. *Experimental eye research*, 88(4):760–768, 2009.

[65] Ted S Acott and Mary J Kelley. Extracellular matrix in the trabecular meshwork. *Experimental eye research*, 86(4):543–561, 2008.

[66] Ted S Acott, Mary J Kelley, Kate E Keller, Janice A Vranka, Diala W Abu-Hassan, Xinbo Li, Mini Aga, and John M Bradley. Intraocular pressure homeostasis: maintaining balance in a high-pressure environment. *Journal of Ocular pharmacology and therapeutics*, 30(2-3):94–101, 2014.

[67] Robert N Weinreb, James D Brandt, David Garway-Heath, and Felipe Medeiros. *Intraocular pressure*, volume 4. Kugler Publications, 2007.

[68] Todd L Maus and Richard F Brubaker. Measurement of aqueous humor flow by fluorophotometry in the presence of a dilated pupil. *Investigative ophthalmology & visual science*, 40(2):542–546, 1999.

[69] Diala W Abu-Hassan, Ted S Acott, and Mary J Kelley. The trabecular meshwork: a basic review of form and function. *Journal of ocular biology*, 2(1), 2014.

[70] Robert L Stamper, Marc F Lieberman, and Michael V Drake. *Becker-Shaffer's diagnosis and therapy of the glaucomas E-Book*. Elsevier Health Sciences, 2009.

[71] Jonathan Alistair Cook, Adriana Paola Botello, Andrew Elders, Alia Fathi Ali, Augusto Azuara-Blanco, Cynthia Fraser, Kirsty McCormack, Jennifer Margaret Burr,

Surveillance of Ocular Hypertension Study Group, et al. Systematic review of the agreement of tonometers with goldmann applanation tonometry. *Ophthalmology*, 119(8):1552–1557, 2012.

[72] Marc M Whitacre and Richard Stein. Sources of error with use of goldmann-type tonometers. *Survey of ophthalmology*, 38(1):1–30, 1993.

[73] William A Argus. Ocular hypertension and central corneal thickness. *Ophthalmology*, 102(12):1810–1812, 1995.

[74] Andrew M Thompson. Moorfields manual of ophthalmology, 2008.

[75] Charles W McMonnies. Glaucoma history and risk factors. *Journal of optometry*, 10(2):71–78, 2017.

[76] C Ross Ethier, Mark Johnson, and Jeff Ruberti. Ocular biomechanics and biotransport. *Annu. Rev. Biomed. Eng.*, 6:249–273, 2004.

[77] Carsten Edmund. Corneal elasticity and ocular rigidity in normal and keratoconic eyes. *Acta ophthalmologica*, 66(2):134–140, 1988.

[78] Jeffrey W Ruberti, Abhijit Sinha Roy, and Cynthia J Roberts. Corneal biomechanics and biomaterials. *Annual review of biomedical engineering*, 13(1):269–295, 2011.

[79] Harden M McConnell and Richard E Robertson. Isotropic nuclear resonance shifts. *The Journal of Chemical Physics*, 29(6):1361–1365, 1958.

[80] Nicolas Olivier, Florent Aptel, Karsten Plamann, Marie-Claire Schanne-Klein, and Emmanuel Beaurepaire. Harmonic microscopy of isotropic and anisotropic microstructure of the human cornea. *Optics express*, 18(5):5028–5040, 2010.

[81] Dawn M Elliott and Lori A Setton. Anisotropic and inhomogeneous tensile behavior of the human anulus fibrosus: experimental measurement and material model predictions. *Journal of biomechanical engineering*, 123(3):256–263, 2001.

[82] Ying Hon, Guo-Zhen Chen, Shu-Hao Lu, David CC Lam, and Andrew KC Lam. In vivo measurement of regional corneal tangent modulus. *Scientific reports*, 7(1):1–8, 2017.

[83] Yuan-cheng Fung. *Biomechanics: circulation*. Springer Science & Business Media, 2013.

[84] Ahmed Elsheikh and Kevin Anderson. Comparative study of corneal strip extensometry and inflation tests. *Journal of the Royal Society Interface*, 2(3):177–185, 2005.

[85] Thomas Olsen and Steffen Sperling. The swelling pressure of the human corneal stroma as determined by a new method. *Experimental eye research*, 44(4):481–490, 1987.

[86] BL Boyce, RE Jones, TD Nguyen, and JM Grazier. Stress-controlled viscoelastic tensile response of bovine cornea. *Journal of biomechanics*, 40(11):2367–2376, 2007.

[87] Marco Lombardo, Giuseppe Lombardo, Giovanni Carbone, Maria P De Santo, Riccardo Barberi, and Sebastiano Serrao. Biomechanics of the anterior human corneal tissue investigated with atomic force microscopy. *Investigative ophthalmology & visual science*, 53(2):1050–1057, 2012.

[88] Kerstyn Comley and Norman Fleck. The compressive response of porcine adipose tissue from low to high strain rate. *International Journal of Impact Engineering*, 46:1–10, 2012.

[89] Ahmed Elsheikh, Defu Wang, Paolo Rama, Marino Campanelli, and David Garway-Heath. Experimental assessment of human corneal hysteresis. *Current eye research*, 33(3):205–213, 2008.

[90] Thasarat S Vajaranant, Shuang Wu, Mina Torres, and Rohit Varma. The changing face of primary open-angle glaucoma in the united states: demographic and geographic changes from 2011 to 2050. *American journal of ophthalmology*, 154(2):303–314, 2012.

[91] Karen Allison, Deepkumar Patel, and Omobolanle Alabi. Epidemiology of glaucoma: the past, present, and predictions for the future. *Cureus*, 12(11), 2020.

[92] Mahmood F Mafee, Afshin Karimi, Jay Shah, Mark Rapoport, and Sameer A Ansari. Anatomy and pathology of the eye: role of mr imaging and ct. *Neuroimaging Clinics*, 15(1):23–47, 2005.

[93] PM Som and HD Curtin. The eye. In *Head and Neck Imaging*, volume 4, pages 441–527, 2003.

[94] Michiel Dubbelman, Henk A Weeber, Rob GL Van Der Heijde, and Hennie J Völker-Dieben. Radius and asphericity of the posterior corneal surface determined by corrected scheimpflug photography. *Acta Ophthalmologica Scandinavica*, 80(4):379–383, 2002.

[95] Sven Jonuscheit, Michael J Doughty, and Norman F Button. On the use of orbscan ii to assess the peripheral corneal thickness in humans: a comparison with ultrasound pachometry measures. *Ophthalmic and Physiological Optics*, 27(2):179–189, 2007.

[96] Elsa Aghaian, Joyce E Choe, Shan Lin, and Robert L Stamper. Central corneal thickness of caucasians, chinese, hispanics, filipinos, african americans, and japanese in a glaucoma clinic. *Ophthalmology*, 111(12):2211–2219, 2004.

[97] Mei-Ju Chen, Yin-Tzu Liu, Chia-Chen Tsai, Yen-Cheng Chen, Ching-Kuang Chou, and Shu-Mei Lee. Relationship between central corneal thickness, refractive error, corneal curvature, anterior chamber depth and axial length. *Journal of the Chinese Medical Association*, 72(3):133–137, 2009.

[98] Michael J Doughty and Sven Jonuscheit. An assessment of regional differences in corneal thickness in normal human eyes, using the orbscan ii or ultrasound pachymetry. *Optometry-Journal of the American Optometric Association*, 78(4):181–190, 2007.

[99] Jody A Summers Rada, Setareh Shelton, and Thomas T Norton. The sclera and myopia. *Experimental eye research*, 82(2):185–200, 2006.

[100] Xiaoyu Liu, Lizhen Wang, Chao Wang, Ganyun Sun, Songyang Liu, and Yubo Fan. Mechanism of traumatic retinal detachment in blunt impact: a finite element study. *Journal of biomechanics*, 46(7):1321–1327, 2013.

[101] GIRÁLDEZ-FERNÁNDEZ MJ. The relationships between ocular optical components and implications in the process of emmetropization. *Arch Soc Esp Oftalmol*, 83:307–316, 2008.

[102] Neville A McBrien, Andrew I Jobling, and Alex Gentle. Biomechanics of the sclera in myopia: extracellular and cellular factors. *Optometry and vision science*, 86(1):E23–E30, 2009.

[103] Sujiv Vurgese, Songhomitra Panda-Jonas, and Jost B Jonas. Scleral thickness in human eyes. *PloS one*, 7(1):e29692, 2012.

[104] Richard E Norman, John G Flanagan, Sophie MK Rausch, Ian A Sigal, Inka Tertinegg, Armin Eilaghi, Sharon Portnoy, John G Sled, and C Ross Ethier. Dimensions of the human sclera: thickness measurement and regional changes with axial length. *Experimental eye research*, 90(2):277–284, 2010.

[105] Timothy W Olsen, Sarah Y Aaberg, Dayle H Geroski, and Henry F Edelhauser. Human sclera: thickness and surface area. *American journal of ophthalmology*, 125(2):237–241, 1998.

[106] Jack Rootman, Bruce Stewart, and Robert Alan Goldberg. *Orbital surgery: a conceptual approach*. Lippincott Williams & Wilkins, 1995.

[107] C Rene, GE Rose, R Lenthall, and I Moseley. Major orbital complications of endoscopic sinus surgery. *British journal of ophthalmology*, 85(5):598–603, 2001.

[108] Timothy A Turvey and Brent A Golden. Orbital anatomy for the surgeon. *Oral and Maxillofacial Surgery Clinics*, 24(4):525–536, 2012.

[109] Kenneth W Wright. Brown's syndrome: diagnosis and management. *Transactions of the American Ophthalmological Society*, 97:1023, 1999.

[110] A Jo, V Rizen, V Nikolic, and B Banovic. The role of orbital wall morphological properties and their supporting structures in the etiology of "blow-out" fractures. *Surgical and Radiologic Anatomy*, 11(3):241–248, 1989.

[111] Ivo Schoemaker, Pepijn PW Hoefnagel, Tom J Mastenbroek, Cornelis F Kolff, Sander Schutte, Frans CT van der Helm, Stephen J Picken, Anton FC Gerritsen, Piotr A Wielopolski, Henk Spekreijse, et al. Elasticity, viscosity, and deformation of orbital fat. *Investigative ophthalmology & visual science*, 47(11):4819–4826, 2006.

[112] D Bremond-Gignac, H Copin, O Cussenot, J-P Lassau, and D Henin. Anatomical histological and mesoscopic study of the adipose tissue of the orbit. *Surgical and Radiologic Anatomy*, 26(4):297–302, 2004.

[113] R Wolfram-Gabel and JL Kahn. Adipose body of the orbit. *Clinical Anatomy: The Official Journal of the American Association of Clinical Anatomists and the British Association of Clinical Anatomists*, 15(3):186–192, 2002.

[114] Jonathan J Dutton. *Radiology of the Orbit and Visual Pathways E-Book*. Elsevier Health Sciences, 2010.

[115] Tarek Shaarawy, Mark B Sherwood, Roger A Hitchings, and Jonathan G Crowston. *Glaucoma E-Book*. Elsevier Health Sciences, 2014.

[116] Creig S Hoyt and David Taylor. *Pediatric Ophthalmology and Strabismus, Expert Consult-Online and Print, 4: Pediatric Ophthalmology and Strabismus*. Elsevier Health Sciences, 2012.

[117] Lee Ann Remington and Denise Goodwin. *Clinical Anatomy and Physiology of the Visual System E-Book*. Elsevier Health Sciences, 2021.

[118] Ph de Gottrau, Stanislav Gajisin, and A Roth. Ocular rectus muscle insertions revisited: an unusual anatomic approach. *Cells Tissues Organs*, 151(4):268–272, 1994.

[119] Eugene Wolff and Roger Warwick. *Eugene Wolff's anatomy of the eye and orbit: including the central connexions, development, and comparative anatomy of the visual apparatus.* WB Saunders Company, 1976.

[120] Lee Ann Remington. Chapter 10 - extraocular muscles. In Lee Ann Remington, editor, *Clinical Anatomy and Physiology of the Visual System (Third Edition)*, pages 182–201. Butterworth-Heinemann, Saint Louis, third edition edition, 2012.

[121] WILLIAM E KREWSON. Comparison of the oblique extraocular muscles. *Archives of Ophthalmology*, 32(3):204–207, 1944.

[122] MJ Reeh, JL Wobig, and JD Wirtschafter. Ophthalmic anatomy. *A manual with some clinical applications. AAO continuing educa-tion in ophthalmology. Rochester: Custom Printing*, pages 86–91, 1981.

[123] Marcos T Doxanas and Richard Lee Anderson. *Clinical orbital anatomy.* Williams & Wilkins, 1984.

[124] Craig A McKeown, Kara Cavuoto, and Robert Morris. Chapter 85 - strabismus surgery. In Creig S Hoyt and David Taylor, editors, *Pediatric Ophthalmology and Strabismus (Fourth Edition)*, pages 860–887.e4. W.B. Saunders, London, fourth edition edition, 2013.

[125] Joseph L Demer, Joel M Miller, and Vadims Poukens. Surgical implications of the rectus extraocular muscle pulleys, 1996.

[126] John D Porter, Vadims Poukens, Robert S Baker, and Joseph L Demer. Structure-function correlations in the human medial rectus extraocular muscle pulleys. *Investigative ophthalmology & visual science*, 37(2):468–472, 1996.

[127] Joseph L Demer, Joel M Miller, Vadims Poukens, Harry V Vinters, and Ben J Glasgow. Evidence for fibromuscular pulleys of the recti extraocular muscles. *Investigative ophthalmology & visual science*, 36(6):1125–1136, 1995.

[128] PR Johnson, JS Stern, MRC Greenwood, and Jules Hirsch. Adipose tissue hyperplasia and hyperinsulinemia in zucker obese female rats: a developmental study. *Metabolism*, 27(12):1941–1954, 1978.

[129] Abbas Samani, Jonathan Bishop, Chris Luginbuhl, and Donald B Plewes. Measuring the elastic modulus of ex vivo small tissue samples. *Physics in Medicine & Biology*, 48(14):2183, 2003.

[130] FangJun Bao, ManLi Deng, XiaoBo Zheng, LinNa Li, YiPing Zhao, Si Cao, AYong Yu, QinMei Wang, JinHai Huang, and Ahmed Elsheikh. Effects of diabetes mellitus on biomechanical properties of the rabbit cornea. *Experimental eye research*, 161:82–88, 2017.

[131] Ji-guo Yu, Fang-jun Bao, Yi-fan Feng, Charles Whitford, Ting Ye, Yan-bing Huang, Qin-mei Wang, and Ahmed Elsheikh. Assessment of corneal biomechanical behavior under posterior and anterior pressure. *Journal of Refractive Surgery*, 29(1):64–71, 2013.

[132] John D Porter, Robert S Baker, Robert J Ragusa, and Jennifer K Brueckner. Extraocular muscles: basic and clinical aspects of structure and function. *Survey of ophthalmology*, 39(6):451–484, 1995.

[133] Sei Yeul Oh, Vadims Poukens, and Joseph L Demer. Quantitative analysis of rectus extraocular muscle layers in monkey and humans. *Investigative ophthalmology & visual science*, 42(1):10–16, 2001.

[134] Reika Kono, Vadims Poukens, and Joseph L Demer. Superior oblique muscle layers in monkeys and humans. *Investigative ophthalmology & visual science*, 46(8):2790–2799, 2005.

[135] Joseph L Demer, Sei Yeul Oh, and Vadims Poukens. Evidence for active control of rectus extraocular muscle pulleys. *Investigative ophthalmology & visual science*, 41(6):1280–1290, 2000.

[136] Gordon L Ruskell, Inga-Britt Kjellevold Haugen, Jan Richard Bruenech, and Frans Van Der Werf. Double insertions of extraocular rectus muscles in humans and the pulley theory. *Journal of Anatomy*, 206(3):295–306, 2005.

[137] Joseph L Demer. The orbital pulley system: a revolution in concepts of orbital anatomy. *Annals of the New York Academy of Sciences*, 956(1):17–32, 2002.

[138] Joseph L Demer. Current concepts of mechanical and neural factors in ocular motility. *Current opinion in neurology*, 19(1):4, 2006.

[139] Jayc Clinton Sedlmayr. *Anatomy, evolution, and functional significance of cephalic vasculature in Archosauria*. Ohio University, 2002.

[140] Bradley N Lemke and Mark J Lucarelli. Anatomy of the ocular adnexa, orbit, and related facial structures. In *Smith and Nesi's ophthalmic plastic and reconstructive surgery*, pages 3–58. Springer, 2012.

[141] Charles Barrett Lockwood. The anatomy of the muscles, ligaments, and fasclae of the orbit, including an account of the capsule of tenon, the check ligaments of the recti, and the suspensory ligaments of the eye. *Journal of Anatomy and Physiology*, 20(Pt 1):i2, 1885.

[142] Catherine Banks, Qasim Husain, and Benjamin S Bleier. Endoscopic endonasal intraconal orbit surgery. *World Journal of Otorhinolaryngology-Head and Neck Surgery*, 6(2):100–105, 2020.

[143] Agnieszka Boszczyk, Henryk Kasprzak, and Agnieszka Jóźwik. Eye retraction and rotation during corvis st 'air puff'intraocular pressure measurement and its quantitative analysis. *Ophthalmic and Physiological Optics*, 37(3):253–262, 2017.

[144] Alireza Karimi, Reza Razaghi, Mahdi Navidbakhsh, Toshihiro Sera, and Susumu Kudo. Quantifying the injury of the human eye components due to tennis ball impact using a computational fluid–structure interaction model. *Sports Engineering*, 19(2):105–115, 2016.

[145] Xiaoqi Geng, Xiaoyu Liu, Wei Wei, Yawei Wang, Lizhen Wang, Kinon Chen, Hongqiang Huo, Yuanjie Zhu, and Yubo Fan. Mechanical evaluation of retinal damage associated with blunt craniomaxillofacial trauma: a simulation analysis. *Translational Vision Science & Technology*, 7(3):16–16, 2018.

[146] Harald Studer, X Larrea, H Riedwyl, and Philippe Büchler. Biomechanical model of human cornea based on stromal microstructure. *Journal of biomechanics*, 43(5):836–842, 2010.

[147] Beomkeun Kim, Seong Beom Lee, Jayone Lee, Sehyun Cho, Hyungmin Park, Sanghoon Yeom, and Sung Han Park. A comparison among neo-hookean model, mooney-rivlin model, and ogden model for chloroprene rubber. *International Journal of Precision Engineering and Manufacturing*, 13(5):759–764, 2012.

[148] V Alastrué, B Calvo, E Pena, and M Doblaré. Biomechanical modeling of refractive corneal surgery. 2006.

[149] Kevin Anderson, Ahmed El-Sheikh, and Timothy Newson. Application of structural analysis to the mechanical behaviour of the cornea. *Journal of the Royal Society Interface*, 1(1):3–15, 2004.

[150] Ji-guo Yu, Fang-jun Bao, Akram Joda, Xun-an Fu, Shi Zhou, Jing Wang, Xiu-li Hu, Qin-mei Wang, and Ahmed Elsheikh. Influence of glucocorticosteroids on the biomechanical properties of in-vivo rabbit cornea. *Journal of the Mechanical Behavior of Biomedical Materials*, 29:350–359, 2014.

[151] SL-Y Woo, AS Kobayashi, WA Schlegel, and C Lawrence. Nonlinear material properties of intact cornea and sclera. *Experimental eye research*, 14(1):29–39, 1972.

[152] David A Hoeltzel, Peter Altman, Kurt Buzard, and Kang-il Choe. Strip extensiometry for comparison of the mechanical response of bovine, rabbit, and human corneas. 1992.

[153] Troels T Andreassen, Anders Hjorth Simonsen, and Hans Oxlund. Biomechanical properties of keratoconus and normal corneas. *Experimental eye research*, 31(4):435–441, 1980.

[154] Gregor Wollensak, Eberhard Spoerl, and Theo Seiler. Stress-strain measurements of human and porcine corneas after riboflavin–ultraviolet-a-induced cross-linking. *Journal of Cataract & Refractive Surgery*, 29(9):1780–1785, 2003.

[155] Ira S Nash, Peter R Greene, and C Stephen Foster. Comparison of mechanical properties of keratoconus and normal corneas. *Experimental eye research*, 35(5):413–424, 1982.

[156] M Van Loocke, CG Lyons, and CK Simms. A validated model of passive muscle in compression. *Journal of biomechanics*, 39(16):2999–3009, 2006.

[157] Shao-Hsuan Chang, Ashkan Mohammadvali, Kai-Jung Chen, You-Ren Ji, Tai-Horng Young, Tsung-Jen Wang, Colin E Willoughby, Kevin J Hamill, and Ahmed Elsheikh. The relationship between mechanical properties, ultrastructural changes, and intrafibrillar bond formation in corneal uva/riboflavin cross-linking treatment for keratoconus. *Journal of Refractive Surgery*, 34(4):264–272, 2018.

[158] Baptiste Coudrillier, Jacek K Pijanka, Joan L Jefferys, Adhiraj Goel, Harry A Quigley, Craig Boote, and Thao D Nguyen. Glaucoma-related changes in the mechanical properties and collagen micro-architecture of the human sclera. *PloS one*, 10(7):e0131396, 2015.

[159] Brad L Boyce, J Mark Grazier, Reese E Jones, and Thao D Nguyen. Full-field deformation of bovine cornea under constrained inflation conditions. *Biomaterials*, 29(28):3896–3904, 2008.

[160] Ahmed Elsheikh, Brendan Geraghty, Paolo Rama, Marino Campanelli, and Keith M Meek. Characterization of age-related variation in corneal biomechanical properties. *Journal of the Royal Society Interface*, 7(51):1475–1485, 2010.

[161] KM Meek. The cornea and sclera. In *Collagen*, pages 359–396. Springer, 2008.

[162] Dong Zhou, Ashkan Eliasy, Ahmed Abass, Petar Markov, Charles Whitford, Craig Boote, Alexander Movchan, Natalia Movchan, and Ahmed Elsheikh. Analysis of x-ray scattering microstructure data for implementation in numerical simulations of ocular biomechanical behaviour. *PloS one*, 14(4):e0214770, 2019.

[163] Sean J Darcy, Timothy A Miller, Robert A Goldberg, J Pablo Villablanca, Joseph L Demer, and George H Rudkin. Magnetic resonance imaging characterization of orbital changes with age and associated contributions to lower eyelid prominence. *Plastic and reconstructive surgery*, 122(3):921–929, 2008.

[164] Hans C Fledelius and Max Stubgaard. Changes in refraction and corneal curvature during growth and adult life: a cross-sectional study. *Acta ophthalmologica*, 64(5):487–491, 1986.

[165] Stephen B Kaye, John R Green, Jonathan Luck, and Ken J Lowe. Dependence of ocular protrusion, asymmetry of protrusion and lateral interorbital width on age. *Acta ophthalmologica*, 70(6):762–765, 1992.

[166] Joel E Pessa, Lisa D Desvigne, Val S Lambros, Jennifer Nimerick, Binu Sugunan, and Vikram P Zadoo. Changes in ocular globe-to-orbital rim position with age: implications for aesthetic blepharoplasty of the lower eyelids. *Aesthetic plastic surgery*, 23(5):337–342, 1999.

[167] Karsten Knudtzon. On exophthalmometry: The result of 724 measurements with hertel's exophthalmometer on normal adult individuals. *Acta Psychiatrica Scandinavica*, 24(3-4):523–537, 1949.

[168] J Lang, WD Schäfer, W Grafen, and B Wallner. Side differences in the position of the corneal apex in relation to the lateral orbital margin (measurements with the hertel exophthalmometer). *Klinische Monatsblatter fur Augenheilkunde*, 187(6):521–524, 1985.

[169] Marylin H White, H Michael Lambert, Marilyn C Kincaid, J Paul Dieckert, and Donald K Lowd. The ora serrata and the spiral of tillaux: anatomic relationship and clinical correlation. *Ophthalmology*, 96(4):508–511, 1989.

[170] Robert A Clark, Joel M Miller, and Joseph L Demer. Location and stability of rectus muscle pulleys. muscle paths as a function of gaze. *Investigative ophthalmology & visual science*, 38(1):227–240, 1997.

[171] Paul Harasymowycz, Catherine Birt, Patrick Gooi, Lisa Heckler, Cindy Hutnik, Delan Jinapriya, Lesya Shuba, David Yan, and Radmila Day. Medical management of glaucoma in the 21st century from a canadian perspective. *Journal of ophthalmology*, 2016, 2016.

[172] Donatella Pascolini and Silvio Paolo Mariotti. Global estimates of visual impairment: 2010. *British Journal of Ophthalmology*, 96(5):614–618, 2012.

[173] RRA Bourne. Worldwide glaucoma through the looking glass, 2006.

[174] Friedrich Homer and Theodore Billroth. Albrecht von graefe (1828-1870): founder of scientific ophthalmology. *Singapore Med J*, 48(9):797, 2007.

[175] Jens Martin Rohrbach. Albrecht von graefe in the present, the past, and the future. *Graefe's Archive for Clinical and Experimental Ophthalmology*, 258(6):1141–1147, 2020.

[176] Meena Chakrabarti, Sonia Rani John, and Arup Chakrabarti. 180 years of evolution in tonometry. *KJ O*, 21:173–181, 2009.

[177] Robert A Moses. Theory of the schiotz tonometer and its empirical calibration. *Transactions of the American Ophthalmological Society*, 69:494, 1971.

[178] William McLean. The development of a tonometer. *American Journal of Ophthalmology*, 2(6):417–419, 1919.

[179] GC Stuckey. Tonometry and the imbert-fick law. *Australian Journal of Opthalmology*, 2(2):68–70, 1974.

[180] Robert A Moses. The goldmann applanation tonometer. *American journal of ophthalmology*, 46(6):865–869, 1958.

[181] Niels Ehlers, Thorkild Bramsen, and Steffen Sperling. Applanation tonometry and central corneal thickness. *Acta ophthalmologica*, 53(1):34–43, 1975.

[182] HANS Goldmann and TH Schmidt. Über applanationstonometrie. *Ophthalmologica*, 134(4):221–242, 1957.

[183] Barun K Nayak, Quresh B Maskati, and Rajul Parikh. The unique problem of glaucoma: under-diagnosis and over-treatment. *Indian journal of ophthalmology*, 59(Suppl1):S1, 2011.

[184] Ahmed Elsheikh, Daad Alhasso, Pinakin Gunvant, and David Garway-Heath. Multiparameter correction equation for goldmann applanation tonometry. *Optometry and Vision Science*, 88(1):E102–E112, 2011.

[185] Frank Bochmann, Claude Kaufmann, and Michael A Thiel. Dynamic contour tonometry versus goldmann applanation tonometry: challenging the gold standard. *Expert Review of Ophthalmology*, 5(6):743–749, 2010.

[186] Evelin Schneider, Hartmut E Kanngiesser, and Christoph Kniestedt. Dynamic contour tonometry. In *Glaucoma*, pages 47–63. Springer, 2006.

[187] Hartmut E Kanngiesser, Christoph Kniestedt, and Yves CA Robert. Dynamic contour tonometry: presentation of a new tonometer. *Journal of glaucoma*, 14(5):344–350, 2005.

[188] Matthew Frederick Anderson, Adriana Agius-Fernandez, and Stephen B Kaye. Comparison of the utility of pascal dynamic contour tonometry with goldmann applanation tonometry in routine clinical practice. *Journal of Glaucoma*, 22(5):422–426, 2013.

[189] Riccardo Vinciguerra, Ahmed Elsheikh, Cynthia J Roberts, Renato Ambrósio Jr, David Sung Yong Kang, Bernardo T Lopes, Emanuela Morenghi, Claudio Azzolini, and Paolo Vinciguerra. Influence of pachymetry and intraocular pretress-strainsure on dynamic corneal response parameters in healthy patients. *Journal of refractive surgery*, 32(8):550–561, 2016.

[190] Kenneth J Myers and Clifford A Scott. The non-contact (" air puff") tonometer: variability and corneal staining. *American Journal of Optometry and Physiological Optics*, 52(1):36–46, 1975.

[191] William E Sponsel, Paul L Kaufman, Thomas I Strinden, Kathleen L DePaul, Harrison N Bowes, Kenneth W Olander, and Howard S Barnebey. Evaluation of the keeler pulsair non-contact tonometer. *Acta Ophthalmologica*, 67(5):567–572, 1989.

[192] Aachal Kotecha. What biomechanical properties of the cornea are relevant for the clinician? *Survey of ophthalmology*, 52(6):S109–S114, 2007.

[193] Ping-Bo Ouyang, Cong-Yi Li, Xiao-Hua Zhu, and Xuan-Chu Duan. Assessment of intraocular pressure measured by reichert ocular response analyzer, goldmann applanation tonometry, and dynamic contour tonometry in healthy individuals. *International journal of ophthalmology*, 5(1):102, 2012.

[194] Guihua Xu, Dennis Shun Lam, and Christopher Kai-shun Leung. Influence of ocular pulse amplitude on ocular response analyzer measurements. *Journal of glaucoma*, 20(6):344–349, 2011.

[195] Michael Sullivan-Mee, Sarah E Lewis, Denise Pensyl, Gretchen Gerhardt, Kathy D Halverson, and Clifford Qualls. Factors influencing intermethod agreement between goldmann applanation, pascal dynamic contour, and ocular response analyzer tonometry. *Journal of glaucoma*, 22(6):487–495, 2013.

[196] Aachal Kotecha, Edward White, Patricio G Schlottmann, and David F Garway-Heath. Intraocular pressure measurement precision with the goldmann applanation, dynamic contour, and ocular response analyzer tonometers. *Ophthalmology*, 117(4):730–737, 2010.

[197] Michael Sullivan-Mee, Gretchen Gerhardt, Kathy D Halverson, and Clifford Qualls. Repeatability and reproducibility for intraocular pressure measurement by dynamic contour, ocular response analyzer, and goldmann applanation tonometry. *Journal of glaucoma*, 18(9):666–673, 2009.

[198] Javier Moreno-Montanés, Miguel J Maldonado, Noelia García, Loreto Mendiluce, Pio J García-Gómez, and María Seguí-Gómez. Reproducibility and clinical relevance of the ocular response analyzer in nonoperated eyes: corneal biomechanical and tonometric implications. *Investigative ophthalmology & visual science*, 49(3):968–974, 2008.

[199] Jiaxu Hong, Jianjiang Xu, Anji Wei, Sophie X Deng, Xinhan Cui, Xiaobo Yu, and Xinghuai Sun. A new tonometer—the corvis st tonometer: clinical comparison with noncontact and goldmann applanation tonometers. *Investigative ophthalmology & visual science*, 54(1):659–665, 2013.

[200] Ashkan Eliasy, Kai-Jung Chen, Riccardo Vinciguerra, Osama Maklad, Paolo Vinciguerra, Renato Ambrósio Jr, Cynthia J Roberts, and Ahmed Elsheikh. Ex-vivo experimental validation of biomechanically-corrected intraocular pressure measurements on human eyes using the corvis st. *Experimental eye research*, 175:98–102, 2018.

[201] Kai-Jung Chen, Akram Joda, Riccardo Vinciguerra, Ashkan Eliasy, Shervin Mir Mohi Sefat, Daniel Kook, Brendan Geraghty, Cynthia J Roberts, and Ahmed Elsheikh. Clinical evaluation of a new correction algorithm for dynamic scheimpflug analyzer tonometry before and after laser in situ keratomileusis and small-incision lenticule extraction. *Journal of Cataract & Refractive Surgery*, 44(5):581–588, 2018.

[202] Hun Lee, Cynthia J Roberts, Renato Ambrósio Jr, Ahmed Elsheikh, David Sung Yong Kang, et al. Changes in biomechanically corrected intraocular pressure and dynamic corneal response parameters before and after transepithelial photorefractive keratectomy and femtosecond laser–assisted laser in situ keratomileusis. *Journal of Cataract & Refractive Surgery*, 43(12):1495–1503, 2017.

[203] Riccardo Vinciguerra, Renato Ambrósio Jr, Ahmed Elsheikh, Cynthia J Roberts, Bernardo Lopes, Emanuela Morenghi, Claudio Azzolini, and Paolo Vinciguerra. Detection of keratoconus with a new biomechanical index. *Journal of refractive surgery*, 32(12):803–810, 2016.

[204] Robert Koprowski, Anita Lyssek-Boron, Anna Nowinska, Edward Wylegala, Henryk Kasprzak, and Zygmunt Wrobel. Selected parameters of the corneal deformation in the corvis tonometer. *Biomedical engineering online*, 13(1):1–16, 2014.

[205] Mohammad-Reza Sedaghat, Hamed Momeni-Moghaddam, AbbasAli Yekta, Ahmed Elsheikh, Mehdi Khabazkhoob, Renato Ambrósio Jr, Nasim Maddah, and Zeynab Danesh. Biomechanically-corrected intraocular pressure compared to pressure measured with commonly used tonometers in normal subjects. *Clinical optometry*, 11:127, 2019.

[206] Cynthia J Roberts, Ashraf M Mahmoud, Jeffrey P Bons, Arif Hossain, Ahmed Elsheikh, Riccardo Vinciguerra, Paolo Vinciguerra, and Renato Ambrósio Jr. Introduction of two novel stiffness parameters and interpretation of air puff–induced biomechanical deformation parameters with a dynamic scheimpflug analyzer. *Journal of refractive surgery*, 33(4):266–273, 2017.

[207] Gábor Holló, Péter Kóthy, and Péter Vargha. Evaluation of continuous 24-hour intraocular pressure monitoring for assessment of prostaglandin-induced pressure reduction in glaucoma. *Journal of glaucoma*, 23(1):e6–e12, 2014.

[208] Matteo Leonardi, Elie M Pitchon, Arnaud Bertsch, Philippe Renaud, and Andre Mermoud. Wireless contact lens sensor for intraocular pressure monitoring: assessment on enucleated pig eyes. *Acta ophthalmologica*, 87(4):433–437, 2009.

[209] Kaweh Mansouri and Tarek Shaarawy. Continuous intraocular pressure monitoring with a wireless ocular telemetry sensor: initial clinical experience in patients with open angle glaucoma. *British Journal of Ophthalmology*, 95(5):627–629, 2011.

[210] Adan Villamarin, Sylvain Roy, Reda Hasballa, Orestis Vardoulis, Philippe Reymond, and Nikolaos Stergiopulos. 3d simulation of the aqueous flow in the human eye. *Medical engineering & physics*, 34(10):1462–1470, 2012.

[211] Evan T Sebastian. The complexity and origins of the human eye: A brief study on the anatomy, physiology, and origin of the eye. 2010.

[212] Junjie Wang. *Numerical simulation of corneal refractive surgery based on improved reconstruction of corneal surface*. The University of Liverpool (United Kingdom), 2016.

[213] Kai-Jung Chen. *Accurate Estimation of Intraocular Pressure and Corneal Material Behaviour Using a Non-Contact Method*. PhD thesis, The University of Liverpool (United Kingdom), 2019.

[214] Ricardo Magalhães, Ahmed Elcleraheikh, Philippe Büchler, Charles Whitford, and Junjie Wang. ¡ b¿ application of particle swarm optimization in inverse finite element modeling to determine the cornea´ s mechanical behavior. *Acta Scientiarum. Technology*, 39(3):325–331, 2017.

[215] Ali Aboulatta, Ahmed Abass, Ahmed Makarem, Ashkan Eliasy, Dong Zhou, Duo Chen, Xiaoyu Liu, and Ahmed Elsheikh. Experimental evaluation of the viscoelasticity of porcine vitreous. *Journal of the Royal Society Interface*, 18(175):20200849, 2021.

[216] Akram Abdelazim Joda, Mir Mohi Sefat Shervin, Daniel Kook, and Ahmed Elsheikh. Development and validation of a correction equation for corvis tonometry. *Computer methods in biomechanics and biomedical engineering*, 19(9):943–953, 2016.

[217] Osama Mohamed Yousef Maklad. *Influence of Fluid-Structure Interaction on Human Eye Biomechanics Under Air Puff Non-Contact Tonometry*. The University of Liverpool (United Kingdom), 2019.

[218] Raymond W Ogden. *Non-linear elastic deformations*. Courier Corporation, 1997.

[219] Richard Moran, Joshua H Smith, and José J García. Fitted hyperelastic parameters for human brain tissue from reported tension, compression, and shear tests. *Journal of biomechanics*, 47(15):3762–3766, 2014.

[220] Anna Leszczynska, Karolin Moehler, Eberhard Spoerl, Lisa Ramm, Robert Herber, Lutz E Pillunat, and Naim Terai. Measurement of orbital biomechanical properties

in patients with thyroid orbitopathy using the dynamic scheimpflug analyzer (corvis st). *Current eye research*, 43(3):289–292, 2018.

221 Ahmed Elsheikh, Daad Alhasso, and Paolo Rama. Assessment of the epithelium's contribution to corneal biomechanics. *Experimental eye research*, 86(2):445–451, 2008.

222 Renato Ambrósio Jr, Ruiz Simonato Alonso, Allan Luz, and Luis Guillermo Coca Velarde. Corneal-thickness spatial profile and corneal-volume distribution: tomographic indices to detect keratoconus. *Journal of Cataract & Refractive Surgery*, 32(11):1851–1859, 2006.

223 Lawrence Yoo, Jason Reed, Andrew Shin, and Joseph L Demer. Atomic force microscopy determination of young s modulus of bovine extra-ocular tendon fiber bundles. *Journal of biomechanics*, 47(8):1899–1903, 2014.

224 Ahmed Elsheikh, Charles Whitford, Rosti Hamarashid, Wael Kassem, Akram Joda, and Philippe Büchler. Stress free configuration of the human eye. *Medical engineering & physics*, 35(2):211–216, 2013.

225 Steven P Ellis. Instability of least squares, least absolute deviation and least median of squares linear regression, with a comment by stephen portnoy and ivan mizera and a rejoinder by the author. *Statistical Science*, 13(4):337–350, 1998.

226 Frederik Michel Dekking, Cornelis Kraaikamp, Hendrik Paul Lopuhaä, and Ludolf Erwin Meester. Basic statistical models. In *A Modern Introduction to Probability and Statistics*, pages 245–268. Springer, 2005.

227 Simon Altmannshofer and Christian Endisch. Robust vehicle mass and driving resistance estimation. In *2016 american control conference (ACC)*, pages 6869–6874. IEEE, 2016.

228 Renato Ambrósio Jr, Bernardo T Lopes, Fernando Faria-Correia, Marcella Q Salomão, Jens Bühren, Cynthia J Roberts, Ahmed Elsheikh, Riccardo Vinciguerra, and Paolo Vinciguerra. Integration of scheimpflug-based corneal tomography and

biomechanical assessments for enhancing ectasia detection. *Journal of Refractive Surgery*, 33(7):434–443, 2017.

[229] Kerstyn Comley and Norman A Fleck. A micromechanical model for the young's modulus of adipose tissue. *International Journal of Solids and Structures*, 47(21):2982–2990, 2010.

[230] Joseph L Demer, Vadims Poukens, Joel M Miller, and Paul Micevych. Innervation of extraocular pulley smooth muscle in monkeys and humans. *Investigative Ophthalmology & Visual Science*, 38(9):1774–1785, 1997.

[231] Boel Bengtsson, M Cristina Leske, Leslie Hyman, Anders Heijl, Early Manifest Glaucoma Trial Group, et al. Fluctuation of intraocular pressure and glaucoma progression in the early manifest glaucoma trial. *Ophthalmology*, 114(2):205–209, 2007.

[232] Niels Ehlers, FINN KRUSE HANSEN, and Henry Aasved. Biometric correlations of corneal thickness. *Acta ophthalmologica*, 53(4):652–659, 1975.

[233] Leon W Herndon, Saira A Choudhri, Terry Cox, Karim F Damji, M Bruce Shields, and R Rand Allingham. Central corneal thickness in normal, glaucomatous, and ocular hypertensive eyes. *Archives of Ophthalmology*, 115(9):1137–1141, 1997.

[234] R Montard, R Kopito, O Touzeau, C Allouch, I Letaief, V Borderie, and L Laroche. Ocular response analyzer: feasibility study and correlation with normal eyes. *Journal Français d'Ophtalmologie*, 30(10):978–984, 2007.

[235] Federico Saenz-Frances, Luis Jañez, Lara Borrego-Sanz, Jose Maria Martinez-de-la Casa, Maria Jerez-Fidalgo, Julian Garcia-Sánchez, and Julian Garcia-Feijoo. Effect of corneal morphometry on dynamic contour and goldmann applanation tonometry. *Journal of glaucoma*, 22(5):380–383, 2013.

[236] Fatih Özcura, Nilgün Yıldırım, Emre Tambova, and Afsun Şahin. Evaluation of goldmann applanation tonometry, rebound tonometry and dynamic contour tonometry in keratoconus. *Journal of optometry*, 10(2):117–122, 2017.

[237] Agnieszka Boszczyk, Henryk Kasprzak, and Damian Siedlecki. Non-contact tonometry using corvis st: analysis of corneal vibrations and their relation with intraocular pressure. *JOSA A*, 36(4):B28–B34, 2019.

[238] Serena JK Park, Ghee Soon Ang, Simon Nicholas, and Anthony P Wells. The effect of thin, thick, and normal corneas on goldmann intraocular pressure measurements and correction formulae in individual eyes. *Ophthalmology*, 119(3):443–449, 2012.

[239] David A Luce. Determining in vivo biomechanical properties of the cornea with an ocular response analyzer. *Journal of Cataract & Refractive Surgery*, 31(1):156–162, 2005.

[240] Michele Lanza, Stefania Iaccarino, Michela Cennamo, Carlo Irregolare, Vito Romano, and Ugo Antonello Gironi Carnevale. Comparison between corvis and other tonometers in healthy eyes. *Contact Lens and Anterior Eye*, 38(2):94–98, 2015.

[241] Seung-hoon Lee, Jung-il Moon, and Youn Hea Jung. Comparison of intraocular pressures measured by the corvis st and other tonometers in normal eyes. *Journal of the Korean Ophthalmological Society*, 60(12):1250–1256, 2019.

[242] Lisa Ramm, Robert Herber, Eberhard Spoerl, Frederik Raiskup, Lutz E Pillunat, and Naim Terai. Intraocular pressure measurement using ocular response analyzer, dynamic contour tonometer, and scheimpflug analyzer corvis st. *Journal of ophthalmology*, 2019, 2019.

[243] Osama Maklad, Ashkan Eliasy, Kai-Jung Chen, JunJie Wang, Ahmed Abass, Bernardo Teixeira Lopes, Vassilis Theofilis, and Ahmed Elsheikh. Fluid-structure interaction based algorithms for iop and corneal material behavior. *Frontiers in bioengineering and biotechnology*, 8:970, 2020.

[244] Ian A Sigal, Hongli Yang, Michael D Roberts, Jonathan L Grimm, Claude F Burgoyne, Shaban Demirel, and J Crawford Downs. Iop-induced lamina cribrosa deformation and scleral canal expansion: independent or related? *Investigative ophthalmology & visual science*, 52(12):9023–9032, 2011.

[245] Renato Ambrósio Jr. Post-lasik ectasia: twenty years of a conundrum. In *Seminars in ophthalmology*, volume 34, pages 66–68. Taylor & Francis, 2019.

[246] William J Dupps Jr and Cynthia J Roberts. Corneal biomechanics: a decade later. *Journal of Cataract & Refractive Surgery*, 40(6):857, 2014.

[247] Giuliano Scarcelli, Roberto Pineda, and Seok Hyun Yun. Brillouin optical microscopy for corneal biomechanics. *Investigative ophthalmology & visual science*, 53(1):185–190, 2012.

[248] Cynthia J Roberts and William J Dupps Jr. Biomechanics of corneal ectasia and biomechanical treatments. *Journal of Cataract & Refractive Surgery*, 40(6):991–998, 2014.

[249] Carolyn Y Shih, Joshua S Graff Zivin, Stephen L Trokel, and James C Tsai. Clinical significance of central corneal thickness in the managementof glaucoma. *Archives of ophthalmology*, 122(9):1270–1275, 2004.

[250] Michaël JA Girard, J-K Francis Suh, Michael Bottlang, Claude F Burgoyne, and J Crawford Downs. Scleral biomechanics in the aging monkey eye. *Investigative ophthalmology & visual science*, 50(11):5226–5237, 2009.

[251] Andrea Curatolo, Judith S Birkenfeld, Eduardo Martinez-Enriquez, James A Germann, Geethika Muralidharan, Jesús Palací, Daniel Pascual, Ashkan Eliasy, Ahmed Abass, Jedrzej Solarski, et al. Multi-meridian corneal imaging of air-puff induced deformation for improved detection of biomechanical abnormalities. *Biomedical optics express*, 11(11):6337–6355, 2020.

[252] Judith Sophie Birkenfeld, Alejandra Varea, Andrea Curatolo, Ashkan Eliasy, Ana Maria Gonzalez, Eduardo Martinez-Enriquez, Ahmed Abass, Bernardo Lopes, Ahmed Elsheikh, Jesus Merayo-Lloves, et al. Corneal biomechanical parameters in healthy and early-stage keratoconus eyes from cross-meridian air-puff deformation oct. *Investigative Ophthalmology & Visual Science*, 63(7):2394–A0197, 2022.

[253] David Bronte-Ciriza, Judith S Birkenfeld, Andrés de la Hoz, Andrea Curatolo, James A Germann, Lupe Villegas, Alejandra Varea, Eduardo Martínez-Enríquez, and Susana Marcos. Estimation of scleral mechanical properties from air-puff optical coherence tomography. *Biomedical Optics Express*, 12(10):6341–6359, 2021.